TECHNISCHE UNIVERSITÄT WIEN
Vienna | Austria

DISSERTATION

Architectural Design of Transition Metal Nitride Thin Films for Improved Mechanical or Electrical Properties

carried out for the purpose of obtaining the degree of Doctor technicae (Dr. techn.), submitted at TU Wien, Faculty of Mechanical and Industrial Engineering, by

Zecui Gao, MSc

[redacted]

Under the supervision of

Univ.Prof. Dipl.-Ing. Dr. **Paul Heinz Mayrhofer**

Institute of Materials Science and Technology-E308, TU Wien

Vienna, August 2022

Reviewed by

Prof. Zaoli Zhang

Erich Schmid Institute of Materials Science

of the Austrian Academy of Sciences

Jahnstrasse 12, 8700 Leoben, Austria

Assoc.Prof. Davide Sangiovanni

Department of Physics, Chemistry, and Biology

Linköping University

SE-58183 Linköping, Sweden

This work was supported by the Austrian COMET Program (project K2 InTribology1, no. 872176) and the Chinese scholarship funding (File No. 201908440933).

I confirm, that going to press of this thesis needs the confirmation of the examination committee.

Affidavit

I declare in lieu of oath, that I wrote this thesis and performed the associated research myself, using only literature cited in this volume. If text passages from sources are used literally, they are marked as such.

I confirm that this work is original and has not been submitted elsewhere for any examination, nor is it currently under consideration for a thesis elsewhere.

I acknowledge that the submitted work will be checked electronically-technically using suitable and state-of-the-art means (plagiarism detection software). On the one hand, this ensures that the submitted work was prepared according to the high-quality standards within the applicable rules to ensure good scientific practice "Code of Conduct" at the TU Wien. On the other hand, a comparison with other student theses avoids violations of my personal copyright.

Date *Signature*

Acknowledgement

During my time as a PhD student, I have received the support and motivation from my colleagues, family, and friends. I would like to extend my true gratitude to them.

Thank you Professor Paul Heinz Mayrhofer for having me on board of your group, providing me with a lot of patience, and trusting me. You are a role model I will always learn from. Your passion for science always inspires me. You have rigorous scientific research methods, keen academic insight, a diligent work style and the spirit of innovation and pioneering. I feel so lucky to be part of the great research group you built.

To Dr. Julian Buchinger and Nikola Koutná, you are the best friends, colleagues and mentors I could have hoped for. You have witnessed every tiny improvement in my scientific work and sport and are always happy for me. Our time together—in the office and multiple runs, swims, rock climbing, and skiing—has profoundly shaped my development as a scientist and as a person. In particular, Julian directed most of the experimental equipment I used, and Nikola supported all the computer simulation parts of this work.

Thanks to all the postdocs who supported me along the way, namely David Holec, Helmut Riedl, Rainer Hahn, Vincent Moraes, Alexander Kirnbauer, Andreas Kretschmer and Matthias Bartosik. Thank you to each of you for your tireless efforts in this group to help me with various issues.

To my colleagues Michael Derflinger, Chun Hu, Jian Jiang, Barbara Schmid, Rebecca Janknecht, Balint Hajas, Lukas Zauner, Oliver Hudak, Christoph Fuger, Ahmed Bahr, Anna Hirle, Sophie Richter, Wei Zhao, Alex Casatta, Ludwig Enzlberger, Stefan Kagerer, Thomas Glechner, Antonia Wagner, and Lukas Löfler. I am delighted to be part of such a talented, motivated, hard-working, friendly, and productive collective of young researchers. I am confident that you will have an exciting future.

Thanks to Philipp Ertelthaler for keeping the lab running and avoiding chaos. All the

work you do in the lab is very commendable. Thanks to Philip Kutrowatz for my excellent TEM and FIB samples, and Tomasz Wojcik for his patient TEM investigations.

Also, my special thanks are owed to my roommate Qian Zheng for always keeping me well fed.

Finally, I would like to thank my family and friends in China for their emotional and spiritual support over the years. We haven't seen each other for three years since the outbreak of the coronavirus.

Preface

The following list contains papers that were prepared, submitted, or published within this thesis.

Paper #1

Ab initio supported development of TiN/MoN superlattice thin films with improved hardness and toughness

Z. C. Gao, J. Buchinger, N. Koutná, T. Wojcik, R. Hahn, P. H. Mayrhofer

Acta Materialia **231**, (2022), https://doi.org/10.1016/j.actamat.2022.117871

Paper #2

The influence of bilayer periods and bilayer ratios on the mechanical properties of TiN/MoN superlattice thin films

Z. C. Gao, J. Buchinger, R. Hahn, C. Zhuo, Z. L. Zhang, P. H. Mayrhofer

Manuscript

Paper #3

Synthesis and electrochemical properties of nanoporous CrN thin film electrodes for supercapacitor applications

Z. C. Gao, Z. X. Wan, Z. T. Wu, X. L. Huang, H. Q. Li, T. F. Zhang, P. H. Mayrhofer, Q. M. Wang

Materials & Design **209**, (2021), https://doi.org/10.1016/j.matdes.2021.109949

Paper #4

Nanostructured zig-zag γ-Mo_2N thin films produced by glancing angle deposition for flexible symmetrical solid-state supercapacitors

Z. C. Gao, T. F. Zhang, Q. M. Wang, P. H. Mayrhofer

submitted to Materials & Design on the 17.07.2022

Futher Co-Author publications

Paper #1

Atomic-scale understanding of the structural evolution in TiN/AlN superlattices during nanoindentation— Part 1: Deformation.

Z. Chen, Y. H. Zheng, Y. Huang, **Z. Gao**, H. P. Sheng, M. Bartosik, P. H. Mayrhofer, Z. L. Zhang

Acta Materialia (2022) 118008, https://doi.org/10.1016/j.actamat.2022.118008

Paper #2

Atomic-scale understanding of the structural evolution in TiN/AlN superlattice during nanoindentation—Part 2: Strengthening

Z. Chen, Y. H. Zheng, Y. Huang, **Z. Gao**, H. P. Sheng, M. Bartosik, P. H. Mayrhofer, Z. L. Zhang

Acta Materialia (2022) 118009, https://doi.org/10.1016/j.actamat.2022.118009

Table of Contents

Abstract

Transition metal nitrides (TMNs) have found widespread use as protective coating materials, combined with reasonably high mechanical, thermal, and chemical resilience with the highest recorded toughness values among all conventional ceramic thin film material classes (i.e., borides, carbides, nitrides, and oxides). Synthesis and structure strategies are continuously developing to cater to the steadily rising requirements of mechanically, chemically, and/or thermally demanding environments. On the one hand, this project mainly aims to expand our understanding of the mechanical behavior of transition metal nitride (TMN) superlattice (SL) thin films by employing advanced micromechanical characterization methods. This will provide information on these materials' mechanical characteristics (strength, deformation limit, stiffness, toughness) under clearly defined loading conditions. TiN/MoN SLs, featuring two materials with similar lattice parameters, but highly disparate elastic moduli, are selected to investigate the impact of bilayer ratios and periods on the mechanical behavior TMN SLs.

On the other hand, this project also aims to expand TMNs in the application of supercapacitor electrode materials. TMNs are very promising due to their high conductivity and structural and chemical stability, providing excellent power efficiency and super long cycle life. For such applications, highly porous structures are needed. Here, two different techniques for preparing such porous structures are presented. One is a spongy porous CrN, which is obtained by chemically removing the Ni phase from a CrN-Ni composite coating. Another one is a zig-zag structured MoN electrode produced by glancing angle deposition.

All of these different coating architectures are successful in their specific fields. The SL structures show a superlattice effect in mechanical and tribological properties improvement, e.g., improved hardness, fracture toughness, and friction coefficient. The porous structures show highly improved electrochemical properties of charging capacitance.

Kurzfassung

Übergangsmetallnitride (englisch: Transition Metal Nitrides, TMNs) finden breite Anwendung als Schutzbeschichtungen, die sich durch eine relativ hohe mechanische, thermische und chemische Belastbarkeit auszeichnen und unter allen herkömmlichen keramischen Dünnschichtwerkstoffen (d. h. Boride, Carbide, Nitride und Oxide) die höchsten Zähigkeitswerte aufweisen. Herstellungs- und Strukturstrategien werden kontinuierlich weiterentwickelt, um den stetig steigenden Anforderungen in mechanisch, chemisch und/oder thermisch anspruchsvollen Umgebungen gerecht zu werden. Dieses Projekt zielt einerseits darauf ab, das Verständnis des mechanischen Verhaltens von Übergitter-Dünnschichten aus Übergangsmetallnitriden (TMNs) durch den Einsatz fortschrittlicher mikromechanischer Charakterisierungsmethoden zu erweitern. Dies liefert Informationen über die mechanischen Eigenschaften dieser Materialien (Festigkeit, Verformungsgrenze, Steifigkeit, Zähigkeit) unter klar definierten Belastungsbedingungen. TiN/MoN-SLs mit zwei Materialien mit ähnlichen Gitterparametern, aber sehr unterschiedlichen Elastizitätsmoduln, werden ausgewählt, um den Einfluss von Doppelschichtverhältnissen und -perioden auf das mechanische Verhalten von TMN-SLs zu untersuchen.

Andererseits zielt dieses Projekt auch darauf ab, TMNs für die Anwendung als Elektrodenmaterial in Superkondensatoren zu erforschen. TMNs sind aufgrund ihrer hohen Leitfähigkeit und ihrer strukturellen und chemischen Stabilität sehr vielversprechend und bieten eine hervorragende Energieeffizienz und eine sehr lange Lebensdauer. Für solche Anwendungen werden hochporöse Strukturen benötigt. Hier werden zwei verschiedene Techniken zur Herstellung solcher porösen Strukturen vorgestellt. Bei der einen Methode handelt es sich um ein schwammiges, poröses CrN, das durch chemisches Entfernen der Ni-Phase aus einer CrN-Ni-Verbundbeschichtung gewonnen wird. Die andere Technik ist eine zick-zack-strukturierte MoN-Elektrode, die durch Abscheidung im flachen Winkel hergestellt wird.

Alle diese unterschiedlichen Dünnschichtarchitekturen sind in ihren jeweiligen Bereichen erfolgreich. Die SL-Strukturen zeigen einen Übergittereffekt, der zur Verbesserung der mechanischen und tribologischen Eigenschaften, z. B. verbesserte Härte, Bruchzähigkeit und Reibungskoeffizient, führt. Die porösen Strukturen zeigen stark verbesserte elektrochemische Eigenschaften der Ladekapazität.

1. Introduction

Conventional ceramic thin film materials, especially, the transition metal nitrides (TMNs), have been auspicious in protective coatings for decades, as they provide various favorable mechanical and chemical properties, such as outstanding adhesion, hardness, corrosion resistance, oxidation resistance, wear resistance, low friction coefficient, and exceptional thermal and/or electrical conductivity [1]. Typically, TMNs have the desired face-centred cubic (FCC) crystal structure, as well as a combination of metallic, ionic, and covalent chemical bonds [2]. Their hardness values are commonly around 25-30 GPa [3], which slightly falls short against most conventional carbide- and diboride-based coating materials. Moreover, TMN hard coatings, and also all other hard protective coating materials, are plagued by critically low intrinsic fracture toughness.

Fracture toughness is an ability of a material to absorb energy during fracturing, especially, under extreme loads. Ideally this is achieved via a combination of high strength and plasticity. The fracture toughness is a critical factor in evaluating the reliability and longevity of a material and protective coatings in particular. In the past decades, most toughness mechanisms studies relied on qualitative toughness estimations based on indentation-based methods, which are heavily influenced by residual film stresses. Recently, owing to the advent of the micromechanical testing method, which is a reliable measurement for coatings on the microscale (e.g., after removing the substrate), our understanding of the toughness-related mechanisms and properties is more complete. Thus, more potential fracture toughness enhancement strategies can be developed. For now, the reported strategies include but are not limited to phase transformation effects [4,5], grain boundary strengthening [6], alloying and/or vacancy tuning [7], and superlattice (SL) structures [8]. Among them, the superlattice is perceived to be the most auspicious one, since it shows a simultaneously improved fracture toughness and hardness, and may combine this with even a lower friction coefficient. While, most other toughness-enhancing

mechanisms inevitably sacrifice some of the more beneficial properties of TMNs.

Koehler firstly proposed the SL structure in the 1970s [9]. He predicted that when two materials can be epitaxially grown in an alternate layer structure and their bilayer periods are reduced to a certain value, they can resist dislocation generation and gliding, thus forming a strong solid. This hard-enhancing theory was soon proved in some metal/metal and ceramic/ceramic superlattice coatings, such as Co/Ag [10], and TiN/VN [11]. Recently, the toughness-enhancing effect of the superlattice structure was discovered for TiN/CrN [12], TiN/WN [8], TiN/AlN [13], TiN/(Cr,Al)N [14]. For example, the TiN/WN system offers a fracture toughness of up to 4.6 MPa√m, which is a more than 50% improved value compared to common binary nitrides, which commonly exhibit ~2 MPa√m. According to these studies, the bilayer period-dependent mechanical-enhancing effect is related to lattice mismatch and elastic properties mismatch (i.e., shear moduli) between the individual layer materials. In this study, we will continue to reveal the mystery of the superlattice effect, as previous studies have definitively confirmed its existence but have failed to provide a clear origin for maximizing resilience.

Except for the SL architecture, we also produced some other interesting architectures, such as a spongy and zig-zag structure, for the application of green energy storage devices, like supercapacitors. The energy in supercapacitor is stored by achieving separation of charge in Helmholtz double layers at the interface between the surface of a conductive electrode and an electrolyte, without chemical reactions [15]. It means that the energy density mostly depends on charge absorbing sites on the electrode surface. Previous studies of TMN supercapacitors, such as TiN, CrN, MoN, VN, and NbN [16-20], have shown their potential for high power density and longevity, contributed to their excellent conductivity and chemical stability. To further contribute to the energy storage career here, several strategies for highly porous TMN coatings are proposed, including chemical etching and glancing angle deposition, for a spongy structure and zig-zag structure fabrication, respectively.

2. Materials systems

This chapter seeks to provide an overview of the most important binary and ternary TMN systems and forms the basis for material selection for research related to the superlattice project and the supercapacitor project. The overview provides the structure, composition, bonding, physical properties, electronic properties, preparation, and applications of these materials from previous studies. Based on this collated information, the materials for the SL and supercapacitor investigations were selected

2.1 Transition metal nitrides

Out of all ceramic thin film materials, transition metal nitrides offer a particularly advantageous blend of properties, such as good chemical and thermal stability, incompressibility and strength, corrosion resistance, high melting points, and electrical and thermal conductivity [21]. They are widely applied as protective coatings [22], diffusion barriers [23], in decorative and optical applications, as well as in the electronic industries [24]. The crystal structures of binary transition-metal nitrides are generally close-packed arrays of the larger metal atoms, with the smaller nitrogen atoms in the interstitial sites. Most TM nitrides commonly adopt a rock-salt (rs) structure. Additionally, they can also crystallize in a number of different structures, such as tetragonal Hf_3N_4 [25], hexagonal MoN [26], orthorhombic Ta_3N_5 [27], and rhombohedral W_2N_3 [28], depending on the window of processing conditions [13]. This structure versatility, as well as mixed chemical bonding, contribute to their multifunctional properties.

Bonding in a close-packed metallic structure involves a simultaneous contribution of covalent, ionic, and (to a lesser extent) metallic bonding to the cohesive energy. As a result, they are typically hard and relatively brittle and have high thermal and electrical conductivities and a metallic character. Some of them even display a superconductivity character. A widely accepted empirical indicator is that more

directional covalent and ionic bonding components lead to higher chemical stability and mechanical strength, while more metallic bonding contributes to better electrical conductivity, adhesion, and ductility. Because the delocalized electrons control the shearing resistance, and hence plastic deformation [29]. According to Pugh and Pettifor [30], ductile materials behave in a ductile manner when the shear-to-bulk-modulus ratio (G/B) is less than 0.5, and the Cauchy pressure is above 0 ($P_{Cauchy} = C_{12}$-C_{44}). With the help of ab initio calculations, Fig 2.1 and Table 2.1 depict some selected cubic TMNs based on these criteria. Besides, valence electron concentration (VEC) is also a toughness indicator [31]. It is understood as the number of valence electrons per formula unit (el./f.u.) and is related to shear-sensitive orbital (d-t_{2g} metal/metal) interactions. Afterwards, Balasubramanian et al. [32] linked the brittle-to-ductile transition to VEC = 10. With the VEC increasing, the shear modulus G and elastic constant C_{44} decrease, suggesting an improved ductility, but with a reduced isotropic elastic modulus and hardness. Only within a narrow region between VEC = 9 and 10, rock-salt nitrides are ductile, and also exhibit high hardness, mechanical and dynamical stability. A further VEC increase induces a mechanical instability transition [33]. Experimentally reported physical properties of TMN films vary widely and largely depend on the composition, the presence and density of vacancies and voids, the shape and size of grains, and the film purity.

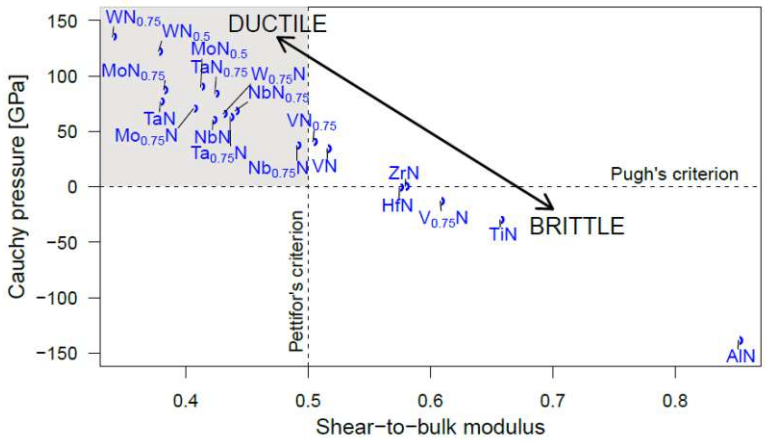

Fig. 2.1: Ab initio calculated brittleness/ductility map for rock-salt transition metal nitrides [34].

Systems	E_f	a	C_{11}	C_{12}	C_{44}	B	G	E	CP	G/B
AlN	-1.26	4.069	426	168	307	257	217	507	-138	0.85
TiN	-1.77	4.255	573	132	162	279	183	451	-30	0.66
ZrN	-1.91	4.618	514	117	118	250	145	364	-1	0.58
HfN	-1.80	4.538	577	121	121	273	157	395	0	0.57
VN	-1.01	4.130	599	163	128	308	159	406	34	0.52
NbN	-1.00	4.426	647	142	82	310	131	345	60	0.42
TaN	-0.91	4.427	717	146	69	340	127	338	77	0.38
CrN	-0.27	4.057	576	209	8	332	45	130	202	0.14
$Ta_{0.75}N$	-1.03	4.305	417	154	91	242	105	276	84	0.42
$TaN_{0.75}$	-0.96	4.381	512	192	108	299	127	333	71	0.41
$Mo_{0.75}N$	-0.22	4.203	656	151	80	319	130	329	87	0.38
$MoN_{0.75}$	-0.27	4.282	643	164	81	279	104	277	98	0.37
$MoN_{0.5}$	-0.23	4.211	508	196	106	300	124	326	90	0.41
TiN/AlN	-1.57	0.19	500	144	209	263	192	464	-56	0.73
TiN/$Ta_{0.75}N$	-1.55	0.05	614	132	144	277	173	431	-9	0.63
TiN/$MoN_{0.5}$	-1.28	0.04	576	133	70	285	124	326	91	0.44
TiN/$WN_{0.5}$	-1.55	0.05	614	132	144	277	173	431	-9	0.63

Table 2.1: Ab initio calculated formation energies, E_f (in eV/at), lattice parameters, a (in Å), elastic constants, C_{ij} (in GPa), polycrystalline bulk, shear, and Young's moduli, B, G, and E (all in GPa), and Cauchy pressures CP (in GPa) for the group IV-VI nitrides, and AlN, and some superlattices (all with fcc structure). Additionally, the shear-to-bulk modulus ratio, G/B, is given as well. The vacancy-free MoN and WN are mechanically unstable; hence their off-stoichiometric counterparts are presented. Lattice parameters mismatch (Δa) of superlattices are presented instead of Lattice parameters. These calculated values are from Refs [34,35].

2.1.1 Group IV nitrides

TiN, ZrN, and HfN are the most stable nitrides among TMNs with the lowest nitrogen equilibrium pressures [36]. They have similar structures and properties: crystallization in the rock-salt phase, melting points above 3000 K (at ambient conditions), chemical stability, high mechanical strength, and good wear resistance [37]. Therefore, they are widely suitable for cutting tools (as protective coatings of tools made of steel or hard

metals), corrosion and abrasion resistant layers for optical components [38], and diffusion barriers in semiconductor technology [39]. Moreover, because of their striking golden color, they are also popular for decorative purposes like for jewelry with excellent scratch resistance [40]. TiN and HfN are superconducting materials, with critical temperatures of 18 and 9.18 K [41,42], respectively. They are also potential in electronics, such as supercapacitor electrode materials [43,44]. Another typical application of TiN is for implants, prostheses and surgical instruments, due to its biocompatibility and polarization resistance [45]. In microelectronics as well as photovoltaics, TiN thin films are also used as diffusion barriers for noble metals such as Ag and Cu.

TiN (as well as other TMNs) are commonly synthesized by unbalanced direct current magnetron sputtering (DCMS), via sputtering of a metal (Me) target in a mixed (Ar+N_2) atmosphere, or non-reactively sputtering of a MeN compound target in a pure Ar atmosphere. The processing conditions, such as the character of the substrate, the partial pressures of the involved gases, the overall pressure in the reaction chamber, as well as the discharge current density, highly influence the microstructure and morphology of TMN thin films. Thus, the exact values of the individual mechanical properties fluctuate noticeably from literature to literature. Usually, a coating with more refined size of columnar (i.e., more equiaxed) grains and a lower density of voids offers an improved overall mechanical property. For instance, TiN could be optimized by applying a relatively low partial pressure of N_2 gas (~30 % of the total pressure) and a high discharge current density. More details about DCMS and film growth will be introduced in the next chapter.

Among the transition metal nitrides, TiN has traditionally inspired and been studied extensively throughout the past decades, attributed to the favorable mixture of all the above-mentioned properties found in TiN. Under equilibrium conditions, TiN_x prefers to form a cubic rock-salt (NaCl, B1 structure) like structure with a wide (N/Me ratio x between 0.67 and 1.3) single-phase field [46]. Ideally, a stoichiometric TiN features a

lattice parameter of approximately 4.25 Å (Ångström: 10^{-10} m), which can vary slightly depending on the residual stress [46]. The preferred crystallographic growth orientation of TiN is highly dependent on the underlying substrate and the processing conditions. Compared to TiN, ZrN and HfN have garnered relatively little attention and are rather used for niche applications. Under equilibrium conditions, the lattice parameters of stoichiometric rs-ZrN and rs-HfN are 4.61 and 4.53 Å, respectively [47]. For polycrystalline ZrN_x, experimentally investigated lattice constants vary from 4.57 to 4.68 Å[48]. Besides the B1 cubic rock-salt phase, ZrN and HfN also have CsCl (B2, *Pm-3m*) and zincblende (B3, *F43m*) type phases, both possessing cubic symmetry. Theoretical analysis confirms the stability trend of phases from most stable to least stable as B1 > B2 > B3 [49].

As shown in Table 2.1, the calculated polycrystalline Young's modulus *E* of rs-TiN, rs-ZrN, and rs-HfN are approximately 451, 364, and 395 GPa, respectively. Correspondingly, their calculated polycrystalline shear moduli *G* are approximately 183, 145, and 157 GPa, respectively. They are relatively brittle because their *G/B* is above 0.5 and their Cauchy pressures is less than 0. The experimentally gauged elastic modulus and hardness of TiN is from 500 - 640 GPa and 20 - 30 GPa at the stoichiometric composition, respectively. For polycrystalline ZrN_x, its hardness is from 15 to 30 GPa, and elastic modulus is from 267 to 424 GPa [50,51]. For a single crystal ZrN (100), its nanoindentation hardness and modulus are at approximately 22.5 GPa and 450 GPa [52]. Single crystal and stoichiometric HfN (001) coating has a lattice constant of 4.52 Å, and nanoindentation-determined hardness and elastic modulus of 25.2 $\pm$ 0.7 GPa and 450 $\pm$ 9 GPa, respectively [53]. The Poisson's ratio ν of TiN, ZrN, and HfN bulk material was determined to be 0.3, 0,19, and 0.35 [36,54], which gives their corresponding shear moduli as 200, 189, and 197 GPa, respectively, according to the following equation:

$$\mathrm{G} = \frac{E}{2(1+\nu)} \qquad (2.1)$$

The fracture toughness of thin TiN coatings produced by reactive DC magnetron

sputtering is broadly studied by micro-mechanical experiments, and mostly at 2.0-3.0 MPa√m [55,56]. The strain energy release rate G_C of thin stoichiometric ZrN coatings were deduced to 29.9 ± 0.8 J/m^2, and the corresponding fracture toughness estimation is 3.33 MPa√m [57]. The fracture toughness of reactive DC magnetron sputtered HfN coatings is as low as 0.3 MPa√m, which is evaluated by a cube corner indentation [58]. In contrast to this, a hot isostatically pressed bulk HfN had a fracture toughness of about 4.5 MPa√m [59].

2.1.2 Group V nitrides

As expected, the TMNs in the group V (VN, NbN, TaN) can also be synthesised via physical vapour deposition techniques, and they also possess exceptional corrosive, tribological, and/or mechanical properties.

VN is also a typical cubic rock-salt structured nitride, with a lattice parameter of 4.13 Å. Compare to TiN, it has a lower melting point (T_m is 2350 K) and weaker mechanical strengths in both experimental and computational studies. Its experimental hardness and indentation moduli values are below 20 and 220 GPa, respectively, even when prepared with a high bias voltage of -150 V during reactive DC magnetron sputtering depositions [60]. The calculated Young's and shear moduli of polycrystalline VN are gauged at around 400 and 150 GPa, respectively. The shear modulus of VN of this arrangement was calculated to be 186 GPa, under the Poisson's ratio measured to be 0.28. However, VN has been proven to have high-temperature wear resistance and a decreased friction coefficient at high-temperature conditions by forming a lubricious oxide, V_2O_5 (T_m = 690 °C), which easily is in liquid form during wear applications [61]. Therefore, the combination of VN with some more mechanically resilient TMNs is popular for high-speed machining without lubrication. It utilizes the advantage tribological properties and overcomes the relatively low hardness of VN. For instance, VN could exist as an alloying compound in solid solution films (such as (Ti,Al,V)N and (Cr,Al,V)N [62]), or in superlattices (i.e., (Ti,Al)N/VN [63], TiN/VN [11]). The hardness of TiN/VN can even reach 56 GPa with a 5.2 nm bilayer period. A ternary

alloy Ti-V-N, containing 23% VN, exhibits a Young's modulus of 307 GPa, and fracture toughness (K_{IC}) of 0.4 $MPam^{0.5}$[64].

NbN and TaN are way more complicated compared to VN. Under different deposition conditions, NbN crystallizes with different phases and even a mixed phase composition. A report mentions that with increasing nitrogen partial pressure during the NbN deposition, the chemical and phase composition of NbN_x transforms from a hexagonal β-Nb_2N (7% P_{N2}), to a hexagonal δ'-NbN (21% P_{N2}), then to a cubic δ-NbN (37% P_{N2}) [65]. Accordingly, the hardness increased from 35 GPa (β-phase) to 40 GPa (δ'-phase), then dropped to 25 GPa for the cubic δ phase. The relative higher hardness of hexagonal β-phase than cubic phase is due to more covalent bonding and higher film density. Also, the δ'-phase films show more compressive residual stresses (3.5 GPa) than the δ and β phase films. Cubic NbN film unveils a lattice parameter of 4.46 Å. Its Young's, bulk, and shear moduli are reported to be 350 GPa, 354 GPa, and 161 GPa, respectively [66]. NbN is also a super-conducting material with a high critical temperature of 14.5 K, when deposited at a sufficiently low temperature (<90 °C) with 15 % P_{N2} (1.06 Pa total pressure) [67]. A study of NbN/MoS_2 superlattice films produced by reactive magnetron sputtering shows an improved hardness and elastic modulus (30.4 GPa and 431 GPa, respectively) compared to the monolithic NbN films (22.8 GPa and 354 GPa, respectively) deposited under the same conditions. The template effect lets the typically hexagonal close packed (hcp)-structured MoS_2 transform to an fcc structure and grow epitaxially with NbN, thereby greatly decreasing the friction coefficient to 0.20–0.30[68]. Analyses of the fracture toughness of NbN have not been conducted yet.

Similar to NbN, TaN also has a great variety of stable and metastable phases with a wide range of phase compositions depending on the nitrogen content [69]. There are three stoichiometric TaN structures that are commonly observed and utilized: the fcc δ phase (a = 4.36 - 4.55 Å), the hexagonal ε (a ≈ 2.99 Å, c ≈ 3.05 Å) and hexagonal θ (a ≈ 3.02 Å, c ≈ 2.97 Å) phases [70]. In this thesis, the elusive B1 δ-TaN phase will be

examined. The synthesis of this structure is very challenging, because the energetically preferred crystal structure of TaN is the stoichiometric hcp ε structure, single-phase δ-TaN is only possible when sputtered under very specific conditions [71]. TaN shows a clear trend in mechanical parameters: δ-TaN provides the highest values for hardness, Young's modulus, and shear modulus of 37, 676, and 213 GPa respectively; θ-TaN shows the lowest readings (hardness, Young's modulus, and shear modulus of ~20.3, 642, and 139 GPa); ε-TaN is mostly in between of δ-TaN and θ-TaN [72]. In addition to these three technically important mononitride phases, several other phases also exist. Under a low nitrogen content and deposition temperature, hexagonal Ta_2N is obtained, as well as the orthorhombic phases Ta_4N and $Ta_6N_{2.5}$. Contrastingly, higher nitrogen partial pressure enables the formation of hcp-Ta_5N_6, tetragonal Ta_4N_5, and orthorhombic Ta_3N_5 [73]. With increasing nitrogen content, TaN_x changed significantly from highly conductive (10^{-1} mΩ cm) to insulating (10^3 mΩ cm) [74]. Therefore, TaN_x can meet various performance requirements of different industries, such as protective layer for magneto-resistance sensors, and diffusion barrier materials for Cu interconnects [72]. The fracture toughness of TaN is still quite unexplored, in this thesis we firstly report that for B1 δ-TaN phase the fracture toughness lies at ~3.2 MPa√m [75].

2.1.3 Group VI nitrides

CrN is another popular member in the TMN family and well-established for industry applications. It shares generally favorable properties of excellent mechanical, thermal and physical properties the same as its category materials, as well as interdependent between morphological, structural, and mechanical behavior [76]. Due to the superior oxidation resistance of CrN (up to 900 K) when compared with TiN, CrN is highly valued as a protective and anti-wear coating, specifically in plastic injection and extrusion systems [77]. The lattice parameters of the B1 NaCl structure CrN are typically between 4.14 Å and 4.19 Å [47], a bit larger than the calculated value of 4.06 Å in Table 3.1. This is because, Table 3.1 only presents the non-magnetic values, while CrN is

paramagnetic at room temperature and anti-ferromagnetic below the Néel temperature. Typical experimental Young's modulus and hardness values of cubic CrN are approximately 410 GPa and 28.6 GPa, respectively. Hardness values up to 38.4 GPa could be obtained for stoichiometric CrN [77]. Hardness values also up to 30 GPa for off-stoichiometric CrN_y ($0.5 < y < 0.9$), when the system consists of a phase mixture of hcp-Cr_2N and fcc-CrN, and the harder hexagonal Cr_2N grains embedded in the matrix of cubic CrN, hindering dislocation movement and crack propagation [78]. The Poisson's ratio of a fcc-CrN coating is typically 0.28, which gives a shear modulus of 156 GPa (using Equation 2.1). The fracture toughness of a sputtered fcc-CrN coating was reported to be 3.13 MPa$\sqrt{m}$ valued by microcantilever bending tests [79].

MoN and WN also have some similar structures and properties. Both of MoN and WN are very sensitive to the nitrogen content as well, therefore, their physical properties are also strongly governed by the nitrogen partial pressure used during deposition. For off-stoichiometric composition, there are three stable phases of them in thermal equilibrium, as depicted in Fig. 3.5. The high-temperature cubic-structured γ-TM_2N (*Fm-3m*) yet with 50% randomly distributed vacancies at the N-sublattices, and it exhibits excellent mechanical and tribological properties, therefore applied as wear-resistant coating [42]. The low-temperature tetragonal-structured β-TM_2N ($I4_1/amd$) also yet with 50% nitrogen vacancies, but ordered [80,81]. Tetragonal t-TM_2N is constructed from perfect cubic B1-TMN by removing 50% of the nitrogen atoms in the [100] and [010] directions [80]. There are not many studies about t-TM_2N yet.

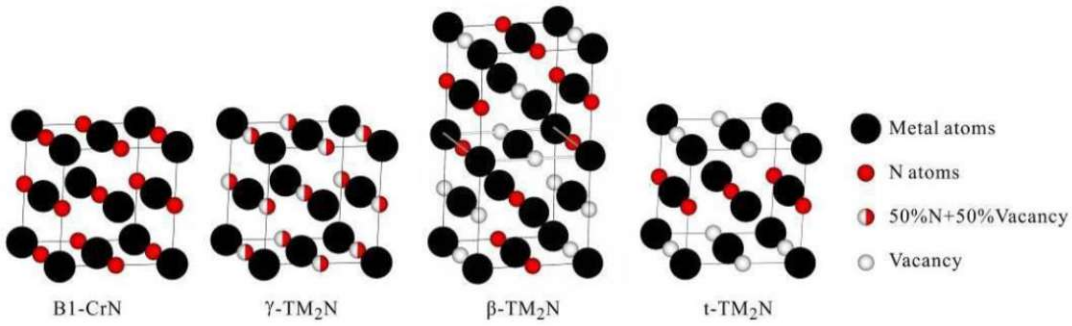

Fig. 2.2: Crystal structure of cubic B1-CrN and γ-TM_2N, β-TM_2N, and t-TM_2N, TM = Mo and W [82]

There are also some metastable MoN with 1:1 stoichiometry, such as ξ-MoN and δ_3-MoN. The cubic-structured ξ-MoN is a vacancy-rich NbO-prototype (*Pm-3m*) phase [83], which is an NaCl-type structure with 25% vacancies at each sublattice [84]. δ_3-MoN (*P6$_3$mc*) is one of the three hexagonal structures (another two are δ_1 and δ_2-MoN) with trigonal Mo clusters and an ordered array of nitrogen atoms, so the atomic arrangement can be described as a slightly deformed superstructure of NiAs. The lattice constants of all these MoN phases are listed in Table 1 of Ref. [26]. Something interesting is that the β-Mo_2N structure is often considered as a tetragonal modification of the cubic γ-Mo_2N phase (a = 0.42 nm) with the lattice constant c doubled, and hexagonal δ_3-MoN has very close a and c lattice constants (a = 0.57 nm, c = 0.56 nm). MoN family is particularly used for superconducting materials: ξ-MoN has the highest superconducting temperature among all refractory binary carbides and nitrides of T_c = 29.4 K, and also more than the hexagonal δ_3-MoN (T_c = 13.8 K), the cubic γ-Mo_2N (T_c = 5–7 K), and the tetragonal β-Mo_2N (T_c = 5.2 K) [25]. MoN exhibit hardness values ranging from 20 to 34 GPa. The δ_3-MoN exhibits a higher hardness of ~33 GPa than that of γ–MoN_x (~23 GPa) because of stronger covalent bonding [42]. Experimental investigated bulk and Young's modulus of cubic MoN_x are at approximately 352 GPa and 462 GPa, respectively. Thus, its shear modulus is estimated to be 180 GPa, according to the following relationship:

$$G = \frac{3KE}{9K-E} \qquad (2.2)$$

The fracture toughness of a DC magnetron sputtered cubic MoN_x coating was firstly reported to be 2.8 ± 0.2 MPa$\sqrt{m}$ valued by free-standing microcantilever bending test in this work [85].

Similarly, depending on the nitrogen content, WN_x has also a big family with a lot of phases as MoN_x, and no perfectly stoichiometric cubic WN exists. Structures of tungsten nitride include a face-centered cubic rock-salt γ-W_2N phase (a = 4.181 Å), a hexagonal WN, a monoclinic WN_2 phase, orthorhombic WN_3, as well as rhombohedral W_2N_3 [28]. The rock-salt structure stabilized by nitrogen vacancies may reportedly occur

for N/W ratios from 0.35–0.93. When x increases from 0.35 to 0.7, *H* decreases from 32 to 26 GPa, at the same time, *E* decreases from 305–275 GP. But with further increased nitrogen content, x > 0.75, *H* increases again due to the formation of a hexagonal phase, also the elastic modulus *E* increases to 430 GPa [86]. The bulk modulus also decreases with the increase in the nitrogen content for the tungsten nitrides [87]. Fracture toughness analyses of sputtered fcc-W_2N films report values of ~3.2 MPa$\sqrt{m}$ [8].

2.2 Post Transition Metal Nitrides

Aluminium is outside of the transition metal section in the periodic table, thus, is classified as a post transition metal. Under equilibrium conditions, AlN unit cell can adopt both a wurtzite structure and a cubic zinc-blend. Experimental measurements estimate the lattice parameter (a) of the zinc-blend structure AlN to be approximately 4.37 Å. The c/a ratio of the wurtzite structure is about 1.60 (c = 4.98 Å). The w-AlN has unusually high thermal conductivity, high electrical resistance, a similar thermal expansion coefficient with silicon, and piezoelectric properties, which is particularly suitable for electronic devices, especially, the semiconductor industry. Below 1000 K, w-AlN is completely stable in air, but above this temperature it starts reacting with air and oxygen, forming an inert amorphous aluminum oxide layer (Al_2O_3), which can protect the nitride from further oxidation up to 1800 K [88]. Conventional binary hard coatings, such as TiN and CrN, are limited to oxidation resistance to ~800 K. Such excellent oxidation-resistant ability of AlN is promising in temperature demanding industries, such as high-speed cutting tools and thermal barrier coatings. However, the poor mechanical properties of the hexagonal w-AlN, which evolves at higher temperatures, limits its progress.

NaCl-AlN is considered to be a metastable compound, it is only stable under high pressure of 16–17 GPa [89]. But under PVD deposition conditions (non-equilibrium), quasi-binary $Ti_{1-x}Al_xN$ coating can be obtained [90,91]. Its structure strongly depends on the Al content. As shown in Fig. 2.3, the coating consists of a supersaturated fcc-

$Ti_{1-x}Al_xN$ solid solution when the Al content is below 60%. The 2.9% lattice misfit between fcc-TiN and fcc-AlN provides the possibility for a large amount of metastable supersaturated solid solutions. With a further increasing of Al content (x = 0.6–0.7), a dual-phase of fcc + hcp exists. When the Al content is more than 70%, a supersaturated hcp $Al_xTi_{1-x}N$ is formed [92]. Except for alloying, metastable fcc-AlN could also be formed by epitaxial growth above strong cubic structured TiN or CrN, when AlN is less than 2 nm-thick [93]. Still, TiN/AlN superlattice structures also exhibit much improved mechanical properties over TiN or AlN, especially with respect to fracture toughness.

Except for the outstanding oxidation resistance, age hardening mechanisms are also attributed to the improved cutting performance of (Ti,Al)N coatings [94]. When cubic (Ti,Al)N is annealed upon 1000 K, it starts spinodal decomposition and forms nanoscale Ti- and Al-enriched coherent domains of (fcc-(Ti, Al)N and fcc-(Al, Ti)N) [95]. The new phase boundaries hinder dislocations movement, thus leading to an increase in hardness [94]. However, the Al-enriched fcc-(Al,Ti)N further transforms towards w-AlN and fcc-TiN, which leads to a sharp decline in hardness as soon as the phase fraction of w-AlN is too high [96,97]. (Cr,Al)N has a similar story to (Ti,Al)N. It also exhibits a metastable supersaturated solid solution structure, and improved oxidation resistance by forming dense and adherent $(Al,Cr)_2O_3$ scales [98]. However, no obvious spinodal decomposition is reported and the formation of the hexagonal w-AlN appears earlier when annealing (Cr,Al)N in vacuum or inert atmosphere [99].

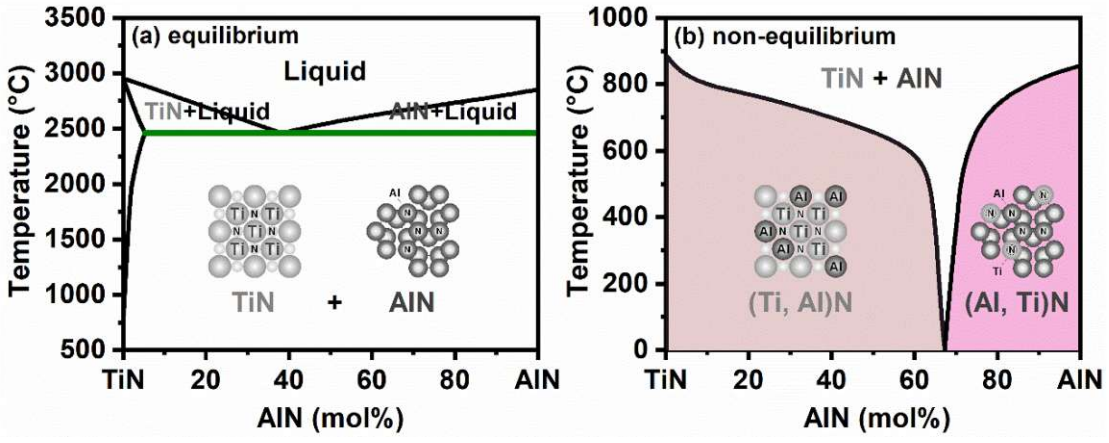

Fig. 2.3: (a) Stable phase diagram [100] and (b) metastable phase diagram of TiN–AlN system [101]

3. Thin Films Manufacturing

There are many techniques that exist for thin films fabrication, such as chemical vapor deposition (CVD) and physical vapor deposition (PVD). Here, we focus on PVD, which uses physical processes to generate a vapor from a solid or liquid target material. Magnetron sputtering is a special PVD technique that uses high-energy ion bombardment to eject atoms from the solid target material into the gas phase (i.e., generate a vapor), which fly to a substrate surface, condensing there and form a thin film. DC magnetron sputtering techniques have been extensively explored and used for thin film production since early 1970s [102]. Magnetron sputtering offers several advantages which makes it suitable not only for research and development, but also for industrial applications. Firstly, nearly all materials can be deposited by magnetron sputtering, regardless of their melting temperature and conductivity; secondly, films of alloys and compounds can be deposited while maintaining similar composition to that of the source material; thirdly, much fewer droplets are introduced into coatings, providing high-quality and high-purity optical, electrical, and decorative coatings with excellent adhesion; finally, it is environmentally friendly with low requirements for deposition temperature and chemical reactants. For non-conductive target materials, radio frequency (RF) magnetron sputtering or pulsed DC sputtering are possible options. Magnetron sputtering sources are divided into balanced and unbalanced. The coatings prepared from balanced magnetron sputtering sources are uniform and mostly used for semiconductor optical films. The coatings prepared from unbalanced magnetron sputtering sources have a strong bonding adhesion and are mostly used for wear resistant and decorative films.

Figure 3.1 shows a common setup for reactive magnetron sputtering. An intended film structure is directly determined by e.g., the deposition environment of temperature, pressure, carrier gas, bias voltage, applied cathode power, and also the surface and interfacial energies of the relevant materials, the lattice mismatch between substrate and film. In this chapter, we introduce the major steps of a DC

sputtering process, including the flux formation of the material to be deposited, the transport regime, and the film growth processes at the substrate surface.

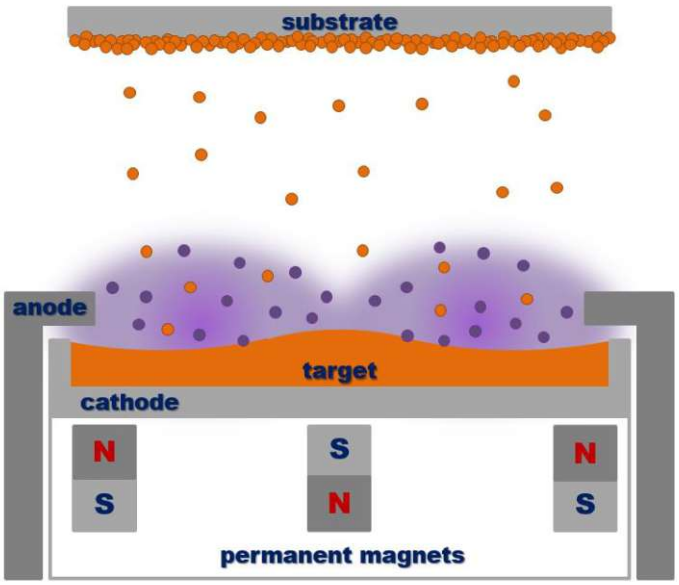

Fig. 3.1: Schematic cross-section of a magnetron sputtering system [103].

3.1 Plasma generation

The first stage is to evacuate the chamber to a high vacuum (usually in a micro torr range) to minimize the residuals of all background gases and potential contaminants. Afterwards, the chamber is refilled with a carrier gas (typically argon) as the working gas for the plasma generation, to a total pressure at the millitorr range. Then a sufficiently high voltage is applied between the electrodes, resulting in the working gas ionization and a glow discharge ignition. In addition, a set of permanent magnets is located behind the cathode/target, so the combination of the electric and magnetic fields within close proximity of the target produces the so-called $\mathbf{E} \times \mathbf{B}$ drift. The electrons (of charge q and velocity v) caught in this drift are spirally bent by the acting Lorentz force, $\mathbf{F}_L = q(\mathbf{E} + \mathbf{v}\times\mathbf{B})$. The bending and prolonging of the electrons' flight paths result in a high degree of gas ionization. The ionized Ar atoms cause collisions with nearby sputtering gas atoms, thus a relatively high-density plasma. Once the plasma is steady established, ionized atoms are accelerated towards the cathode/target,

resulting in energetic collisions with the target surface. Upon collisions, Ar ions eject ions, atoms, and atomic clusters from the target bulk material through a collisional cascade. The secondary electrons generated during the collision further ionize the Ar atoms through impact ionization. Therefore, the plasma remains under a certain pressure threshold (1-50 millitorr). At too high pressure, the electrons experience too many collisions that they are gradually stripped of kinetic energy and direction. At the same time, the discharge also becomes unsustainable, as they cannot move from the cathode to the anode in the atmosphere [104]. The plasma density can also be increased by introducing a magnetic field at the target cathode surface and using the magnetic field to confine charged particles. This allows the combination of a beneficial low total pressure while at the same time having a high plasma density at the close vicinity of the target.

For a reactive sputtering process, oxygen and/or nitrogen gas (with a controlled partial pressure) is required in the chamber during the film growth. Compared to the (RF) sputtered non-reactive oxide, nitride or oxynitride films (through sputtering of the respective compound targets), reactive DC sputtered films allow for a more precisely controlled film stoichiometry. The deposition rate of DC sputtering is generally much higher than for RF sputtering, but still mostly depends on the partial pressure of reactive gases in the chamber. With increasing the partial pressure of the reactive gas from 0 to 100%, the deposition rate decreases and the possibility of arcing (especially if non-conducting compounds form at the metallic target) increases dramatically. At the same time, the outermost surface of the metal target will transition from a pure metal state to a "transition" state, and then, a fully oxide/nitride state ("poisoned" state) [105]. The partial pressure of the reactive gas has to be lowered significantly to remove the compound layer from the target surface. Remaining the target in the "transition" state at all times can produce a good film stoichiometry at a relatively high deposition rate. A higher applied cathode power also ensures stable plasma, high ion energies, and high attraction of the Ar ions to the target surface. However, if the current is set too high, the process becomes unstable, ions are being

implanted into the target, and they penetrate too far into the target to sputter any atoms. Another potential problem at high power is overheating of the cathode. The Curie temperature of the magnets in the magnetron may be exceeded, causing them to lose their magnetization. Figure 3.2 shows the sputter yield of various elements resolved by their atomic number.

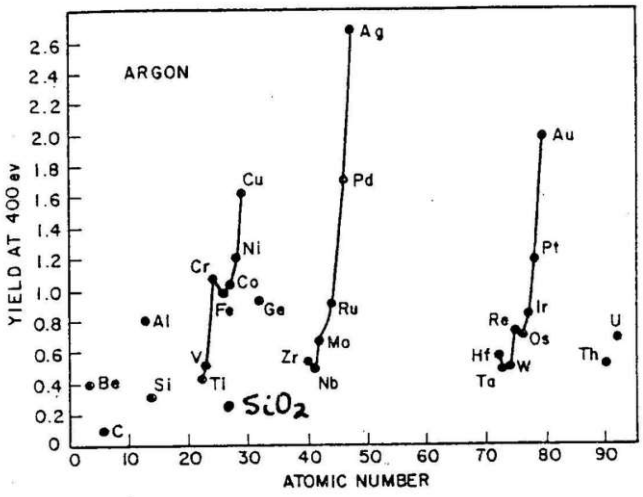

Fig. 3.2: Sputtering yield as a function of atomic number of the target [106]

The process of transporting the sputtered atoms to substrate is mainly depending on the chamber pressure and the kinetic energy of the sputtered atoms. Generally, low pressure and high kinetic energy expand the "range" of sputtered atoms and tend to provide relatively high deposition rates. The mean free path of the moving atoms increases with decreasing pressure, due to fewer collisions with other atoms before reaching the substrate surface. The transport mode can be classified as directional flux or diffusive flux depending on the energy of the sputtered atoms. The directional flux describes the motion of atoms with energies greater than ~2 eV in the plasma. Such energetic atoms scatter at small angles and retain the directional momentum and energy acquired during sputtering until they hit the substrate surface. They are mainly propagated in straight lines. Therefore, shadowing effects might happen. A way to prevent this is to rotate the substrate holder during the deposition process. The propagation of low-energy (~0.1 eV) atoms is diffusive. These atoms quickly give up

their directional momentum, so their transport to the substrate surface is governed by diffusion through the chamber. If sufficient information about the initial state of the sputtered atoms is provided, Monte Carlo simulations can be used to simulate the transport process for a given system [107].

3.2 Film Nucleation and Growth

A film grows when the sputtered atoms continually accumulate on the substrate surface until a critical nucleus size is reached. It is a highly nonequilibrium process due to the thermal effect and ionic bombarding. Typically, nucleation and growth occur simultaneously during a coating deposition. Roughly speaking, there are three growth modes: island growth (or Volmer-Weber), layer-by-layer growth (or Frank-van der Merwe), and mixed layer + island growth (or Stranski-Kastranov) [104]. More precisely, the preferred growth mode is governed by the following criteria [104].

$$\gamma_s < \gamma_f + \gamma_i - \beta\Delta\mu \; and \; \varphi \rightarrow island \; growth \; preferred$$

$$\gamma_s > \gamma_f + \gamma_i - \beta\Delta\mu \; and \; \varphi \rightarrow layered \; growth \; preferred$$

As the criteria outlined above suggest, the growth modes are mainly depending on the surface energies of the substrate (γ_s), surface energies of the growing film (γ_f), the interfacial energy between the substrate and the film (γ_i), as well as on the supersaturation of the film. Where, β is a scaling factor, Δμ is the supersaturation of the film, and φ is the wetting angle between the film and the substrate. Island growth occurs if the adatoms bond to each other stronger than to the substrate material and/or if they diffuse slowly. The nuclei grow until they coalesce to form a thin film, resulting in a polycrystalline structure and consequently contain many column and grain boundaries. Contrary, if the adatoms preferentially bond with the substrate material rather than other adatoms and/or diffuse rapidly, then the dominant epitaxial single-crystal structure is formed. This mode requires slow growth rates and high temperatures to achieve high atomic mobility. When the surface is fully wet by the layer growth, a mixed mode may occur and then islands start to form.

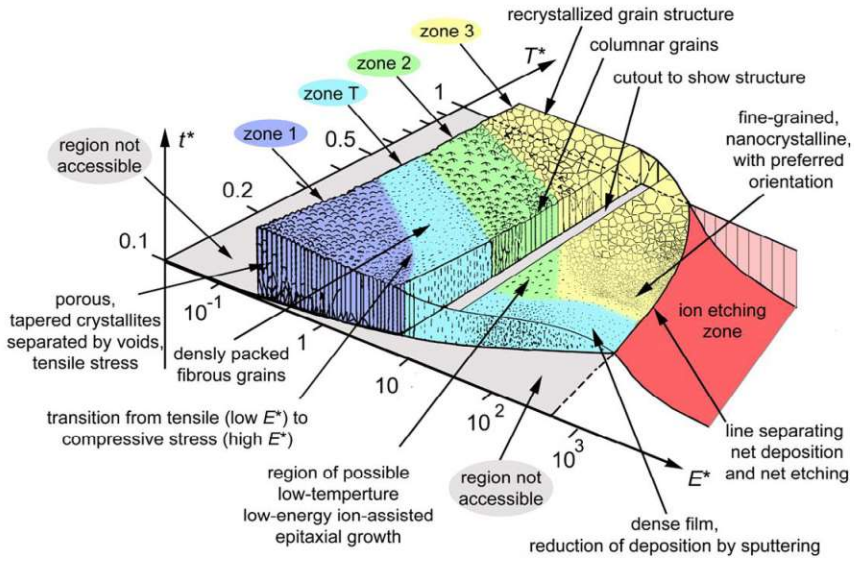

Fig. 3.3: Advanced structure zone diagram [108]

The Structure Zone Model (SZM), proposed by Messier and revised by Thornton and Anders [108], predicts a final film morphology and granular structure by the available energy of the adatoms. It is a function of various parameters, including temperature, pressure, and bias voltage. As shown in Figure 3.3, the SZM is divided into zones: zone I, zone T, zone II, and zone III. The contained parameters basically are the bombarding particle energy E* (x-axis), the melting temperature ratio between the substrate and the coating, $T^*=T_S/T_C$ (y-axis), and film thickness t (z-axis). It illustrates that increased deposition temperature and ion energy could result in an enhanced mobility of adatoms, thus the film morphology transfer from a porous and often even amorphous microstructure to a densely packed fibrous microstructure (zone T). During this time, voids are filled, and residual stress changes from tensile to compressive. With the further elevation in temperature and ion energy, as well as lowering of pressure, columnar morphologies begin to form (zone II), and finally, a recrystallized grain structure (zone III) is formed. Zone II is not an ideal morphology for protective coatings because of the long uninterrupted boundaries of columnar grains, which can act as fast diffusion channels and crack initiation sites, thus, reducing the oxidation and fracture resistance of the material.

The ion energy can be also increased by a negative bias voltage applied to the

substrate. A reasonable bias voltage of ~-50 V helps to provide sufficient kinetic energy to the particles so that most voids are filled (or other undesirable macroscopic growth defects are removed), the grain structure is refined, and the defect content and residual stress state of the growing film is somehow optimized. But extensive bias power may lead to re-sputtering events, reducing film growth rate. Because, the high energy can easily destroy smaller nuclei and favor their sputtering, and lead to increased desorption activities. Zone I is desirable for supercapacitor porous coatings and zone T for the superlattice dense coatings in this work. It is always crucial to determine the appropriate parameters for a coating deposition.

4. Architectural design

For a long time, people have been continuously studying various factors that affect the properties of materials and mastering the ways to improve the properties, to meet the ever-increasing demands for an improved application-orientated industry. Besides the ever-lasting new materials exploration, new architectures also offer the possibility to explore material properties from a new angle and meet special applications. This chapter introduces some promising architectures, including alloying/doping, nanocomposite, multilayer, and porous structures to improve the coatings' mechanical and/or electrochemical properties.

4.1 Alloying and/or doping architecture

Alloying is the most straightforward and successful mechanical and thermal properties improvement strategy. The alloying elements form IIIB-VB act as substitution of metal atoms at the metallic sublattice. Adding new elements to existing coating systems changes basic physical properties such as hardness, the lattice constant, grain size, preferred orientation, coefficient of thermal expansion, and oxidation resistance, ultimately affecting coating performance. For example, to further improve the performance of conventional (Ti,Al)N and (Cr,Al)N coatings, a variety of transition metal elements, including V, Nb, Ta, Mo, W, etc., have been employed to improve the ductility due to enhanced occupancy of d-t_{2g} metallic states by the valence electrons of alloying substitutional elements [109-111]. And, the lattice distortion induced by alloying would hinder the movement of dislocations and thereby increase the hardness of the coating. However, some alloying elements lead to negative effects. The effect of the addition of alloying elements on the hardness of the coating can be considered from two aspects. 1) alloying will change the chemical bonding between the atoms and change the hardness of the coating. 2) the solid solution of alloying elements cause lattice distortion, which hinders the movement of dislocations, thereby increasing the hardness of the coating. There is a definite change

in both lattice and micro structures after alloying. For instance, 10% of B can highly distort the $Ti_{0.33}Al_{0.67}N$ coating into fully hcp structure with pronounced (110) orientation, but still offers improved hardness [112]. Contrary, 10% of Hf, or Nb, or Y, can promote the formation of the hcp structure to $Ti_{0.33}Al_{0.67}N$, weakening the bonding and causing the hardness to decrease [112,113].

When the addition of a second element in small concentrations (<1000 ppm) is used, and no change in the crystal structure of the first material, we name it doping. The effect of doping will be a change in the properties of the doped material superficial only. In semiconductor production, doping is the intentional introduction of impurities into an intrinsic semiconductor for the purpose of modulating its electrical, optical and structural properties. Dopants may be interstitial or substitutional to the crystal structure of the host. In TMNs, the small non-metal elements of C, Si, O, and B can substitute elements at the N sublattice.

4.2 Nanocomposite Architecture

The nanocomposite coating is a coating composed of two or more nano-sized grains including crystalline and amorphous phases. The most representative nanocomposite coating is nc-TiN/a-Si_3N_4 [114], which is obtained through phase separation between TiN and Si_3N_4 during a Ti-Si-N deposition. But the microstructure of such a Ti-Si-N coating is highly depending on the deposition conditions and Si content: for < 3 at.% Si, and low deposition temperature, the formation of a (Ti,Si_x)N solid solution with fine nanocrystalline structures; for 3 – 10 at.% Si, Si_xN starts separating from the TiN phase and separates columnar crystal grains with a thickness of 0.5−0.7 nm and can have a coherent relationship with adjacent TiN grains [115]; for > 10 at.% Si, a fully percolating three-dimensional Si_3N_4 amorphous phase is formed encapsulating nano-columnar TiN crystals [116]. This composite structure hinders the movement of dislocations and the generation and propagation of cracks, therefore results in a significant improvement in mechanical properties, such as super hardness (> 40 GPa) [117]. The hardness largely depends on the degree of phase separation between TiN and Si_xN

phase as well as their relative phase composition. In addition to the Ti-Si-N coating, nanocomposite coatings are also available in other Si-containing systems such as (V,Si)N [118], (Cr,Si)N [119], (Zr,Si)N [120], (Ti,Al,Si)N [121]. Contributed by the higher crystallization temperature of amorphous Si_xN and the three-dimensional network structure, these composite coatings also possess a high thermal stability, the high hardness is maintained up to annealing temperatures of 900−1000 °C [122]. However, the residual stress of the Ti-Si-N is twice that of TiN [123], which limits their industrial application to some extent. Therefore, an alternative to (Ti,Si)N is to deposit multilayer or nanolayer structure together with other nitrides, e.g. (Cr,Al)N/Ti-Si-N [124], (Ti,Al)N/Ti-Si-N [125].

Another representative nanocomposite coating is to combine ceramic coatings with chemically inert heavy elements (e.g. Au[126], Cu [127], Ta [128], Ni [17], or Ag [129,130]), or solid lubricants (like graphite, diamond like carbon (DLC), MoS_2 [131]). The addition phases are insoluble in hard coatings, and offer the possibility to improve coating hardness, fracture toughness, thermal stability, corrosion resistant, and reduce the friction coefficient [128].

4.3 Porous Architecture

Porous films are more well known in various chemical applications and sensor device architectures. The extraordinarily high specific surface area offers an amount of charge adsorb and/or chemical reaction positions, which is vital in the catalyst and electrode industry. Nowadays, TMNs are also getting favorable in supercapacitor electrodes due to their high conductivity and structural and chemical stability. Especially, the PVD-produced TMN thin films offer improved power efficiency and enhanced cycle life because of being binder-free. Although PVD usually produces TMN thin films with relatively dense structures, still, some successful cases are reported which allow to make them as porous as possible. The most straightforward way is to adjust deposition parameters. According to the nucleation processes and structure zone models, a relatively high deposition pressure and low deposition temperature

and low bias potential will lead to lower atomic diffusion process resulting in island growth processes [132]. A highly-energetic Ar or Kr ion plasma etching process immediately after the deposition can further increase the specific surface area. The high energy is offered by a high bias potential of more than -200 V. The highly energetic ion bombardment resputters part of the particles forming the coating, preferably those being weakly bonded like at grain boundaries [44].

Another possibility to prepare porous structures is a selective chemical leaching, where for example Cu or Ni is chemically dissolved from ceramic-Cu/Ni coatings. A magnetron sputtered CrN-Cu coating is getting porous by 3–4 days of immersing in a 0.5 M HNO_3 [133]. A 3 hour treatment of an arc-plated CrN-Ni coating in 3 M HCl solution leads to a 4 times higher specific capacitance [17]. This chemical etching process results in the formation of both macropores (>50 nm) and mesopores (2~50 nm), and if beneficial for high peak currents and low internal losses, and high specific energy when used in supercapacitors.

Glancing angle deposition (GLAD) is another very useful technique for fabricating porous thin films with engineered morphology and structures. GLAD requires a variable and controllable target-to-substrate angle alignment during the physical vapor deposition process. The material can uniquely build up on the substrate by rotating the sample at an oblique angle to the deposition plume. In terms of nucleation processes and structure zone models, the origin of the columnar structure characteristic of GLAD films is due to the atomic-scale ballistic shadowing effect and surface diffusion. Because the GLAD process provides precise nanoscale control over the film structure, characteristics such as the mechanical, magnetic, and optical properties of the deposited film may be engineered for various applications [134].

4.4 Superlattices Architecture

In 1970, Koehler[9] firstly proposed the method of enhancing the strength of materials by using a laminate structure of thin layers of two materials, which are

chemically different but structurally similar, thus allow to grow coherent layers upon each other. The layered arrangement leads to a strength increase by at least two effects: For very thin layers, more energy is required to generate a dislocation and if they are formed, their propagation into the neighboring layers is hampered by different shear moduli of the layers. These strengthening effects were experimentally validated by Lehoczky [135] using an Al/Cu system: The yield strength and the tensile fracture strength of the Al/Cu multilayer films were ~3 times larger than those of monolithic Al and Cu films. Afterwards, a large number of nano-multilayer film systems were developed, including the metal/ceramic systems (e.g., Cu/CrN [136]) and the ceramic/ceramic systems (e.g., TiN/NbN [137], TiN/CrN [138]). They all presented a more or less superlattice effect of simultaneously increasing hardness, fracture toughness, and tribological performance. The superlattice effects on these properties are based on the elastic modulus difference model [9], the Hall–Petch model [139], the supermodulus effect model [140,141], and/or the coherency strain model [142,143]. To allow for an epitaxial growth, and to reduce the strains present at the interface, the involved crystal structures are expected to be close in lattice parameters and thermal expansion coefficients. But to extract the superlattice effect, the elastic constants should be different [144]. The mechanical but also the tribological properties of superlattice coatings depend on their bilayer periods and the layer thickness ratio of a bilayer. As shown in Fig. 4.1, the bilayer period is the sum thickness of two adjacent layers, and the bilayer ratio is the thickness ratio between two adjacent layers. The bilayer period significantly influences the coherency stresses and associated misfit dislocation densities.

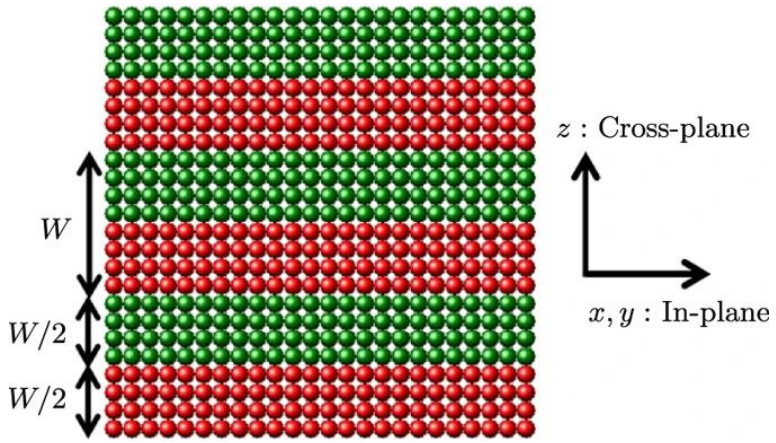

Fig. 4.1: Schematic illustration of the considered superlattice structures [145].

5. Fracture toughness of ceramic thin films

It is critical for most structural materials to have both, high strength and high toughness. However, these two properties are usually mutually exclusive. For most critical safety applications, materials with higher toughness are even more important than higher strength because brittle failures or catastrophic rupture events are undesirable. Superlattice structures are already well known (essentially since the report by Hahn et al. [12] for simultaneously improving material hardness and toughness. To further clarify the toughening mechanisms of superlattice structure, this chapter gives a very brief overview of the brittle fracture mechanics, some intrinsic toughening mechanisms, and a reliable micro-fracture toughness test technique, the micro-cantilever bending test

5.1 Linear elastic fracture mechanics

According to the degree of plastic deformation before/during a fracture process, the fracture mechanics of ductile and brittle materials are generally categorized into linear elastic fracture mechanics and elastic-plastic fracture mechanics. As ceramic thin films (like ceramics in general) have relatively low fracture toughness and no deformation before breakage, we only focus on linear elastic fracture mechanics [146].

5.1.1 Griffith's criterion

In theory, the fracture strength of a crystal refers to the maximum stress required to separate the crystal atoms, which has a certain relationship with the elastic modulus of the crystal. The elastic modulus (Young's modulus *E* and shear modulus *G*) represents the bonding force between atoms, the force required to produce an incremental deformation. Actually, for most engineering materials, especially brittle materials, like glass and ceramics, the real fracture strength is often 100–1000 times lower than their theoretical cleavage stress. In World War I, an English aeronautical engineer, A. A. Griffith [147], firstly reconciled these conflicting observations. He noted

that numerous cracks with different lengths and orientations lead to high stress at the crack tip, and thus crack propagation (and fracture) occurs at a much lower applied stress than the theory would have implied. Since then, quantitative fracture analysis of cracked solids has been conducted by considering the extension of crack propagation rather than the separation of two perfect crystal planes.

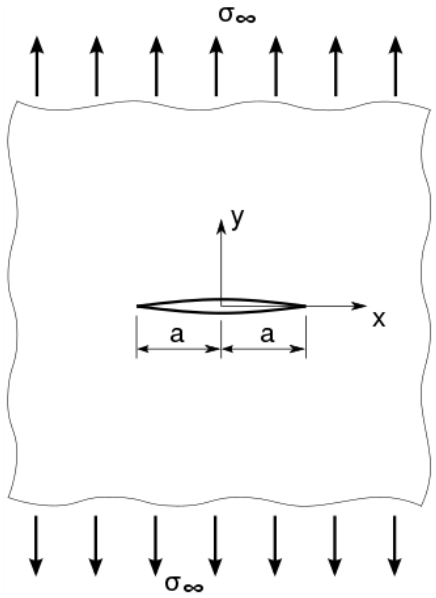

Fig. 5.1: A through-thickness crack in an infinitely wide plate subjected to a remote tensile stress σ [148].

To verify the flaw hypothesis, Griffith introduced an artificial flaw in his experimental glass specimen, as shown in Fig. 5.1. The experiments showed that the product of the square root of the flaw length (a) and the stress at fracture (σ_f) was nearly constant, which is expressed by the equation:

$$\sigma_f \sqrt{a} \approx const. \qquad (5.1)$$

Griffith explained this relation in an energetic approach: when the elastic energy released by crack growth exceeds the energy required for creating a new surface, the crack propagates. The reduction in stored energy and the surface energy associated with the crack formation (crack growth) can mathematically be expressed using Eq. 5.2:

$$\mathrm{dU} = \mathrm{d}U_{el} - dU_o \Longrightarrow \frac{\sigma^2}{E} \cdot \pi \cdot a \cdot da \cdot t - \gamma_s \cdot 2 \cdot da \cdot t \qquad (5.2)$$

Where U_{el} is the energy (elastic strain energy) within the material promoting the crack growth. U_o is the surface energy of the material. σ is the applied stress (or internally stored stress, or the combination of both; hence, the active stress on the crack), a is the half-length of an internal crack, t is the plate thickness, γ_s is the specific surface energy, and E is the Young's modulus [GPa].

As long as $\frac{\partial U}{\partial a} \leq 0$, the crack will not grow, as the release in stored energy is smaller than the increase in surface energy. For the threshold, $\frac{\partial U}{\partial a} = 0$, the lowering in stored energy equals the cost to increase the crack surface. Thus, the critical active stress σ_c for the crack growth can be expressed as:

$$\sigma_c = \sqrt{\frac{2\gamma_s E}{\pi a}} \qquad (5.3)$$

In ideally brittle materials (i.e., purely cleavage fracture), the energy release rate G^*—the rate at which energy is absorbed by the growth of the crack—is the change in surface energy, $G^* \cdot da \cdot t = \gamma_s \cdot 2 \cdot da \cdot t$. Thus, $G^* = 2\gamma_s$, the factor 2 is because the inner crack has two surfaces (upper and lower part of the crack). For the simple case of a thin rectangular plate with a crack perpendicular to the load, the energy release rate becomes:

$$G^* = \frac{\pi {\sigma_c}^2 a}{E} \qquad (5.4)$$

Here, E is the effective Young's modulus.

$$E = \begin{cases} E \ \ (plane\ stress) \\ \frac{E}{(1-\nu^2)} \ \ (plane\ strain)' \end{cases} \qquad (5.5)$$

where ν is Poisson's ratio.

If the active stress is larger than the critical stress ($\sigma > \sigma_c$) – i.e., $\frac{\pi \sigma^2 a}{E} > G^*$ – the crack will grow. Griffith's criterion neglects any plasticity at the crack tip (thus,

$G^* = 2\gamma_s$). Although this is extremely unlikely in real applications, Griffth's criterion continues to be a cornerstone in modern fracture mechanics. Microplastic deformations contribute to G^* and would increase it beyond $2\gamma_s$. To use the linear elastic fracture mechanics (which forms the basis of the Griffith criterion), the plastic zone in front of the crack tip needs to be very small compared to the specimen geometry.

5.1.2 Stress intensity factor *K*

For calculating the amount of energy available for fracture in terms of the asymptotic stress and displacement fields around a crack tip in a linear elastic application was prompted by Irwin and his colleagues during the world war II [149]. Although the load on a crack can be arbitrary, Irwin found any state could be reduced to a combination of three independent stress intensity factors [150], as shown in Fig. 5.2: Model I, the opening mode (a tensile stress normal to the plane of the crack); Mode II, the sliding mode (a shear stress acting parallel to the plane of the crack and perpendicular to the crack front); and Mode III, the tearing mode (a shear stress acting parallel to the plane of the crack and parallel to the crack front).

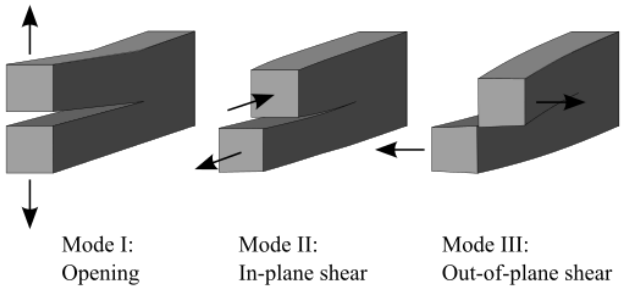

Fig. 5.2: The three modes of crack extension [148]

This asymptotic expression for the stress field in mode I loading (which represents the most demanding loading condition for crack growth) is related to the stress intensity factor K_I [MPa√m.], derived from complex stress functions depending on the crack geometry and loading conditions. It is given by:

$$\begin{pmatrix}\sigma_x\\ \sigma_y\\ \tau_{xy}\end{pmatrix} = \frac{K_I}{\sqrt{2\pi r}} cos(\theta/2) \begin{pmatrix}1-\sin(\theta/2)\sin(3\theta/2)\\ 1+\sin(\theta/2)\sin(3\theta/2)\\ \sin(\theta/2)\cos(3\theta/2)\end{pmatrix} \quad (5.6)$$

$$\sigma_z = \begin{cases} 0, plane\ stress\ state\ on\ sample\ surface \\ v(\sigma_x+\sigma_y), plane\ strain\ state\ in\ sample\ center \end{cases} \quad (5.7)$$

Where, σ_x, σ_y, and τ_{xy} are the Cauchy stresses, θ is the angle with respect to the plane of the crack, and r is the distance from the crack tip, as shown in Fig. 5.3.

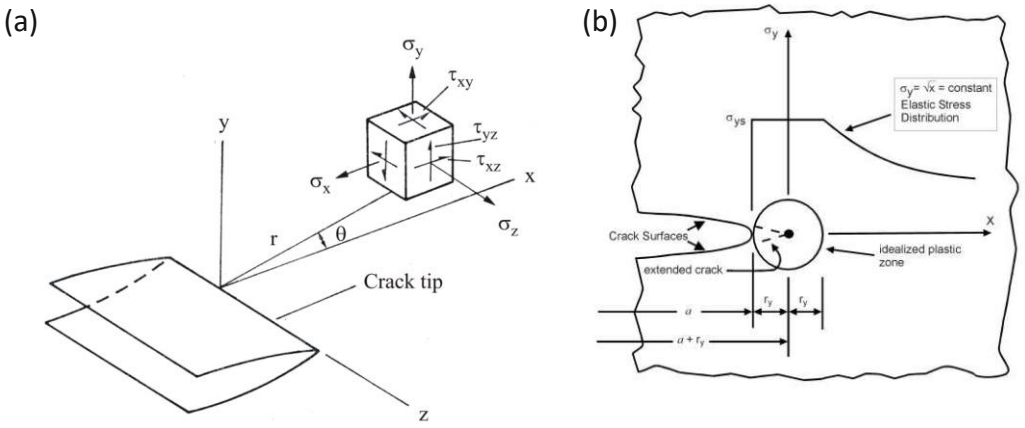

Fig. 5.3: Coordinate axes and distribution of stresses in the vicinity of a crack tip (a), small-scale yield model for restricted crack tip plastic deformation (b) [151].

The stress intensity factor K_I is a system property related to geometry and material. Therefore, it is necessary to introduce a dimensionless correction factor, Y, in order to characterize the geometry. This geometric shape factor is given by an empirically determined series and accounts for the type and geometry of the crack. More details of cantilever geometric factors are in the next section.

With the help of the stress intensity factor *K*:

$$K = Y \cdot \sigma \cdot \sqrt{\pi a}, \quad (5.8)$$

The Griffith-criterion-based Eq. (5.4) can be expressed as:

$$K_c = \sqrt{G^* \cdot E}. \quad (5.9)$$

As the material will yield wherever the local stress is larger than the yield strength, yielding limits the active stress near the crack tip. Thus, the critical value of the stress intensity factor in mode I loading, K_{IC}, measured under plane strain conditions is known as the plane strain fracture toughness, denoted K_{Ic}:

$$K_{IC} = Y\sigma_y\sqrt{\pi a}, \tag{5.10}$$

where σ_y is the yield strength. For purely brittle materials, σ_y equals the fracture stress σ_f. K_{IC} is a size- and geometry-independent material constant. For ceramic coatings, K_{IC} ~ 1-10 [MPa √m]. All three modes have a different K_C value, and typically $K_{IC} < K_{IIC}$ or K_{IIIC}.

5.1.3 Crack tip plastic zone

For numerical studies in fracture mechanics, it is often appropriate to represent the crack as a round-tipped notch, where the geometrically relevant stress concentration region replaces the singularity at the crack tip [152]. It has been found that the stress concentration at the crack tip in real materials has a finite value, and it is larger than the nominal stress imposed on the specimen. Plastic deformation will occur at the crack tip due to the high stresses generated by the sharp stress concentration, thus blunting the crack. This deformation mainly depends on the magnitude and direction of the applied stress, the crack length, and the specimen's geometry. To estimate the extent of this plastic deformation, Irwin equated the yield strength to the y-direction stress along the x-axis and solved for the crack tip radius. The radius value determined was the distance along the x-axis where the stress perpendicular to the crack direction would equal the yield strength; thus, Irwin found that the extent of plastic deformation was [153]:

$$r_p = \frac{K_C^2}{2\pi\sigma_y^2} \tag{5.11}$$

Fig. 5.3(b) describes a schematic model of the plastic zone and the stresses ahead of the crack tip. Models of ideal material have shown that the material outside the

plastic zone is stressed as if the crack were centered in the plastic zone. This estimate of the size of the plastic zone at the crack tip can be used to more accurately analyze the behavior of the material when a crack occurs, which is useful to many structural scientists because it gives a good estimate of how the material behaves when subjected to stress. For example, if K_C is high, it can be deduced that the material is tough, and if σ_y is low, one knows that it is ductile. If the extent of the plastic zone is small to features of the structural geometry and to the physical length of the crack, meaning the sample dimension D_{min} is larger than the plastic zone size: $D_{min} > 2.5\left(\frac{K_{IC}}{\sigma_y}\right)^2$, we still assume that the Griffth's criterion is valid, and thus linear elastic fracture mechanics apply [154].

5.2 Intrinsic toughening mechanisms

Toughening mechanisms are mainly divided into extrinsic and intrinsic ones. Extrinsic toughening mechanisms are processes that act behind the crack tip to resist its further opening. For example, fiber bridging in composite materials, where fibers hold the two fracture surfaces together after the crack propagates through the matrix [146]. Intrinsic toughening mechanisms are processes that act in front of the crack tip to increase the material's toughness. These are often related to the structure and bonding of the base material, as well as microstructural features and additives. Any changes to the base material that increases its ductility can also be considered intrinsic toughening. The following examples of intrinsic toughening mechanisms are used to increase the toughness of ceramic materials for applications such as ceramic cutting tools and thermal barrier coatings on jet engine turbine blades.

Superlattice structures are an effective example of intrinsic toughening mechanisms by introducing interfaces and alternative bonding structures. The presence of grains in a material also affects its toughness and crack propagation properties. In front of the crack, as the material yields, a plastic zone may appear. Outside this area, the material remains elastic. Fracture conditions are most favorable

at the boundary between the plastic and elastic zones, so cracks are commonly initiated by grain cleavage at this location. This results in crack bifurcation and cracks path changes due to grain boundaries. The alternating bonding structure introduces coherency strains and hinders dislocation movement in the materials, thus contributing to increasing the fracture toughness.

Phase transformations and phase decompositions are also viable intrinsic toughening methods. When a material undergoes one or more displacive (e.g. martensitic) phase transitions, this results in an almost instantaneous change in the volume of the material. Such transition is triggered by a change in the stress state of the material, such as an increase in tensile stress, and usually occurs in opposition to the applied stress. Therefore, when a material is subjected to local stretching, such as in front of a crack tip, it may undergo a phase transition that increases its volume, reduces local tensile stresses, and hinders crack propagation in the material. For example, the yttria-stabilized zirconia [155]. For ceramic-like coatings a corresponding mechanism was proposed for AlN-containing materials using the example of CrN/AlN multilayers [5]. The CrN/AlN multilayers with rather thin AlN layers (~3 nm) showed a significantly higher fracture toughness – with a slow crack growth – than the CrN coating or the CrN/AlN multilayer with thicker AlN layers (~10 nm). This is because the thin AlN layers are epitaxially (with the fcc-CrN) stabilized in their metastable fcc structure, whereas the thick AlN layers are essentially present with their stable hexagonal wurtzite type structure (w-AlN). Upon loading and in front of a crack tip (with increased tensile or shear stresses), the fcc-AlN can phase transform towards the w-AlN. This phase transformation is connected with a massive volume expansion reducing the active stresses at the crack tip. Inclusions in a material such as second phase particles can act similar to brittle grains that can affect toughness by deflecting crack propagation. The fracture or deagglomeration of inclusions may be caused by externally applied stresses or by dislocations arising from the inclusion's needed to maintain coherency with its surrounding matrix. If the inclusion density is high, additional inclusions may fracture within the plastic zone and connect. If the alloying

element content is too small to generate second phase particles in a material, they can still affect crack propagation by introducing defects, such as dislocations and vacancies, or by changing the cohesive strength of grain, phase, and column boundaries. The latter are typically the weak links through which the crack most favorably expands in ceramic-like coatings.

5.3 Micro-Cantilever bending test

The experimental procedure for determining toughness usually involves uniaxial compression or tensile tests, measuring the area under the resulting stress-strain curve. To minimize the influence of the substrate on the measurement, the fracture toughness of thin films should be conducted on substrate-free coating material. However, traditional fracture toughness measurement techniques were developed to study bulk materials. Only recently, with the development of in-situ micromechanical testing, it has become possible to accurately determine the fracture toughness of thin films without the influence of the substrate and thus, e.g., biaxial residual macro stresses. The most popular micro-fracture tests are single cantilever bending and pillar splitting tests. Cantilever bending is more tolerant to misalignment and has a high success rate but is more complex, especially in sample preparation [156]. Pillar splitting is more time-efficient, but the interfaces and anisotropy cannot be tested [157]. Furthermore, notched microcantilever bending tests involve much lower loads than micropillar splitting and are thus generally preferred for the measurement of linear elastic fracture properties, since the high compressive loads can induce considerably (sometimes even plastic) deformation of the tested geometry before cracks are initiated, which complicates the extraction process of the fracture toughness from the test data. Therefore, all the fracture toughness data in this work have been measured by cantilever bending tests.

Freestanding microcantilevers with predefined dimensions are milled using a focused ion beam (FIB). Removing the substrate underneath the probed area of the film ensures that the material is macroscopically relaxed and residual macro stresses

are released. Many different cantilever geometries have been investigated, e.g., triangular [158], rectangular [156], pentagonal [159]. Among them, the most popular one is the pre-notched rectangular cantilever. Also, the pre-notch is machined by FIB, forming a finite notch tip radius. However, the ion beam, e.g., a gallium source, may result in ion implantation, leading to residual stresses or embrittlement in the region around the crack tip, affecting the measured K_{IC}. Furthermore, the milling rate at the edges is higher than the center, leading to a non-uniform notch depth. Matoy et al. [156] proposed material bridges on both sides of the notch to minimize the so-called curtaining effect for a notch as well as to allow for a very sharp crack formation (upon the breaking of these bridges). The fracture of the bridge introduces a natural fine pre-split of predetermined length unaffected by FIB, providing a very sharp crack front [160]. Cantilever bending has progressively extended its applicability to various brittle/semi-brittle materials. A typical brittle micro-cantilever with notches, material bridges, and a fracture cross-section after failure are shown in Fig. 5.4. Here, F denotes the load by a displacement-controlled indenter, w and b are the width and breadth of the cantilever, l is the distance between the pre-crack and the position at which the load is applied, a_0 is the exact pre-crack depth. All geometry factors are in the unit of nm. Loading until failure and recording the force-displacement curve provides the maximum force at fracture F_f.

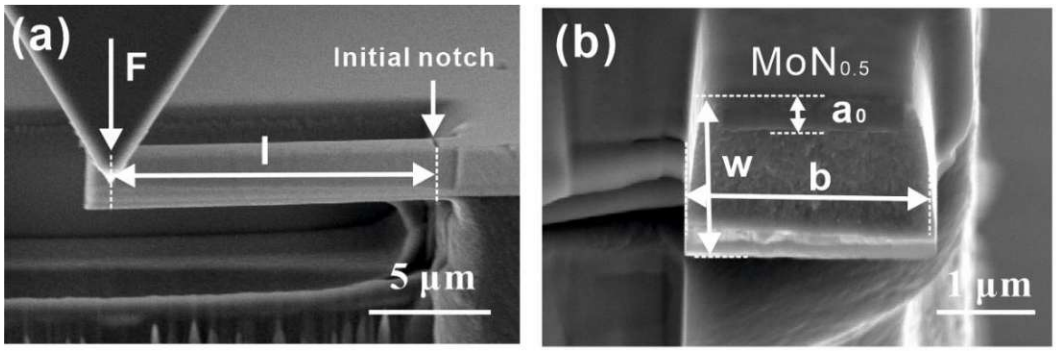

Fig. 5.4: SEM image of a typical micro-cantilever ($MoN_{0.5}$ coating) loaded by a wedge tip (a) and its cross-section after fracture (b).

In the case of brittle materials, by analyzing the area of the resulting fracture surface,

the exact depth of the pre-crack, and the maximum force, the plane strain fracture toughness K_{IC} can be calculated using equation (5. 12):

$$K_{IC} = \frac{F_f}{b \cdot w^{3/2}} f\left(\frac{a_0}{w}\right) \qquad (5.12)$$

Where $f\left(\frac{a_0}{w}\right)$ is a shape function of the pre-crack depth a_0 and the microcantilever width w, and it can be calculated by the following cubic polynomial fitting equation:

$$f\left(\frac{a_0}{w}\right) = 1.46 + 24.36\left(\frac{a_0}{w}\right) - 47.21\left(\frac{a_0}{w}\right)^2 + 75.18\left(\frac{a_0}{w}\right)^3 \qquad (5.12)$$

Microcantilever testing is prone to the length scale effect. The dimensions of the cantilever influence the measured fracture toughness noticeably below a certain threshold of the sample volume, which depends on the size of the plastic zone to the sample thickness. Matoy et al. [156] suggested to use the calculated shape function for specific aspect ratios (l:w:b = 5:2.1:1.7, and $0.45 < a_0/w < 0.55$) of cantilever beams. However, it is almost impossible to control the beam dimensions during FIB preparation. But, Iqbal et al. [161] demonstrated that the geometry factor showing slight changes in the aspect ratio during FIB milling would not falsify the fracture toughness results as much as originally feared. In this study, we keep all cantilevers at ~2 µm thickness, adhere to l:w:b = 5:1:1, and keep the depth of notches at 300-500 nm.

A high-temperature bending test is necessary to provide insight into the impact of thermally induced intermixing of the individual layers and the associated loss of clearly defined interfaces on the toughness-related properties of TMN SLs. The potential influence of interdiffusion between the layers in a TMN SL on fracture toughness has been noted in the past, however have so far been limited to ex situ annealing studies. In-situ high-temperature micromechanical tests could provide unprecedented insight into the effect of such thermally activated processes directly at application-relevant temperatures.

6. References

[1] Rafaja D, Wüstefeld C, Motylenko M, Schimpf C, Barsukova T, Schwarz M R, Kroke E. Interface phenomena in (super)hard nitride nanocomposites: from coatings to bulk materials[J]. Chemical Society Reviews, 2012, 41(15): 5081-5101.

[2] Veprek S. The search for novel, superhard materials[J]. Journal of Vacuum Science & Technology A, 1999, 17(5): 2401-2420.

[3] Zhang Z, Ghasemi A, Koutná N, Xu Z, Grünstäudl T, Song K, Holec D, He Y, Mayrhofer P H, Bartosik M. Correlating point defects with mechanical properties in nanocrystalline TiN thin films[J]. Materials & Design, 2021, 207: 109844.

[4] Bartosik M, Rumeau C, Hahn R, Zhang Z L, Mayrhofer P H. Fracture toughness and structural evolution in the TiAlN system upon annealing[J]. Scientific Reports, 2017, 7: 16476.

[5] Schlögl M, Kirchlechner C, Paulitsch J, Keckes J, Mayrhofer P H. Effects of structure and interfaces on fracture toughness of CrN/AlN multilayer coatings[J]. Scripta Materialia, 2013, 68(12): 917-920.

[6] Bartosik M, Hahn R, Zhang Z L, Ivanov I, Arndt M, Polcik P, Mayrhofer P H. Fracture toughness of Ti-Si-N thin films[J]. International Journal of Refractory Metals & Hard Materials, 2018, 72: 78-82.

[7] Hahn R, Kirnbauer A, Bartosik M, Kolozsvari S, Mayrhofer P H. Toughness of Si alloyed high-entropy nitride coatings[J]. Materials Letters, 2019, 251: 238-240.

[8] Buchinger J, Koutná N, Chen Z, Zhang Z, Mayrhofer P H, Holec D, Bartosik M. Toughness enhancement in TiN/WN superlattice thin films[J]. Acta Materialia, 2019, 172: 18-29.

[9] Koehler J S. Attempt to Design a Strong Solid[J]. Physical Review B, 1970, 2(2): 547-551.

[10] Kingetsu T, Sakai K. Perpendicular magnetic anisotropy and structures of epitaxial Co/Ag and Co/Au metallic superlattices[J]. Journal of Applied Physics, 1993, 73(11): 7622-7626.

[11] Helmersson U, Todorova S, Barnett S A, Sundgren J E, Markert L C, Greene J E. Growth of single-crystal TiN/VN strained-layer superlattices with extremely high mechanical hardness[J]. Journal of Applied Physics, 1987, 62(2): 481-484.

[12] Hahn R, Bartosik M, Soler R, Kirchlechner C, Dehm G, Mayrhofer P H. Superlattice effect for enhanced fracture toughness of hard coatings[J]. Scripta Materialia, 2016, 124: 67-70.

[13] Fallman M, Chen Z, Zhang Z L, Mayrhofer P H, Bartosik M. Mechanical properties and epitaxial growth of TiN/AlN superlattices[J]. Surface & Coatings Technology, 2019,

375: 1-7.

[14] Buchinger J, Wagner A, Chen Z, Zhang Z L, Holec D, Mayrhofer P H, Bartosik M. Fracture toughness trends of modulus-matched TiN/(Cr,Al)N thin film superlattices[J]. Acta Materialia, 2021, 202: 376-386.

[15] Libich J, Máca J, Vondrák J, Čech O, Sedlaříková M. Supercapacitors: Properties and applications[J]. Journal of Energy Storage, 2018, 17: 224-227.

[16] Wei B B, Ming F W, Liang H F, Qi Z B, Hu W S, Wang Z C. All nitride asymmetric supercapacitors of niobium titanium nitride-vanadium nitride[J]. Journal of Power Sources, 2021, 481: .

[17] Gao Z, Wan Z, Wu Z, Huang X, Li H, Zhang T F, Mayrhofer P H, Wang Q. Synthesis and electrochemical properties of nanoporous CrN thin film electrodes for supercapacitor applications[J]. Materials & Design, 2021, 209: 109949.

[18] Akbar Sial Q, Thai Duy L, Singh R, Iqbal S, Yeasmin R, Lee Y-J, Kalanur S S, Seo H. A multifunctional TiN/Ni electrode for wearable supercapacitor and sensor with an insight into charge storage mechanism[J]. Applied Surface Science, 2021, 555: 149718.

[19] He T, Zhang W, Manasa P, Ran F. Quantum dots of molybdenum nitride embedded in continuously distributed polyaniline as novel electrode material for supercapacitor[J]. Journal of Alloys and Compounds, 2020, 812: 152138.

[20] Qin P, Huang C, Gao B, Pi C R, Fu J J, Zhang X M, Huo K F, Chu P K. Ultrathin carbon layer-encapsulated TiN nanotubes array with enhanced capacitance and electrochemical stability for supercapacitors[J]. Applied Surface Science, 2020, 503.

[21] Navinsek B, Seal S. Transition metal nitride functional coatings[J]. JOM, 2001, 53(9): 51-54.

[22] Bobzin K. High-performance coatings for cutting tools[J]. CIRP Journal of Manufacturing Science and Technology, 2017, 18: 1-9.

[23] Kong J-Z, Li C, Sun X-Y, Xuan Y, Zhai H-F, Li A-D, Wang Q-Z, Zhou F. Improved tribological properties and corrosion protection of CrN coating by ultrathin composite oxide interlayer[J]. Applied Surface Science, 2021, 541: 148606.

[24] Ouendi S, Robert K, Stievenard D, Brousse T, Roussel P, Lethien C. Sputtered tungsten nitride films as pseudocapacitive electrode for on chip micro-supercapacitors[J]. Energy Storage Materials, 2019, 20: 243-252.

[25] Kazmanli M K, Ürgen M, Cakir A F. Effect of nitrogen pressure, bias voltage and substrate temperature on the phase structure of Mo–N coatings produced by cathodic arc PVD[J]. Surface and Coatings Technology, 2003, 167(1): 77-82.

[26] Jauberteau I, Bessaudou A, Mayet R, Cornette J, Jauberteau J L, Carles P, Merle-Méjean T. Molybdenum Nitride Films: Crystal Structures, Synthesis, Mechanical,

Electrical and Some Other Properties[J]. Coatings, 2015, 5(4).

[27] Koller C M, Marihart H, Bolvardi H, Kolozsvári S, Mayrhofer P H. Structure, phase evolution, and mechanical properties of DC, pulsed DC, and high power impulse magnetron sputtered Ta–N films[J]. Surface and Coatings Technology, 2018, 347: 304-312.

[28] Song L, Wang Y-X. First-principles study of W, WN, WN2, and WN3[J]. physica status solidi (b), 2010, 247(1): 54-58.

[29] Oyama S T. Introduction to the chemistry of transition metal carbides and nitrides. In: The Chemistry of Transition Metal Carbides and Nitrides--S.T. Oyama, ed. Dordrecht: Springer Netherlands, 1996: 1-27.

[30] Pugh S F. Relations between the elastic moduli and the plastic properties of polycrystalline pure metals[J]. Philosophical Magazine, 1954, 45(367): 823-843.

[31] Holec D, Friak M, Neugebauer J, Mayrhofer P H. Trends in the elastic response of binary early transition metal nitrides[J]. Physical Review B, 2012, 85(6): 9.

[32] Balasubramanian K, Khare S V, Gall D. Valence electron concentration as an indicator for mechanical properties in rocksalt structure nitrides, carbides and carbonitrides[J]. Acta Materialia, 2018, 152: 175-185.

[33] Jhi S-H, Louie S G, Cohen M L, Morris J W. Mechanical Instability and Ideal Shear Strength of Transition Metal Carbides and Nitrides[J]. Physical Review Letters, 2001, 87(7): 075503.

[34] Koutná N. Superlattice design for nitride-based thin films[J]. Dissertation, Technische Universität Wien, 2021.

[35] Koutná N, Brenner A, Holec D, Mayrhofer P H. High-throughput first-principles search for ceramic superlattices with improved ductility and fracture resistance[J]. Acta Materialia, 2021, 206: 116615.

[36] Perry A J. A contribution to the study of poisson's ratios and elasticconstants of TiN, ZrN and HfN[J]. Thin Solid Films, 1990, 193–194, Part 1(0): 463-471.

[37] Abadias G. Stress and preferred orientation in nitride-based PVD coatings[J]. Surface and Coatings Technology, 2008, 202(11): 2223-2235.

[38] Reddy N R, Kumari M M, Shankar M V, Reddy K R, Joo S W, Aminabhavi T M. Photocatalytic hydrogen production from dye contaminated water and electrochemical supercapacitors using carbon nanohorns and TiO2 nanoflower heterogeneous catalysts[J]. Journal of Environmental Management, 2021, 277.

[39] Zhang Q, Ma J, Lei M, Quhe R. Metallic MoN layer and its application as anode for lithium-ion batteries[J]. Nanotechnology, 2018, 29(16): 165402.

[40] Chen L, Du Y, Wang S Q, Wang A J, Xu H H. Mechanical properties and microstructural evolution of TiN coatings alloyed with Al and Si[J]. Materials Science

and Engineering: A, 2009, 502(1-2): 139-143.

[41] Spengler W, Kaiser R, Christensen A N, Müller-Vogt G. Raman scattering, superconductivity, and phonon density of states of stoichiometric and nonstoichiometric TiN[J]. Physical Review B, 1978, 17(3): 1095-1101.

[42] Wang S, Antonio D, Yu X, Zhang J, Cornelius A L, He D, Zhao Y. The Hardest Superconducting Metal Nitride[J]. Scientific Reports, 2015, 5(1): 13733.

[43] Achour A, Porto R L, Soussou M A, Islam M, Boujtita M, Aissa K A, Le Brizoual L, Djouadi A, Brousse T. Titanium nitride films for micro-supercapacitors: Effect of surface chemistry and film morphology on the capacitance[J]. Journal of Power Sources, 2015, 300: 525-532.

[44] Gao Z, Wu Z, Zhao S, Zhang T, Wang Q. Enhanced capacitive property of HfN film electrode by plasma etching for supercapacitors[J]. Materials Letters, 2019, 235: 148-152.

[45] Liao S-C, Chen C-Y, Hsu Y-H, Li C-T, Hsieh C-C, Tsai M-S, Chan M-Y, Lee C-H, Wang S-H, Ng S-K, Tsou H-K, Wu W-Y. In vitro and in vivo biocompatibility study of surface modified TiN deposited on Ti6Al4V using high-power impulse magnetron sputtering technique[J]. Surface and Coatings Technology, 2020, 394: 125814.

[46] Zhang L, Yang H, Pang X, Gao K, Volinsky A A. Microstructure, residual stress, and fracture of sputtered TiN films[J]. Surface and Coatings Technology, 2013, 224(0): 120-125.

[47] Zhou L, Holec D, Mayrhofer P H. Ab initio study of the alloying effect of transition metals on structure, stability and ductility of CrN[J]. Journal of Physics D: Applied Physics, 2013, 46(36): 365301.

[48] Fillit R Y, Perry A J, Strandberg C. X-ray elastic constants, stress profiling and composition of physically vapor deposited ZrN films[J]. Thin Solid Films, 1991, 197(1): 47-55.

[49] Srivastava A, Diwan B D. Structural and elastic properties of ZrN and HfN: ab initio study[J]. Canadian Journal of Physics, 2014, 92(9): 1058-1061.

[50] Purandare Y P, Ehiasarian A P, Hovsepian P E. Structure and properties of ZrN coatings deposited by high power impulse magnetron sputtering technology[J]. Journal of Vacuum Science & Technology A, 2011, 29(1): 011004.

[51] Zhiguo Z, Tianwei L, Jun X, Xinlu D, Chuang D. N-rich Zr–N films deposited by unbalanced magnetron sputtering enhanced with a highly reactive MW-ECR plasma[J]. Surface and Coatings Technology, 2006, 200(16): 4918-4922.

[52] Mei A B, Howe B M, Zhang C, Sardela M, Eckstein J N, Hultman L, Rockett A, Petrov I, Greene J E. Physical properties of epitaxial ZrN/MgO(001) layers grown by reactive magnetron sputtering[J]. Journal of Vacuum Science & Technology A, 2013, 31(6): 061516.

[53] Török E, Perry A J, Chollet L, Sproul W D. Young's modulus of TiN, TiC, ZrN and HfN[J]. Thin Solid Films, 1987, 153(1): 37-43.

[54] Chen X-J, Struzhkin Viktor V, Wu Z, Somayazulu M, Qian J, Kung S, Christensen Axel N, Zhao Y, Cohen Ronald E, Mao H-k, Hemley Russell J. Hard superconducting nitrides[J]. Proceedings of the National Academy of Sciences, 2005, 102(9): 3198-3201.

[55] Massl S, Thomma W, Keckes J, Pippan R. Investigation of fracture properties of magnetron-sputtered TiN films by means of a FIB-based cantilever bending technique[J]. Acta Materialia, 2009, 57(6): 1768-1776.

[56] Kataria S, Srivastava S K, Kumar P, Srinivas G, Siju, Khan J, Rao D V S, Barshilia H C. Nanocrystalline TiN coatings with improved toughness deposited by pulsing the nitrogen flow rate[J]. Surface & Coatings Technology, 2012, 206(19-20): 4279-4286.

[57] Huang J-H, Chen Y-H, Wang A-N, Yu G-P, Chen H. Evaluation of fracture toughness of ZrN hard coatings by internal energy induced cracking method[J]. Surface and Coatings Technology, 2014, 258: 211-218.

[58] García-González L, Zamora-Peredo L, Flores-Ramírez N, Garnica-Romo M G, Hernández-Torres J. Influence of Nitrogen Flow Rates on the Structure, Hardness, and Electrical Resistivity of HfN Coatings by DC Sputtering[J]. Journal of Materials Engineering and Performance, 2015, 24(4): 1558-1564.

[59] Desmaison-Brut M, Montintin J, Valin F, Boncoeur M. Mechanical properties and oxidation behaviour of HIPed hafnium nitride ceramics[J]. Journal of the European Ceramic Society, 1994, 13(4): 379-386.

[60] Caicedo J C, Zambrano G, Aperador W, Escobar-Alarcon L, Camps E. Mechanical and electrochemical characterization of vanadium nitride (VN) thin films[J]. Applied Surface Science, 2011, 258(1): 312-320.

[61] Ge F, Zhu P, Meng F, Xue Q, Huang F. Achieving very low wear rates in binary transition-metal nitrides: The case of magnetron sputtered dense and highly oriented VN coatings[J]. Surface and Coatings Technology, 2014, 248: 81-90.

[62] Franz R, Mitterer C. Vanadium containing self-adaptive low-friction hard coatings for high-temperature applications: A review[J]. Surface and Coatings Technology, 2013, 228: 1-13.

[63] Mayrhofer P H, Hovsepian P E, Mitterer C, Münz W D. Calorimetric evidence for frictional self-adaptation of TiAlN/VN superlattice coatings[J]. Surface and Coatings Technology, 2004, 177-178: 341-347.

[64] Latella B A, Gan B K, Davies K E, McKenzie D R, McCulloch D G. Titanium nitride/vanadium nitride alloy coatings: mechanical properties and adhesion characteristics[J]. Surface and Coatings Technology, 2006, 200(11): 3605-3611.

[65] Sandu C S, Benkahoul M, Parlinska-Wojtan M, Sanjinés R, Lévy F. Morphological, structural and mechanical properties of NbN thin films deposited by reactive

magnetron sputtering[J]. Surface and Coatings Technology, 2006, 200(22): 6544-6548.

[66] Benkahoul M, Zayed M K, Sandu C S, Martinu L, Klemberg-Sapieha J E. Structural, tribo-mechanical, and thermal properties of NbAlN coatings with various Al contents deposited by DC reactive magnetron sputtering[J]. Surface and Coatings Technology, 2017, 331: 172-178.

[67] Bacon D D, English A T, Nakahara S, Peters F G, Schreiber H, Sinclair W R, van Dover R B. Properties of NbN thin films deposited on ambient temperature substrates[J]. Journal of Applied Physics, 1983, 54(11): 6509-6516.

[68] Zhang E, Liu J, Li W. Microstructures, mechanical and tribological properties of NbN/MoS2 nanomultilayered films deposited by reactive magnetron sputtering[J]. Vacuum, 2019, 160: 205-209.

[69] Friedrich A, Winkler B, Juarez-Arellano E A, Bayarjargal L. Synthesis of Binary Transition Metal Nitrides, Carbides and Borides from the Elements in the Laser-Heated Diamond Anvil Cell and Their Structure-Property Relations[J]. Materials, 2011, 4(10): 1648-1692.

[70] Stampfl C, Freeman A J. Stable and metastable structures of the multiphase tantalum nitride system[J]. Physical Review B, 2005, 71(2): 024111.

[71] Shin C S, Gall D, Desjardins P, Vailionis A, Kim H, Petrov I, Greene J E, Odén M. Growth and physical properties of epitaxial metastable cubic TaN(001)[J]. Applied Physics Letters, 1999, 75(24): 3808-3810.

[72] Kim D-k, Lee H, Kim D, Keun Kim Y. Electrical and mechanical properties of tantalum nitride thin films deposited by reactive sputtering[J]. Journal of Crystal Growth, 2005, 283(3): 404-408.

[73] Shin C S, Kim Y W, Gall D, Greene J E, Petrov I. Phase composition and microstructure of polycrystalline and epitaxial TaNx layers grown on oxidized Si(001) and MgO(001) by reactive magnetron sputter deposition[J]. Thin Solid Films, 2002, 402(1): 172-182.

[74] Yu L, Stampfl C, Marshall D, Eshrich T, Narayanan V, Rowell J M, Newman N, Freeman A J. Mechanism and control of the metal-to-insulator transition in rocksalt tantalum nitride[J]. Physical Review B, 2002, 65(24): 245110.

[75] Hahn R, Koutná N, Wójcik T, Davydok A, Kolozsvári S, Krywka C, Holec D, Bartosik M, Mayrhofer P H. Mechanistic study of superlattice-enabled high toughness and hardness in MoN/TaN coatings[J]. Communications Materials, 2020, 1(1): 62.

[76] Hurkmans T, Lewis D B, Paritong H, Brooks J S, Munz W D. Influence of ion bombardment on structure and properties of unbalanced magnetron grown CrNx coatings[J]. Surface & Coatings Technology, 1999, 114(1): 52-59.

[77] Mayrhofer P H, Tischler G, Mitterer C. Microstructure and mechanical/thermal properties of Cr–N coatings deposited by reactive unbalanced magnetron

sputtering[J]. Surface and Coatings Technology, 2001, 142-144: 78-84.

[78] Hones P, Martin N, Regula M, L vy F. Structural and mechanical properties of chromium nitride, molybdenum nitride, and tungsten nitride thin films[J]. Journal of Physics D: Applied Physics, 2003, 36(8): 1023-1029.

[79] Sebastiani M, Johanns K E, Herbert E G, Pharr G M. Measurement of fracture toughness by nanoindentation methods: Recent advances and future challenges[J]. Current Opinion in Solid State and Materials Science, 2015, 19(6): 324-333.

[80] Klimashin F F, Koutna N, Euchner H, Holec D, Mayrhofer P H. The impact of nitrogen content and vacancies on structure and mechanical properties of Mo-N thin films[J]. Journal of Applied Physics, 2016, 120(18).

[81] Inumaru K, Baba K, Yamanaka S. Synthesis and Characterization of Superconducting β-Mo2N Crystalline Phase on a Si Substrate: An Application of Pulsed Laser Deposition to Nitride Chemistry[J]. Chemistry of Materials, 2005, 17(24): 5935-5940.

[82] Zhou L. First-principles studies of CrN-based materials[J]. PhD dissertation, Vienna University of Tecnology, 2015.

[83] Liu Z T Y, Zhou X, Gall D, Khare S V. First-principles investigation of the structural, mechanical and electronic properties of the NbO-structured 3d, 4d and 5d transition metal nitrides[J]. Computational Materials Science, 2014, 84: 365-373.

[84] Linker G, Schmidt H, Politis C, Smithey R, Ziemann P. Magnetic susceptibility and defect structure of B1 phase MoN sputtered films[J]. Journal of Physics F: Metal Physics, 1986, 16(12): 2167-2175.

[85] Gao Z, Buchinger J, Koutná N, Wojcik T, Hahn R, Mayrhofer P H. Ab initio supported development of TiN/MoN superlattice thin films with improved hardness and toughness[J]. Acta Materialia, 2022, 231: 117871.

[86] Wen M, Meng Q N, Yu W X, Zheng W T, Mao S X, Hua M J. Growth, stress and hardness of reactively sputtered tungsten nitride thin films[J]. Surface and Coatings Technology, 2010, 205(7): 1953-1961.

[87] Ozsdolay B D, Mulligan C P, Guerette M, Huang L, Gall D. Epitaxial growth and properties of cubic WN on MgO(001), MgO(111), and Al2O3(0001)[J]. Thin Solid Films, 2015, 590: 276-283.

[88] Zhang R F, Sheng S H, Veprek S. First principles studies of ideal strength and bonding nature of AIN polymorphs in comparison to TiN[J]. Applied Physics Letters, 2007, 91(3).

[89] Gorczyca I, Christensen N E, Perlin P, Grzegory I, Jun J, Bockowski M. High pressure phase transition in aluminium nitride[J]. Solid State Communications, 1991, 79(12): 1033-1034.

[90] Leyendecker T, Lemmer O, Esser S, Ebberink J. The development of the PVD coating TiAlN as a commercial coating for cutting tools[J]. Surface and Coatings Technology, 1991, 48(2): 175-178.

[91] Münz W D. Titanium aluminum nitride films: A new alternative to TiN coatings[J]. Journal of Vacuum Science & Technology A, 1986, 4(6): 2717-2725.

[92] Wahlström U, Hultman L, Sundgren J E, Adibi F, Petrov I, Greene J E. Crystal growth and microstructure of polycrystalline $Ti_{1-x}Al_xN$ alloy films deposited by ultra-high-vacuum dual-target magnetron sputtering[J]. Thin Solid Films, 1993, 235(1): 62-70.

[93] Chawla V, Holec D, Mayrhofer P H. Stabilization criteria for cubic AlN in TiN/AlN and CrN/AlN bi-layer systems[J]. Journal of Physics D: Applied Physics, 2013, 46(4): 045305.

[94] Chen L, Du Y, Mayrhofer P H, Wang S Q, Li J. The influence of age-hardening on turning and milling performance of Ti-Al-N coated inserts[J]. Surface and Coatings Technology, 2008, 202(21): 5158-5161.

[95] Mayrhofer P H, Hultman L, Schneider J M, Staron P, Clemens H. Spinodal decomposition of cubic $Ti_{1-x}Al_xN$: Comparison between experiments and modeling[J]. International Journal of Materials Research, 2007, 98(11): 1054-1059.

[96] Kimura A, Hasegawa H, Yamada K, Suzuki T. Effects of Al content on hardness, lattice parameter and microstructure of Ti1-xAlxN films[J]. Surface and Coatings Technology, 1999, 120–121: 438-441.

[97] Pac M J, Giljean S, Rousselot C, Richard F, Delobelle P. Microstructural and elasto-plastic material parameters identification by inverse finite elements method of Ti(1 – x)AlxN (0<x<1) sputtered thin films from Berkovich nano-indentation experiments[J]. Thin Solid Films, 2014, 569: 81-92.

[98] He L, Chen L, Xu Y, Du Y. Thermal stability and oxidation resistance of Cr1-xAlxN coatings with single phase cubic structure[J]. Journal of Vacuum Science & Technology a, 2015, 33(6).

[99] Xu Y X, Riedl H, Holec D, Chen L, Du Y, Mayrhofer P H. Thermal stability and oxidation resistance of sputtered Ti–Al–Cr–N hard coatings[J]. Surface and Coatings Technology, 2017, 324: 48-56.

[100] Spencer P J. Computational thermochemistry: from its early Calphad days to a cost-effective role in materials development and processing[J]. Calphad, 2001, 25(2): 163-174.

[101] Liu S, Chang K, Mráz S, Chen X, Hans M, Music D, Primetzhofer D, Schneider J M. Modeling of metastable phase formation for sputtered Ti1-xAlxN thin films[J]. Acta Materialia, 2019, 165: 615-625.

[102] Greene J E. Review Article: Tracing the recorded history of thin-film sputter deposition: From the 1800s to 2017[J]. Journal of Vacuum Science & Technology A, 2017, 35(5): 05C204.

[103] https://nano.mff.cuni.cz/nanomaterials-group/instruments/magnetron-sputtering-systems.

[104] Berlin, Heidelberg: Springer Berlin Heidelberg : Imprint: Springer,, 2015: 1 online resource (XIII, 379 pages 413 illustrations).

[105] Arif M, Eisenmenger-Sittner C. In situ assessment of target poisoning evolution in magnetron sputtering[J]. Surface and Coatings Technology, 2017, 324: 345-352.

[106] Wasa K, Kanno I, Kotera H. Handbook of sputter deposition technology: fundamentals and applications for functional thin films, nano-materials and MEMS[M]. William Andrew, 2012.

[107] Petrov P K, Volpyas V A, Chakalov R A. Three-dimensional Monte Carlo simulation of sputtered atom transport in the process of ion-plasma sputter deposition of multicomponent thin films[J]. Vacuum, 1999, 52(4): 427-434.

[108] Anders A. A structure zone diagram including plasma-based deposition and ion etching[J]. Thin Solid Films, 2010, 518(15): 4087-4090.

[109] Sangiovanni D G, Chirita V, Hultman L. Electronic mechanism for toughness enhancement in TixM1 − xN (M=Mo and W)[J]. Physical Review B, 2010, 81(10): 104107.

[110] Peng B, Li H Q, Zhang Q, Xu Y X, Wei T F, Wang Q M, Zhang F G, Kim K H. High-temperature thermal stability and oxidation resistance of Cr and Ta co-alloyed Ti - Al - N coatings deposited by cathodic arc evaporation[J]. Corrosion Science, 2020, 167.

[111] Chen Y H, Roa J J, Yu C H, Johansson-Jõesaar M P, Andersson J M, Anglada M J, Odén M, Rogström L. Enhanced thermal stability and fracture toughness of TiAlN coatings by Cr, Nb and V-alloying[J]. Surface and Coatings Technology, 2018, 342: 85-93.

[112] Kutschej K, Fateh N, Mayrhofer P H, Kathrein M, Polcik P, Mitterer C. Comparative study of $Ti_{1-x}Al_xN$ coatings alloyed with Hf, Nb, and B[J]. Surface and Coatings Technology, 2005, 200(1–4): 113-117.

[113] Moser M, Mayrhofer P H. Yttrium-induced structural changes in sputtered Ti1 −xAlxN thin films[J]. Scripta Materialia, 2007, 57(4): 357-360.

[114] Meng W J, Zhang X D, Shi B, Tittsworth R C, Rehn L E, Baldo P M. Microstructure and mechanical properties of Ti–Si–N coatings[J]. Journal of Materials Research, 2002, 17(10): 2628-2632.

[115] Zhang S, Sun D, Fu Y, Du H. Effect of sputtering target power on microstructure and mechanical properties of nanocomposite nc-TiN/a-SiN_x thin films[J]. Thin Solid Films, 2004, 447-448: 462-467.

[116] Vaz F, Rebouta L, Goudeau P, Girardeau T, Pacaud J, Riviére J P, Traverse A. Structural transitions in hard Si-based TiN coatings: the effect of bias voltage and temperature[J]. Surface and Coatings Technology, 2001, 146–147: 274-279.

[117] Kong M, Zhao W, Wei L, Li G. Investigations on the microstructure and hardening mechanism of TiN/Si_3N_4 nanocomposite coatings[J]. Journal of Physics D: Applied Physics, 2007, 40(9): 2858.

[118] Huang F, Ge F, Zhu P, Wang H, Meng F, Li S. Superhard V-Si-N coatings (>50GPa) with the cell-like nanostructure prepared by magnetron sputtering[J]. Surface and Coatings Technology, 2013, 232: 600-605.

[119] Wang Q M, Kim K H. Microstructural control of Cr–Si–N films by a hybrid arc ion plating and magnetron sputtering process[J]. Acta Materialia, 2009, 57(17): 4974-4987.

[120] Dong Y, Zhao W, Yue J, Li G. Crystallization of Si3N4 layers and its influences on the microstructure and mechanical properties of ZrN/Si_3N_4 nanomultilayers[J]. Applied Physics Letters, 2006, 89(12): 121916.

[121] Dong Y, Mei F, Hu X, Li G, Gu M. Ti–Al–Si–N nanocrystalline composite films synthesized by reactive magnetron sputtering[J]. Materials Letters, 2005, 59(2): 171-174.

[122] Pei F, Xu Y X, Chen L, Du Y, Zou H K. Structure, mechanical properties and thermal stability of $Ti_{1-x}Si_xN$ coatings[J]. Ceramics International, 2018, 44(13): 15503-15508.

[123] Nose M, Deguchi Y, Mae T, Honbo E, Nagae T, Nogi K. Influence of sputtering conditions on the structure and properties of Ti–Si–N thin films prepared by r.f.-reactive sputtering[J]. Surface and Coatings Technology, 2003, 174–175: 261-265.

[124] Wang H T, Xu Y X, Chen L. Optimization of Cr–Al–N coating by multilayer architecture with TiSiN insertion layer[J]. Journal of Alloys and Compounds, 2017, 728: 952-958.

[125] Chang C-L, Chen W-C, Tsai P-C, Ho W-Y, Wang D-Y. Characteristics and performance of TiSiN/TiAlN multilayers coating synthesized by cathodic arc plasma evaporation[J]. Surface and Coatings Technology, 2007, 202(4–7): 987-992.

[126] Voevodin A A, Hu J J, Fitz T A, Zabinski J S. Tribological properties of adaptive nanocomposite coatings made of yttria stabilized zirconia and gold[J]. Surface and Coatings Technology, 2001, 146-147: 351-356.

[127] Musil J, Hruby H, Zeman P, Zeman H, Cerstvy R, Mayrhofer P H, Mitterer C. Hard and superhard nanocomposite Al-Cu-N films prepared by magnetron

sputtering[J]. Surface & Coatings Technology, 2001, 142: 603-609.

[128] Hu C, Xu Y X, Chen L, Pei F, Du Y. Mechanical properties, thermal stability and oxidation resistance of Ta-doped CrAlN coatings[J]. Surface and Coatings Technology, 2019, 368: 25-32.

[129] Kelly P J, Li H, Benson P S, Whitehead K A, Verran J, Arnell R D, Iordanova I. Comparison of the tribological and antimicrobial properties of CrN/Ag, ZrN/Ag, TiN/Ag, and TiN/Cu nanocomposite coatings[J]. Surface and Coatings Technology, 2010, 205(5): 1606-1610.

[130] Muratore C, Voevodin A A, Hu J J, Zabinski J S. Tribology of adaptive nanocomposite yttria-stabilized zirconia coatings containing silver and molybdenum from 25 to 700°C[J]. Wear, 2006, 261(7): 797-805.

[131] Holbery J D, Pflueger E, Savan A, Gerbig Y, Luo Q, Lewis D B, Munz W D. Alloying MoS2 with Al and Au: structure and tribological performance[J]. Surface & Coatings Technology, 2003, 169: 716-720.

[132] Chen L, Liu C, Zhang Z. Novel (111) oriented γ-Mo_2N thin films deposited by magnetron sputtering as an anode for aqueous micro-supercapacitors[J]. Electrochimica Acta, 2017, 245: 237-248.

[133] Wei B, Mei G, Liang H, Qi Z, Zhang D, Shen H, Wang Z. Porous CrN thin films by selectively etching CrCuN for symmetric supercapacitors[J]. Journal of Power Sources, 2018, 385: 39-44.

[134] Daniel R, Meindlhumer M, Baumegger W, Todt J, Zalesak J, Ziegelwanger T, Mitterer C, Keckes J. Anisotropy of fracture toughness in nanostructured ceramics controlled by grain boundary design[J]. Materials & Design, 2019, 161: 80-85.

[135] Lehoczky S L. Strength enhancement in thin-layered Al-Cu laminates[J]. Journal of Applied Physics, 1978, 49(11): 5479-5485.

[136] Kim Y J, Byun T J, Lee H Y, Han J G. Effect of bilayer period on CrN/Cu nanoscale multilayer thin films[J]. Surface & Coatings Technology, 2008, 202(22-23): 5508-5511.

[137] Shinn M, Hultman L, Barnett S A. Growth, Structure, and Microhardness of Epitaxial Tin/Nbn Superlattices[J]. Journal of Materials Research, 1992, 7(4): 901-911.

[138] Yashar P, Barnett S A, Rechner J, Sproul W D. Structure and mechanical properties of polycrystalline CrN/TiN superlattices[J]. Journal of Vacuum Science & Technology A, 1998, 16(5): 2913-2918.

[139] Anderson P M, Li C. Hall-Petch relations for multilayered materials[J]. Nanostructured Materials, 1995, 5(3): 349-362.

[140] Baker S P, Nix W D. Intrinsic Stresses in Compositionally Modulated Au-Ni Thin-Films and the Supermodulus Effect[J]. Journal of Materials Research, 1994, 9(12):

3145-3152.

[141] Cammarata R C. The supermodulus effect in compositionally modulated thin films[J]. Scripta Metallurgica, 1986, 20(4): 479-486.

[142] Wagner A, Holec D, Mayrhofer P H, Bartosik M. Enhanced fracture toughness in ceramic superlattice thin films: On the role of coherency stresses and misfit dislocations[J]. Materials & Design, 2021, 202: 109517.

[143] Forsén R, Schramm I C, Persson P O Å, Mücklich F, Odén M, Ghafoor N. Nanostructuring and coherency strain in multicomponent hard coatings[J]. APL Materials, 2014, 2(11): 116104.

[144] Barnett S A, Madan A, Kim I, Martin K. Stability of nanometer-thick layers in hard coatings[J]. MRS Bulletin, 2003, 28(03): 169-172.

[145] Mizuno H, Mossa S, Barrat J-L. Beating the amorphous limit in thermal conductivity by superlattices design[J]. Scientific Reports, 2015, 5(1): 14116.

[146] Ritchie R O. The conflicts between strength and toughness[J]. Nat Mater, 2011, 10(11): 817-822.

[147] Griffith A A, Taylor G I. VI. The phenomena of rupture and flow in solids[J]. Philosophical Transactions of the Royal Society of London. Series A, Containing Papers of a Mathematical or Physical Character, 1921, 221(582-593): 163-198.

[148] https://en.wikipedia.org/wiki/Fracture_mechanics.

[149] Irwin G R. Analysis of Stresses and Strains Near the End of a Crack Traversing a Plate[J]. Journal of Applied Mechanics, 1957, 24(3): 361-364.

[150] Williams M C. Stresses in concentrated polymer solutions: Part I. Shear dependence of viscosity[J]. AIChE Journal, 1966, 12(6): 1064-1070.

[151] Berto F, Pook L P, Campagnolo A. Corner point singularities under in-plane and out-of-plane loading: a review of recent results[J]. Engineering Solid Mechanics 2017, 5: 167-176.

[152] Liu M, Gan Y, Hanaor D A H, Liu B, Chen C. An improved semi-analytical solution for stress at round-tip notches[J]. Engineering Fracture Mechanics, 2015, 149: 134-143.

[153] Ast J, Ghidelli M, Durst K, Göken M, Sebastiani M, Korsunsky A M. A review of experimental approaches to fracture toughness evaluation at the micro-scale[J]. Materials & Design, 2019, 173: 107762.

[154] Saxena A K, Brinckmann S, Völker B, Dehm G, Kirchlechner C. Experimental conditions affecting the measured fracture toughness at the microscale: Notch geometry and crack extension measurement[J]. Materials & Design, 2020, 191: 108582.

[155] Liang Y L, Pearson R A. The toughening mechanism in hybrid epoxy-silica-rubber nanocomposites (HESRNs)[J]. Polymer, 2010, 51(21): 4880-4890.

[156] Matoy K, Schönherr H, Detzel T, Schöberl T, Pippan R, Motz C, Dehm G. A comparative micro-cantilever study of the mechanical behavior of silicon based passivation films[J]. Thin Solid Films, 2009, 518(1): 247-256.

[157] Sebastiani M, Johanns K E, Herbert E G, Carassiti F, Pharr G M. A novel pillar indentation splitting test for measuring fracture toughness of thin ceramic coatings[J]. Philosophical Magazine, 2015, 95(16-18): 1928-1944.

[158] Žagar G, Pejchal V, Mueller M G, Michelet L, Mortensen A. Fracture toughness measurement in fused quartz using triangular chevron-notched micro-cantilevers[J]. Scripta Materialia, 2016, 112: 132-135.

[159] Di Maio D, Roberts S G. Measuring fracture toughness of coatings using focused-ion-beam-machined microbeams[J]. Journal of Materials Research, 2005, 20(2): 299-302.

[160] Brinckmann S, Matoy K, Kirchlechner C, Dehm G. On the influence of microcantilever pre-crack geometries on the apparent fracture toughness of brittle materials[J]. Acta Materialia, 2017, 136: 281-287.

[161] Iqbal F, Ast J, Göken M, Durst K. In situ micro-cantilever tests to study fracture properties of NiAl single crystals[J]. Acta Materialia, 2012, 60(3): 1193-1200.

7. Contribution to the Field

Overall, the aim of this thesis is to improve the mechanical or electrical properties of transition metal nitride thin films by architectural design. Especially, the promising toughness-enhancing superlattice effect is explored. Paper #1 (published) and #2 (in manuscript) contribute towards an improved understanding of the fracture behaviour of the sputtered TiN/MoN SLs by controlling the bilayer periods and bilayer ratios. Paper #3 (in manuscript) aims to modify the ceramic superlattices' strength by doping atomic levels of metalloid Si at the interfaces of TiN/TaN superlattices. Finally, paper #4 (published) and #5 (submitted) describe the specific area capacitance enhancing strategies of the CrN and MoN electrodes by chemical etching and glancing angle deposition, respectively.

7.1 Paper #1 and #2

Ab initio supported development of TiN/MoN superlattice thin films with improved hardness and toughness

Based on semi-empirical toughness indicators, calculated by density functional theory (DFT), the combination of TiN and MoN is highly auspicious because of their significant shear moduli mismatch (60 GPa) and considerable lattice mismatch (0.05 Å), which would allow for a superlattice effect. Therefore, in this study, we used unbalanced DC reactive magnetron sputtering to synthesize a series of TiN/MoN SLs with various bilayer periods and bilayer ratios, and compared them with monolithically grown TiN, MoN, and (Ti,Mo)N solid solutions. XRD and TEM were conducted to determine the structural characteristics of the manufactured thin films. The existing studies on MoN_x demonstrated that MoN_x preferentially crystallizes in hexagonal structures, while their metastable rock salt phase can be stabilized by 50% of randomly distributed nitrogen lattice vacancies ($MoN_{0.5}$, i.e., x = 0.5). In this study, also the formation of an ordered MoN_x (with ordered nitrogen vacancies) was proven by transmission electron microscopy. The ordering of the N-vacancies typically leads

to a tetragonal phase (c = 2a). Microcantilever bending tests and nanoindentation proved the TiN/MoN SL with 10 nm bilayer period and 1:1 bilayer ratio to be superior to the other SL's and the monolithically grown coatings TiN, MoN, and (Ti,Mo)N solid solutions. This SL coating also outperforms the others for their tribological properties (obtained by bi-directional wear tests).

7.2 Paper #3

Synthesis and Electrochemical Properties of Nanoporous CrN Thin Film Electrodes for Supercapacitor Application

Transition metal nitride films, fabricated by physical vapor deposition, have attracted much attention for supercapacitor electrode applications due to their high electrical conductivity, crystallinity, purity, uniformity, structural and chemical stability, and mechanical strength. In combination with being binder-free, these are promising characteristics for flexible and on-chip micro-supercapacitor applications. However, the relatively dense structure and smooth surface when prepared by conventional magnetron sputtering limit their applicability in the field of supercapacitor electrode coatings. Because the capacitive performance of a supercapacitor is highly dependent on the quantity of ions absorbed at the electrode surfaces. To overcome this shortfall porous CrN coatings are prepared from CrN-Ni composite coatings by chemically removing the metallic Ni phase. Most important is that the metallic Ni phase is uniformly distributed in the CrN matrix and forms an interconnected network. The CrN coating with the highest porosity was obtained through chemically leaching (3 h bath in 3 M HCl solution) the Ni phase almost completely from the CrN-Ni composite that had an original Ni phase fraction of 54%. Thereby, the specific capacitance could be increased by a factor of ~80 as compared to the as-deposited CrN and CrN–Ni thin films.

7.3 Paper #4

Nanostructured zig-zag γ-Mo_2N thin films produced by glancing angle deposition

for flexible symmetrical solid-state supercapacitors

Encouraged by the previous reports on the high potential of the glancing angle deposition (GLAD) technique in tailoring the growth morphology, we developed a zig-zag structured porous γ-Mo_2N coating by DC glancing angle magnetron sputtering. In contrast to the simple columnar γ-Mo_2N electrode, the zig-zag electrode exhibits a 4-times higher specific area capacitance due to its open porous nanostructure. Moreover, a solid-state symmetric supercapacitor device was produced with two identical zig-zag γ-Mo_2N electrodes. The device achieved both superior high energy density and power density, excellent cycling stability, and desirable mechanical flexibility.

8. Concluding Statement and Outlook

The research conducted pinpoints important architectural design strategies for improved mechanical or electrochemical properties of transition metal nitride thin films. We studied the superlattice architecture for mechanical properties improvement and the porous architecture for the enhancement of electrochemical properties. This thesis demonstrates that the superlattice architecture, the decoration of the interfaces with specific dopants, and specific growth defects (dislocations, vacancies, interstitials) allow to significantly and simultaneously enhance the hardness, fracture toughness, and tribological properties of TMN thin films.

With the help of TiN/MoN SLs, we have studied the effect of various bilayer periods as well as bilayer ratios on the mechanical properties of TMN SLs. The results show a coherent growth structure of the individual layers and an enhancement of hardness, fracture toughness, and tribological properties of single-phased crystalline SL films on MgO (100) substrates as compared to their monolithically grown constitutions. The results further show that the variation of the bilayer ratio has a weaker effect on the mechanical properties than the variation of the bilayer period. Moreover, we also showed that within the TiN/MoN_x SLs, $MoN_{0.5}$ is not only present in its most stable form, fcc-$MoN_{0.5}$ (with disordered N vacancies), but also with a tetragonal $MoN_{0.5}$ phase (with ordered N vacancies).

The TiN/TaN system provides an even larger shear modulus mismatch (80 GPa) combined with a larger lattice mismatch (0.14 Å), than the TiN/MoN system (60 GPa and 0.05 Å). By forming TiN/X/TaN superlattices, where X refers to C, B, or Si, we further investigated the effect of modifying the interface chemistry between TiN and TaN on their mechanical properties. For this, between each layer (TiN and TaN) a very thin (in the order of a few monolayers) C, B, or Si layer was added. The decoration of the interfaces with Si resulted in a significant increase in hardness to 40 ~GPa and fracture toughness to ~3.5 MPa$\sqrt{m}$. These values are about 30% respectively 20% higher than those obtained for the TiN/TaN SL without the doped interfaces. Also, the

decoration of the interfaces with B leads to improved properties, yielding again ~40 GPa hardness and even 4.3 MPa√m fracture toughness. Decorating the interfaces with C led only to a minor improvement of these properties as compared to the TiN/TaN SL.

Future activities with respect to mechanical properties, beyond the scope of this thesis but building on the knowledge gained by the PhD thesis, will concentrate on (Ti,Al)N/AlN SLs. Interesting is the effect of the bilayer period on the structure if the AlN layers and how this influences the high-temperature fracture toughness.

With the help of porous structures, we have tuned the supercapacitor abilities of CrN and MoN coatings. A sponge-like architecture was realized for CrN coatings through chemically leaching the Ni phase from a CrN-Ni composite. Contrary, a zig-zag open columnar and porous structure was realized for MoN through glancing angle deposition with periodically alternating the angle of incidence of the sputtered flux. The results exhibit an 80-times higher specific area capacitance for the porous CrN electrode compared to the as-deposited CrN-Ni (before removal of the Ni phase) or CrN electrodes. The zig-zag structured MoN electrode presents a 4-times higher specific area capacitance than the more columnar MoN electrode, due to its open and porous nanostructure. Moreover, the supercapacitor device with zig-zag MoN electrodes also achieved both, superior high energy density and power density, combined with excellent cycling stability, and desirable mechanical flexibility

Acta Materialia 231 (2022) 117871

Contents lists available at ScienceDirect

Acta Materialia

journal homepage: www.elsevier.com/locate/actamat

Full length article

Ab initio supported development of TiN/MoN superlattice thin films with improved hardness and toughness

Zecui Gao[a,*], Julian Buchinger[a], Nikola Koutná[a,b], Tomasz Wojcik[a], Rainer Hahn[a], Paul Heinz Mayrhofer[a]

[a] Institute of Materials Science and Technology, Technische Universität Wien, Getreidemarkt 9, Vienna 1060, Austria
[b] Department of Physics, Chemistry, and Biology (IFM), Linköping University, Linköping SE-58183, Sweden

ARTICLE INFO

Article history:
Received 20 December 2021
Revised 16 March 2022
Accepted 21 March 2022
Available online 23 March 2022

Keywords:
PVD thin films
Superlattices
Fracture toughness
DFT
MoN_y

ABSTRACT

Motivated by density functional theory (DFT)-derived ductility indicators for face centered cubic (fcc, rocksalt) structured $TiN/MoN_{0.5}$ superlattices and $Ti_{0.5}Mo_{0.5}N_{0.75}$ solid solutions, TiN/MoN_y superlattice (SL) thin films with bilayer periods Λ of 2.4, 3.9, 6.6, 9.9, and 23.0 nm and corresponding solid solutions were developed by DC reactive magnetron sputtering. These SLs allow for improved hardness H and critical fracture toughness K_{IC}, with both peaking at the same bilayer period Λ of 9.9 nm (where the $MoN_{0.5}$ layers crystallize with the ordered β-Mo_2N phase); $H = 34.8 \pm 1.6$ GPa and $K_{IC} = 4.1 \pm 0.2$ MPa$\sqrt{m}$. The correspondingly prepared fcc-$Ti_{0.5}Mo_{0.5}N_{0.77}$ solid solution has $H = 31.4 \pm 1.5$ GPa and $K_{IC} = 3.3 \pm 0.2$ MPa$\sqrt{m}$. Thus, especially the fracture toughness shows a significant superlattice effect. This is suggested by DFT—by the increase of the Cauchy pressure from −19 to +20 GPa for the 001-direction (while that in the 100-direction remained high, above 83 GPa) upon increasing Λ from 3 to 4 nm.

Together, experimental and computational investigations prove the importance of optimized bilayer periods for highest strength and fracture toughness, as well as optimized N-content for the solid solutions.

1. Introduction

Ceramic thin films (i.e., transition metal borides, carbides, nitrides, and oxides) deposited by physical vapor deposition (PVD), are renowned for their outstanding stiffness and hardness in the machining and forming tool industry [1–3]. Since hardness and fracture toughness are largely mutually exclusive, this means that ceramic thin films are severely compromised in many applications by a low intrinsic fracture toughness [4]. Therefore, significant research efforts are directed towards breaking down the adverse relationship [5]. The optimization of the fracture toughness has been further complicated by a lack of reliable testing methods. Lately, the development of *in situ* micromechanical testing methods—which usually involve the focused ion beam (FIB) machining of micropillars [6], clamped microbeams [7], or free-standing single-supported cantilevers [8] for example—has caused research activities on the fracture toughness of various thin films to surge.

Numerous strategies have been proposed to increase the resistance of ceramic films against crack propagation, including alloying with ductile phase toughening (e.g., Mo_2BC [9], and TiMeN [Me = Mo W, Nb, and Ta] [10]), nanostructure toughening (e.g., Ti-Si-N [11]), anion-vacancy-induced toughening (e.g., VMoN and VWN [12]), nano-multilayer/superlattice (SL) toughening [13–16], and toughening by optimizing the valence electron concentration [17,18]. Specifically, SLs, which are characterised by the alternating deposition of chemically disparate and structurally coherent nanolayers, have shown significant potential to simultaneously enhance the hardness and the fracture toughness of transition metal nitrides [13]. The so-called SL effect was first reported by Helmersson et al. [19] and Barnett and Madan [15,20], who showed that the hardness values of TiN/VN and TiN/NbN SL films considerably exceeds their constituent components. In both instances, the hardness also showed a clear dependence on the bilayer period Λ, i.e., the cumulative thickness of two adjacent layers in a SL. Chu and Barnett [21] proposed that such noticeable bilayer period-dependent hardness enhancement primarily originates from a hindrance of dislocation glide within SL layers and across interfaces, and/or the coherence strains in the interfaces as a result of the lat-

* Corresponding author.
E-mail address: zecui.gao@tuwien.ac.at (Z. Gao).

https://doi.org/10.1016/j.actamat.2022.117871

tice mismatch of the two components. Later, micromechanical cantilever bending tests on TiN/CrN [22], TiN/WN [23], and MoN/TaN [24] SLs showed that the SL effect could induce overlapping peaks of fracture toughness and hardness. The difference between the elastic moduli of the constituents was demonstrated to be an essential prerequisite for the SL effect in TiN/WN, which featured a significant shear modulus difference of 60 GPa, while the lattice mismatch was minimized [23]. The lattice mismatch (and thus coherency strains and/or misfit dislocations) was shown to enhance fracture toughness, but caused a weaker Λ dependence in the TiN/$Cr_{0.37}Al_{0.63}N$ SLs, consisting of layers with almost identical shear moduli and a sizeable lattice mismatch [25].

Recently, high-throughput density functional theory (DFT) calculations of Koutná et al. [26] identified rocksalt-structured TiN/$MoN_{0.5}$ SLs (i.e., 50% vacancies on the N sublattice of the MoN layers) as a particularly promising system for simultaneous enhancement of hardness and toughness within the family of ceramic superlattice coatings. According to the authors, TiN/$MoN_{0.5}$ SL is chemically, mechanically, as well as dynamically stable, and offers excellent ductility, fracture toughness, as well as interfacial tensile strength. Similar to the TiN/$WN_{0.5}$ SL, TiN/$MoN_{0.5}$ SL features a very small lattice mismatch but largely disparate elastic moduli, which result in different dislocation line energies within the layers, thus, providing a good basis for the superlattice effect. Previous modeling and experimental results further suggest that face centered (fcc, rocksalt (NaCl) type with B1 cubic symmetry) MoN_y can be stabilised by vacancies on the nitrogen sublattice [27,28].

PVD allows to synthesise various sub-nitrides of molybdenum, such as the high-temperature phase fcc γ-Mo_2N (having a nitrogen-deficient fcc lattice) and the low-temperature phase β-Mo_2N (having an ordered tetragonal lattice). Both phases exist over a wide range of stoichiometry MoN_y, with fcc γ-Mo_2N across the range from β-Mo_2N ($0.38 \leq y \leq 0.66$) to y values above 1 [29]. For nitrogen compositions y between 0.6 and 0.75, ordering of the nitrogen sublattice in γ-MoN_y is energetically preferred, see Refs. [30,31], where this was conveniently noted as γ'-MoN_y.

In this combined experimental and computational work, we aim to expand the current understanding of nitrogen-vacancy-stabilized fcc structured TiN/MoN_y (y = 0.5–0.7) superlattices, $Ti_{1-x}Mo_xN_y$ solid solutions (with $x \sim 0.5$), and MoN_y thin films. Additionally, the studied TiN/MoN_y SL system provides further insight into the simultaneous toughening and hardening effect of the SL architecture on ceramic thin films. Our methods on the experimental side include X-ray diffraction, scanning electron microscopy, transmission electron microscopy, *in-situ* micromechanical experiments, and nanoindentation. The results are supported on the theoretical side by DFT calculations.

2. Experimental and computational details

2.1. Computational details

Density Functional Theory (DFT) calculations were carried out with the aid of the Vienna Ab-initio Simulation Package (VASP) [32,33] together with plane-wave projector augmented wave (PAW) pseudopotential [34] and the Perdew-Burke-Ernzerhof generalized gradient approximation (GGA) [35]. The plane-wave cut-off energy of 600 eV and the reciprocal space sampling with Γ-centered Monkhorst-Pack meshes [36] ensured a total energy accuracy of at least 10^{-3} eV/at. Equilibrium lattice constants of the face centered cubic rocksalt (Fm-3m) TiN and MoN structures were evaluated by fitting the minimum of the energy vs. volume curve. Additionally, the fcc $MoN_{0.75}$ and $MoN_{0.5}$ variants [37,38]—containing 25 and 50% of quasirandomly-distributed [39] N vacancies on the N sublattice—were considered. The fcc $Ti_{0.5}Mo_{0.5}N_y$ solid solutions, and 001-oriented fcc TiN/MoN_y superlattices (following preferential orientation of our coatings, no other orientation was considered)—with Mo/(Ti+Mo) ratio, x, of 0.5 and y = {1, 0.75, 0.5} (thus, featuring 0, 25, and 50% of N vacancies on the N sublattice)—were fully optimized by relaxing their volume, cell shape, and atomic positions. Relative chemical stability of the binaries (TiN, MoN_y), solid solutions ($Ti_{0.5}Mo_{0.5}N_y$), and superlattices (TiN/MoN_y) was estimated by calculating their formation energy,

$$E_f = (E_{tot} - n_{Ti}\mu_{Ti} - n_{Mo}\mu_{Mo} - n_N\mu_N)/(n_{Ti} + n_{Mo} + n_N) \quad (1)$$

where E_{tot} is the total energy of the system, n_{Ti} (n_{Mo}, n_N) is the number of Ti (Mo, N) atoms, and μ_{Ti} (μ_{Mo}, μ_N) is the corresponding chemical potential, conventionally set to total energy per atom of the hexagonal close packed hcp-Ti (body centered cubic bcc-Mo, N_2 molecule). Mechanical stability [40] and elastic moduli were assessed from the elastic constants, calculated using the stress-strain approach [40,41]. The relative tendency for brittle/ductile behavior was estimated by calculating the Cauchy pressure, *CP* [10,42], defined as $CP = C_{12} - C_{44}$. Since fcc TiN/MoN_y superlattices possess overall tetragonal elastic symmetry with more independent elastic constants (C_{11}, C_{33}, C_{12}, C_{23}, C_{44}, and C_{66}) than cubic systems (C_{11}, C_{12}, and C_{44}), one can introduce in-plane *CP* values ($CP_{100} = C_{23} - C_{44} = CP_{010} = C_{13} - C_{55}$) and out-of-plane *CP* values ($CP_{001} = C_{12} - C_{66}$) for our 001-oriented SLs, being indicators of in-plane and out-of-plane ductility, respectively. For these SLs, with tetragonal elastic symmetry, the homogenized *CP* values are obtained by averaging CP_{001}, CP_{100}, and CP_{010}. Additionally, the inherent tendency for brittleness/ductility [43] was estimated using the shear-to-bulk modulus ratio, *G/B*.

2.2. Coating deposition

Various $Ti_{1-x}Mo_xN_y$ solid solutions and TiN/MoN_y superlattice (SL) thin films with bilayer periods (Λ) of 2.4, 3.9, 6.6, 9.9, and 23.0 nm were developed by a reactive unbalanced magnetron sputtering of one 3-inch Ti target and one 2-inch Mo target (99.99% purity for both, Plansee Composite Materials GmbH), in mixed Ar + N_2 atmospheres within an AJA Orion 5 system. After mounting the ultrasonically precleaned (in acetone and ethanol for 5 min each) polished single-crystalline Si (001-oriented, 20 × 7 × 0.38 mm^3) and MgO (001-oriented, 10 × 10 × 0.50 mm^3) substrates to a rotary substrate holder and evacuating the chamber to a base pressure of roughly 10^{-4} Pa, they were thermally cleaned at 400 °C (as obtained from calibration samples) for 20 min. However, the actual temperature during a deposition would be higher than 400 °C, due to the plasma irradiation. Afterwards, the substrates were Ar ion etched for 10 min by applying a DC potential of −750 V and using an Ar flow rate of 20 sccm at a pressure of 6 Pa.

The working gas pressure for all depositions was 0.4 Pa. The targets were DC-powered by ENI RPG-50 plasma generators, with a current density of 17.54 mA/cm^2 for the 3-inch Ti target (800 mA) and 25.46 mA/cm^2 for the 2-inch Mo target (500 mA). During a deposition, the substrates were DC biased with −50 V for a comparable dense growth morphology for all coatings. Four different MoN_y coatings were synthesized by varying the nitrogen partial pressure with a flow rate ratio [$f_{N2} = F_{N2}/(F_{N2} + F_{Ar})$] variation from 0.2 to 0.5. As the sum of $F_{N2} + F_{Ar}$ was kept constant with 10 sccm, the F_{N2} was set to 2, 3, 4, or 5 sccm. This variation allowed us to identify the best f_{N2} for the combination with TiN and the corresponding deposition rate, needed for controlled development of the SLs. All SLs were deposited with f_{N2} = 0.3 (F_{N2} =3 sccm and F_{Ar} = 7 sccm). The N_2 partial pressure is 0.14 Pa, at this condition. The six different bilayer periods were realized through computer-controlled shutters above the Ti and Mo targets. The total deposition time was 222 min, to obtain ~2 μm thick coatings.

For comparison, TiN, MoN_y, and $Ti_{1-x}Mo_xN_y$ solid solution thin films were prepared with identical conditions, powering of the tar-

gets (Ti target (800 mA) and Mo target (500 mA)), bias potential (−50 V), substrate temperature (400 °C), and f_{N2} = 0.3. Only for the $Ti_{1-x}Mo_xN_y$ solid solutions, the deposition time was reduced to 111 min as here the Ti and Mo targets were operated simultaneously, without shutter switching. To consider the higher N-consumption when powering the Ti and Mo sources simultaneously, one $Ti_{1-x}Mo_xN_y$ solid solution was also prepared with a higher f_{N2} of 0.5.

2.3. Chemical and structural characterization

All coatings were investigated by energy-dispersive X-ray spectroscopy (EDS, Philips XL30) to obtain their overall composition. Their crystal structures grown on Si and MgO substrates were analyzed by X-ray diffraction (XRD) in Bragg-Brentano configuration, featuring Cu K_α X-ray source (operated with 45 kV and 40 mA). Thicknesses and cross-sectional morphologies were studied by scanning electron microscopy (SEM), with an FEI Quanta 250, at an accelerating voltage of 10 kV. More detailed cross-sectional investigations of the microstructure were done by transmission electron microscopy (TEM, FEI TECNAI F20), at an acceleration voltage of 200 kV, combined with selected-area electron diffraction (SAED) analysis and scanning TEM (STEM) imaging.

2.4. Mechanical properties

Indentation hardness and modulus of the thin films grown on MgO were obtained using an ultra-micro indentation system (UMIS), equipped with a Berkovich diamond indenter tip [44–46]. The measurements were load-controlled, with forces ranging from 3 to 45 mN, and 31 indentations were carried out for each sample. We excluded the indentations exceeding an indentation depth of 10% of the coating thickness to avoid respectively minimize substrate interferences [47]. Measuring the curvature of coated MgO substrates was investigated by an optical profilometer (Nanovea PS50), and knowing the thickness of film and substrate, the biaxial modulus of the substrate, allows calculating the residual stresses using the Stoney equation formula given in [48].

The critical fracture toughness K_{IC} of the same films deposited on MgO is obtained through micromechanical bending tests. For this, free-standing microcantilevers were produced using a focused ion beam (FIB) system (FEI Quanta 200 3D featuring a Ga ion source) [25] Optimized geometries of cantilevers (dimensions of thickness w, breadth $b \approx w$, and length $l \approx 7w$) were machined using an ion beam current of 1.0 nA for coarse milling, and 0.5 nA for final cuts, at an acceleration voltage of 30 kV. On all cantilevers, a notch with depth a_0 of 300-500 nm (as shown in Fig. S1b) was milled with 50 pA. Small material bridges (50–100 nm wide) were left on both sides of the notch, to initiate the formation of a very sharp pre-crack at the notch base [49–51]. Notched cantilevers provide intrinsic toughness values of a material. Otherwise, due to the FIB preparation of the notch and the connected relatively large notch radius, the fracture toughness would be overestimated. For each coating sample, 6 microcantilevers were machined and tested (loading in the growth direction of the films). The bending tests were conducted with an *in-situ* SEM/FIB nanomechanical MEMS-based testing system (FT-NMT04, FemtoTools), equipped with a wedge-shaped diamond tip (10 µm width). The experiments were performed in displacement-controlled mode at 5 nm/s, loading until failure.

The critical fracture toughness, K_{IC}, is calculated as:

$$K_{IC} = f(a_0/w) \cdot F_m l / b w^{3/2} \quad (2)$$

where, F_m is the load at failure and l is the bending length from the notch to the point of force application. All other cantilever dimensions are defined in Fig. S1a. The dimensionless geometry factor $f(a_0/w)$–adopted from Matoy et al. [52] based on the work of Di Maio and Roberts [8]–can be obtained for our rectangular cantilevers by:

$$f(a_0/w) = 1.46 + 24.36(a_0/w) - 47.21(a_0/w)^2 + 75.18(a_0/w)^3 \quad (3)$$

As our micromechanical bending tests and the specimen geometries fulfil the traditional criteria associated with K_{IC}, we keep the subscripts "C" instead of "Q", which would indicate that the obtained values are only conditional. These criteria are that the sample dimension (w, a_0, and ligament size $w - a_0$) needs to be larger than the plastic zone (such as $a_0 \geq 2.5(K_{IC}/\sigma_y)^2$, with σ_y being the 0.2% yield strength) [53]. Using our results, presented later, and estimating σ_y with 1/3 of the hardness (according to the Tabor relation [54]) the a_0 values should be larger than 0.1–0.3 µm, which is the case for all of our samples yielding a_0 values in the range 0.3–0.5 µm.

The plane strain energy release rate G_C (in J/m^2) for isotropic ideal brittle materials can be related to K_{IC} with:

$$G_C = K_{IC}^2\left(1 - \nu^2\right)/E \quad (4)$$

For the Young's modulus E, we used the indentation modulus, and for the Poisson's ratio ν, we used the DFT-values (0.27 for TiN/MoN SLs with $\Lambda \approx 4$ nm, 0.23 for TiN, and 0.32 for $MoN_{0.5}$).

The fracture energy release rate J_n is calculated dividing the total strain energy with the fracture surface area under the notch after [55]:

$$J_n = \int F dx / b(w - a_0) \quad (5)$$

where, $\int F\,dx$ is the integral area under the load-deflection curve.

The experimental measurements are quoted based on the sample mean and standard deviation. For quantities derived from two or more independently measured attributes, error propagation is used to estimate the inaccuracy of the derived quantities.

3. Results and discussion

3.1. Ab initio studies

To support experimental investigations presented in the following sections, quantum-mechanical ab initio calculations were carried out. First, we estimated the relative chemical stability of TiN/MoN_y superlattices, their TiN and MoN_y building blocks, as well as $Ti_{0.5}Mo_{0.5}N_y$ solid solutions, all based on the face centered cubic (fcc) rocksalt (Fm-3m) phase. Consistently with preferential orientation of our coatings (discussed later), all computationally studied superlattices had (001) interfaces. The N substoichiometry (MoN_y, $y < 1$) was modeled via N vacancies, and motivated by the well-known thermodynamic driving force for vacancy formation in the fcc MoN [37,56,57]—often deposited in its $MoN_{0.5}$ variant [30,31]—as well as by chemical analysis of our own films (shown later). We note that various types of point defects unavoidably accompany physical vapor deposition processes. In particular, nitrogen vacancies are very common in the group 5 and 6 transition metal nitrides [58–60] due to their stabilisation effect on the cubic phase. As shown by Ozsdolay et al. [61] for epitaxial cubic MoN_x/MgO(001) layers, N vacancies may be also accompanied by metal vacancies. Contrarily, vacancies in TiN (group 4 nitride) are energetically unfavorable (see e.g., Fig. 6 in Ref. [62]). Furthermore, although various defect types should be anticipated in TiN/MoN SL films—following Ref. [61] a combination of N and Mo vacancies could be quite likely especially for MoN_x with $x = 0.75$ and 1—our idealised superlattice model assumes sharp interfaces and

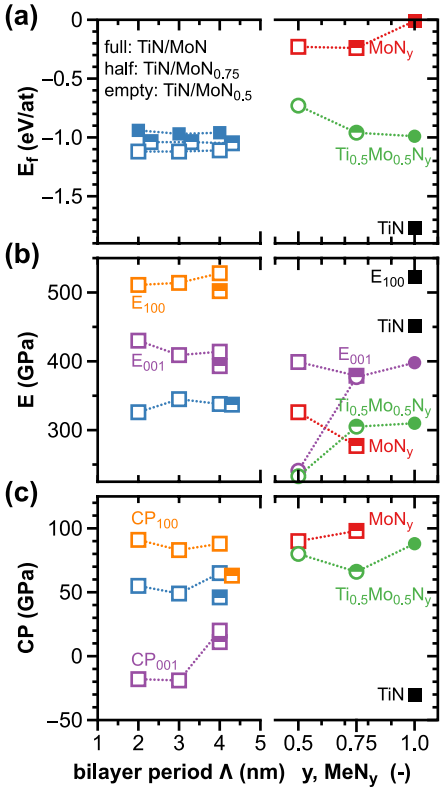

Fig. 1. Ab initio calculated formation energies E_f **(a)**, Young's moduli (E, E_{100}, and E_{001}) **(b)** and Cauchy pressures (CP, CP_{100}, and CP_{001}) **(c)** for TiN, MoN_y, and $Mo_{0.5}Ti_{0.5}N_y$ solid solutions, as well as some TiN/MoN_y superlattices (with bilayer periods Λ of approx. 2, 3, and 4 nm). The orange and violet data points in panels **(b, c)** denote Young's moduli and Cauchy pressures in the [100] and [001] direction, i.e., in-plane and out-of-plane to interfaces of the superlattices, respectively. For fcc TiN, MoN_y, and $Mo_{0.5}Ti_{0.5}N_y$ solid solutions $E_{100} = E_{001}$ and $CP = CP_{100} = CP_{001}$. Full, half, and open symbols denote a N/Me ratio (N/Mo ratio), y, of 1, 0.75, and 0.5 for the fcc-binaries and solid solutions (TiN/MoN_y SLs), respectively.

non-metal vacancies in MoN layers as the *predominant* point defect type mainly responsible for the N substoichiometry (for illustration, see high energetic costs of Ti or N vacancies in TiN layers of TiN/WN SLs, in Ref. [23] Fig. 1).

For all the investigated bilayer periods, Λ ≈ {2, 3, 4} nm, DFT calculations, Fig. 1(a), suggest that TiN/MoN_y SLs energetically prefer to crystallise with 50% of N vacancies in fcc-MoN layers (note that the result for the lowest bilayer period has already been presented in Ref. [26]). Formation energies, E_f, of TiN/$MoN_{0.75}$ SLs lie about 0.08 eV/at higher, and those of defect-free TiN/MoN SLs show an even larger increase, by 0.15–0.18 eV/at, compared to their TiN/$MoN_{0.5}$ counterparts. Therefore, especially stabilisation of the fully stoichiometric SLs seems unlikely. Taking formation energy of a SL, E_f (SL), and subtracting formation energies of the corresponding building blocks, $1/2E_f$ (TiN) and $1/2E_f$ (MoN_y), we obtain the superlattice mixing enthalpy. For all the here studied SLs—out of which TiN/$MoN_{0.5}$ are the most relevant, as later underpinned also by evaluation of mechanical stability—their mixing enthalpy is slightly negative, varying between −0.05 and −0.09 eV/at, which is a sign of negligible energetic costs of interfaces. In fact, the negative mixing enthalpy even suggests an energetic gain. This indication is supported also by generally higher E_f of $Ti_{0.5}Mo_{0.5}N_y$ solid solutions, y = {1, 0.75, 0.5}, compared to TiN/$MoN_{0.75}$ and TiN/$MoN_{0.5}$ SLs. The $Ti_{0.5}Mo_{0.5}N_{0.5}$ variant, i.e., with 50% of vacancies on the N sublattice, is clearly energetically unfavorable, while $Ti_{0.5}Mo_{0.5}N_{0.75}$ and $Ti_{0.5}Mo_{0.5}N_{1.0}$ exhibit similar E_f values, suggesting a fairly wide range of N stoichiometries ($0.75 \leq y \leq 1$) accessible experimentally (depending on the N_2 supply).

Evaluation of mechanical stability [40] based on elastic constants (listed in Table 1) confirms the well-known instability of the fcc (defect-free) MoN [63,64], while the vacancy-variants, $MoN_{0.75}$ and $MoN_{0.5}$ are stable in the fcc structure. Comparing the calculated C_{11} and C_{44} elastic constants with reference values for epitaxial cubic MoN_x/MgO(001) layers [61] yields a perfect agreement (only 6 GPa difference) between our DFT values for $MoN_{0.5}$ and measurements for $MoN_{0.69}$ (no experimental C_{ij} values for $MoN_{0.5}$ are available), whereas the DFT data for $MoN_{0.75}$ lie in-between those recorded for $MoN_{0.69}$ and $MoN_{0.75}$. Our calculations further indicate that the $Ti_{0.5}Mo_{0.5}N_y$ solid solutions, y = {1, 0.75, 0.5}, are mechanically stable, while the defect-free TiN/MoN SLs are unstable (or nearly unstable) for Λ ≈ {2, 3} nm (Λ ≈ 4 nm) due to the negative (or only slightly positive) C_{44} elastic constant, indicating instability with respect to shearing. This is why we did not add this data set to Fig. 1b and c. The TiN/$MoN_{0.75}$ SL are mechanically stable for the largest investigated bilayer period, Λ ≈ 4 nm, while the instability of the SLs with Λ ≈ {2, 3} nm—again due to negative C_{44} elastic constant—might be a consequence of small lateral sizes of our SL model enforcing rather ordered vacancy distributions. We note that increasing the N vacancy content at the N-sublattice in MoN layers from 25% (TiN/$MoN_{0.75}$) to 37.5% (TiN/$MoN_{0.625}$, not shown) increases the C_{44} elastic constant, hence, contributes to mechanical stabilisation of interfaces. The energetically most stable SLs, TiN/$MoN_{0.5}$, are predicted to be mechanically stable for all bilayer periods. The calculated elastic constants (see Table 1) were further used to estimate mechanical properties of selected (mechanically stable) systems. Specifically, Fig. 1b depicts the polycrystalline Young's moduli, E, together with their directional values in the [100] and [001] direction, E_{100} and E_{001}. Possessing cubic elastic symmetry, the binary (TiN, MoN_y) systems and $Ti_{0.5}Mo_{0.5}N_y$ solid solutions yield $E_{100} = E_{001}$, while the overall tetragonal SLs exhibit generally different E_{100} and E_{001} values, indicating differences between the in-plane (parallel to interfaces) vs. out-of-plane SL strength. Our DFT calculations ascribe the overall highest polycrystalline as well as directional Young's moduli to TiN (E = 451 GPa, E_{100} = 523 GPa), while both $MoN_{0.75}$ (E = 277 GPa, E_{100} = 379 GPa) and $MoN_{0.5}$ (E = 326 GPa, E_{100} = 399 GPa) yield significantly lower values. The E (E_{100}) moduli of $Ti_{0.5}Mo_{0.5}N_y$ decrease from 310 (398) down to 233 (241) GPa with y decreasing from 1 to 0.5, hence with decreasing the N sublattice occupancy. Similar to solid solutions, the TiN/$MoN_{0.5}$ SLs yield rather low polycrystalline E moduli (326–345 GPa). However, the predicted directional E_{001} values (409–430 GPa) exceed those of the solid solutions, and the E_{100} moduli (511–528 GPa) are almost as high as those of TiN, hence indicating high out-of-plane and even superior in-plane strength for the SLs.

Together with high strength, an essential prerequisite for superior fracture toughness is ductility. On the level of chemical bonding, the tendency for ductile behavior can be estimated by the Cauchy pressure, CP (Fig. 1c), and the shear-to-bulk modulus ratio, G/B (Table 1). According to Pettifor et al.'s [65] and Pugh's [43] criteria, a ductile material possesses $CP > 0$ and $G/B < 0.5$, respectively. Here CP and G/B values are not interpreted as strict boundaries between brittleness/ductility, but provide a relative comparison within fcc-based transition metal nitride materials. Fig. 1c compares the SL in-plane vs. out-of-plane ductility indicated by directional Cauchy pressures, CP_{100} and CP_{001}, respectively. The effective Cauchy pressure, CP, calculated as an average of CP_{100}, CP_{010} (= CP_{100}), and CP_{001}, gives a single homogenized value for the SL (note that $CP = CP_{100} = CP_{010} = CP_{001}$ for all other systems, i.e., with cubic elastic symmetry). With negative Cauchy pressure (−30 GPa) and G/B = 0.66, TiN exhibits the most brittle behavior of the considered systems. The $MoN_{0.75}$ and $MoN_{0.5}$, on the other

Table 1
Ab initio calculated formation energies, E_f (in eV/at), lattice parameters, a (in Å), elastic constants, C_{ij} (in GPa), polycrystalline bulk, shear, and Young's moduli, B, G, and E (all in GPa), directional Young's moduli and Cauchy pressures, $E_{[hkl]}$ and $CP_{[hkl]}$ (in GPa) for TiN, MoN_y, $Ti_{0.5}Mo_{0.5}N_y$, and TiN/MoN_y superlattices (all with fcc respectively slightly tetragonal structure). Additionally, the shear-to-bulk modulus ratio, G/B, is given as well. The vacancy-free MoN is mechanically unstable; hence no elastic moduli are presented. The lattice parameter a of the SLs denotes the in-plane lattice parameter (a_{100}); we note that out-of-plane lattice parameters are slightly higher than in-plane values due to the Poisson's contraction, and they also vary depending on the distance from interfaces.

Systems	E_f	a_{100}	C_{11}	C_{12}	C_{13}	C_{33}	C_{44}	B	G	E	E_{100}	E_{001}	CP	CP_{100}	CP_{001}	G/B
TiN	−1.77	4.255	573	132	132	573	162	279	183	451	523	523	−30	−30	−30	0.66
MoN	−0.01	4.337	549	212	212	549	−43	–	–	–	–	–		–	–	–
$MoN_{0.75}$	−0.24	4.284	477	180	180	477	81	279	104	277	379	379	98	98	98	0.37
$MoN_{0.5}$	−0.23	4.202	508	196	196	508	106	300	124	326	399	399	90	90	90	0.41
$Ti_{0.5}Mo_{0.5}N$	−0.99	4.309	498	185	185	498	96	289	117	310	398	398	88	88	88	0.4
$Ti_{0.5}Mo_{0.5}N_{0.75}$	−0.96	4.254	463	165	165	463	99	264	116	305	377	377	66	66	66	0.44
$Ti_{0.5}Mo_{0.5}N_{0.5}$	−0.73	4.196	348	166	166	348	86	227	88	233	241	241	80	80	80	0.39
TiN/$MoN_{0.625}$, Λ=2 nm	−1.08	4.258	584	146	163	512	68	291	120	317	515	439	68	95	13	0.41
TiN/$MoN_{0.5}$, Λ =2 nm	−1.12	4.250	576	133	161	503	70	285	124	326	511	430	91	91	−18	0.44
TiN/$MoN_{0.5}$, Λ=3 nm	−1.12	4.248	582	132	167	487	84	287	133	345	514	409	83	83	−19	0.46
TiN/$MoN_{0.5}$, Λ=4 nm	−1.12	4.248	601	141	173	495	85	296	129	338	528	414	88	88	20	0.44

hand, yield the overall highest CP (98 and 90 GPa for $y = 0.75$ and $y = 0.5$, respectively) and the lowest G/B values (0.37 and 0.41 for $y = 0.75$ and $y = 0.5$, respectively). The $Ti_{0.5}Mo_{0.5}N_y$ solid solutions are also identified as intrinsically ductile, yielding G/B = 0.39–0.44 and $CP = CP_{100}$ of 66–88 GPa, which exceeds DFT-calculated Cauchy pressure values of many transition metal nitrides, including ZrN, HfN, $Ti_{0.5}M_{0.5}N$ with M = [Hf, Ta, Cr], or $Zr_{0.5}M_{0.5}N$ with M = [Hf, Nb, V, Ta] (see Table 1 in Ref. [4]). Here, both ductility criteria point towards an increased ductile behavior with increasing N for $y \geq 0.75$ (from $Ti_{0.5}Mo_{0.5}N_{0.75}$ to $Ti_{0.5}Mo_{0.5}N_{1.0}$; the formation of $Ti_{0.5}Mo_{0.5}N_{0.5}$ is quite energetically unfavorable). Similar high Cauchy pressures are found in-plane for TiN/$MoN_{0.5}$ SLs (CP_{100} = 83–91 GPa), while the out-of-plane values, CP_{001}, reach only −19 to +20 GPa. Our calculations, therefore, indicate an excellent basis for SL in-plane plasticity in contrast to rather brittle behavior in the direction orthogonal to interfaces. The in-plane SL characteristics are relevant for, e.g., microcantilever bending experiments and nanoindentation, inducing local in-plane strains (e.g., sideways from the indenter), and any shear-loading during application (like during frictional contacts). Additionally, the considerable increase in CP_{001} from −19 to +20 GPa upon increasing Λ from 3 to 4 nm (while CP_{100} remains high) already hints towards an improved ductile behavior also out-of-plane for even larger bilayer periods.

We note that the above presented DFT results do not reflect important contributions to strength and ductility at the microscale, in particular, the material's microstructure. Furthermore, only SLs with low bilayer periods have been investigated so far, showing essentially no Λ-dependence of formation energies (e.g., E_f of different TiN/$MoN_{0.5}$ SLs varied by less than 0.01 eV/at), and a rather weak Λ-dependence of elastic properties, but a strong Λ-dependence for CP_{001} (for $\Lambda \geq 2$, as mentioned above). Small changes of the SL in-plane lattice parameter (which decreases from 4.250 Å to 4.234 Å for TiN/$MoN_{0.5}$ SLs with $\Lambda \approx 2$ nm and $\Lambda \approx$ 4 nm), is also a sign for Λ-induced changes of interface strains. In order to reveal microstructural effects in TiN/MoN_y SL films as well as to understand the role of the bilayer period (especially when increasing Λ beyond 4 nm), we further proceed with experimental results.

3.2. Composition and structure

Before developing TiN/MoN_y SL thin films, we carefully analyzed the composition as well as structure of Mo-N coatings prepared with N_2 flow rate ratios, $f_{N2} = F_{N2}/(F_{Ar}+F_{N2})$, of 0.2, 0.3, 0.4, and 0.5. As proposed in previous works [27,28,30,66], the structure, phase stability, and mechanical properties of Mo-N highly depend on the N content. Independent on the N_2-supply during

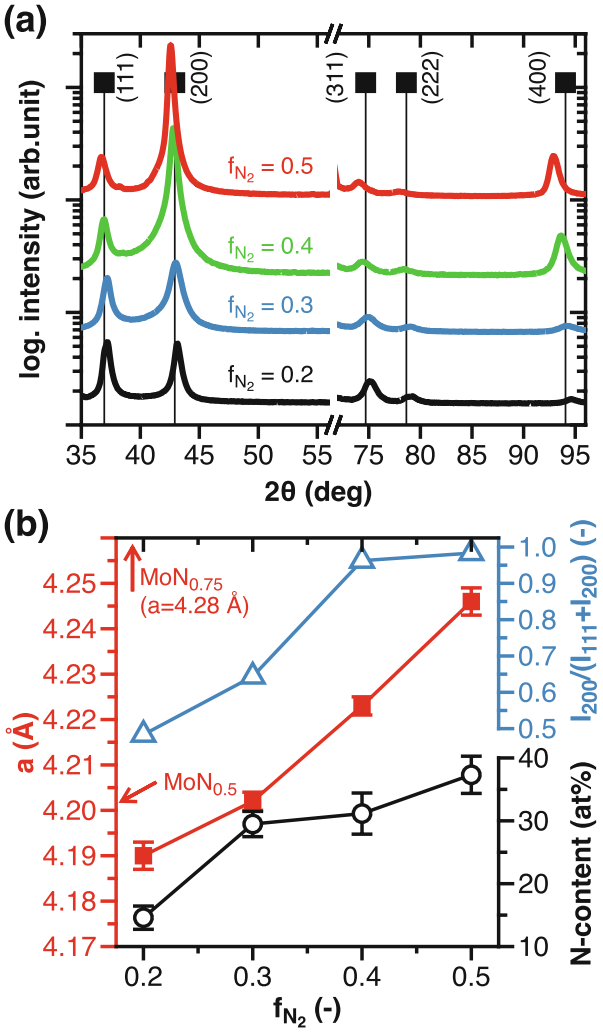

Fig. 2. XRD patterns **(a)** and lattice parameters (red line with full symbols), XRD peak intensity ratio $[I_{200}/(I_{111}+I_{200})]$ (blue line with empty triangle symbols), and EDS-obtained nitrogen content **(b)** of MoN_y coatings **(b)**, for the four N_2 flow rate ratios (f_{N2}) used. All on Si (001) substrates.

deposition, all Mo-N coatings are single-phase face centered cubic structured (fcc, B1, rocksalt), Fig. 2a, in accord to previous PVD studies. With increasing f_{N2} from 0.2 to 0.5, the lattice parameter increases from 4.19 ± 0.01 to 4.24 ± 0.01 Å, and the peak intensity ratio $[I_{200}/(I_{111}+I_{200})]$ increases from 0.48 to 0.98, respec-

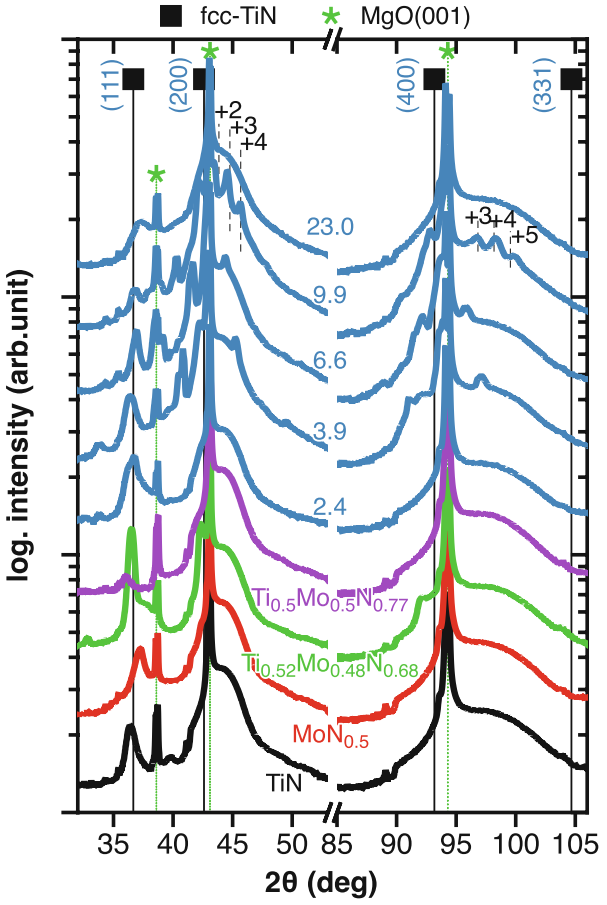

Fig. 3. XRD patterns of the TiN/$MoN_{0.5}$ SLs (labeled with the bilayer period in nm) and the monolithically grown TiN, $MoN_{0.5}$, and $Ti_{1-x}Mo_xN_y$ solid solutions (all grown on MgO (001) substrates). For the SLs with Λ = 3.9, 6.6 and 9.9 nm satellite peaks are clearly detectable, which are assigned for the Λ = 9.9 nm case.

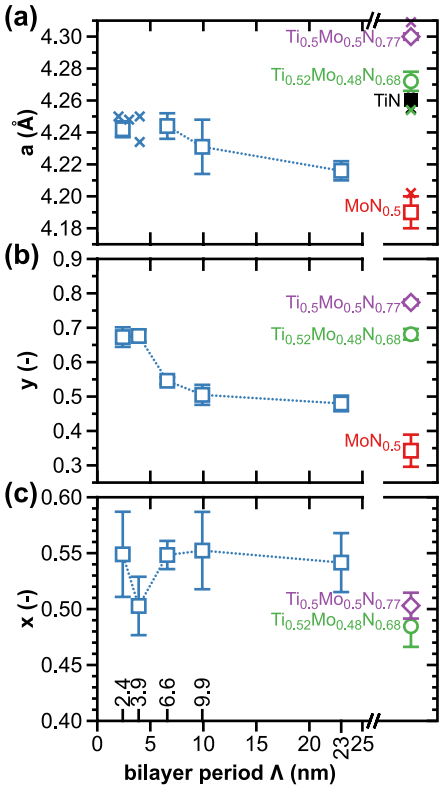

Fig. 4. Lattice parameters *a* **(a),** EDS-obtained N/metal ratio *y* **(b)** and Mo/(Mo+Ti) ratio *x* **(c)** of the superlattice TiN/$MoN_{0.5}$ coatings (averaged across all layers) and the monolithically grown TiN, $MoN_{0.5}$, and $Ti_{1-x}Mo_xN_y$ solid solutions (all grown on MgO (001) substrates). The crosses indicate the ab initio obtained lattice parameter (see Table 1), where the larger value for the Λ = 4 nm SL is for TiN/$MoN_{0.75}$ and the others are for TiN/$MoN_{0.5}$. The crosses for the $Ti_{0.5}Mo_{0.5}N_y$ solid solution cover the *a* range 4.254–4.309 Å valid for *y* = 0.75 and 1.0, respectively.

tively, Fig. 2b. Based on the comparison of the lattice parameter variation with DFT calculated lattice parameters for fcc-MoN_y (4.28 Å for $MoN_{0.75}$ and 4.20 Å for $MoN_{0.5}$, marked in Fig. 2b) [37] and considering the qualitative EDS data (see Fig. 2b), we simply name the MoN_y coatings prepared with f_{N2} = 0.3 and 0.5 as $MoN_{0.5}$ and $MoN_{0.75}$, respectively. We note, however, that the DFT model only assumes N vacancies, while also Mo vacancies may be present—as shown for epitaxial cubic MoN_x/MgO(001) layers [61]—which would affect lattice parameter values. In combination with our previous studies on TiN [11], f_{N2} = 0.3 was selected for the development of the monolithic TiN and $MoN_{0.5}$, and the SL films. To complement the study, also two $Ti_{1-x}Mo_xN_y$ solid solutions were prepared with f_{N2} = 0.3 and 0.5, which are named $Ti_{0.52}Mo_{0.48}N_{0.68}$ and $Ti_{0.5}Mo_{0.5}N_{0.77}$, respectively, based on their EDS-obtained Mo/(Ti+Mo) ratio, *x*, and N/metal ratio, *y* (shown later also in Fig. 4).

Based on the deposition rates obtained for the $MoN_{0.5}$ and TiN, TiN/$MoN_{0.5}$ SLs with similar $MoN_{0.5}$ and TiN layer thicknesses ℓ ($\ell_{TiN} \sim \ell_{MoN0.5}$) were developed. Their individual bilayer periods (2.4, 3.9, 6.6, 9.9, 23.0 nm) are simply estimated by dividing the total coating thickness by the total number of bilayers. Fig. 3 shows their XRD patterns together with those of TiN, $MoN_{0.5}$, and the $Ti_{0.52}Mo_{0.48}N_{0.68}$ and $Ti_{0.5}Mo_{0.5}N_{0.77}$ solid solutions grown on MgO (001) substrates. All coatings show a single-phase fcc structure with a strong (001) orientation, except for the $Ti_{0.52}Mo_{0.48}N_{0.68}$ solid solution, which shows a strong (111) XRD peak in addition. The TiN/$MoN_{0.5}$ SLs with Λ from 3.9 to 9.9 nm clearly exhibit satellite peaks (for example, the Λ = 9.9 SL), which illustrate sharp interfaces [67]. With increased Λ, these satellite peaks come closer to the main diffraction peak (200) [20], and higher-order satellite peaks are barely resolved [68]. For the SL with Λ = 23.0 nm, the satellite peaks are too close to the main peak, and for the SL with Λ = 2.4 nm, the individual TiN and $MoN_{0.5}$ layers are too thin to be resolved, therefore barely any satellite peaks can be observed for both of them. The XRD pattern of the SL with Λ = 2.4 nm is very comparable to those of the solid solutions $Ti_{0.52}Mo_{0.48}N_{0.68}$ and $Ti_{0.5}Mo_{0.5}N_{0.77}$. Because the individual satellite reflections of the SLs overlap with those from the ordered β-Mo_2N phase, the $MoN_{0.5}$ layers could also be present with this phase (which we actually proved by detailed SAED studies, presented later). Contrary to the XRD studies of the individual MoN_y thin films (Fig. 2), which only showed a single-phase fcc-MoN_y structure.

When the diffracting crystal planes are stacked with a small wavelength of sinusoidal modulation in atomic scattering factors and/or interplanar spacings, According to Eltoukhy and Greene [69], Λ can be calculated directly from the angular positions of the positive or negative satellites ($\theta_\pm$) relative to the Bragg angle (θ_B), by the formula:

$$\sin\theta_\pm = \sin\theta_B \pm m\lambda/2\Lambda \quad (7)$$

where λ is the X-ray wavelength, and *m* is the order of the superlattice reflection. Following this calculation, our TiN/MoN_y SLs have modulation periods (Λ) of 2.8 ± 0.2, 3.9 ± 0.7, 6.1 ± 0.8, and 9.9 ± 0.7 nm, roughly in line with those estimated from the total coating thickness being 2.4, 3.9, 6.6, and 9.9 nm, respectively. For all samples, their negative satellite peaks are roughly similar in intensity to the positive ones, due to the similar X-ray scat-

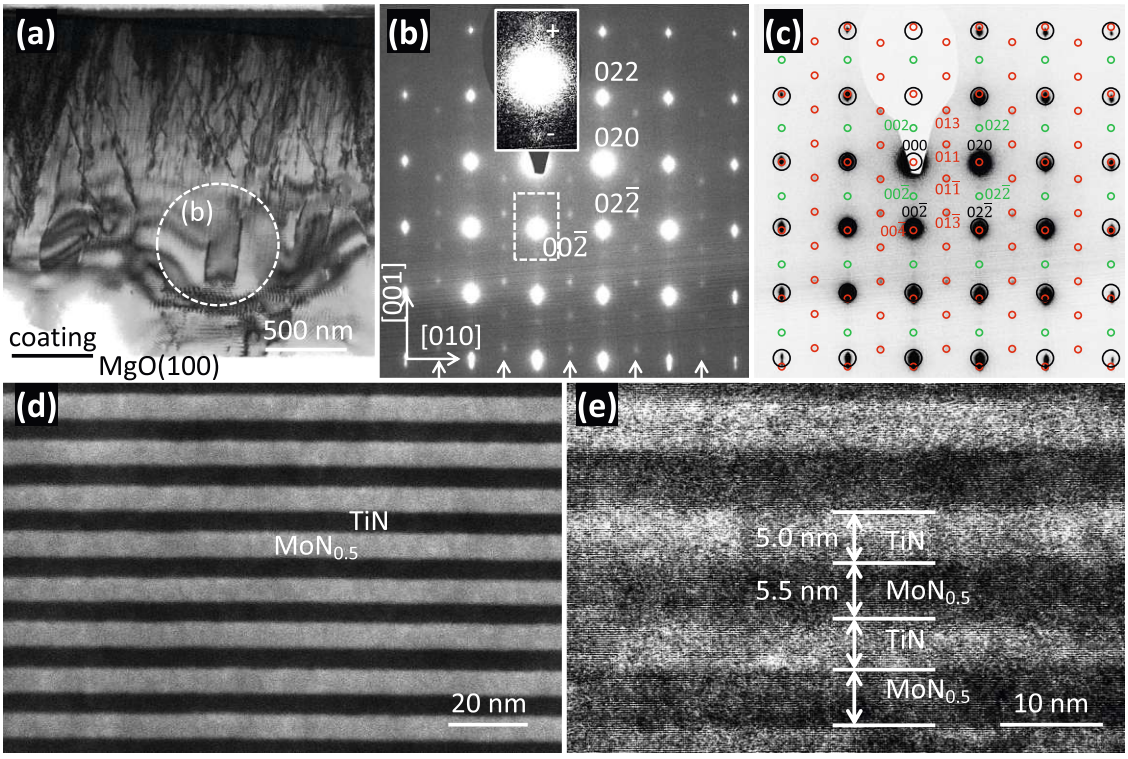

Fig. 5. Representative cross-sectional TEM images of the superlattice TiN/$MoN_{0.5}$ coatings using the sample with a bilayer period of 9.9 nm, on MgO (001) substrate. **(a)** Bright field overview image of the (100) cross section with indicated positions for the SAED pattern. **(b)** [100] SAED pattern with the most intense reflections from the rocksalt fcc TiN/$MoN_{0.5}$ lattice. Along [001], satellite reflections appear systematically due to the TiN/$MoN_{0.5}$ superlattice. These are marked by +/− in the enlargement of the area delimited by a white rectangular. The additional smaller reflections (along the columns marked with the small arrows) stem from the ordered tetragonal β-Mo_2N phase of the $MoN_{0.5}$ layers. **(c)** Simulated SAED pattern combining the reflections of TiN (larger black circles) and β-Mo_2N (smaller red and green circles) overlaid on the inverted SAED image from (b). **(d)** Detailed STEM image from the substrate near region. **(e)** Lattice-resolved high-resolution TEM micrograph.

tering factors and lattice spacings between fcc-$MoN_{0.5}$ and TiN [70]. The XRD patterns are used to obtain the lattice parameters, plotted in Fig. 4a. The N/metal ratio, y (Fig. 4b), using EDS obtained data, decreases with increased bilayer period, which fits the observed concomitant decreased lattice parameter. This decrease in y and a actually suggests that for small Λ values, the MoN_y layers contain more N than for larger Λ values. Energetically, TiN/$MoN_{0.75}$ SLs are only slightly less preferred than TiN/$MoN_{0.5}$ SLs, and with $\Lambda = 4$ nm, the TiN/$MoN_{0.75}$ SL is already mechanically stable (Fig. 1 and Table 1). Additional DFT calculations proved that TiN/$MoN_{0.625}$ SLs are mechanically stable already for $\Lambda = 2$ nm. Thus, directly close to the TiN layers, the MoN_y layers will have more N (supported by the surplus of N as the TiN layers would also grow stoichiometric with a lower f_{N2}). As with larger Λ, there are fewer interfaces and interface-near regions, the overall N-content decreases and also the lattice parameter ($a_{MoN0.5} < a_{MoN0.75}$).

The Mo/(Ti+Mo) ratios (x, obtained from the entire coating) are between 0.50 and 0.55 for all superlattices (Fig. 4c), hence, considering that the lattice parameter of $MoN_{0.5}$ (4.202 Å, DFT-data, Table 1) is slightly below that of TiN (4.242 Å literature data from JCPDF, or 4.255 Å, DFT-data, Table 1), $\ell_{MoN0.5}$ should be $\sim\ell_{TiN}$. Also, in-line with the N/metal ratio, $Ti_{0.5}Mo_{0.5}N_{0.77}$ exhibits a slightly larger lattice parameter than $Ti_{0.52}Mo_{0.48}N_{0.68}$.

Fig. 5 presents TEM and SAED images of the $\Lambda = 9.9$ nm TiN/$MoN_{0.5}$ superlattice grown on MgO (001). The TEM overview image (Fig. 5a) shows a dense growth morphology without an obvious columnar structure. The thickness of the TEM sample increases from the bottom (interface to the MgO (001) substrate) to the top, therefore especially at the top there is a higher density of strain-features present. The SAED pattern (Fig. 5b, projected perpendicular to the [100] zone axis) shows an fcc structure with diffraction spot streaks (along [001]) due to the different lattice parameters along this direction of the individual TiN and $MoN_{0.5}$ layers. Additional smaller spots decorating the larger ones along this 001-direction (marked with + and – in the enlarged rectangle) indicate the superlattice structure, analogous to the observations by XRD. In Fig. 5c, this SAED image is overlaid with simulated SAED patterns of TiN (larger black circles) and the ordered tetragonal β-Mo_2N (smaller red and green circles). This clearly shows that within the 010-direction the lattice parameters of both structures are nearly identical, allowing for the excellent epitaxial growth, whereas along [001] the $MoN_{0.5}$ structure is slightly shorter with a c/a ratio of 1.96. Based on the comparison between measured and simulated SAED, the small reflections along the columns marked with arrows in Fig. 5b, clearly indicate that the $MoN_{0.5}$ layers crystallize with the ordered tetragonal β-Mo_2N phase.

The STEM image (Fig. 5d) shows the regular contrast modulation due to the alternating layering of TiN and $MoN_{0.5}$. Again, columns are not visible, only strain fields due to the epitaxial growth of the SL onto MgO (001). The individual layers are very flat with distinct interfaces to each other. The bright layers in this Z-contrast high angle annular dark-field (HAADF) image represent $MoN_{0.5}$, while the TiN layers yield a darker contrast due to their lower average atomic number. Contrary, the $MoN_{0.5}$ layers show darker contrast in the high-resolution TEM (HRTEM) image (Fig. 5e) because of the increased scattering of electrons. The continuous lattice fringes across various TiN and $MoN_{0.5}$ layers prove their high epitaxial relation. The slightly thicker $MoN_{0.5}$ layer ($\ell_{MoN0.5} = 5.5$ nm; $\ell_{TiN} = 5.0$ nm) is in-line with the Mo/(Ti+Mo) ratio of $x = 0.55$ for this coating. The slightly larger bilayer pe-

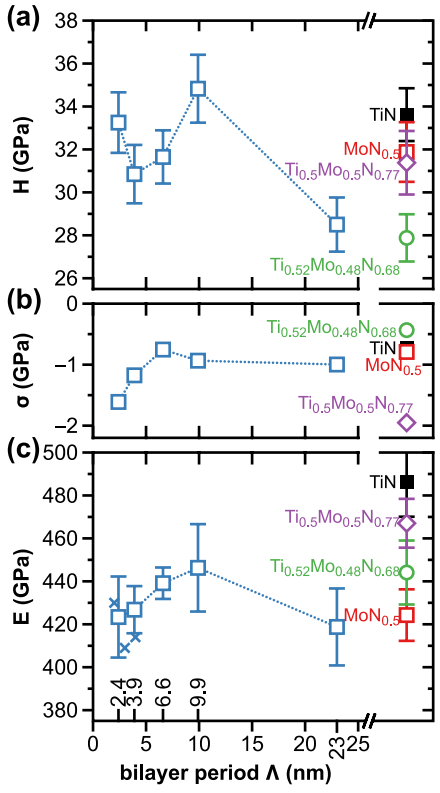

Fig. 6. Indentation hardness H **(a)**, biaxial residual stress σ **(b)**, and indentation modulus E **(c)** of the TiN/$MoN_{0.5}$ SLs and the monolithically grown TiN, $MoN_{0.5}$, and $Ti_{1-x}Mo_xN_y$ solid solutions (all on MgO (001) substrates). The crosses indicate the ab initio obtained E_{100} moduli (compare Fig. 1 and Table 1).

riod of 10.5 (instead of the 9.9 nm obtained from dividing the total coating thickness (from STEM) by the number of bilayers) agrees with the value obtained from the XRD satellite peak positions (9.9 ± 0.7 nm). Overall, the TEM analyses demonstrate that the TiN/$MoN_{0.5}$ superlattices on MgO (001) possess a high quality and a sharp compositional contrast at the interface, in excellent agreement with XRD investigations.

3.3. Indentation hardness and modulus

The indentation hardness H of the TiN/MoN_y SLs initially decreases from 33.3 ± 1.4 to 30.9 ± 1.4 GPa, with increasing Λ from 2.4 to 3.9 nm. After passing the valley, the hardness peaks at 34.8 ± 1.6 GPa (Λ = 9.9 nm), then, falling down to 28.8 ± 1.3 GPa (Λ = 23.0 nm), Fig. 6a. Comparing these data with those obtained from monolithically grown coatings suggest that there is not much deviation from a rule-of-mixture behavior between TiN and $MoN_{0.5}$, having 33.6 ± 1.2 and 31.9 ± 1.4 GPa, respectively. The hardness for TiN is very comparable to that of a previous study (31.7 ± 0.2 GPa [23]), which was also grown on MgO (001) using the same machine (but with a slightly lower bias of −40 V and a higher f_{N2} of 0.47 combined with a higher sputtering current of 1 A). The reported hardness for MoN_y strongly depends on the chemical composition, where within single-phase fcc structured materials, the highest value of 33.0 ± 1.7 GPa is obtained for $MoN_{0.5}$ [28]. For higher and lower N contents, the hardness declines. For example, for ~40 at% N ($MoN_{0.67}$, prepared at an N_2-to-total pressure ratio of 0.69), the hardness is 28.0 ± 2.0 GPa [28], which is very close to the value of our $Ti_{0.52}Mo_{0.48}N_{0.68}$ solid solution (27.9 ± 1.1 GPa), which was prepared with f_{N2} = 0.3. The higher N-containing solid solution, $Ti_{0.5}Mo_{0.5}N_{0.77}$ (prepared with f_{N2} = 0.5), presents a hardness of 31.4 ± 1.5 GPa, which is comparable to TiN and $MoN_{0.5}$, and also previously published data of $Ti_{1-x}Mo_xN_y$ coatings [71].

The comparison of the Λ = 23 nm SL with the monolithically grown films TiN, $MoN_{0.5}$, $Ti_{0.52}Mo_{0.48}N_{0.68}$ (f_{N2} = 0.3), and $Ti_{0.5}Mo_{0.5}N_{0.77}$ (f_{N2} = 0.5), as well as with the above-mentioned published H values for fcc-MoN_y—the highest value for $MoN_{0.5}$, which declines for higher and lower N content—suggests that this SL is composed of TiN and N-deficient fcc-$MoN_{0.5-z}$ [72]. The higher frequency of switching between Ti and Mo target for the SL with lower Λ can account for the less prone N_2-depletion of the working gas. Please see Fig. 2, showing that decreasing f_{N2} from 0.3 to 0.2 results in the formation of N-deficient fcc-$MoN_{0.5-z}$. Contrary, the chemistry of TiN is not that sensitive to f_{N2}.

The hardness of the SL with the smallest bilayer period of 2.4 nm is 33.2 ± 1.4 GPa and still between that of TiN and $MoN_{0.5}$. Reasons for the higher residual compressive stresses of this SL with Λ = 2.4 nm, Fig. 6b, can be interfacial effects, such as a higher contribution (due to more interfaces per coating thickness) from intermixed regions of adjacent layers, distorted metastable phases formed in the interface-near region, as well as oscillations of the d-spacings close to the interfaces [72,73]. The latter effects have been studied in detail by ab initio calculations of MoN-TaN superlattices [74]. Essentially, only the SL with Λ = 9.9 nm is harder than TiN while having the same compressive residual stresses of ~−1 GPa but much lower indentation modulus, Fig. 6c.

The indentation modulus E of the SL coatings shows a comparable variation with the bilayer period as the hardness and peaks with 446 ± 20 GPa at Λ of 9.9 nm. Coherency strains by lattice-mismatched layers can cause increased elastic constants [75], explaining the initial increase in E with increasing Λ. The formation of misfit dislocations when exceeding a certain layer thickness will relax these strains, and thus the E declines again. The monolithic $MoN_{0.5}$ and TiN coatings yield E of 424 ± 12 GPa and 486 ± 16 GPa, respectively, is in reasonable agreement with previously published data of 430 ± 25 GPa for $MoN_{0.5}$ [30] and 452 ± 3 GPa for TiN [23]. The DFT calculated Young's moduli are E_{100} = 399 GPa for $MoN_{0.5}$ and E_{100} = 523 GPa for TiN, where the differences come from microstructural effects and other defects than N vacancies, in particular, also Mo vacancies could be present in the coatings and are disregarded by the model. Thus, both experiments and DFT calculations confirm that the layer materials for our superlattice coatings, $MoN_{0.5}$ and TiN, possess significantly different E moduli, while their lattice parameters are rather close with 4.20 Å for $MoN_{0.5}$ and 4.25 Å for TiN. According to previous literature reports, this provides a basis for increased resistance to dislocation motion across layers when the layers are thick enough for dislocations [21,76,77]. The $Ti_xMo_{1-x}N_y$ solid solutions exhibit E values of 444 ± 15 GPa for $Ti_{0.52}Mo_{0.48}N_{0.68}$ and 467 ± 11 GPa for $Ti_{0.5}Mo_{0.5}N_{0.77}$, and are thus higher as those obtained by DFT for $Ti_{0.5}Mo_{0.5}N_{0.75}$ (E_{100} = 377 GPa) and $Ti_{0.5}Mo_{0.5}N$ (E_{100} = 398 GPa). The DFT calculated polycrystalline Youngs' modulus for vacancy-free $Ti_{0.5}Mo_{0.5}N$ is reported with 344 GPa [10], while we obtained E = 310 GPa (Table 1).

3.4. Fracture toughness evaluation

In Fig. S1a, a wedge indenter tip and a free-standing microcantilever are shown directly before testing. Figs. S1b through S1f depict the SEM micrographs of the fractured surface after bending testing for the SLs with increasing Λ from 2.4 to 23.0 nm, and those for TiN, $MoN_{0.5}$, and the $Ti_{0.5}Mo_{0.5}N_{0.77}$ solid solution are given in Fig. S1g, h, and i, respectively. These fracture cross sections show that only TiN exhibits a pronounced columnar growth morphology, whereas the other ones are very smooth and suggest very dense growth morphologies as proven by TEM investigations, as

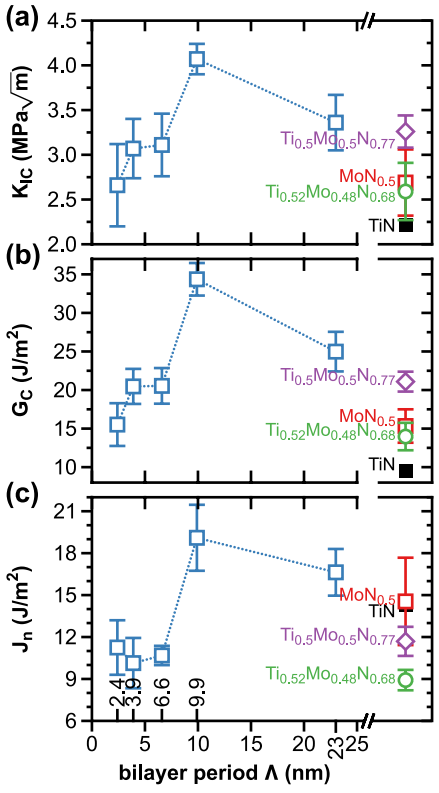

Fig. 7. Critical fracture toughness K_{IC} **(a)**, strain energy release rate G_C **(b)**, and fracture energy release rate J_n **(c)**, for the TiN/MoN_y SLs and the monolithically grown TiN, $MoN_{0.5}$, and $Ti_{1-x}Mo_xN_y$ solid solutions (all on MgO (001) substrates).

shown in Fig. 5 for the SL with Λ = 9.9 nm. The fracture surfaces of all SLs and the $MoN_{0.5}$ and $Ti_{1-x}Mo_xN_y$ coatings do not show any evidence for a microstructure-related different crack-propagation. All cantilevers failed at the FIB-fabricated pre-notch, and all the initial thin material bridges and notch depths a_0 are visible in Fig. S1.

Representative load-deflection curves of all tested cantilevers are shown in Fig. S2a (presenting the SL coatings) and Fig. S2b (presenting the monolithically grown coatings). For TiN, only one cantilever is measured (therefore no error bar for the obtained values, which are presented later), which is in perfect agreement in *H*, *E*, and fracture toughness (K_{IC}) with previously published data [78]. All cantilevers provided perfectly linear load–deflection curves until fracture, but please be aware that their dimensions are different, and thus direct comparison of the individual load-deflection curves is not possible.

Contrary to the *H* and *E* dependence (Fig. 6), the fracture toughness K_{IC} of the SLs massively changes with the bilayer period and peaks at 4.1 ± 0.2 MPa$\sqrt{m}$ with Λ = 9.9 nm, Fig. 7a. The SL with the smallest bilayer period of 2.4 nm exhibits a K_{IC} of 2.7 ± 0.2 MPa$\sqrt{m}$, which is perfectly between those of TiN (2.2 MPa$\sqrt{m}$) and $MoN_{0.5}$ (2.8 ± 0.2 MPa$\sqrt{m}$). Opposed to this behavior, the SL with the largest bilayer period of 23.0 nm exhibits a K_{IC} of 3.4 ± 0.3 MPa$\sqrt{m}$, which is even above that of the $Ti_{0.5}Mo_{0.5}N_{0.77}$ solid solution (3.3 ± 0.2 MPa$\sqrt{m}$). The latter provided the highest K_{IC} value among the monolithically prepared coatings studied here. Interesting to note is also that the K_{IC} values nicely follow the DFT-derived ductility criteria combined with the *E*-moduli. These suggested, Fig. 1, increasing *E*-moduli and *CP* values with increasing N-content of the $Ti_{0.5}Mo_{0.5}N_y$ solid solution, in agreement with the increased K_{IC} values from $Ti_{0.52}Mo_{0.48}N_{0.68}$ to $Ti_{0.5}Mo_{0.5}N_{0.77}$. The ductility criteria also hint towards increasing *CP* values for Λ above 4 nm, while at the same time, the *E*-moduli are not declining. In accord with the higher K_{IC} values for Λ ≥ 4 nm

The fracture toughness values of the TiN/$MoN_{0.5}$ SLs (with Λ ≥ 3.9 nm) and the N-rich solid solution, $Ti_{0.5}Mo_{0.5}N_{0.77}$, compare positively to those of other ceramic coatings (tested with the same machine and cantilever geometry), such as TiN/CrN SLs (peak of 2.0 ± 0.2 MPa$\sqrt{m}$ at Λ = 6.2 nm) [22], TiN/SiN_x nanocomposite (~4.6 ± 0.6 MPa$\sqrt{m}$ at 8.5 at% Si) [79], $Ti_{0.54}Al_{0.46}N$ (~3.5 ± 0.3 MPa$\sqrt{m}$) [80], as well as the Ti–X–C system (X = Ta, W, Nb, Mo, and V; ~ 2.0 MPa$\sqrt{m}$ [81]). Depending on the material-combination chosen to prepare superlattices, the so-called "superlattice effect" is sometimes more pronounced for lattice mismatched or shear modulus mismatched layers. For example, while a lattice mismatch only causes a mild superlattice effect on the fracture toughness for modulus-matched TiN/$Cr_{0.37}Al_{0.63}N$ SLs (Δa = 0.14 Å), having a broad maximum at 2.5 ± 0.1 MPa$\sqrt{m}$ for Λ between 7.3 and 14 nm [25]; the modulus mismatch causes a pronounced superlattice effect for the lattice-matched TiN/WN SLs (ΔE_{100} = 67 GPa), exhibiting a peak with 4.6 ± 0.2 MPa$\sqrt{m}$ at Λ = 10.2 nm [23]. However, the TaN/MoN_y SLs have a large lattice mismatch but similar shear moduli and still provide a distinct superlattice effect with a K_{IC} peak of 3.0 ± 0.2 MPa$\sqrt{m}$ at Λ = 5.2 nm [24]. The TiN/$MoN_{0.5}$ SLs studied here have a lattice mismatch (Δa = 0.05 Å) and a modulus mismatch (ΔG = 59 GPa), guaranteeing that their fracture toughness is noticeably dependent on the bilayer period and providing values above those of the monolithically prepared films.

The strain energy release rate G_C has the same trend as K_{IC}, Fig. 7b because the indentation modulus *E* only mildly varies with Λ. The G_C peak of 34.4 ± 2.1 J/m^2 for the SL with Λ = 9.9 nm is massively above that of the $Ti_{0.5}Mo_{0.5}N_{0.77}$ solid solution, which provides the highest value of 21.1 ± 1.3 J/m^2 among the monolithically grown coatings studied here (TiN, $MoN_{0.5}$, and $Ti_{1-x}Mo_xN_y$).

When comparing these experimental data (K_{IC} and G_C) with the DFT-derived intrinsic ductility criteria and *E* moduli, we find a good correlation between the SLs and solid solutions, where DFT only captured Λ values up to 4 nm. For such SLs, the ductility criteria are comparable to the $Ti_{0.5}W_{0.5}N_y$ solid solutions (Table 1), but their in-plane E moduli (E_{100}) are larger (with comparable out-of-plane values, E_{001}). The clearly enhance fracture toughness for the Λ = 9.9 nm SL—as compared to SLs with smaller Λ and the fcc-$Ti_{1-x}Mo_xN_y$ solid solutions—points towards the importance of dislocation activities, which do require a certain minimum layer thickness.

The fracture energy release rate J_n, calculated by dividing the area under the load-displacement curves with the corresponding fracture surface (Eq. (5)), is given in Fig. 7c. Although the SLs with Λ = 9.9 and 23.0 nm still provide much higher J_n values than the other SLs, their difference to TiN and $MoN_{0.5}$ is not that pronounced anymore (as was the case for K_{IC} and G_C). Also, the order within the monolithically grown coatings basically reversed (TiN and $MoN_{0.5}$ provide the highest J_n) values but basically lowest K_{IC} and G_C values, Fig. 7). This suggests that especially for TiN and $MoN_{0.5}$ the fracture surface seems to be more underestimated when simply using the projected area than it is for the other coatings and especially the SLs. In other words, the real fracture surface for TiN and $MoN_{0.5}$ is larger.

4. Summary and conclusions

We have developed highly 001-oriented fcc-structured TiN/MoN_y SLs with bilayer period variations of Λ = 2.4, 3.9, 6.6, 9.9, and 23.0 nm as well as fcc-$Ti_{1-x}Mo_xN_y$ solid solutions (*x* ~0.5 and *y* ~0.75), to deepen current understanding of interface-

induced strengthening and toughening effects in TiN-based ceramic superlattices.

DFT calculations indicated that 001-oriented TiN/MoN_y SLs (with Λ = 2–4 nm) energetically prefer to crystallise with ~50% of N vacancies in MoN_y layers (i.e., $MoN_{0.5}$), while the $Ti_{0.5}Mo_{0.5}N_y$ solid solutions were predicted to be the most energetically stable for $0.75 \leq y \leq 1$. Detailed XRD studies show that all SLs and solid solutions are single-phase fcc-structured, and the comparison with DFT-obtained lattice parameters (supported by EDS investigations) hints towards a composition according to TiN/$MoN_{0.5}$ and $Ti_{0.5}Mo_{0.5}N_{0.77}$. The SLs with Λ = 2.4 and 3.9 nm have higher N-contents and larger lattice parameters. Thus, their MoN_y layers are close to $MoN_{0.75}$ (DFT obtained lattice parameters for $MoN_{0.5}$ and $MoN_{0.75}$ are 4.202 and 4.284 Å, respectively).

On the nanoscale, intrinsic ductility criteria suggest excellent basis for plasticity for both $Ti_{0.5}Mo_{0.5}N_{0.75}$ solid solutions and TiN/$MoN_{0.5}$ SLs, while the later also show high elastic moduli (comparable even to TiN). In agreement with these, the SLs and $Ti_{0.5}Mo_{0.5}N_{0.77}$ outperform TiN during *in-situ* micromechanical bending tests yielding higher fracture toughness values K_{IC}. Especially, the latter shows a pronounced superlattice effect and peaks with 4.1 ± 0.2 MPa$\sqrt{m}$ at Λ = 9.9 nm. The other SLs are comparable to $Ti_{0.5}Mo_{0.5}N_{0.77}$ with K_{IC} ~3.2 MPa$\sqrt{m}$, while TiN has only ~2.2 MPa$\sqrt{m}$. The hardness of the SLs also peaks at Λ = 9.9 nm, but with H = 34.8 ± 1.6 GPa only slightly higher values are obtained than for TiN, $MoN_{0.5}$, and $Ti_{0.5}Mo_{0.5}N_{0.77}$ yielding 33.6 ± 1.2, 31.9 ± 1.4, and 31.4 ± 1.5 GPa, respectively. Detailed TEM and SAED studies of the 9.9-nm-SL showed that the $MoN_{0.5}$ layers crystallize with the ordered tetragonal β-Mo_2N phase in accord to DFT, which also yielded tetragonal distortion of the layers.

DFT not just guided the development of TiN/$MoN_{0.5}$ SLs with high fracture toughness and also helped to explain their lattice parameter and stoichiometry variation with the bilayer period. It also indicated the similarities between the low-bilayer-period SLs and the solid solutions and pointed towards increased ductility for bilayer periods beyond 4 nm.

Our studies furthermore showed that the epitaxial growth influences the preference for a certain crystal structure. While this might seem obvious it is rather interesting that the epitaxial growth of materials – which show perfect single-phase fcc structures with comparable lattice parameters (~4.25 Å for TiN and ~4.20 Å for $MoN_{0.5}$) when grown independently – leads to different crystal structures. When grown onto fcc-TiN layers, the $MoN_{0.5}$ layers prefer to crystallize with the ordered tetragonal β-Mo_2N structure, which is rarely obtained especially when prepared by PVD at higher temperatures.

Data availability

The data that support the findings of this study are available from the authors on reasonable request.

Declaration of Competing Interest

The authors declare that they have no known competing or financial interests, or personal relationships, that could have influenced the work reported in this paper.

Acknowledgments

The authors acknowledge the use of the facilities of USTEM and XRC at the TU Wien. ZCG highly appreciates the support from Chinese scholarship funding (File No. 201908440933) during her PhD at TU Wien. PHM is supported by the Austrian COMET Program (project K2 InTribology1, no. 872176). NK acknowledges the Austrian Science Fund, FWF, (T-1308). The computational results presented have been achieved using the Vienna Scientific Cluster (VSC). The simulated SAED patters are obtained using P.A. Stadelmann JEMS – EMS java version https://www.jems-swiss.ch/. The authors acknowledge TU Wien Bibliothek for financial support through its Open Access Funding Program.

Supplementary materials

Supplementary material associated with this article can be found, in the online version, at doi:10.1016/j.actamat.2022.117871.

References

[1] P.H. Mayrhofer, C. Mitterer, L. Hultman, H. Clemens, Microstructural design of hard coatings, Prog. Mater. Sci. 51 (2006) 1032–1114, doi:10.1016/j.pmatsci.2006.02.002.
[2] A. Inspektor, P.A. Salvador, Architecture of PVD coatings for metalcutting applications: a review, Surf. Coat. Technol. 257 (2014) 138–153, doi:10.1016/j.surfcoat.2014.08.068.
[3] S. Veprek, M.J.G. Veprek-Heijman, Industrial applications of superhard nanocomposite coatings, Surf. Coat. Technol. 202 (2008) 5063–5073, doi:10.1016/j.surfcoat.2008.05.038.
[4] H. Kindlund, D.G. Sangiovanni, I. Petrov, J.E. Greene, L. Hultman, A review of the intrinsic ductility and toughness of hard transition-metal nitride alloy thin films, Thin Solid Films 688 (2019) 137479, doi:10.1016/j.tsf.2019.137479.
[5] D.G. Sangiovanni, Inherent toughness and fracture mechanisms of refractory transition-metal nitrides via density-functional molecular dynamics, Acta Mater. 151 (2018) 11–20, doi:10.1016/j.actamat.2018.03.038.
[6] M. Sebastiani, K.E. Johanns, E.G. Herbert, F. Carassiti, G.M. Pharr, A novel pillar indentation splitting test for measuring fracture toughness of thin ceramic coatings, Philos. Mag. 95 (2015) 1928–1944, doi:10.1080/14786435.2014.913110.
[7] B.N. Jaya, S. Bhowmick, S.A.S. Asif, O.L. Warren, V. Jayaram, Optimization of clamped beam geometry for fracture toughness testing of micron-scale samples, Philos. Mag. 95 (2015) 1945–1966, doi:10.1080/14786435.2015.1010623.
[8] D. Di Maio, S.G. Roberts, Measuring fracture toughness of coatings using focused-ion-beam-machined microbeams, J. Mater. Res. 20 (2005) 299–302, doi:10.1557/JMR.2005.0048.
[9] R. Soler, S. Gleich, C. Kirchlechner, C. Scheu, J.M. Schneider, G. Dehm, Fracture toughness of Mo2BC thin films: intrinsic toughness versus system toughening, Mater. Des. 154 (2018) 20–27, doi:10.1016/j.matdes.2018.05.015.
[10] D.G. Sangiovanni, V. Chirita, L. Hultman, Electronic mechanism for toughness enhancement in $Ti_xM_{1-x}N$ (M=Mo and W), Phys. Rev. B 81 (2010) 104107, doi:10.1103/PhysRevB.81.104107.
[11] M. Bartosik, R. Hahn, Z.L. Zhang, I. Ivanov, M. Arndt, P. Polcik, P.H. Mayrhofer, Fracture toughness of Ti-Si-N thin films, Int. J. Refract. Met. Hard Mater. 72 (2018) 78–82, doi:10.1016/j.ijrmhm.2017.12.015.
[12] K. Hanna, Toughness enhancement in hard single-crystal transition-metal nitrides: V-Mo-N and V-W-N alloys, PhD dissertation, Linköping University Electronic Press (2014). doi:10.3384/diss.diva-106472.
[13] M. Schlögl, C. Kirchlechner, J. Paulitsch, J. Keckes, P.H. Mayrhofer, Effects of structure and interfaces on fracture toughness of CrN/AlN multilayer coatings, Scr. Mater. 68 (2013) 917–920, doi:10.1016/j.scriptamat.2013.01.039.
[14] Z. Chen, M. Lou, D. Geng, Y.X. Xu, Q. Wang, J. Zheng, R. Zhu, Y. Chen, K.H. Kim, Effect of the modulation geometry on mechanical and tribological properties of TiSiN/TiAlN nano-multilayer coatings, Surf. Coat. Technol. 423 (2021) 127586, doi:10.1016/j.surfcoat.2021.127586.
[15] S. Barnett, A. Madan, Superhard superlattices, Phys. World 11 (1998) 45–48.
[16] A. Wagner, D. Holec, P.H. Mayrhofer, M. Bartosik, Enhanced fracture toughness in ceramic superlattice thin films: on the role of coherency stresses and misfit dislocations, Mater. Des. 202 (2021) 109517, doi:10.1016/j.matdes.2021.109517.
[17] T. Glechner, R. Hahn, T. Wojcik, D. Holec, S. Kolozsvári, H. Zaid, S. Kodambaka, P.H. Mayrhofer, H. Riedl, Assessment of ductile character in superhard Ta-C-N thin films, Acta Mater. 179 (2019) 17–25, doi:10.1016/j.actamat.2019.08.015.
[18] T. Glechner, S. Lang, R. Hahn, M. Alfreider, V. Moraes, D. Primetzhofer, J. Ramm, S. Kolozsvári, D. Kiener, H. Riedl, Correlation between fracture characteristics and valence electron concentration of sputtered Hf-C-N based thin films, Surf. Coat. Technol. 399 (2020) 126212, doi:10.1016/j.surfcoat.2020.126212.
[19] U. Helmersson, S. Todorova, S.A. Barnett, J.E. Sundgren, L.C. Markert, J.E. Greene, Growth of single-crystal TiN/VN strained-layer superlattices with extremely high mechanical hardness, J. Appl. Phys. 62 (1987) 481–484, doi:10.1063/1.339770.
[20] M. Shinn, L. Hultman, S.A. Barnett, Growth, structure, and microhardness of epitaxial Tin/Nbn superlattices, J. Mater. Res. 7 (1992) 901–911, doi:10.1557/Jmr.1992.0901.
[21] X. Chu, S.A. Barnett, Model of superlattice yield stress and hardness enhancements, J. Appl. Phys. 77 (1995) 4403–4411, doi:10.1063/1.359467.
[22] R. Hahn, M. Bartosik, R. Soler, C. Kirchlechner, G. Dehm, P.H. Mayrhofer, Superlattice effect for enhanced fracture toughness of hard coatings, Scr. Mater. 124 (2016) 67–70, doi:10.1016/j.scriptamat.2016.06.030.

[23] J. Buchinger, N. Koutná, Z. Chen, Z. Zhang, P.H. Mayrhofer, D. Holec, M. Bartosik, Toughness enhancement in TiN/WN superlattice thin films, Acta Mater. 172 (2019) 18–29, doi:10.1016/j.actamat.2019.04.028.

[24] R. Hahn, N. Koutná, T. Wójcik, A. Davydok, S. Kolozsvári, C. Krywka, D. Holec, M. Bartosik, P.H. Mayrhofer, Mechanistic study of superlattice-enabled high toughness and hardness in MoN/TaN coatings, Commun. Mater. 1 (2020) 62, doi:10.1038/s43246-020-00064-4.

[25] J. Buchinger, A. Wagner, Z. Chen, Z.L. Zhang, D. Holec, P.H. Mayrhofer, M. Bartosik, Fracture toughness trends of modulus-matched TiN/(Cr,Al)N thin film superlattices, Acta Mater. 202 (2021) 376–386, doi:10.1016/j.actamat.2020.10.068.

[26] N. Koutná, A. Brenner, D. Holec, P.H. Mayrhofer, High-throughput first-principles search for ceramic superlattices with improved ductility and fracture resistance, Acta Mater. 206 (2021) 116615, doi:10.1016/j.actamat.2020.116615.

[27] F.F. Klimashin, H. Euchner, P.H. Mayrhofer, Computational and experimental studies on structure and mechanical properties of Mo-Al-N, Acta Mater. 107 (2016) 273–278, doi:10.1016/j.actamat.2016.01.063.

[28] F.F. Klimashin, H. Riedl, D. Primetzhofer, J. Paulitsch, P.H. Mayrhofer, Composition driven phase evolution and mechanical properties of Mo–Cr–N hard coatings, J. Appl. Phys. 118 (2015) 025305, doi:10.1063/1.4926734.

[29] A.J. Perry, A.W. Baouchi, J.H. Petersen, S.D. Pozder, Crystal structure of molybdenum nitride films made by reactive cathodic arc evaporation, Surf. Coat. Technol. 54-55 (1992) 261–265, doi:10.1016/S0257-8972(09)90060-3.

[30] F.F. Klimashin, N. Koutna, H. Euchner, D. Holec, P.H. Mayrhofer, The impact of nitrogen content and vacancies on structure and mechanical properties of Mo-N thin films, J. Appl. Phys. (2016) 120, doi:10.1063/1.4966664.

[31] F. Anğay, L. Löfler, F. Tetard, D. Eyidi, P. Djemia, D. Holec, G. Abadias, Structure, stress, and mechanical properties of Mo-Al-N thin films deposited by dc reactive magnetron cosputtering: role of point defects, J. Vac. Sci. Technol. A 38 (2020) 053401, doi:10.1116/6.0000292.

[32] G. Kresse, D. Joubert, From ultrasoft pseudopotentials to the projector augmented-wave method, Phys. Rev. B 59 (1999) 1758–1775, doi:10.1103/PhysRevB.59.1758.

[33] G. Kresse, J. Furthmüller, Efficiency of ab-initio total energy calculations for metals and semiconductors using a plane-wave basis set, Comput. Mater. Sci. 6 (1996) 15–50, doi:10.1016/0927-0256(96)00008-0.

[34] W. Kohn, L.J. Sham, Self-consistent equations including exchange and correlation effects, Phys. Rev. 140 (1965) A1133, doi:10.1103/PhysRev.140.A1133.

[35] J.P. Perdew, K. Burke, M. Ernzerhof, Generalized gradient approximation made simple, Phys. Rev. Lett. 77 (1996) 3865–3868, doi:10.1103/PhysRevLett.77.3865.

[36] H.J. Monkhorst, J.D. Pack, Special points for Brillouin-zone integrations, Phys. Rev. B 13 (1976) 5188–5192, doi:10.1103/PhysRevB.13.5188.

[37] N. Koutna, D. Holec, O. Svoboda, F.F. Klimashin, P.H. Mayrhofer, Point defects stabilise cubic Mo-N and Ta-N, J. Phys. D Appl. Phys. 49 (2016), doi:10.1088/0022-3727/49/37/375303.

[38] A. Kirnbauer, A. Kretschmer, C.M. Koller, T. Wojcik, V. Paneta, M. Hans, J.M. Schneider, P. Polcik, P.H. Mayrhofer, Mechanical properties and thermal stability of reactively sputtered multi-principal-metal Hf-Ta-Ti-V-Zr nitrides, Surf. Coat. Technol. 389 (2020), doi:10.1016/j.surfcoat.2020.125674.

[39] S.H. Wei, L.G. Ferreira, J.E. Bernard, A. Zunger, Electronic properties of random alloys: special quasirandom structures, Phys. Rev. B 42 (1990) 9622–9649, doi:10.1103/PhysRevB.42.9622.

[40] F. Mouhat, F.X. Coudert, Necessary and sufficient elastic stability conditions in various crystal systems, Phys. Rev. B 90 (2014) 224104, doi:10.1103/PhysRevB.90.224104.

[41] R. Yu, J. Zhu, H.Q. Ye, Calculations of single-crystal elastic constants made simple, Comput. Phys. Commun. 181 (2010) 671–675, doi:10.1016/j.cpc.2009.11.017.

[42] H.Y. Niu, X.Q. Chen, P.T. Liu, W.W. Xing, X.Y. Cheng, D.Z. Li, Y.Y. Li, Extra-electron induced covalent strengthening and generalization of intrinsic ductile-to-brittle criterion, Sci. Rep. 2 (2012), doi:10.1038/srep00718.

[43] S.F. Pugh, Relations between the elastic moduli and the plastic properties of polycrystalline pure metals, Philos. Mag. 45 (1954) 823–843, doi:10.1080/14786440808520496.

[44] W.C. Oliver, G.M. Pharr, An improved technique for determining hardness and elastic modulus using load and displacement sensing indentation experiments, J. Mater. Res. 7 (1992) 1564–1583, doi:10.1557/JMR.1992.1564.

[45] S.M. Han, R. Saha, W.D. Nix, Determining hardness of thin films in elastically mismatched film-on-substrate systems using nanoindentation, Acta Mater. 54 (2006) 1571–1581, doi:10.1016/j.actamat.2005.11.026.

[46] A.C. Fischer-Cripps, Critical review of analysis and interpretation of nanoindentation test data, Surf. Coat. Technol. 200 (2006) 4153–4165, doi:10.1016/j.surfcoat.2005.03.018.

[47] R. Saha, W.D. Nix, Effects of the substrate on the determination of thin film mechanical properties by nanoindentation, Acta Mater. 50 (2002) 23–38, doi:10.1016/S1359-6454(01)00328-7.

[48] G.C.A.M. Janssen, M.M. Abdalla, F. van Keulen, B.R. Pujada, B. van Venrooy, Celebrating the 100th anniversary of the Stoney equation for film stress: developments from polycrystalline steel strips to single crystal silicon wafers, Thin Solid Films 517 (2009) 1858–1867, doi:10.1016/j.tsf.2008.07.014.

[49] S. Brinckmann, K. Matoy, C. Kirchlechner, G. Dehm, On the influence of microcantilever pre-crack geometries on the apparent fracture toughness of brittle materials, Acta Mater. 136 (2017) 281–287, doi:10.1016/j.actamat.2017.07.014.

[50] A. Riedl, R. Daniel, M. Stefenelli, T. Schöberl, O. Kolednik, C. Mitterer, J. Keckes, A novel approach for determining fracture toughness of hard coatings on the micrometer scale, Scr. Mater. 67 (2012) 708–711, doi:10.1016/j.scriptamat.2012.06.034.

[51] S. Brinckmann, C. Kirchlechner, G. Dehm, Stress intensity factor dependence on anisotropy and geometry during micro-fracture experiments, Scr. Mater. 127 (2017) 76–78, doi:10.1016/j.scriptamat.2016.08.027.

[52] K. Matoy, H. Schönherr, T. Detzel, T. Schöberl, R. Pippan, C. Motz, G. Dehm, A comparative micro-cantilever study of the mechanical behavior of silicon based passivation films, Thin Solid Films 518 (2009) 247–256, doi:10.1016/j.tsf.2009.07.143.

[53] A.K. Saxena, S. Brinckmann, B. Völker, G. Dehm, C. Kirchlechner, Experimental conditions affecting the measured fracture toughness at the microscale: notch geometry and crack extension measurement, Mater. Des. 191 (2020) 108582, doi:10.1016/j.matdes.2020.108582.

[54] J.R. Cahoon, W.H. Broughton, A.R. Kutzak, The determination of yield strength from hardness measurements, Metall. Trans. 2 (1971) 1979–1983, doi:10.1007/BF02913433.

[55] A.T. Zehnder, Fracture Mechanics, Springer Science+Business Media, 2012.

[56] K. Balasubramanian, L. Huang, D. Gall, Phase stability and mechanical properties of $Mo_{1-x}N_x$ with $0 \leq x \leq 1$, J. Appl. Phys. 122 (2017) 195101, doi:10.1063/1.4998686.

[57] F.F. Klimashin, L. Lobmaier, N. Koutná, D. Holec, P.H. Mayrhofer, The MoN–TaN system: role of vacancies in phase stability and mechanical properties, Mater. Des. 202 (2021) 109568, doi:10.1016/j.matdes.2021.109568.

[58] K. Balasubramanian, S.V. Khare, D. Gall, Energetics of point defects in rocksalt structure transition metal nitrides: thermodynamic reasons for deviations from stoichiometry, Acta Mater. 159 (2018) 77–88, doi:10.1016/j.actamat.2018.07.074.

[59] A.B. Mei, H. Kindlund, E. Broitman, L. Hultman, I. Petrov, J.E. Greene, D.G. Sangiovanni, Adaptive hard and tough mechanical response in single-crystal B1 VNx ceramics via control of anion vacancies, Acta Mater. 192 (2020) 78–88, doi:10.1016/j.actamat.2020.03.037.

[60] S. Karimi Aghda, D. Music, Y. Unutulmazsoy, H.H. Sua, S. Mráz, M. Hans, D. Primetzhofer, A. Anders, J.M. Schneider, Unravelling the ion-energy-dependent structure evolution and its implications for the elastic properties of (V,Al)N thin films, Acta Mater. 214 (2021) 117003, doi:10.1016/j.actamat.2021.117003.

[61] B.D. Ozsdolay, K. Balasubramanian, D. Gall, Cation and anion vacancies in cubic molybdenum nitride, J. Power Sources 705 (2017) 631–637, doi:10.1016/j.jallcom.2017.02.072.

[62] Z. Zhang, A. Ghasemi, N. Koutná, Z. Xu, T. Grünstäudl, K. Song, D. Holec, Y. He, P.H. Mayrhofer, M. Bartosik, Correlating point defects with mechanical properties in nanocrystalline TiN thin films, Mater. Des. 207 (2021) 109844, doi:10.1016/j.matdes.2021.109844.

[63] G.L.W. Hart, B.M. Klein, Phonon and elastic instabilities in MoC and MoN, Phys. Rev. B 61 (2000) 3151–3154, doi:10.1103/PhysRevB.61.3151.

[64] E.I. Isaev, S.I. Simak, I.A. Abrikosov, R. Ahuja, Y.K. Vekilov, M.I. Katsnelson, A.I. Lichtenstein, B. Johansson, Phonon related properties of transition metals, their carbides, and nitrides: a first-principles study, J. Appl. Phys. 101 (2007) 123519, doi:10.1063/1.2747230.

[65] D.G. Pettifor, M. Aoki, J.N. Murrell, A. Cottrell, A.M. Stoneham, R. Haydock, J.E. Inglesfield, J.B. Pendry, Bonding and structure of intermetallics: a new bond order potential, Philos. Trans. R. Soc. Lond. Ser. A Phys. Eng. Sci. 334 (1991) 439–449, doi:10.1098/rsta.1991.0024.

[66] I. Jauberteau, A. Bessaudou, R. Mayet, J. Cornette, J.L. Jauberteau, P. Carles, T. Merle-Méjean, Molybdenum nitride films: crystal structures, synthesis, mechanical, electrical and some other properties, Coatings 5 (2015), doi:10.3390/coatings5040656.

[67] A. Madan, Y.Y. Wang, S.A. Barnett, C. Engström, H. Ljungcrantz, L. Hultman, M. Grimsditch, Enhanced mechanical hardness in epitaxial nonisostructural Mo/NbN and W/NbN superlattices, J. Appl. Phys. 84 (1998) 776–785, doi:10.1063/1.368137.

[68] R.M. Fleming, D.B. McWhan, A.C. Gossard, W. Wiegmann, R.A. Logan, X-ray diffraction study of interdiffusion and growth in (GaAs)n(AlAs)m multilayers, J. Appl. Phys. 51 (1980) 357–363, doi:10.1063/1.327310.

[69] A.H. Eltoukhy, J.E. Greene, Compositionally modulated sputtered InSb/GaSb superlattices: crystal growth and interlayer diffusion, J. Appl. Phys. 50 (1979) 505–517, doi:10.1063/1.325643.

[70] D. Holec, M. Friak, J. Neugebauer, P.H. Mayrhofer, Trends in the elastic response of binary early transition metal nitrides, Phys. Rev. B 85 (2012) 9, doi:10.1103/PhysRevB.85.064101.

[71] Q. Yang, L.R. Zhao, P.C. Patnaik, X.T. Zeng, Wear resistant TiMoN coatings deposited by magnetron sputtering, Wear 261 (2006) 119–125, doi:10.1016/j.wear.2005.07.008.

[72] Z. Zhang, X. Gu, D. Holec, M. Bartosik, P.H. Mayrhofer, H.P. Duan, Superlattice-induced oscillations of interplanar distances and strain effects in the CrN/AlN system, Phys. Rev. B 95 (2017) 155305, doi:10.1103/PhysRevB.95.155305.

[73] N. Koutna, P. Rehak, Z. Chen, M. Bartosik, M. Fallmann, M. Cerny, Z. Zhang, M. Friak, M. Sob, P.H. Mayrhofer, D. Holec, Correlating structural and mechanical properties of AlN/TiN superlattice films, Scr. Mater. 165 (2019) 159–163, doi:10.1016/j.scriptamat.2019.02.021.

[74] N. Koutná, D. Holec, M. Friák, P.H. Mayrhofer, M. Šob, Stability and elasticity of metastable solid solutions and superlattices in the MoN–TaN system: first-principles calculations, Mater. Des. 144 (2018) 310–322, doi:10.1016/j.matdes.2018.02.033.

[75] A.F. Jankowski, T. Tsakalakos, The effect of strain on the elastic constants of noble metals, J. Phys. F Met. Phys. 15 (1985) 1279 0305-4608/15/i=6/a=013.

[76] J.S. Koehler, Attempt to design a strong solid, Phys. Rev. B 2 (1970) 547–551, doi:10.1103/PhysRevB.2.547.
[77] J.W. Gahn, Hardening by spinodal decomposition, Acta Metall. 11 (1963) 1275–1282, doi:10.1016/0001-6160(63)90022-1.
[78] A.N. Wang, G.P. Yu, J.H. Huang, Fracture toughness measurement on TiN hard coatings using internal energy induced cracking, Surf. Coat. Technol. 239 (2014) 20–27, doi:10.1016/j.surfcoat.2013.11.010.
[79] M. Sperr, Z.L. Zhang, Y.P. Ivanov, P.H. Mayrhofer, M. Bartosik, Correlating elemental distribution with mechanical properties of TiN/SiNx nanocomposite coatings, Scr. Mater. 170 (2019) 20–23, doi:10.1016/j.scriptamat.2019.05.020.
[80] W.M. Seidl, M. Bartosik, S. Kolozsvári, H. Bolvardi, P.H. Mayrhofer, Influence of Ta on the fracture toughness of arc evaporated Ti-Al-N, Vacuum 150 (2018) 24–28, doi:10.1016/j.vacuum.2018.01.028.
[81] M. Bielawski, K.Y. Chen, Computational evaluation of adhesion and mechanical properties of nanolayered erosion-resistant coatings for gas turbines, J. Eng. Gas. Turbines Power (2011) 133, doi:10.1115/1.4002158.

The influence of bilayer periods and ratios on mechanical and tribological properties of TiN/MoN superlattice thin films

Zecui Gao*, [a], Julian Buchinger [a], Rainer Hahn [a], Zhuo Chen [b], Zaoli Zhang [b], Paul Heinz Mayrhofer [a]

[a] Institute of Materials Science and Technology, Technische Universität Wien, Getreidemarkt 9, 1060, Vienna, Austria

[b] Erich Schmid Institute of Materials Science, Austrian Academy of Sciences, A-8700 Leoben, Austria

Abstract

Building on a preceding study, which described the bilayer-period-dependent superlattice effect on the hardness and fracture toughness of TiN/MoN_y superlattice (SL) thin films with a balanced bilayer ratio ($\lambda = \ell_{TiN}:\ell_{MoN}$) of 1:1, this work explores the influence of bilayer ratios and the N content on the superlattice effect. Therefore, TiN/MoN_y SLs were produced with bilayer ratios of 1:0.5, 1:1, and 1:2, and 1:2.7 and bilayer periods (Λ) ranging from 2 to 23 nm (for all four bilayer ratios). The SLs with a bilayer ratio of 1:2.7 were deposited under higher nitrogen partial pressure than the other SLs.

All SLs – independent of bilayer period, bilayer ratio, and nitrogen content – present a rocksalt structure, with high-order satellite peaks during X-ray diffraction. The tetragonal β-Mo_2N phase is detected for the SLs with Λ = 7.3 nm ($\ell_{TiN}:\ell_{MoN}$ = 1:2) and 9.9 nm ($\ell_{TiN}:\ell_{MoN}$ = 1:1). The SLs with bilayer ratios of 1:0.5 and 1:2 do not show a significant superlattice effect in hardness *H* and critical fracture toughness K_{IC}, but they demonstrate good tribological performance with a low coefficient of friction μ. Contrary, the SLs with $\ell_{TiN}:\ell_{MoN}$ = 1:2.7 provide strongly bilayer-period-dependent *H*

and K_{IC} values peaking at Λ = 9.3 nm. Among all SLs investigated, those with ℓ_{TiN}:ℓ_{MoN} = 1:1 provide the best blend of mechanical properties, such as H = 34.8 ± 1.6 GPa, K_{IC} = 4.1 ± 0.2 MPa√m, and μ = 0.27 for Λ = 9.9 nm. Overall, the experimental investigations prove the importance of optimized bilayer periods and bilayer ratios, as well as heterogeneous microstructures in general, for improving the superlattice effect.

Keywords: PVD thin films; Superlattices; Fracture toughness; MoN_y; bilayer periods and ratios

*Correspondence: zecui.gao@tuwien.ac.at

1. Introduction

Transition metal nitride (TMN) thin films have been widely used as protective coating materials against mechanically, chemically, and/or thermally demanding environments [1-3]. However, ceramic thin films in general are severely compromised in many applications by a low intrinsic fracture toughness (K_{IC}) [4, 5]. Thus, several toughness enhancement approaches and mechanisms have been reported. For example, the valence electron concentration (VEC) driven effect – alloying with metal or non-metal species to optimise the bonding character [6]. For example, alloying Ti-Al-N films with 15 at.% Ta improves their hardness from 31.5 ± 1.5 to 35.1 ± 1.0 GPa, and their K_{IC} from 3.5 ± 0.3 to 4.7 ± 0.2 MPa√m) [7]. Also, the grain-boundary-strengthening mechanism in Ti-Si-N nanocomposite coatings has been shown to significantly increase their hardness (from 32.1 ± 0.9 to 37.6 ± 1.5 GPa) and critical fracture toughness (from 3.0 ± 0.2 to 4.5 ± 0.6 MPa√m) compared to Ti-Si-N solid solution coatings with identical levels of Si alloying [8]. Furthermore, the superlattice (SL) effect, which optimises the mechanical properties (hardness and fracture toughness) of ceramic thin films via periodically alternating coherency strain fields in a nanolaminated and modulated structure with heterogeneous components [9-13]. Advanced multilayer coatings have also received widespread attention for wear resistance applications [14, 15].

The superlattice (SL) effect was reported for the first time in the 1970s for metal-to-metal systems [16-18], but has also been explored thoroughly for ceramic coating systems since then. Especially with the advent of reliable Micro-Electro-Mechanical

System (MEMS)-based in-situ micromechanical testing methods [19], research efforts on the governing mechanisms and potential enhancement strategies of the toughness-related properties of ceramic thin films have been intensified. TMNs are relatively simple in structure, synthesis, and analysis, compared to the other functional ceramics (i.e., transition metal carbides, oxides, and diborides), therefore, TMN SLs are widely studied, including TiN/CrN [20], TiN/WN [21], MoN/TaN [22], and TiN/(Cr,Al)N SLs [23], as well as the TiN/MoN SL [24], which is also subject of the present study. Among these TMN SLs, TiN/WN SLs depicted the best hardness and fracture toughness, with TiN/MoN SLs following closely behind, similar to first-principles calculations [25].

The preceding study of TiN/MoN SLs combined experimental methods [24] with density functional theory (DFT) modelling [26], and demonstrated a distinct superlattice effect. The peak hardness (34.8 ± 1.6 GPa) and fracture toughness (4.1 ± 0.2 MPa$\sqrt{m}$) were located at a bilayer period Λ of 9.9 nm and a bilayer ratio of 1:1 (equal thickness of TiN and MoN layers). Therewith, the peak fracture toughness significantly exceeds the corresponding monolithic rs-TiN (2.2 MPa$\sqrt{m}$), rs-$MoN_{0.5}$ (2.7 ± 0.4 MPa$\sqrt{m}$), and rs-$(Ti,Mo)N_{0.77}$ solid solution (3.2 ± 0.2 MPa$\sqrt{m}$). The crystal structure of TiN/MoN_y SL is generally rocksalt (face-centered cubic), for which the MoN_y layer crystallizes with 50% vacancies on the N sublattice (i.e., $MoN_{0.5}$ or Mo_2N). However, a weak reflection of tetragonal β-MoN_y was detected by the selected area electron diffraction study. β-MoN_y is an ordered tetragonal structure, often considered a tetragonal adjustment of the cubic γ-MoN_y phase with a doubled lattice constant c (space group, I41/amd) [27]. The β-MoN_y phase has less mechanical but higher

thermodynamic stability than the γ-MoN_y phase [28]. Synthesis routes and characterization of β-MoN_y have been rarely reported.

In this work, we aim to expand the current understanding of the nitrogen-vacancy-stabilized TiN/MoN_y superlattices, including the influence of microstructure, nitrogen content, bilayer ratios and periods on mechanical properties.

2. Experimental details

2.1 Coating deposition

This study is based on the previous study of TiN/MoN_y superlattice thin films (ℓ_{TiN}:ℓ_{MoN} = 1:1, and Λ ~ 2–23 nm) [24]. Therefore, all the samples in this study were prepared under identical conditions to enable comparison. A total of 12 samples were produced, including TiN/MoN_y superlattices with 3 bilayer ratios ℓ_{TiN}:ℓ_{MoN} of 1:0.5, 1:2, and 1:2.7, and for each bilayer ratio there are 4 different bilayer periods (Λ), which are designed to be 3, 6, 9, and 18 nm. However, the real bilayer periods are estimated by three ways: 1) dividing the total coating thickness measured by scanning electron microscopy (SEM) with the total number of bilayers; 2) via the satellite peaks in the X-ray diffraction (XRD) patterns; 3) high-resolution and scanning transmission electron microscopy HRTEM/STEM.

All of the thin films were synthesized with an AJA International Orion 5 lab-scale unbalanced magnetron sputtering deposition system, equipped with a computer-controlled shutter system. The thin films were deposited on polished single-crystalline MgO (100-oriented, size of 10 × 10 × 0.5 mm^3) substrates, which were firstly ultrasonically cleaned in acetone and then in ethanol for 5 min each, and then

mounted on a substrate holder. After that, the holder was placed in a vacuum chamber (base pressure about 10^{-4} Pa), and thermally purged at 500 °C for half an hour. The holder was rotated above the targets at a speed of 60 rpm, and the target-to-substrate distance was ~100 mm. High-energy plasma etching, with a DC potential of –750 V between the cathode (target) and anode (holder), under a total pressure of 6 Pa (filled the chamber with Ar, at a flow rate of 20 sccm), was performed prior to deposition to remove the remnant layers and contaminants from the substrate surface.

The target materials were a 3-inch Ti and a 2-inch Mo, which were DC-powered by ENI RPG-50 plasma generators with 800 mA (340 W) and 500 mA (220 W), respectively. Both targets have a purity of 99.95 % and are supplied by Plansee Composite Materials GmbH. The deposition was run in a mixed Ar+N_2 atmosphere, with a total pressure of 0.4 Pa, a substrate temperature of 400 °C, and a bias potential of –50 V, to get a dense coating morphology. For the 8 TiN/MoN_y SL coatings with ℓ_{TiN}:ℓ_{MoN} = 1:0.5 and 1:2, the flow rate of Ar (F_{Ar}) and N_2 (F_{N2}) were 7 and 3 sccm, respectively. The N_2 flow rate ratio ($f_{N2} = F_{N2}/(F_{Ar}+F_{N2})$) was thus 0.3 (with a N_2 partial pressure of 0.14 Pa). The other 4 TiN/MoN_y SLs with ℓ_{TiN}:ℓ_{MoN} = 1:2.7 were synthesized under a higher nitrogen partial pressure of 0.23 Pa (f_{N2} = 5 sccm/10 sccm = 0.5). These SL coatings with different bilayer periods and ratios were realized through computer-controlled shutters above the Ti and Mo targets. The total deposition time was ~222 min, to get ~2 μm thin SL coatings. Further deposition details can be found in Ref. [24].

2.2 Chemical and structural characterization

The crystal structures were analysed by an XRD system in Bragg-Brentano

configuration, featuring a Cu K_α X-ray source (operated with 45 kV and 40 mA). The range of investigated diffraction angles spanned from 20 to 100 deg. The coating surface and cross-sectional morphologies, as well as the in-situ microcantilever bending tests were carried out by a field emission scanning electron microscopy (FESEM, ZEISS Sigma 500 VP) at an acceleration voltage of 10 kV and a beam current of 0.4 nA. The chemical composition was investigated by energy-dispersive X-ray spectroscopy (EDS, Philips XL30). The SL coating with the most pronounced satellite reflexes (ℓ_{TiN}:ℓ_{MoN} = 1:2 and Λ= 7.2 nm) was chosen for more detailed cross-sectional investigations of the microstructure by transmission electron microscopy (TEM, JEOL 2100F), equipped with an image-side C_S–corrector, and capable of selected-area electron diffraction (SAED) analysis. The high-resolution TEM (HRTEM) images shown in this paper were taken under sufficiently small aberration coefficients, slight over-focus conditions (close to the Scherzer defocus), and with a resolution of 1.2 Å at 200 kV.

2.3 Mechanical properties

The mechanical properties investigated in this study include indentation hardness *H* and modulus *E*, fracture toughness, and wear resistance. *H* and *E* of the thin films were determined using an Ultra Micro Indentation System (UMIS, Fischer–Cripps Laboratories) equipped with a Berkovich diamond indenter tip. 31 indentations were carried out for each sample, with forces ranging from 3 to 45 mN, in load-controlled mode. To reduce substrate interferences, the maximum indentation depth was 0.2 µm, equalling ~10% of the coating thickness [29].

The critical fracture toughness K_{IC} of all the samples was measured with microcantilever bending tests, using an in-situ SEM/FIB nanomechanical MEMS-based testing system (FT-NMT04, FemtoTools), equipped with a 10 µm width wedge-shaped diamond tip. For the tests, 6 free-standing microcantilevers were ion-milled for each sample, using a dual focused ion beam (FIB) system (DBFEI Quanta 200 3D, a Ga ion source, 30 kV). The geometrical ratio of the cantilevers was 1:1:5 (width : breadth : length) [23], where the cantilever width is equal to the coating thickness of ~2.0 µm. During FIB cutting, coarse milling was carried out at a beam current of 1.0 nA, which was then reduced to 0.5 nA for the final cross-cleaning. After that, a notch of ~1.8 µm length and ~400 nm depth was milled into every cantilever, using a current of 50 pA, leaving two small material bridges of ~100 nm wide on either side of the notch. The microcantilever bending test was performed in a displacement-controlled mode at 5 nm/s. Loading was conducted against the growth direction of the film on the opposite side of the notch until failure.

Tribological tests were carried out with a bi-directional ST3001 Tribo tester, using a Chrome steel 52100 5mm diameter ball. The friction force was recorded and displayed during this test. The program used included the facility to automatically stop the test when the coating has failed (determined by a rise in coefficient of friction µ to a previously defined value), while also giving the number of cycles to failure. Preliminary wear tests were performed with varying table speed, load, and wear track length. After testing the performance of the coatings in various conditions of loads and rates, the final tests (reported here) were conducted with a load of 5N, 150 mm·min^{-1} table

speed, 2 mm displacement, and 700 sliding cycles. All the tribo-tests were carried out at room temperature and in air of normal humidity. For each sample, at least 3 wear tests were performed to obtain reliable data. After a tribo-test, a ball crater device (TEER-BC-I) was used to determine the coating thickness and adherence.

The residual stresses of the coatings were calculated using the modified Stoney Equation given in [30], after obtaining a curvature of the coatings by an optical profilometer (Nanovea PS50), the thickness of film and substrate, and the biaxial modulus of the substrate.

The experimental measurements are quoted in terms of sample mean and standard deviation. For quantities derived from two or more independently measured properties, error propagation was used to estimate the inaccuracy of the derived quantity.

3. Results

3.1 Composition and Structure

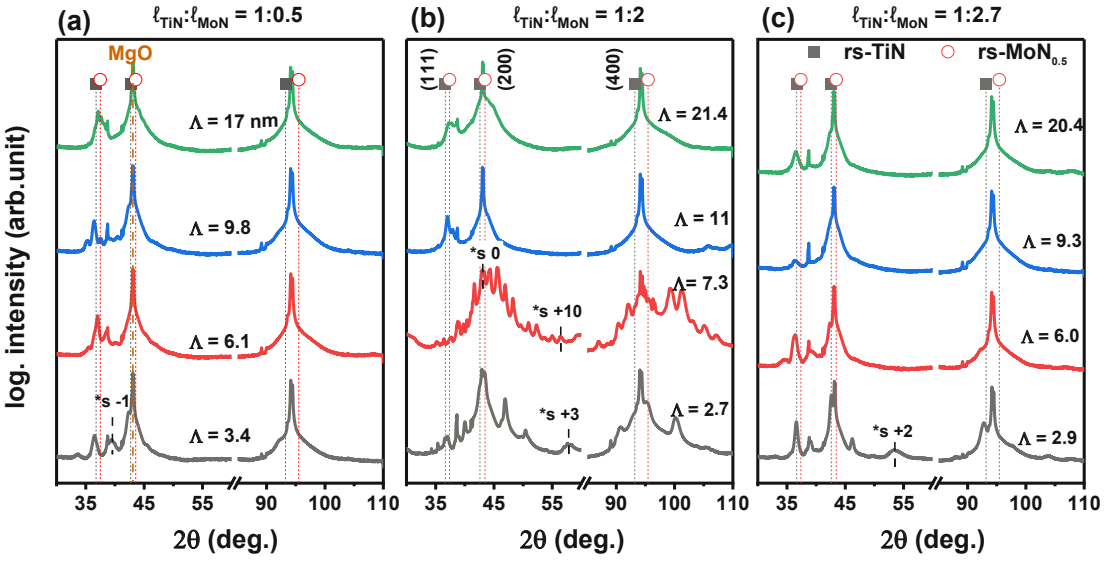

Fig. 1: XRD patterns of TiN/MoN$_y$ SLs with different bilayer ratios of ℓ_{TiN}:ℓ_{MoN} = 1:0.5 **(a)**, 1:2 **(b)**,

and 1:2.7 **(c)**. The labelled individual bilayer period values are estimated by the SEM-based coating thickness. Some of the highest order detectable satellite peaks are marked. All coatings were grown on single crystalline MgO (100) substrates.

The XRD patterns of all the 12 TiN/MoN_y SLs on MgO (001) substrates, presented in Fig. 1, show that they are clearly single-phased face-centred cubic (B1 rock-saltlike, rs) structured along the (200) orientation. The main Bragg peaks (200) of all the TiN/MoN_y SLs are in between those of the single-phased rs-TiN (200) and rs-$MoN_{0.5}$ (200), which hints at an average lattice constant of the SLs, in between rs-TiN and rs-$MoN_{0.5}$, even for the SLs produced at a higher nitrogen partial pressure (which was used for the ℓ_{TiN}:ℓ_{MoN} ratio of 1:2.7, Fig. 1c). As depicted in Fig. 1, some of the SLs exhibit higher order satellite reflections around the (200) and (400) peak. Satellite peaks are the fingerprints of a superlattice architecture with a high epitaxial quality, and well-defined and sharp interfaces. Generally, more satellite peaks indicate sharper interfaces. Due to the rapid interlayer diffusion of high-frequency components, such high order satellites are not often observed [31].

The coating with the most pronounced satellite peaks (Fig. 1b, ℓ_{TiN}:ℓ_{MoN} = 1:2, and Λ = 7.3 nm), is investigated in more detail by XRD (Fig. 2a) and cross-sectional HRTEM (Fig. 2b).

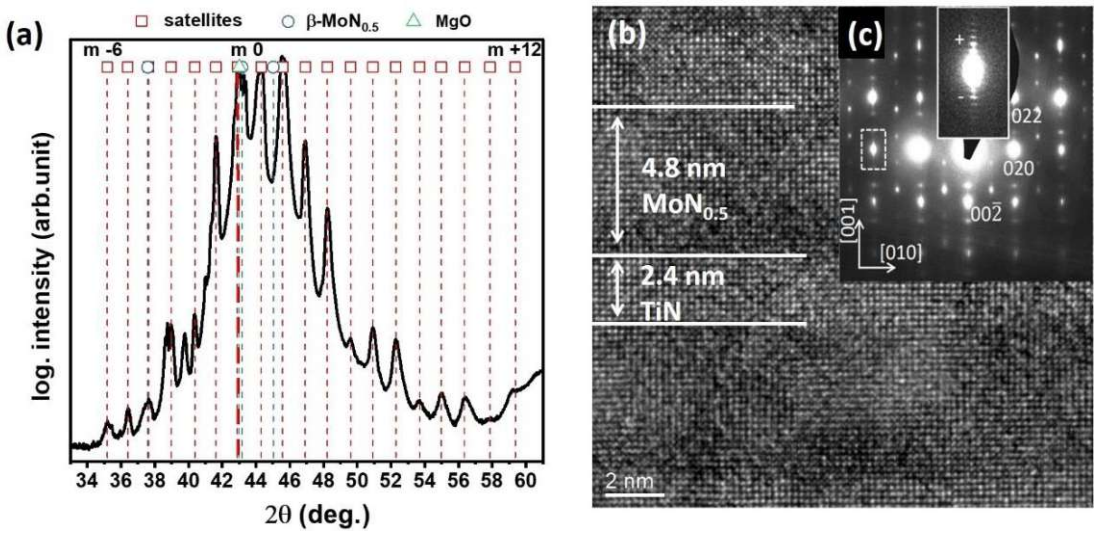

Fig. 2: **(a)** X-ray pattern of the superlattice TiN/MoN_y coating (Λ = 7.3 nm, and ℓ_{TiN}: ℓ_{MoN} = 1:2) with simulated satellite positions (red dashed lines) according to Equation 1. The bold red dashed line corresponds to the main Bragg reflection (200). The blue dashed lines are from tetragonal β-Mo_2N reflection, referring to PDF card 25-1368. The green dashed line is the MgO (200) reflection, referring to PDF card 65-0476. **(b)** Lattice-resolved cross sectional high-resolution TEM micrograph of this sample. **(c)** Its [100] SAED pattern with the most intense reflections from the rocksalt fcc TiN/$MoN_{0.5}$ lattice.

During XRD (Fig. 2a), this SL coating even exhibits +12th-order harmonic satellites, much more than the most superlattice thin films, including the best TiN/MoN_y SL of a previous study (Λ = 9.9 nm and ℓ_{TiN}:ℓ_{MoN} = 1:1 [24]), which exhibits at most +4th-order satellites. Following Equation 1 [32]:

$$\sin\theta_{\pm} = \sin\theta_B \pm m\lambda/2\Lambda \quad (1)$$

where $\theta_{\pm}$ is the angular position of the positive or negative satellites, relative to the Bragg angle (θ_B), λ is the X-ray wavelength, and m is the order of the reflection, the bilayer period Λ of the TiN/MoN_y SL (ℓ_{TiN}:ℓ_{MoN} = 1:2 and Λ = 7.3 nm) is 7.27 nm, which exactly matches the 7.26 nm estimated from the total SEM-obtained coating thickness

(by dividing with the total number of bilayers, which have been given to the computer controlled deposition recipe). The intensities of the positive and negative satellites are not equal because the sample contains a modulation in both the scattering power and the interplanar spacing of rs-TiN and rs-MoN_y. Possible reasons that the other SL coatings do not have that many clearly visible satellite reflections may be due to reduced interfacial coherence, or that their satellites are covered by the shoulder of the main diffraction peak [12] and/or lost in the background [33].

As shown in Fig. 2b, the lattice-resolved high-resolution TEM (HRTEM) clearly reveals an epitaxial single crystalline rocksalt structure. The continuous lattice fringes across various TiN and $MoN_{0.5}$ layers prove their high epitaxial relation, since crystal structure and lattice constants between rs-TiN and rs-$MoN_{0.5}$ are relatively close (Δa ~0.05 Å). The $MoN_{0.5}$ layers show a darker contrast in the HRTEM image because of more scattering electrons of $MoN_{0.5}$ than TiN. The sample's bilayer period is determined to be ~7.2 nm by TEM, and the thickness of the $MoN_{0.5}$ layers (4.8 nm) is double that of the TiN layers (2.4 nm). Thus, in excellent agreement with the bilayer periods obtained by the SEM-obtained thickness measurement and the calculations using the XRD satellite reflections.

The analysis of the selected-area electron diffraction pattern (SAED), Fig. 2c, further indicates that the overall film is stabilized in the rock-salt structure. Along the projection direction of <001>, satellite reflections are systematically present due to the different lattice parameters along this direction of the individual TiN and $MoN_{0.5}$ layers, as marked by +/- in the enlarged white rectangular area in Fig. 2c. This confirms that

the periodic SL has a fully epitaxial growth of the cubic structures, aligning with XRD investigations. Next to the satellite reflections, there are additional smaller reflections along the <001> direction in between the cubic reflections, indicating that the MoN_y layer crystallizes with the tetragonal β-$MoN_{0.5}$ phase. This also has 50% nitrogen vacancies (like the rs-$MoN_{0.5}$ phase), but in an ordered arrangement, as well as a c/a ratio of 1.92 [34, 35]. No obvious β-$MoN_{0.5}$ phase was detected during XRD because of the overlapping signal from the individual satellite reflections and the cubic reflections.

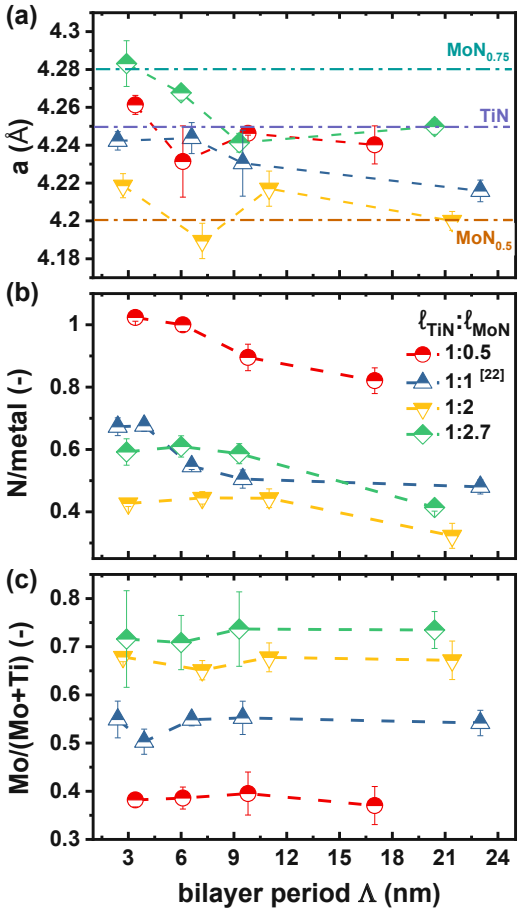

Fig. 3: Lattice parameters **(a)**, as well as EDS-obtained N/metal ratio **(b)** and Mo/(Mo+Ti) ratio **(c)** of the TiN/MoN_y superlattices (averaged across all layers), with Λ varying from 3 to 23 nm, and ℓ_{TiN}:ℓ_{MoN} ratios of 1:0.5, 1:1 (ref.[24]), 1:2, and 1:2.7. The dot-dash lines in **(a)** are the lattice parameters of the monolithic rs-TiN, rs-$MoN_{0.5}$, and rs-$MoN_{0.75}$, derived from DFT-calculation in ref. [26].

The lattice parameters of TiN/MoN_y SLs produced in this study, as well as the previous study [24], Fig. 3a, are calculated according to Bragg's law from their XRD patterns. The horizontal lines mark lattice parameters of the monolithic rs-TiN (4.25 Å), rs-$MoN_{0.5}$ (4.20 Å), and rs-$MoN_{0.75}$ (4.28 Å) phases as obtained from DFT-calculations [26]. As depicted earlier, the lattice parameters of the TiN/MoN_y SLs with ℓ_{TiN}:ℓ_{MoN} of 1:0.5, 1:1, and 1:2 are roughly in between those of rs-TiN and rs-$MoN_{0.5}$. With decreasing bilayer ratios (ℓ_{TiN}:ℓ_{MoN}), which means increasing MoN_y layer thickness relative to TiN, the overall lattice parameters decrease from ~4.25 Å to ~4.22 Å. The SLs with ℓ_{TiN}:ℓ_{MoN} of 1:2.7 exhibit the largest lattice parameters of ~4.26 Å, which are in between that rs-TiN and the higher N-containing rs-$MoN_{0.75}$. Please remember, these SLs (ℓ_{TiN}:ℓ_{MoN} = 1:2.7) were prepared with a higher N_2 flow rate ratio f_{N2} of 0.5 instead of 0.3 used for the other SLs. Monolithically prepared rs-MoN_y coatings reveal an increase in their lattice parameters from ~4.20 to ~4.24 Å when increasing f_{N2} from 0.3 to 0.5.

The N-to-metal ratio of the TiN/MoN_y SLs, Fig. 3b, can illustrate the nitrogen vacancies in a TiN/MoN_y SL coating, since for a perfect rocksalt structure, the ratio should be 1 and metal interstitials are heavily unlikely for such nitrides. Obviously, with decreasing the ℓ_{TiN}:ℓ_{MoN} from 1:0.5 to 1:2, the N-to-metal ratios decrease considerably from ~1 to ~0.4, because of the increasing contribution of the MoN_y layers with their nitrogen vacancies. However, because the SLs with ℓ_{TiN}:ℓ_{MoN} = 1:2.7 are prepared with a higher f_{N2}, their N-to-metal ratios are above those with an ℓ_{TiN}:ℓ_{MoN} = 1:2. For the SLs with the same bilayer ratio, the N/metal ratio decreases with increased bilayer periods.

This agrees with the lattice parameter trends, and suggests that the MoN_y layers contain more N at the interface to the TiN layers due to the template effect. As for the SL coatings with ℓ_{TiN}:ℓ_{MoN} = 1:0.5, the N/metal ratio even is 1 with Λ ~3 nm (i.e., having 1 nm thin MoN_y layers), the template effect seems to be effective up to 1 nm. Therefore, even N/metal ratios of 1 are possible, although TiN/MoN SLs (with 1:1 stoichiometry of the MoN layers, and ℓ_{TiN}:ℓ_{MoN} = 1:1 and Λ = 2, 3, 4 nm) are mechanically unstable [24]. Thus, our data suggest that the thicker TiN layers help to stabilize these mechanically (energetically they have a negative formation energy). We don't want to overinterpret these EDS obtained N/metal ratios, but they clearly suggest that the interface-near regions of the MoN_y layers are richer in N. Therefore, the SLs with ℓ_{TiN}:ℓ_{MoN} = 1:2 have the lowest N/metal ratios, as there (for the same Λ) the overall contribution of interface-near regions of MoN_y layers is four-times lower as for ℓ_{TiN}:ℓ_{MoN} = 1:0.5.

As shown in Fig. 3c, within the same bilayer ratio, the TiN/MoN_y SLs roughly keep the same Mo/(Ti+Mo) ratios. For the SL investigated in detail by HRTEM (Fig. 2b, Λ = 7.3 nm, ℓ_{TiN}:ℓ_{MoN} = 1:2) this ratio is ~0.66, which is obtained if the MoN_y layers are twice as thick as the TiN layers. Thus, this is in perfect agreement with the TEM study as well as the bilayer ratios obtained from the SEM-based thickness measurements.

3.2 Mechanical and tribological properties

The mechanical and tribological properties of the TiN/MoN_y SLs investigated in this study include indentation hardness *H* and modulus *E* (Fig. 4), fracture toughness K_{IC} (Fig. 5), as well as coefficient of friction (Fig. 6), which all show more or less

dependencies on the bilayer periods and bilayer ratios.

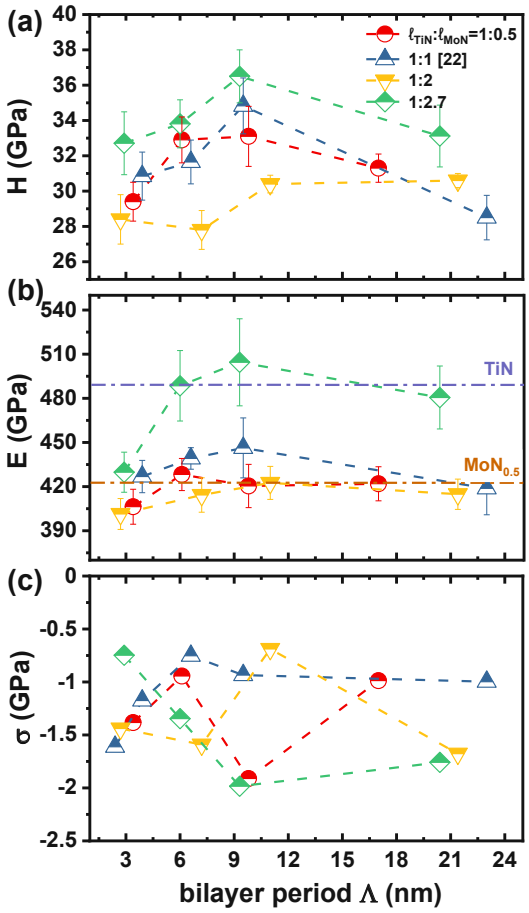

Fig. 4: Indentation hardness *H* **(a)** and modulus *E* **(b)**, and biaxial residual stresses *σ* **(c)** of the TiN/MoN_y SLs with Λ ranging from 3 to 23 nm, and ℓ_{TiN}: ℓ_{MoN} of 1:0.5, 1:1 [24], 1:2, and 1:2.7. The dash-dotted horizontal lines in **(b)** are the indentation moduli of monolithic rs-TiN and rs-$MoN_{0.5}$, taken from [24].

As depicted in Fig. 4a, the higher N-containing TiN/MoN_y SLs (ℓ_{TiN}:ℓ_{MoN} = 1:2.7, prepared with f_{N2} = 0.5) show higher indentation hardness and modulus than the other SLs. They also show a pronounced superlattice effect with H and E peaking at 36.5 ± 1.5 GPa and 504 ± 29 GPa, respectively, for a bilayer period of 9.3 nm, where unfortunately also the compressive residual stresses peak with –1.9 GPa (Fig.4c). Within the other SLs prepared under a lower f_{N2} of 0.3, those with a bilayer ratio

ℓ_{TiN}:ℓ_{MoN} of 1:1 yield the highest hardness peak with 34.8 ± 1.6 GPa at Λ = 9.9 nm. Importantly, this superlattice exhibits a relatively low compressive residual stress of −1 GPa and a low *E* modulus of 446 ± 20 GPa. The SLs with bilayer ratios of 1:0.5 and 1:2 exhibit weaker superlattice effects and bilayer period dependencies, with overall lower *H* and *E* values. While the indentation of these SL series is similar, their *H* values are different especially for bilayer periods between 3 and 12 nm. Interestingly the SL (Λ = 6.1 nm, ℓ_{TiN}:ℓ_{MoN} = 1:0.5) has a higher hardness (32.9 ± 1.3 GPa) combined with lower compressive stress (−1 GPa) than the SL (Λ = 7.3 nm, ℓ_{TiN}:ℓ_{MoN} = 1:2), which is actually the softest among all SLs studied here. This SL was also studied in detail by HRTEM (Fig. 2b) and presented the most pronounced satellite reflexes during XRD (Fig. 1b and 2a). The detailed SAED investigations (Fig. 2c) during TEM suggested that the MoN_y layers crystallize actually with the β-$MoN_{0.5}$ phase, which has a lower hardness than the rs-$MoN_{0.5}$ phase [28]. Consequently, based on the detailed investigations by XRD, TEM, and nanoindentation – and the very comparable deposition procedure for the SLs presented here, which would result in comparable interface sharpness between the TiN and MoN_y layers – not the better superlattice quality is responsible for the most pronounced superlattice reflexes during XRD of the SL with Λ = 7.3 nm and ℓ_{TiN}:ℓ_{MoN} = 1:2, but the highest fraction of the β-$MoN_{0.5}$ phase. Contrary to rs-$MoN_{0.5}$, the β-$MoN_{0.5}$ phase has itself an ordered arrangement of vacancies at the N-sublattice (ideally for $MoN_{0.5}$, 50% of the N-sites are vacant).

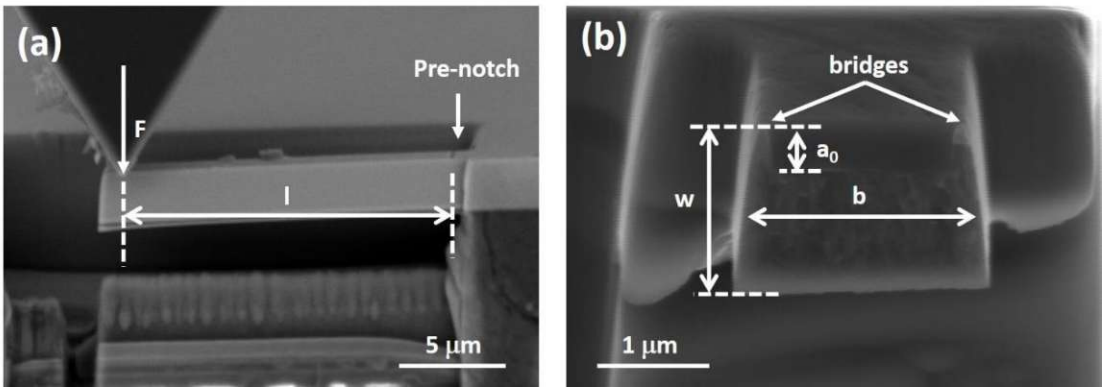

Fig. 5: Depiction of a micromechanical bending test on a free-standing cantilever **(a)**, and the cross-sectional SEM image of the cantilever after fracture **(b)**.

The critical fracture toughness investigations of all the TiN/MoN_y SLs were carried out by in-situ micromechanical free-standing cantilever bending tests. Fig. 5 depicts a representative free-standing microcantilever before (Fig. 5a) and after (Fig. 5b) micromechanical bending test. The cantilever has a geometry ratio of ~1 : 1 : 5 (w : b : l), a visible pre-notch, and two thin bridges. The thin side bridges (Fig. 5b) aim to initiate a very sharp pre-crack at the notch base, to provide an intrinsic toughness value [36-38]. The fracture cross-section image of SL presented in Fig. 5b (Λ = 7.3 nm, ℓ_{TiN}:ℓ_{MoN} = 1:2) shows a very dense morphology, and no obvious columnar structure.

Based on cantilever geometry, notch depth (a_0), and the loading curve, the critical fracture toughness K_{IC} of brittle materials can be calculated by the following equation [19, 39, 40]:

$$K_{IC} = \frac{F_c l}{b w^{3/2}} f\left(\frac{a_0}{w}\right) \quad (2)$$

where, F_C denotes the load at failure, and f(a_0/w) stands for a dimensionless geometry factor. For a brittle rectangular cantilever, f(a_0/w) is [41]:

$$f\left(\frac{a_0}{w}\right) = 1.46 + 24.36\left(\frac{a_0}{w}\right) - 47.21\left(\frac{a_0}{w}\right)^2 + 75.18\left(\frac{a_0}{w}\right)^3 \quad (3)$$

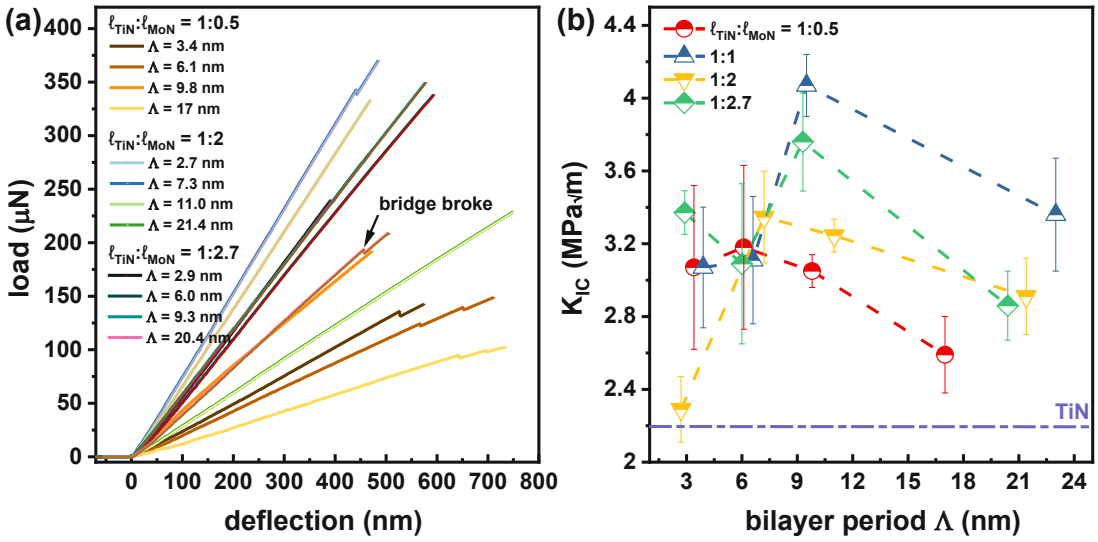

Fig. 6: The load–deflection curves **(a)** and critical fracture toughness K_{IC} **(b)** for the TiN/MoN_y SLs with Λ ranging from 2 to 23 nm, and ℓ_{TiN}:ℓ_{MoN} ratios of 1:0.5, 1:1, 1:2, and 1:2.7. The critical fracture toughness of the monolithic rs-TiN (dash-dotted horizontal line in **(b)**) and the SLs having an ℓ_{TiN}:ℓ_{MoN} ratio of 1:1 are taken from [24].

Fig. 6a presents load-deflection curves of all the SLs. All the curves are linear, indicating ideal brittle failure. The small irregularity points before failure come from the fracture of the bridges. According to finite element studies, the thin bridges suffer the maximum stresses during loading, thus will break first [36] and thereby generate very sharp pre-crack at the notch base. The integral area under the load-deflection curve indicates the energy release rate during deformation. Due to differences in cantilever dimensions, however, this cannot offer a reliable comparison of toughness. The critical fracture toughness, K_{IC}, which can be calculated by equation 2 and 3, on the other hand, offers a dimension-resolved comparison of toughness. The results of K_{IC} are presented in Fig. 6b. Although K_{IC} of the SLs varies strongly with different bilayer periods and ratios, they are significantly higher than that of the monolithic rs-TiN,

which is 2.2 MPa√m. Compared to the hardness, the fracture toughness shows a more pronounced superlattice effect, even for bilayer ratios of ℓ_{TiN}:ℓ_{MoN} = 1:0.5 and 1:2. As obtained for the hardness, the SLs with bilayer ratios of ℓ_{TiN}:ℓ_{MoN} = 1:1 and 1:2.7 provide the highest fracture toughness, which peaks with 4.1 ± 0.2 and 3.8 ± 0.3 MPa√m at Λ = 9.9 and 9.3 nm, respectively. The SL with the most pronounced satellites reflexes and the supposedly highest fraction of β-$MoN_{0.5}$ (ℓ_{TiN}:ℓ_{MoN} = 1:2 and Λ ~ 7.3 nm) performs better in terms of fracture toughness (being clearly in the middle range with 3.3 ± 0.3 MPa√m) than hardness (lowest hardness among all SLs studied here).

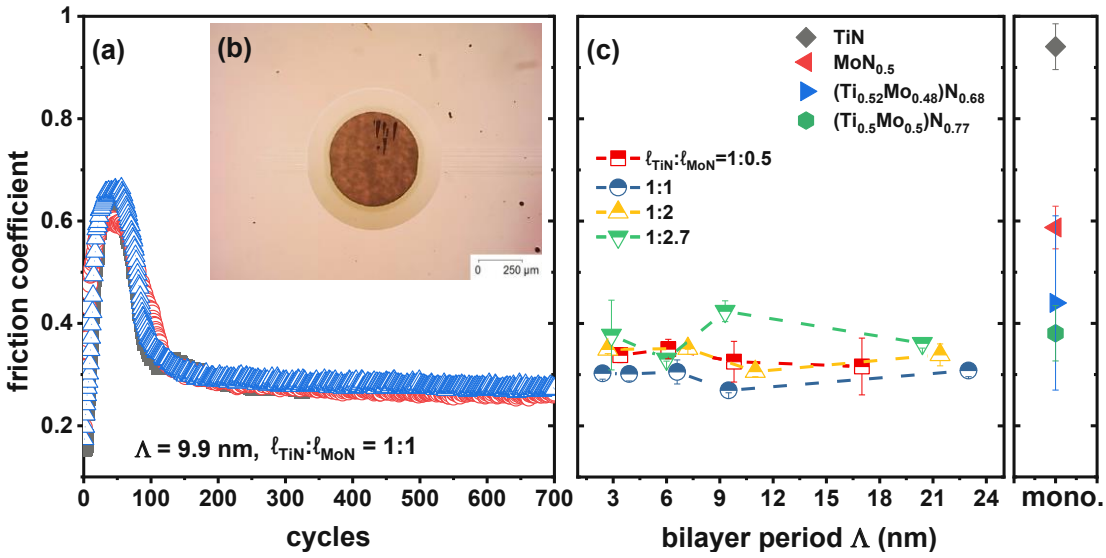

Fig. 7: Coefficient of friction, μ, curves as a function of the sliding cycles for the SL (Λ = 9.9 nm and ℓ_{TiN}: ℓ_{MoN} = 1:1) sample tested three times at room temperature in air of normal humidity **(a),** and a light optical image of the surface after ball cratering test on the wear track **(b)**. Average coefficient of friction values after 700 cycles for all TiN/MoN_y SLs, as well as the monolithic TiN, $MoN_{0.5}$, and the (Ti,Mo)N_y solid solution thin films **(c)**. The latter three films were used for the study reported in detail in [24].

Fig. 7a shows the coefficient of friction curve of the SL with Λ = 9.9 nm and ℓ_{TiN}:ℓ_{MoN}

= 1:1, which has the lowest average coefficient of friction of 0.27 ± 0.004 after the running in period (Fig. 7b). All three runs for this SL have very close results, indicating excellent repeatability. At the beginning, the coefficient of friction increases markedly to 0.63. After this running-in period, which last for about 100 sliding cycles, the coefficient of friction drops to 0.27, and remains constant after 200 cycles until the end of the test. Fig. 7b presents a light optical microscopy image of a ball crater – obtained via a calo-wear device – on the wear track of this SL. The very smooth scrape after ball catering suggests for an excellent adhesion to the substrate. The barely visible wear track after the 700 sliding cycles illustrates a high wear resistance of this coating. Fig. 7c gives the coefficient of frictions of all the samples at their end of the experiment (between 600 and 700 cycles). The solid solutions $(Ti_{0.52}Mo_{0.48})N_{0.68}$ and $(Ti_{0.5}Mo_{0.5})N_{0.77}$ outperform with coefficient of frictions of 0.44 ± 0.17 and 0.38 ± 0.05, respectively, binaries TiN (0.94 ± 0.04) and $MoN_{0.5}$ (0.59 ± 0.04) coatings. These coatings were studied in detail for their growth morphology and mechanical properties in Ref. [24]. The SL coatings further outperform even these solid solution films, where especially the SLs with a bilayer ratio of 1:1 always provides the lowest coefficient of friction among the bilayer periods studied (Λ = 9.9 nm).

4. Discussion

The TiN/MoN_y SLs studied here, compare positively to other SL ceramic coatings both in hardness and fracture toughness (tested with similar methods and under comparable conditions), with peak values of 34.8 ± 1.6 GPa and 4.1 ± 0.2 MPa√m (at ℓ_{TiN}:ℓ_{MoN} = 1:1 and Λ = 9.9 nm), respectively. Other SL ceramic coatings and their peak

values for H and K_{IC} are for example, TiN/CrN SLs (24.2 ± 0.9 GPa at Λ = 8.6 nm, and 2.0 ± 0.2 MPa√m at Λ = 6.2 nm) [20], TiN/CrAlN SLs (28.7 ± 0.2 GPa and 2.5 ± 0.1 MPa√m, at Λ = 7.3 nm) [23], and TaN/$MoN_{0.5}$ SLs (31.2 ± 1.6 GPa and 2.97 ± 0.21 MPa√m, at Λ = 5.2 nm) [22]. A notable example of SLs outperforming TiN/MoN_y are TiN/$WN_{0.5}$ SLs (36.7 ± 0.2 GPa and 4.6 ± 0.6 MPa√m, at Λ = 6.2 nm) [21]. According to these previous reports, both the elastic and lattice mismatch of two adjacent SL component layers, as well as the valence electron concentration (VEC) mainly contribute towards the strength and toughness enhancement of the SL architecture [13, 16, 42].

One of the requirements for a pronounced SL effect mentioned by previous studies is a large shear modulus mismatch (ΔG) of the SL components. ΔG of rs-TiN and rs-$MoN_{0.5}$ is 59 GPa (G = 124 GPa for rs-$MoN_{0.5}$, and 183 GPa for rs-TiN) [43], which is much larger than the elastically matched TiN/(Cr,Al)N SLs, but a bit less than the TiN/$WN_{0.5}$ SLs (ΔG = 67 GPa). The same dislocation slip-systems for the two SL components allow dislocations to glide across layer interfaces at small bilayer periods. But the different shear moduli of the layer materials lead to different dislocation line energies, which hinder the dislocation movement across the interfaces, particularly as the bilayer period increases from small bilayer periods towards the peak value. Upon a further increase in bilayer period beyond the peak value, the strength/hardness decreases again as dislocation glide within the individual layers becomes easier and starts to dominate. Thus, the peak in strength/hardness occurs at the bilayer period, where the stresses required to move dislocations across interfaces is equal to the stresses required to initiate glide within the individual layers. In case of different slip

systems for the contributing layers, dislocation glide across the interfaces might eventually become the strength-limiting factor. The maximum hardness for the various TiN-based superlattices is typically measured for bilayer periods in the range of 5 to 10 nm.

Dislocation motion can also be inhibited by coherency stresses that arise in SL architecture. When a layer is epitaxially grown on a substrate or another layer with different in-plane lattice parameters, coherency stresses are induced. The same cubic structure and relatively small lattice mismatch of rs-$MoN_{0.5}$ and rs-TiN (Δa = 0.05 Å) lead to a coherent growth, and introduce periodical coherency strains (compressive in TiN layer, tensile in MoN_y layer). These alternating strain fields exert forces on dislocations and hinder their glide across interfaces, as well as effectively enhancing energy dissipation by alternating the crack path and deflection at interfaces, when the bilayer period lies within the critical layer thickness of the SL components. These strains are relaxed at larger layer thicknesses by the introduction of interfacial misfit dislocations [44-47]. Since the lattice parameter of rs-$MoN_{0.5}$ is smaller than that of rs-TiN, the misfit dislocations are introduced in the MoN_y layers, when they exceed a critical thickness. Also, due to the lower shear modulus of rs-$MoN_{0.5}$ than that of rs-TiN, it requires more force to drive dislocations glide from MoN_y into TiN. External stresses will be required to drive dislocations across interfaces, providing a basis for increased resistance to dislocation motion across the individual layers.

The leading mechanism for the superlattice effect is still not completely clear. According to Buchinger et al. [23] , the modulus mismatch causes a more pronounced

superlattice effect than the lattice mismatch, by comparing the modulus-matched TiN/$Cr_{0.37}Al_{0.63}N$ SLs (Δa = 0.14 Å) to the lattice-matched TiN/$WN_{0.5}$ SLs (ΔG = 67 GPa) [21]. Hahn et al. [22] proposed a distinct fracture toughness improvement for the TaN/$MoN_{0.5}$ SLs with a relatively large Δa (0.1 Å) and small ΔG (32 GPa). However, comparison within these SL systems is complicated, especially for the MoN_y, WN_y, and/or Ta_yN-containing SLs, which could have microstructural heterogeneity and various N-to-metal ratios.

The mechanisms mentioned above sound reasonable for the TiN/MoN_y SLs with a 1:1 bilayer ratio, but not for the SLs with a 1:2 bilayer ratio, which have no distinct superlattice effect, and no hardness enhancement even with sharp interfaces. This might be because TiN has a much lower formation energy (–1.77 eV/at) than $MoN_{0.5}$ (–0.23 eV/at), so TiN will consume nitrogen firstly. For the limited nitrogen partial pressure of 0.14 Pa (f_{N2} = 0.3), these SL provide the lowest N-to-metal ratio (based on EDS) among all SL studied here, allowing to promote the formation of the tetragonal β-$MoN_{0.5}$ (having ordered vacancies at the N-sublattice) as shown by the SAED investigations (Fig. 2c). This is in contrast to the other SLs prepared with the same f_{N2}, which exhibit a higher N-to-metal ratio, and therefore most likely a lower fraction of the tetragonal β-$MoN_{0.5}$, see for example Ref. 22 presenting HRTEM for the SL with a bilayer ratio of 1:1. When more nitrogen partial pressure is provided (0.23 Pa, f_{N2} = 0.5), the TiN/MoN_y SLs have a distinct superlattice effect again (and a much higher N-to-metal ratio), even with a bilayer ratio of 1:2.7. This together suggests that the tetragonal β-$MoN_{0.5}$ (which is not preferred for high hardness) more likely forms for

reduced nitrogen supply.

As for the coefficient of friction, the SLs with a bilayer ratio of 1:1 – which provide highest hardness and fractur toughness combined with lowest compressive stresses – also outperform the other SLs. The lowest coefficient of friction is 0.27, obtained at a bilayer period of 9.9 nm, where also H and K_{IC} peaked. This indicates that superior tribological performance requires high hardness and high fracture toughness. However, the various SLs studied here do not show a pronounced dependence of their coefficient of friction on the bilayer period. The value of 0.27 is lower than that provided by most nitride ceramic coatings and their multilayers, such as MoN_x/SiN_x (0.52) [48], Cr(C,N)/CrN (0.45) [49], AlN/CrN (0.54) [50], TiN/WN (0.35), and TiN/CrN (0.5) [51]. However, some carbide multilayers display even better tribological behaviour by forming lubricating amorphous carbon on the surface during wear tests, such as TaC/SiC (0.2) [48], and a more remarkable example, nc-TaC/a-C film (0.05) [52].

5. Summary and Conclusions

Following the previous study of TiN/MoN_y SLs (with bilayer periods (Λ) of 3–23 nm and a bilayer ratio (ℓ_{TiN}:ℓ_{MoN}) of 1:1), in this study, we have further developed more TiN/MoN_y SLs, with a similar bilayer period range, but different bilayer ratios of 1:0.5 and 1:2, to expand the understanding of the superlattice effects for the TiN/MoN_y system.

XRD investigations show that all the SLs have a single-phased fcc-structure. Some of the SLs displayed high-quality high-order satellite reflexes, especially the one with ℓ_{TiN}:ℓ_{MoN} = 1:2 and Λ = 7.3 nm. A detailed TEM and SAED study of this SL also showed

distinct satellite reflections and that the MoN_y layers essentially crystallize in their ordered tetragonal β-$MoN_{0.5}$ phase. Therefore, this SL – although providing pronounced satellite reflexes during XRD, which would suggest for a high-quality superlattice – actually provides the lowest hardness. Nevertheless, the fracture toughness is in the middle region of all SLs studied here. The formation of the ordered tetragonal β-$MoN_{0.5}$ phase can be suppressed when increasing the provided nitrogen supply during growth. Therefore, the SLs prepared with f_{N2} = 0.5 (instead of 0.3) even allow for excellent hardness if the bilayer ratio is 1:2.7 (H = 36.5 ± 1.5 GPa for Λ = 9.3 nm). The SLs with a bilayer ratio of 1:1 clearly outperform the others in terms of a combination of high hardness with high fracture toughness and low compressive residual stresses and low coefficient of friction. Interestingly the peak values in *H* (34.8 ± 1.6 GPa) and K_{IC} (4.1 ± 0.2 MPa√m) combined with low values in compressive residual stresses (–1 GPa) and coefficient of friction (0.27) coincide with their corresponding bilayer period of 9.9 nm. However, most of the various SLs studied here (12 different ones) outperform the monolithic binaries (TiN and MoN_y) as well as solid solutions $(Ti,Mo)N_y$ – prepared under the same deposition conditions – in terms of fracture toughness and coefficient of friction.

Our studies showed that controlling the heterogeneous microstructures and the intrinsic mechanical properties of the individual material components (e.g., β-$MoN_{0.5}$ vs. rs-$MoN_{0.5}$) is important for a pronounced superlattice effect. Overall, the superlattice concept is of great importance to optimise hardness, fracture toughness, as well as tribological performance, which is underlined by comparing the values of

the SLs above to those of the monolithically prepared films.

Declaration of interests

The authors declare that they have no known competing or financial interests, or personal relationships, that could have influenced the work reported in this paper.

Data Availability

The data that support the findings of this study are available from the authors on reasonable request.

Acknowledgements

The authors acknowledge the use of the facilities of USTEM and XRC at the TU Wien. Special thanks to Dr. Hailin Sun and Dr. Joanne Stallard, from the Teer Coatings company, for doing all the tribological tests in this work. The authors thank Dr. Tomasz Wojcik for the initial TEM study, and thank Dr. Nikola Koutná for the DFT calculation support. ZCG further highly appreciates the support from Chinese scholarship funding (File No. 201908440933) during her PhD study at TU Wien. PHM is supported by the Austrian COMET Program (project K2 InTribology1, no. 872176).

References

[1] P.H. Mayrhofer, C. Mitterer, L. Hultman, H. Clemens, Microstructural design of hard coatings, Prog. Mater. Sci. 51 (2006) 1032-1114. https://doi.org/10.1016/j.pmatsci.2006.02.002

[2] A. Inspektor, P.A. Salvador, Architecture of PVD coatings for metalcutting applications: A review, Surf. Coat. Technol. 257 (2014) 138-153. https://doi.org/10.1016/j.surfcoat.2014.08.068

[3] S. Veprek, M.J.G. Veprek-Heijman, Industrial applications of superhard nanocomposite coatings, Surf. Coat. Technol. 202 (2008) 5063-5073. http://doi.org/10.1016/j.surfcoat.2008.05.038

[4] H. Kindlund, D.G. Sangiovanni, I. Petrov, J.E. Greene, L. Hultman, A review of the intrinsic ductility and toughness of hard transition-metal nitride alloy thin films, Thin Solid Films 688 (2019) 137479. https://doi.org/10.1016/j.tsf.2019.137479

[5] D.G. Sangiovanni, Inherent toughness and fracture mechanisms of refractory transition-metal nitrides via density-functional molecular dynamics, Acta Mater. 151 (2018) 11-20. https://doi.org/10.1016/j.actamat.2018.03.038

[6] D.G. Sangiovanni, V. Chirita, L. Hultman, Toughness enhancement in TiAlN-based quarternary alloys, Thin Solid Films 520 (2012) 4080-4088. http://dx.doi.org/10.1016/j.tsf.2012.01.030

[7] W.M. Seidl, M. Bartosik, S. Kolozsvári, H. Bolvardi, P.H. Mayrhofer, Influence of Ta on the fracture toughness of arc evaporated Ti-Al-N, Vacuum 150 (2018) 24-28. https://doi.org/10.1016/j.vacuum.2018.01.028

[8] M. Sperr, Z.L. Zhang, Y.P. Ivanov, P.H. Mayrhofer, M. Bartosik, Correlating elemental distribution with mechanical properties of TiN/SiNx nanocomposite coatings, Scr. Mater. 170 (2019) 20-23. http://doi.org/10.1016/j.scriptamat.2019.05.020

[9] M. Schlögl, C. Kirchlechner, J. Paulitsch, J. Keckes, P.H. Mayrhofer, Effects of structure and interfaces on fracture toughness of CrN/AlN multilayer coatings, Scr. Mater. 68 (2013) 917-920. https://doi.org/10.1016/j.scriptamat.2013.01.039

[10] U. Helmersson, S. Todorova, S.A. Barnett, J.E. Sundgren, L.C. Markert, J.E. Greene, Growth of single-crystal TiN/VN strained-layer superlattices with extremely high mechanical hardness, J. Appl. Phys. 62 (1987) 481-484. doi:http://dx.doi.org/10.1063/1.339770

[11] S. Barnett, A. Madan, Superhard superlattices, Phys. World 11 (1998) 45-48.

[12] M. Shinn, L. Hultman, S.A. Barnett, Growth, Structure, and Microhardness of Epitaxial Tin/Nbn Superlattices, Journal of Materials Research 7 (1992) 901-911. http://doi.org/10.1557/Jmr.1992.0901

[13] X. Chu, S.A. Barnett, Model of superlattice yield stress and hardness enhancements, J. Appl. Phys. 77 (1995) 4403-4411. https://doi.org/10.1063/1.359467

[14] P.E. Hovsepian, W.D. Münz, A. Medlock, G. Gregory, Combined cathodic arc/unbalanced magnetron grown CrN/NbN superlattice coatings for applications in the cutlery industry, Surf. Coat. Technol. 133–134 (2000) 508-516. 10.1016/S0257-8972(00)00921-X

[15] P.E. Hovsepian, D.B. Lewis, W.D. Münz, S.B. Lyon, M. Tomlinson, Combined cathodic arc/unbalanced magnetron grown CrN/NbN superlattice coatings for corrosion resistant applications, Surf. Coat. Technol. 120–121 (1999) 535-541. 10.1016/S0257-8972(99)00439-9

[16] J.S. Koehler, Attempt to Design a Strong Solid, Phys. Rev. B 2 (1970) 547-551. https://doi.org/10.1103/PhysRevB.2.547

[17] R.C. Cammarata, The supermodulus effect in compositionally modulated thin films, Scr. Metall. 20 (1986) 479-486. http://dx.doi.org/10.1016/0036-9748(86)90239-5

[18] S.P. Baker, W.D. Nix, Intrinsic Stresses in Compositionally Modulated Au-Ni Thin-Films and the

Supermodulus Effect, Journal of Materials Research 9 (1994) 3145-3152. Doi 10.1557/Jmr.1994.3145

[19] D. Di Maio, S.G. Roberts, Measuring fracture toughness of coatings using focused-ion-beam-machined microbeams, Journal of Materials Research 20 (2005) 299-302. https://doi.org/10.1557/JMR.2005.0048

[20] R. Hahn, M. Bartosik, R. Soler, C. Kirchlechner, G. Dehm, P.H. Mayrhofer, Superlattice effect for enhanced fracture toughness of hard coatings, Scr. Mater. 124 (2016) 67-70. https://doi.org/10.1016/j.scriptamat.2016.06.030

[21] J. Buchinger, N. Koutná, Z. Chen, Z. Zhang, P.H. Mayrhofer, D. Holec, M. Bartosik, Toughness enhancement in TiN/WN superlattice thin films, Acta Mater. 172 (2019) 18-29. https://doi.org/10.1016/j.actamat.2019.04.028

[22] R. Hahn, N. Koutná, T. Wójcik, A. Davydok, S. Kolozsvári, C. Krywka, D. Holec, M. Bartosik, P.H. Mayrhofer, Mechanistic study of superlattice-enabled high toughness and hardness in MoN/TaN coatings, Communications Materials 1 (2020) 62. https://doi.org/10.1038/s43246-020-00064-4

[23] J. Buchinger, A. Wagner, Z. Chen, Z.L. Zhang, D. Holec, P.H. Mayrhofer, M. Bartosik, Fracture toughness trends of modulus-matched TiN/(Cr,Al)N thin film superlattices, Acta Mater. 202 (2021) 376-386. https://doi.org/10.1016/j.actamat.2020.10.068

[24] Z. Gao, J. Buchinger, N. Koutná, T. Wojcik, R. Hahn, P.H. Mayrhofer, Ab initio supported development of TiN/MoN superlattice thin films with improved hardness and toughness, Acta Mater. 231 (2022) 117871. https://doi.org/10.1016/j.actamat.2022.117871

[25] H. Wang, H. Zeng, Q. Li, J. Shen, Superlattice supertoughness of TiN/MN (M=V, Nb, Ta, Mo, and W): First-principles study, Thin Solid Films 607 (2016) 59-66. https://doi.org/10.1016/j.tsf.2016.03.061

[26] N. Koutná, A. Brenner, D. Holec, P.H. Mayrhofer, High-throughput first-principles search for ceramic superlattices with improved ductility and fracture resistance, Acta Mater. 206 (2021) 116615. https://doi.org/10.1016/j.actamat.2020.116615

[27] Z.N. Jaf, H.A. Miran, Z.-T. Jiang, M. Altarawneh, Molybdenum nitrides from structures to industrial applications, (2021). doi:10.1515/revce-2021-0002

[28] H.S. Abdelkader, A. Rabahi, M. Benaissa, M.K. Benabadji, Theoretical investigation of structural and mechanical stability of Mo2N, Solid State Commun. 314-315 (2020) 113919. https://doi.org/10.1016/j.ssc.2020.113919

[29] R. Saha, W.D. Nix, Effects of the substrate on the determination of thin film mechanical properties by nanoindentation, Acta Mater. 50 (2002) 23-38. https://doi.org/10.1016/S1359-6454(01)00328-7

[30] G.C.A.M. Janssen, M.M. Abdalla, F. van Keulen, B.R. Pujada, B. van Venrooy, Celebrating the 100th anniversary of the Stoney equation for film stress: Developments from polycrystalline steel strips to single crystal silicon wafers, Thin Solid Films 517 (2009) 1858-1867. https://doi.org/10.1016/j.tsf.2008.07.014

[31] A. Madan, Y.-y. Wang, S.A. Barnett, C. Engström, H. Ljungcrantz, L. Hultman, M. Grimsditch, Enhanced mechanical hardness in epitaxial nonisostructural Mo/NbN and W/NbN superlattices, J. Appl. Phys. 84 (1998) 776-785. doi:http://dx.doi.org/10.1063/1.368137

[32] A.H. Eltoukhy, J.E. Greene, Compositionally modulated sputtered InSb/GaSb superlattices: Crystal growth and interlayer diffusion, J. Appl. Phys. 50 (1979) 505-517. doi:http://dx.doi.org/10.1063/1.325643

[33] R.M. Fleming, D.B. McWhan, A.C. Gossard, W. Wiegmann, R.A. Logan, X ‐ ray diffraction study of interdiffusion and growth in (GaAs)n(AlAs)m multilayers, J. Appl. Phys. 51 (1980) 357-363. http://doi.org/10.1063/1.327310

[34] A.J. Perry, A.W. Baouchi, J.H. Petersen, S.D. Pozder, Crystal structure of molybdenum nitride films made by reactive cathodic arc evaporation, Surf. Coat. Technol. 54-55 (1992) 261-265. https://doi.org/10.1016/S0257-8972(09)90060-3

[35] K. Inumaru, K. Baba, S. Yamanaka, Synthesis and Characterization of Superconducting β-Mo2N Crystalline Phase on a Si Substrate: An Application of Pulsed Laser Deposition to Nitride Chemistry, Chemistry of Materials 17 (2005) 5935-5940. 10.1021/cm050708i

[36] S. Brinckmann, K. Matoy, C. Kirchlechner, G. Dehm, On the influence of microcantilever pre-crack geometries on the apparent fracture toughness of brittle materials, Acta Mater. 136 (2017) 281-287. https://doi.org/10.1016/j.actamat.2017.07.014

[37] A. Riedl, R. Daniel, M. Stefenelli, T. Schöberl, O. Kolednik, C. Mitterer, J. Keckes, A novel approach for determining fracture toughness of hard coatings on the micrometer scale, Scr. Mater. 67 (2012) 708-711. https://doi.org/10.1016/j.scriptamat.2012.06.034

[38] S. Brinckmann, C. Kirchlechner, G. Dehm, Stress intensity factor dependence on anisotropy and geometry during micro-fracture experiments, Scr. Mater. 127 (2017) 76-78. https://doi.org/10.1016/j.scriptamat.2016.08.027

[39] A.K. Saxena, S. Brinckmann, B. Völker, G. Dehm, C. Kirchlechner, Experimental conditions affecting the measured fracture toughness at the microscale: Notch geometry and crack extension measurement, Mater. Des. 191 (2020) 108582. https://doi.org/10.1016/j.matdes.2020.108582

[40] J.R. Cahoon, W.H. Broughton, A.R. Kutzak, The determination of yield strength from hardness measurements, Metallurgical Transactions 2 (1971) 1979-1983. https://doi.org/10.1007/BF02913433

[41] K. Matoy, H. Schönherr, T. Detzel, T. Schöberl, R. Pippan, C. Motz, G. Dehm, A comparative micro-cantilever study of the mechanical behavior of silicon based passivation films, Thin Solid Films 518 (2009) 247-256. https://doi.org/10.1016/j.tsf.2009.07.143

[42] J.W. Gahn, Hardening by spinodal decomposition, Acta Metall. 11 (1963) 1275-1282. https://doi.org/10.1016/0001-6160(63)90022-1

[43] D. Holec, M. Friak, J. Neugebauer, P.H. Mayrhofer, Trends in the elastic response of binary early transition metal nitrides, Phys. Rev. B 85 (2012) 9. http://doi.org/10.1103/PhysRevB.85.064101

[44] F.F. Klimashin, H. Riedl, D. Primetzhofer, J. Paulitsch, P.H. Mayrhofer, Composition driven phase evolution and mechanical properties of Mo–Cr–N hard coatings, J. Appl. Phys. 118 (2015) 025305. http://doi.org/10.1063/1.4926734

[45] Z. Zhang, X. Gu, D. Holec, M. Bartosik, P.H. Mayrhofer, H.P. Duan, Superlattice-induced oscillations of interplanar distances and strain effects in the CrN/AlN system, Phys. Rev. B 95 (2017) 155305. https://doi.org/10.1103/PhysRevB.95.155305

[46] N. Koutna, P. Rehak, Z. Chen, M. Bartosik, M. Fallmann, M. Cerny, Z. Zhang, M. Friak, M. Sob, P.H. Mayrhofer, D. Holec, Correlating structural and mechanical properties of AlN/TiN superlattice films, Scr. Mater. 165 (2019) 159-163. http://doi.org/10.1016/j.scriptamat.2019.02.021

[47] N. Koutná, D. Holec, M. Friák, P.H. Mayrhofer, M. Šob, Stability and elasticity of metastable solid solutions and superlattices in the MoN–TaN system: First-principles calculations, Mater. Des. 144 (2018) 310-322. https://doi.org/10.1016/j.matdes.2018.02.033

[48] S. Du, K. Zhang, M. Wen, P. Ren, Q. Meng, C. Hu, W. Zheng, Tribochemistry dependent tribological behavior of superhard TaC/SiC multilayer films, Surf. Coat. Technol. 337 (2018) 492-500. https://doi.org/10.1016/j.surfcoat.2018.01.064

[49] B. Warcholinski, A. Gilewicz, Z. Kuklinski, P. Myslinski, Hard CrCN/CrN multilayer coatings for tribological applications, Surf. Coat. Technol. 204 (2010) 2289-2293. https://doi.org/10.1016/j.surfcoat.2009.12.019

[50] Y.-S. Yang, T.-P. Cho, Y.-C. Lin, Effect of coating architectures on the wear and hydrophobic properties of Al–N/Cr–N multilayer coatings, Surf. Coat. Technol. 259 (2014) 172-177.

https://doi.org/10.1016/j.surfcoat.2014.01.058

[51] D.D. Kumar, N. Kumar, S. Kalaiselvam, S. Dash, R. Jayavel, Wear resistant super-hard multilayer transition metal-nitride coatings, Surfaces and Interfaces 7 (2017) 74-82. https://doi.org/10.1016/j.surfin.2017.03.001

[52] D. Nilsson, F. Svahn, U. Wiklund, S. Hogmark, Low-friction carbon-rich carbide coatings deposited by co-sputtering, Wear 254 (2003) 1084-1091. https://doi.org/10.1016/S0043-1648(03)00340-5

Materials & Design 209 (2021) 109949

Contents lists available at ScienceDirect

Materials & Design

journal homepage: www.elsevier.com/locate/matdes

Synthesis and electrochemical properties of nanoporous CrN thin film electrodes for supercapacitor applications

Zecui Gao [a,b], Zhixin Wan [c], Zhengtao Wu [a], Xueli Huang [a], Haiqing Li [a], Teng Fei Zhang [a,*], Paul Heinz Mayrhofer [b], Qimin Wang [a,*]

[a] School of Electromechanical Engineering, Guangdong University of Technology, Guangzhou 510006, China
[b] Institute of Materials Science and Technology, Technische Universität Wien, Getreidemarkt 9, 1060 Vienna, Austria
[c] School of Materials Science & Engineering, Sun Yat-sen University, Guangzhou 510006, China

HIGHLIGHTS

- Sufficient Ni content leads to an interconnected Ni-network in the CrN–Ni coating.
- Nanoporous CrN can be obtained by HCl etching of CrN–Ni.
- Nanoporous CrN has an ~ 80% higher specific capacitance than CrN.
- Guideline to prepare porous transition metal nitrides with a high specific surface area.

GRAPHICAL ABSTRACT

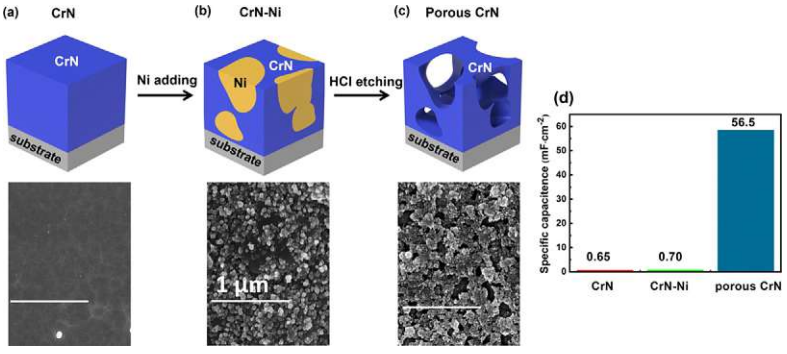

ARTICLE INFO

Article history:
Received 27 March 2021
Revised 26 June 2021
Accepted 28 June 2021
Available online 29 June 2021

Keywords:
PVD thin film
Nanoporous supercapacitor
Specific capacitance
porous CrN

ABSTRACT

Transition metal nitrides (TMN) have received widespread consideration as supercapacitor materials for a variety of energy storage applications. An important requirement to such electrode materials is a very high specific surface area, which is typically obtained through a percolating pore-network. Here, we use arc ion plating to prepare CrN-Ni composite coatings with 0, 30.4, 54.2, and 77.6 at.% Ni. Detailed X-ray diffraction and X-ray photoelectron spectroscopy showed that the coatings consist of CrN phases next to metallic Ni. Post-deposition treatments with HCl solutions lead to selective leaching, causing a porous nanostructure for the Ni-containing CrN coatings. From there, the coating with 54.2 at.% Ni in its as-deposited state provided the highest (electrode-geometric-area)-specific capacitance after the HCl treatment, giving 58.5 mF·cm^{-2} at 1.0 mA·cm^{-2} in a 0.5 M H_2SO_4 aqueous electrolyte. This value is about 80 times higher than for the as-deposited coatings or the Ni-free CrN. Consequently, our strategy to combine TMNs with metallic Ni and its subsequent treatment with HCl is highly effective in enlarging the specific surface area and adsorption sites. It allows to significantly enhance the energy storage performance of TMN thin film supercapacitors.

1. Introduction

Owing to the high charge–discharge efficiency, long service life and environmental compatibility, supercapacitors (SCs) have received widespread consideration to be used alone – or in combi-

* Corresponding authors.
E-mail addresses: tfzhang@gdut.edu.cn (T.F. Zhang), qmwang@gdut.edu.cn (Q. Wang).

https://doi.org/10.1016/j.matdes.2021.109949
0264-1275/

nation with other energy storage options – to offer improved power efficiency and enhanced cycle life. Therefore, SCs are available for many energy storage applications, such as regenerative braking, short-term energy storage, miniaturized energy storage devices, and emergency power supplies [1–4]. Typically, there are two storage mechanisms for SCs: 1) electrochemical double-layer capacitors (EDLC, electrochemical adsorption/desorption only occur on the surface of the electrodes, like carbons) and 2) pseudo-capacitor (electrosorption, reduction–oxidation reactions, and intercalation processes, like oxides). Thus, an ideal SC should have a high specific surface area for charge adsorption and/or chemical reaction [5,6]. As the most important constituent of SCs, various electrode materials have been extensively developed in recent years, both in their compositional and morphological design. The most common one is shaping high conductive carbon-based materials to specific morphologies (such as, nanotube, nanofiber, nanowire, nanoflower, and nanorods [7,8]), which are then covered with transition metal oxides (TMO, such as Co_3O_4, MnO_2, Nb_2O_5, TiO_2, TiO_3, HfO_2,and RuO_2) [9–19] to obtain their combinations as TMO@C or TMO/C. The other option is to dope the shaped carbon with N/O/S/P [20–26]. This is a mutually beneficial cooperation of EDLC and pseudocapacitor, getting a massively increased specific surface area for chemical reactions and charge absorptions, and greatly increasing energy density [27]. The comparison of their specific capacitance is depicted in the supplementary data, in Table S1. However, their fabrication is quite complicated and sometimes not eco-friendly, involving hydrofluoric acid etching and annealing.

Except for carbons and oxides, there are also lots of other SC electrodes, such as carbides (e.g., TiC [28]), sulfides (e.g., TiS [29]), nitrides (e.g., TiN [30]), and borocarbonitrides [31]. Among them, the physical vapor deposited (PVD) transition metal nitride (TMN) thin films are very promising [32]. The reported TMN electrodes, such as CrN [33–35], TiN [30,36,37], VN [38,39], Mo_2N [40–42], and TiNbN [43] have exhibited good performance in service life, as a result of their high conductivity, high structural and chemical stability, and have found also their position for supercapacitor applications. PVD techniques, especially magnetron sputtering and arc ion plating, are widely used in high-quality TMN coating fabrication [44,45]. PVD-produced transition metal nitride (TMN) film electrodes have many advantages over traditional powder-type electrode materials, including binder-free fabrication, good adhesion, uniformity, and easily controlled composition and thickness. This makes them promising candidates for flexible thin-film supercapacitors and on-chip micro-supercapacitors. The specific capacitance of TMN electrode materials is based on the high-speed electrostatic adsorption. Storing the charge on the electrodes and the interface of active materials at the electrolyte, requires a very large relative ion-accessible surface area. Therefore, the main work of the present study focuses on how to obtain a sufficiently porous structure and rough surface of PVD TMN thin films. Recently we showed that the (electrode-geometric-area)-specific capacitance C_a of magnetron sputtered ~ 1-μm-thin HfN can be improved from 0.7 to 5.6 $mF{\cdot}cm^{-2}$ by a post-deposition etching with Ar plus Kr ion beams, enlarging its specific surface area [46]. This is in the range of magnetron sputtered TiN, exhibiting a C_a value of ~ 3 $mF{\cdot}cm^{-2}$ for the ~ 1-μm-thin film, increasing to 8.8 $mF{\cdot}cm^{-2}$ for the 2.2-μm-thin film [36]. CrN (1.1 μm thin) provides already in its as-deposited state – by conventional magnetron sputtering – a much higher C_a value of 12.8 $mF{\cdot}cm^{-2}$ [34], which further can be improved to 17.7 $mF{\cdot}cm^{-2}$ [33] or even 35.4 $mF{\cdot}cm^{-2}$ [35] using glancing angle deposition. When preparing a porous CrN out of a magnetron co-sputtered CrN-Cu coating – by a subsequent selective chemical etching for 3–4 days with an 0.5 M HNO_3 – the specific capacitance can also be improved to 31.3 $mF{\cdot}cm^{-2}$ [47]. Here, we use a corresponding technique, but show that through the combination of CrN with Ni a faster formation of the porous structure can be obtained (3 h in 3 M HCl) allowing for a specific capacitance of even 58.5 $mF{\cdot}cm^{-2}$. All these C_a values refer to a current density of 1.0 $mA{\cdot}cm^{-2}$ or a scanning rate of 100 $mV{\cdot}s^{-1}$, further data of some literature values are given in the Table S1.

Previously reported works have been mainly focusing on the optimization of material selection, composition, and deposition parameters of the thin films, while in this study, a novel microstructure design strategy was applied to synthesize nanoporous thin film electrodes through PVD and subsequent selective chemical etching processes. This combined procedure for CrN-Ni thin films showed a remarkably enhanced capacitive performance as compared with other reported thin film systems. Generally, the combination of nitride coatings with Cu [48–52], Ni [53–55], Ta [56], or Ag [57,58], is warmly welcome for reducing the friction coefficient, enhancing the toughness, increasing plastic deformation and corrosion resistance. The ductile metallic phase is percolating throughout the typically brittle, but corrosion resistant TMN matrix [59]. Here, we used arc ion plating to prepare a CrN matrix – CrN combines high strength [60] with excellent corrosion [61] and oxidation resistance [62], and specific capacitance [34] – in which metallic Ni is uniformly distributed. After the deposition, the Ni is thoroughly etched away using an HCl solution, to prepare a sponge-like CrN coating. A schematic illustration of the fabrication process of the porous CrN thin films is shown in Fig. 1. We provide a detailed study on how the Ni content and the chemical etching parameters influence the microstructure, morphology, and electrochemical properties of these CrN-Ni thin films. The maximum (electrode-geometric-area)-specific capacitance value for the porous (after etching) CrN–Ni thin films exceeds those of the as-deposited CrN–Ni and CrN by a factor of ~ 80. The strategy outlined here, can be universally applied for modifying the surface and cross-sectional morphology of TMN films and enlarge their specific surface area and adsorption sites. This procedure shows great potential for optimizing the energy storage performance of TMN thin film supercapacitors.

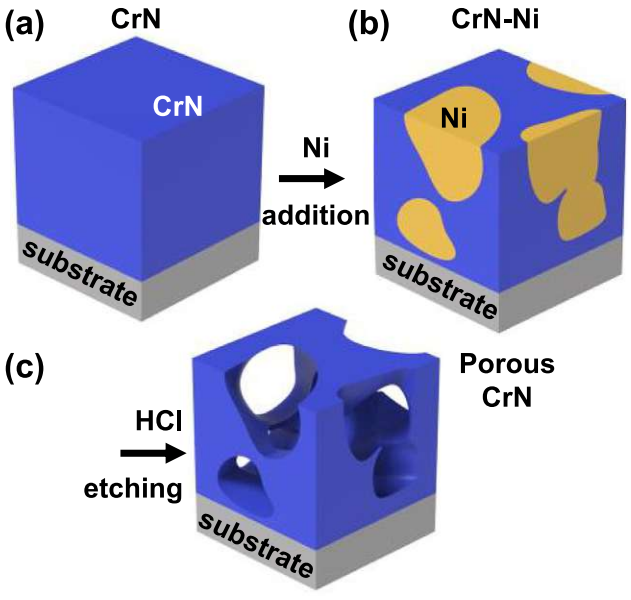

Fig. 1. Schematic illustration of the fabrication process for porous CrN thin films: **(a)** as-deposited CrN, **(b)** as-deposited CrN–Ni, and **(c)** porous CrN films.

2. Experimental

2.1. Samples preparation

CrN–Ni thin films with various Ni contents were deposited by arc ion plating (MD800, DG Huasheng, Inc.) using a Cr target (99.95% purity) and a $Ni_{80}Cr_{20}$ (20 at.% Cr) alloy target (99.95% purity). These two targets are placed horizontally at an angle of 100° to each other facing the substrate holder, which rotated with a speed of 1.5 rpm during the deposition, at a mean distance of 20 cm. The polished monocrystalline Si (1 0 0)-oriented substrates ($10 \times 10 \times 0.5$ mm^3) were ultrasonically cleaned in ethanol and deionized water successively and dried by nitrogen gas before being mounted to the substrate holder. The system was evacuated to a base pressure of at least 5×10^{-3} Pa. Prior to deposition, a 30-min etching process using Ar^+ and Kr^+ from a booster ion source (Pinnacle, Advanced Energy, Inc.) was conducted with a pressure of 2.0 Pa and a pulsed substrate bias potential of − 600 V to remove oxides and contaminants from the surface. Afterwards, a CrN adhesion layer (~0.3 μm thin) was deposited using 1.0 Pa N_2 atmosphere, 100 A target current, and − 100 V pulsed bias potential. The subsequent CrN–Ni layer (~0.7 μm thin) was deposited with the same N_2 atmosphere of 1.0 Pa, pulsed bias potential of − 100 V, and deposition temperature of 400 °C. The Ni content of these CrN–Ni top layers was varied by adjusting the current applied to the $Ni_{80}Cr_{20}$ and Cr targets, as listed in Table 1, using a pulsed DC power supply (DSP12A1, ZONGXINDA, Chengdu, Ict.) and adjusting the duty cycle to 15% and the frequency to 10 kHz.

We systematically varied the concentration of Ni in the CrN–Ni top layer (from 0 to 78 at.%), the exposure time in the HCl solution (from 1 to 18 h), and the intensity of the HCl solution (from 1 to 4 mol·l^{-1}). During this etching process, the samples were removed from the HCl solution every hour, and washed with deionized water, dried with nitrogen, and tested for their specific capacitance.

2.2. Structural and chemical characterizations

The surface and cross-section morphologies of the as-deposited thin films and their best (classified through their area-specific capacitance) porous products (after the HCl solution treatment) were investigated by scanning electron microscopy (SEM, FEI Nova NanoSEM 430) at an accelerating voltage of 15 kV. The chemical composition of the samples was determined by using an integrated energy dispersive X-ray spectroscopy (Oxford instruments X-Max^N). The surface morphology of the thin films was also measured using atomic force microscopy (AFM, Bruker Dimension FastScan), with a dimension of 20×20 μm^2, in peak force tapping mode. The root-mean-square roughness (R_q) was calculated from three consecutive measurements for each sample. X-ray diffraction (XRD) in a Bragg–Brentano configuration, using a Bruker D8 Advance diffractometer (Cu Kα X-ray source, 40 kV, and 40 mA), was employed to investigate the crystal structure of the thin films. The chemical bonding states of the thin films were studied by X-ray photoelectron spectroscopy (XPS) with a Thermo Fisher Escalab 250Xi spectrometer using a monochromatic Al Kα source (15 kV and 15 mA). Initially, individual element survey scans were performed to detect the elements in all samples. Prior to these measurements, the surface of the coatings was Ar-ion etched (with an energy of 3 keV over an area of 3×3 mm^2) for 3.5 min to remove surface contaminants. The recorded spectra were calibrated by the C 1 s binding energy of 284.8 eV.

2.3. Electrochemical characterizations

An electrochemical workstation (AMETEK, 1470E) with a conventional three-electrode setup (working electrodes: the coatings presented here; reference electrode: Ag/AgCl [KCl saturated]; counter electrode: Pt plate), was used to evaluate the electrochemical properties of as-deposited and etched CrN-Ni thin films in a 0.5 M H_2SO_4 aqueous electrolyte. The specific capacitance was measured by cyclic voltammetry (CV) and galvanostatic charge–discharge (GCD), at a controlled potential window, scan rate, and current density. The conductivity and interfaces were investigated using electrochemical impedance spectroscopy (EIS), at an open-circuit voltage of 0.6 V, a disturbing voltage of 5 mV, and a frequency range of 0.01 – 100000 Hz. The cycling stability was tested by CV measurements at a constant scan rate of 100 mV·s^{-1} for 2000 cycles at room temperature.

The (electrode-geometric-area)-specific capacitance (C_a, mF·cm^{-2}) of the thin film supercapacitors was calculated from galvanostatic charge–discharge by using [34]:

$$C_a = (I \times \Delta t)/S \times \Delta U \quad (1)$$

where I (mA) is the discharge current, Δt (s) is the discharge time, ΔU (V) is the potential window between the lowest and the highest potentials (U_a and U_b, respectively), and S (cm^2) is the geometric area of the working electrode.

Integrating the area of one CV cycle, the specific capacitance of the thin film supercapacitors can also be obtained, using the following equation [34]:

$$C_a = \int_{U_b}^{U_a} I(V)dV/2 \times v \times S \times (U_a - U_b) \quad (2)$$

where $\int_{U_b}^{U_a} I(V)dV$ is the integral current area and v (mV·s^{-1}) is the scan rate. This was used to calculate the retention rate of the capacitance during the 2000 cycle service life investigation.

3. Results and discussions

3.1. Structure and morphology

The chemical compositions of the as-deposited CrN–Ni thin films and those after a distinct HCl solution treatment (next paragraph) are given in Table 1. For easier reading, our thin films are named as CrN, CrN-Ni_{30}, CrN-Ni_{54}, and CrN-Ni_{78} according to their Ni-content of 0, 30.4, 54.2, and 77.6 at.% in the as-deposited state, respectively. This increase in Ni-content is obtained by incrementally increasing the arc ion plating current at the $Ni_{0.8}Cr_{0.2}$ target

Table 1
Target currents, etching time, and compositions of the CrN–Ni thin films in the as-deposited state and after the treatment in a 3.0 mol·l^{-1} HCl bath (indicated with an asterisk).

Sample	CrN	CrN*	CrN-Ni_{30}	CrN-Ni_{30}*	CrN-Ni_{54}	CrN-Ni_{54}*	CrN-Ni_{78}	CrN-Ni_{78}*
Cr target current (A)	90		90		80		0	
$Ni_{80}Cr_{20}$ target current (A)	0		50		80		90	
3.0 M HCl etching time (h)		18		11		3		4
N (at.%)	48.9	49.9	36.5	50.0	15.1	49.4	8.3	23.7
Cr (at.%)	51.1	50.1	33.1	41.8	20.7	43.5	14.1	22.3
Ni (at.%)	0	0	30.4	8.2	54.2	7.1	77.6	54.0

from 0 to 90 A and simultaneously decreasing the current at the Cr target from 90 to 0 A, see Table 1. Therefore, their Cr and N contents decreased continuously from around 50 to 10 at.%.

Detailed studies on the effect of the HCl solution concentration over the potential range from −0.2 and 0.8 V showed best results in current density for the CrN-Ni_{54} thin film (as measured by the cyclic voltammetry (CV) at a scan rate of 100 mV·s^{-1} and galvanostatic charge–discharge (GCD) at a current density of 1.0 mA·cm^{-2}), when using a 3.0 mol·l^{-1} concentration (the curves for the individual HCl concentrations are provided in the supplementary data Fig. S1). The area-specific capacitance C_a of the Ni-containing samples CrN-Ni_{30}, CrN-Ni_{54}, and CrN-Ni_{78} peaked with 11 h, 3 h, and 4 h of dissolution time within the 3.0 M HCl bath, respectively, see Fig. 2a (and supplementary data Fig. S2). The samples providing the C_a peak-values are indicated with an asterisk: CrN-Ni_{30}* (11 h treatment time), CrN-Ni_{54}* (3 h treatment time), and CrN-Ni_{78}* (4 h treatment time). As expected, there is no change for the Ni-free CrN thin film, but the sample CrN* refers to the maximum treatment time of 18 h in the 3.0 M HCl solution. Fig. 2b shows the C_a peak-values for our samples with respect to the C_a values in their as-deposited state, obtained at a current density of 1.0 mA·cm^{-2}. This comparison clearly shows that the highest C_a value with ~ 58.5 mF·cm^{-2} is obtained with the CrN-Ni_{54} coating (54.2 at.% Ni), followed by ~ 18.0 mF·cm^{-2} for the CrN-Ni_{78} coating (77.6 at.% Ni). When compared to their as-deposited condition, the CrN-Ni_{30}, CrN-Ni_{54}, and CrN-Ni_{78} coatings experienced an increase in their C_a values by a factor of ~ 16, 80, and 11, respectively, clearly highlighting the massive improvement in C_a due to the HCl treatment. This is because, by the HCl treatment a porous structure is formed, which will be presented later. The Ni content of the samples massively decreased due to the HCl solution treatment, from 30.4 to 8.2 at.% for CrN-Ni_{30}, from 54.2 to 7.1 at.% for CrN-Ni_{54}, and from 77.6 to 54.0 at.% for CrN-Ni_{78}, see Table 1. As expected, the chemical composition of the Ni-free CrN sample shows no obvious difference before and after 18 h of HCl etching, indicating the excellent chemical stability of CrN. Due to the etching procedure – as most of the Ni is etched away especially for the CrN-Ni_{30} and CrN-Ni_{54} coatings – also their overall Cr content increased to 41.8 and 43.5 at.%, respectively, Table 1. The HCl solution nicely changed its color into green, due to Ni dissolution (Fig. S3, supplementary data). Due to the very high Ni content of the CrN-Ni_{78} coating – basically a Ni matrix with CrN precipitates is formed – chemical etching with the 3.0 M HCl would require significantly longer times for a more pronounced dissolution. The removal of Ni from the CrN-Ni_{30} and CrN-Ni_{54} coatings is promoted by their high fraction of phase-boundaries between Ni and CrN supporting access of the HCl solution.

XRD investigations of the as-deposited coatings show the face centered cubic (fcc) CrN phase, see their (1 1 1) and (2 0 0) diffraction peaks at 37.5 and 43.7° in Fig. 3a. The small peak at the left-hand shoulder of the (2 0 0) fcc CrN peak for the CrN-Ni_{54} coating might indicate the presence of a small fraction of the hexagonal Cr_2N phase. For the other coatings, this is probably hidden behind their relatively broader XRD peaks. With increasing Ni-content, the XRD peaks at 44.5 and 51.8° (indicative for the (1 1 1) and (2 0 0) lattice plane distances of fcc-Ni) increase in intensity. No nickel nitride phase could be detected, in agreement to the known weak nitride forming tendency of Ni [63]. After the HCl solution treatment, almost no crystalline Ni phase can be detected anymore for CrN-Ni_{30}* and CrN-Ni_{54}*, see Fig. 3b. Contrary, the CrN-Ni_{78}* coating still shows a pronounced crystalline Ni phase content in agreement with the chemical investigations, see Table 1. The profile of the XRD peaks from the CrN phase did not change due to the HCl solution treatment (please compare Fig. 3a and b), especially when considering the changed contribution from the Ni phase. This furthermore indicates the excellent chemical stability and corrosion resistance of CrN.

SEM top view investigations of the coatings clearly show the formation of a porous structure due to the HCl solution treatment, when Ni was present in the as-deposited state. The Ni-free CrN thin film exhibits a dense and smooth surface before and after etching, see Fig. 4a and b, respectively, again underlining the excellent corrosion resistance of CrN [64]. The 30.4 at.% Ni containing sample (CrN-Ni_{30}) shows some small particles at the surface (Fig. 4c), which were removed by the etching treatment (CrN-Ni_{30}*, Fig. 4d). The sensitivity to the HCl solution treatment suggests these particles to be metallic Ni. Independent on the HCl solution treatment-time, the surface of this sample always was rather smooth, indicating that the Ni content of this sample (CrN-Ni_{30}) is too low to allow its complete percolation throughout the matrix. In other words, the metallic Ni phase is not interconnected but rather present as pockets encapsulated by the corrosion-resistant ceramic CrN.

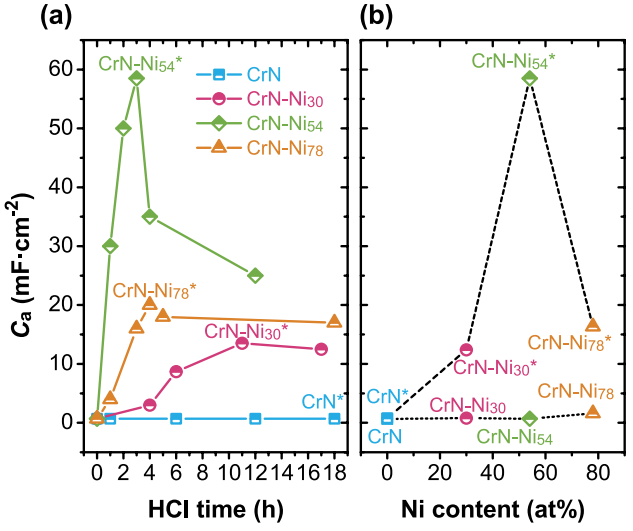

Fig. 2. **(a)** Comparison of specific capacitance of the coatings CrN, CrN-Ni_{30}, CrN-Ni_{54}, and CrN-Ni_{78} after different immersion times in HCl solution (current density: 1.0 mA·cm^{-2}). **(b)** Comparison of the peak-values in specific capacitance of these samples to their as-deposited state (current density: 1.0 mA·cm^{-2}).

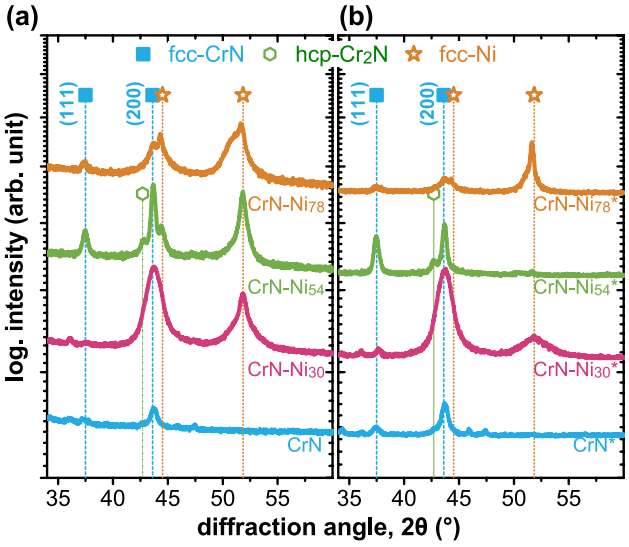

Fig. 3. XRD patterns of **(a)** as-deposited coatings and **(b)** coatings after the HCl treatment for various times to obtain their highest specific capacitance (Fig. 2).

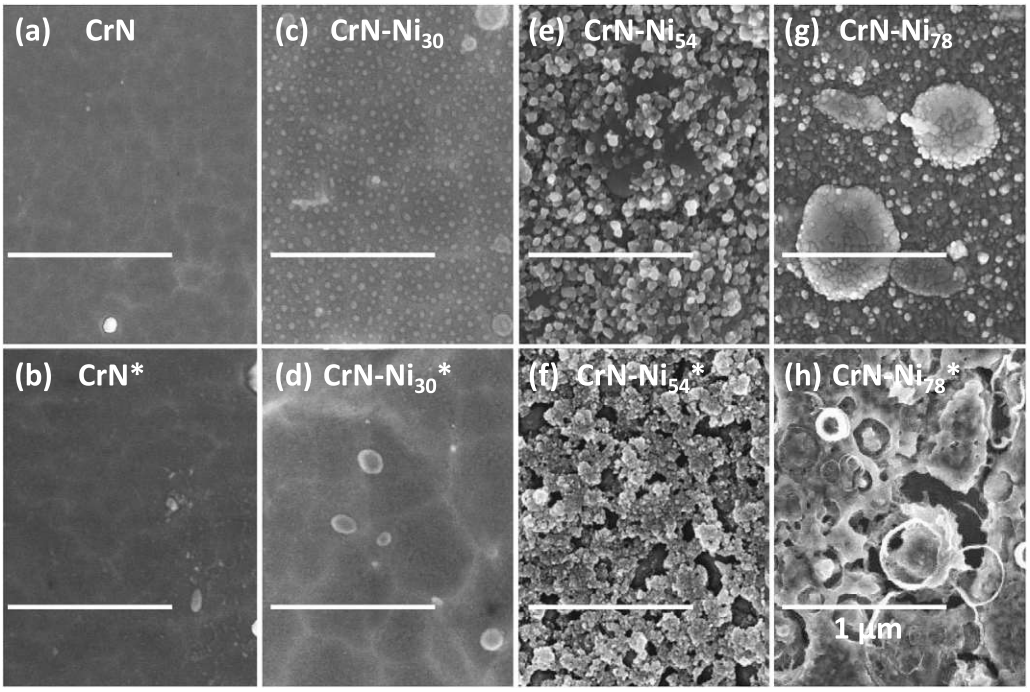

Fig. 4. Top-view SEM images of CrN **(a and b)**, CrN-Ni_{30} **(c and d)**, CrN-Ni_{54} **(e and f)**, and CrN-Ni_{78} **(g and h)** coatings in their as-deposited state and after the HCl treatment to obtain their highest specific capacitance (Fig. 2), respectively. The white horizontal line has the same length in all SEM images and represents the scale bar of 1 μm.

The CrN-Ni_{54} coating (54.2 at.% Ni) shows much larger particles at the surface already in its as-deposited state, Fig. 4e. After the 3 h treatment in the HCl bath, the SEM top-view investigations already indicate for a sponge-like morphology with a high porosity (CrN-Ni_{54}*, Fig. 4f). Consequently, here the Ni content was sufficiently high to allow for the formation of an interconnected Ni-network in the as-deposited state. Our data furthermore show that the HCl solution treatment-time needs to be controlled, to allow that most of the Ni-phase is dissolved, leading to a maximization of the porosity. However, if the treatment time is too long, the remaining CrN-skeleton may be separated from the CrN adhesion layer and influence the electrodes' service life.

The impressions from the top-view SEM investigations are in-line with detailed AFM analysis (supplementary data Fig. S4, scanning over a surface area of 20 × 20 μm^2) yielding root mean square roughness (R_q) values of 7.8 and 152.0 nm for the coatings CrN and CrN-Ni_{54}, respectively. By the HCl solution treatment for 3 h, the R_q value of the CrN-Ni_{54} coating increased further to 185.0 nm. The SEM top-view investigations already indicated the increased surface roughness by this HCl solution treatment (compare Fig. 4e and f).

Further increasing the Ni content to 77.6 at.% leads to a coating (CrN-Ni_{78}) that shows already in the as-deposited state (Fig. 4g) a less promising surface quality than the CrN-Ni_{54} coating. The surface is characterized by fewer homogenously distributed particles, but some very large ones as well. After a 4 h treatment in the HCl bath, ring-shaped holes formed at the surface, suggesting that especially at the CrN–Ni interfaces the dissolution kinetic is faster. In general, these SEM investigations indicate that for this sample the Ni content is too high. Thus, out of the three Ni-containing CrN samples, the CrN-Ni_{54} coating showed the most promising formation of a porous material after the HCl solution treatment, based on these SEM top-view investigations.

Whether the formed pores also expand throughout the coating thickness was studied by SEM fracture cross-sections, Fig. 5. The Ni-free CrN thin film shows the most compact cross-sectional morphology in the as-deposited state (Fig. 5a), which is only a bit influenced by the HCl treatment for 18 h (Fig. 5b). In agreement with the plan-view SEM investigations (Fig. 4), also the cross-sectional morphology of the CrN-Ni_{30} coating is only slightly influenced by the HCl solution treatment. Considering the noticeable change in Ni content (from 30.4 down to 8.2 at.%) this is somehow surprising and suggests the formation of rather small pores. Contrary, the CrN-Ni_{54} coating shows a significant change in cross-sectional morphology across the entire thickness of the Ni-containing part, due to the HCl solution treatment. Already in its as-deposited state, this coating is characterized by a rather rough cross-sectional morphology due to the competitive growth of the Ni and CrN phases. These SEM studies nicely show that the generated pores (due to the dissolution of most of the Ni-phase, please remember that here the Ni-content decreased from 54.2 to 7.1 at.%) percolate throughout the entire outer CrN–Ni layer (Fig. 5f). The highest Ni containing coating, CrN-Ni_{78}, reveals a smoother appearance especially of the surface-near region in the as-deposited state (Fig. 5g), with even some pores present underneath this area. However, after the HCl solution treatment, no percolating pore-network formed (Fig. 5h). The studies furthermore show that all samples have nearly the same entire coating thickness of ~ 1.0 μm.

Based on these SEM top-view (Fig. 4) and SEM fracture cross-section (Fig. 5) studies, we can conclude that the most effective form of a fully percolating pore-network, due to the HCl solution treatment, is obtained for the 54.2 at.% Ni containing coating, CrN-Ni_{54}. This coating exhibits a high porosity after the HCl treatment (considering that the coating thickness remained the same, but its Ni content decreased from 54.2 to 7.1 at.%), with well-distributed pore-sizes (Fig. 6), where ~ 30-nm-sized ones build the highest fraction. According to Huang et al. [65], the most ideal pore size for providing aqueous electrolyte pools and fast ionic transport channels for supercapacitor electrodes is in the range 2–50 nm. Smaller pores (<2 nm) – smaller than the size of solvated electrolyte ions – do not contribute to energy storage, and larger pores (>50 nm) do not provide a sufficient specific surface. Although the CrN-Ni_{78}* is also very porous (Fig. 4h), the pore size is not nicely distributed. CrN-Ni_{54}* offers the highest area-

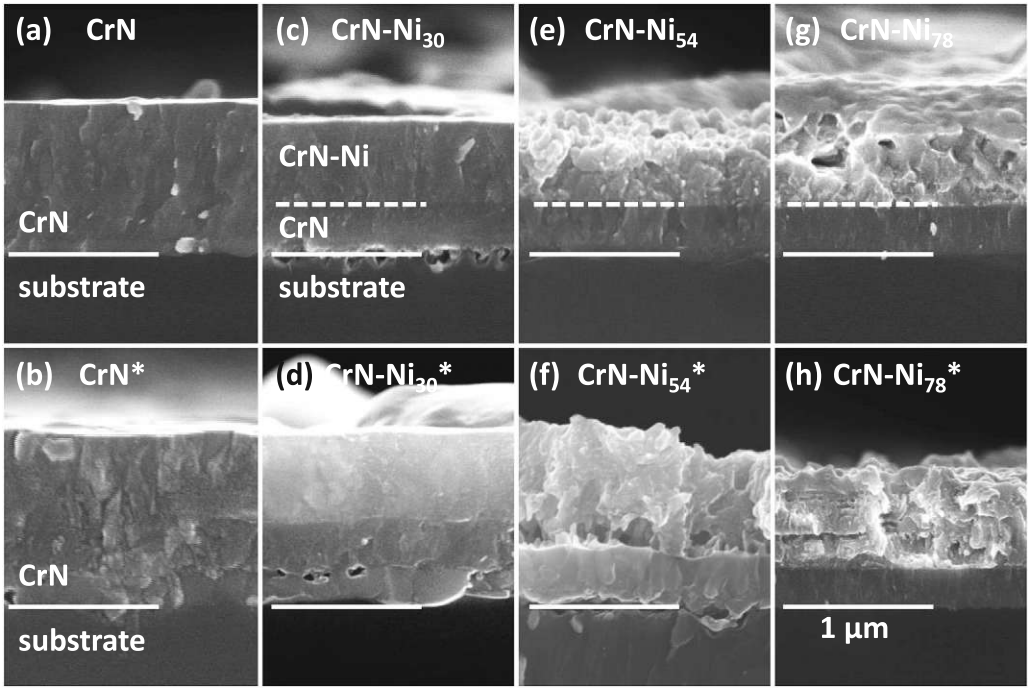

Fig. 5. Fracture cross-sectional SEM images of CrN **(a and b)**, CrN-Ni_{30} **(c and d)**, CrN-Ni_{54} **(e and f)**, and CrN-Ni_{78} **(g and h)** coatings in their as-deposited state and after the 3.0 M HCl treatment to obtain their highest specific capacitance (Fig. 2), respectively. The solid and dashed white horizontal lines have the same length in all SEM images and represent the scale bar of 1 µm. The dashed line indicates the interface between CrN adhesion layer and CrN-Ni coating, the solid line indicates the interface between Si substrate and CrN adhesion layer.

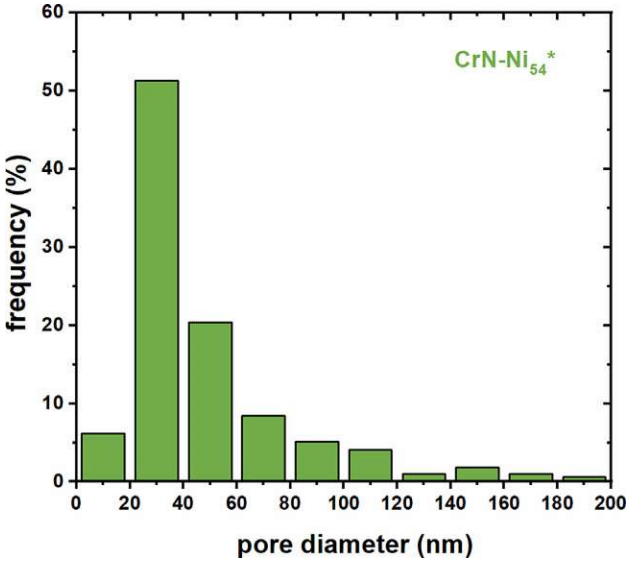

Fig. 6. Pore size distribution (as obtained by digital image processing of Fig. 4f) of the CrN-Ni_{54} after the 3.0 M HCl treatment (CrN-Ni_{54}*) to obtain its highest specific capacitance (Fig. 2).

specific capacitance C_a among all coatings and HCl-treated coatings studied, which is also depicted in Fig. 2.

This most promising sample, CrN-Ni_{54}, was studied in detail by XPS to characterize any changes in their chemical bonding states from the as-deposited state to the HCl-treated state. Before these measurements, their surface was Ar-ion etched to a depth of ~ 50 nm to avoid interference by unwanted surface contaminations. The XPS spectra of the CrN-Ni_{54} coating prior-to and after the HCl treatment are almost identical; therefore, we only briefly concentrate on the N 1 s, Cr 2p, and Ni $2p_{3/2}$ XPS core-level spectra. The N 1 s XPS core-level spectra of CrN-Ni_{54} (Fig. 7a) and CrN-Ni_{54}* (Fig. 7b) are very similar even with their contributions from CrN (binding energy between 396.5 and 397.8 eV [66]) and Cr_2N (binding energies between 397.5 and 398.0 eV). The major contribution comes from CrN, in agreement with XRD studies, which indicated only a tiny fraction of the Cr_2N phase. The Cr $2p_{3/2}$ XPS core-level spectra also suggest the presence of Cr_2O_3 (at 576.1 eV [67]), but also here, the features at 574.8 eV (indicative for CrN [67]) and 576.1 eV (indicative for Cr_2N) are almost identical prior-to and after the HCl treatment, Fig. 7c and d, respectively. A small contribution of Ni–O bonds next to the major metallic Ni (at about 852.8 eV) can also be concluded from the Ni $2p_{3/2}$ XPS core-level spectra of this sample prior-to and after the HCl treatment, Fig. 7e and f, respectively. In excellent agreement with XRD, the XPS studies do not show any Ni–N bonds in these films.

3.2. Electrochemical properties

To demonstrate the merits of the porous structure, we compared the electrochemical performance of our samples (CrN, CrN-Ni_{30}, CrN-Ni_{54}, and CrN-Ni_{78}) in their as-deposited state with that after the HCl treatment providing their C_a peak-values (CrN*, CrN-Ni_{30}*, CrN-Ni_{54}*, and CrN-Ni_{78}*) using a three-electrode system. The CV curves at a scan rate of 100 $mV{\cdot}s^{-1}$ show that the as-deposited samples (Fig. 8a) and the HCl treated samples (Fig. 8b) demonstrate appropriate symmetry, which allows for a good electric double-layer energy storage mechanism. The much more extensive range in current density for the HCl treated samples, the y-axis of Fig. 8b, than that of the as-deposited ones, Fig. 8a, is due to their massively higher C_a values. Similarly, the GCD curves, measured with a current density of 1.0 mA·cm-2, are nearly symmetric. The times for obtaining the discharge-peak also massively increase due to the HCl solution treatment. Please compare Fig. 8c and d, which again demonstrates the significant improvement in specific capacitance.

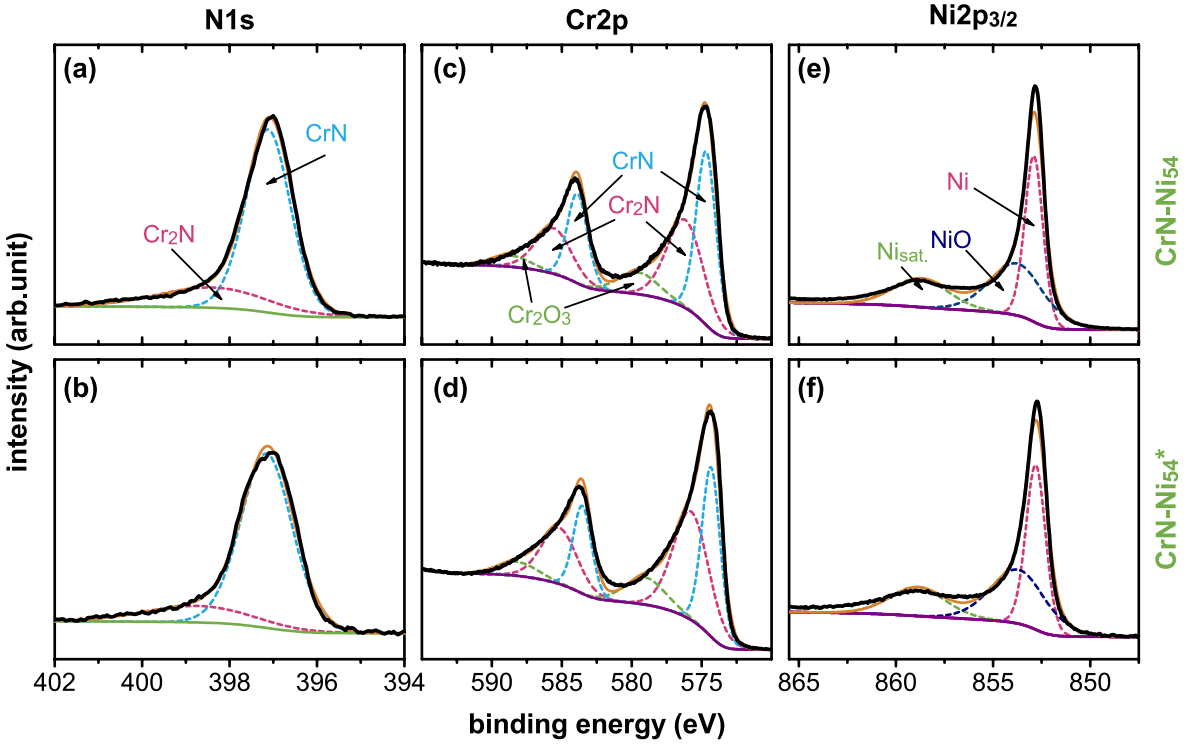

Fig. 7. XPS core-level spectra of **(a and b)** N 1 s, **(c and d)** Cr 2p, and **(e and f)** Ni $2p_{3/2}$ energy regions for the CrN-Ni_{54} coating in its as-deposited state (CrN-Ni_{54}) and after the 3.0 M HCl treatment (CrN-Ni_{54}*) to obtain its highest specific capacitance (Fig. 2), respectively.

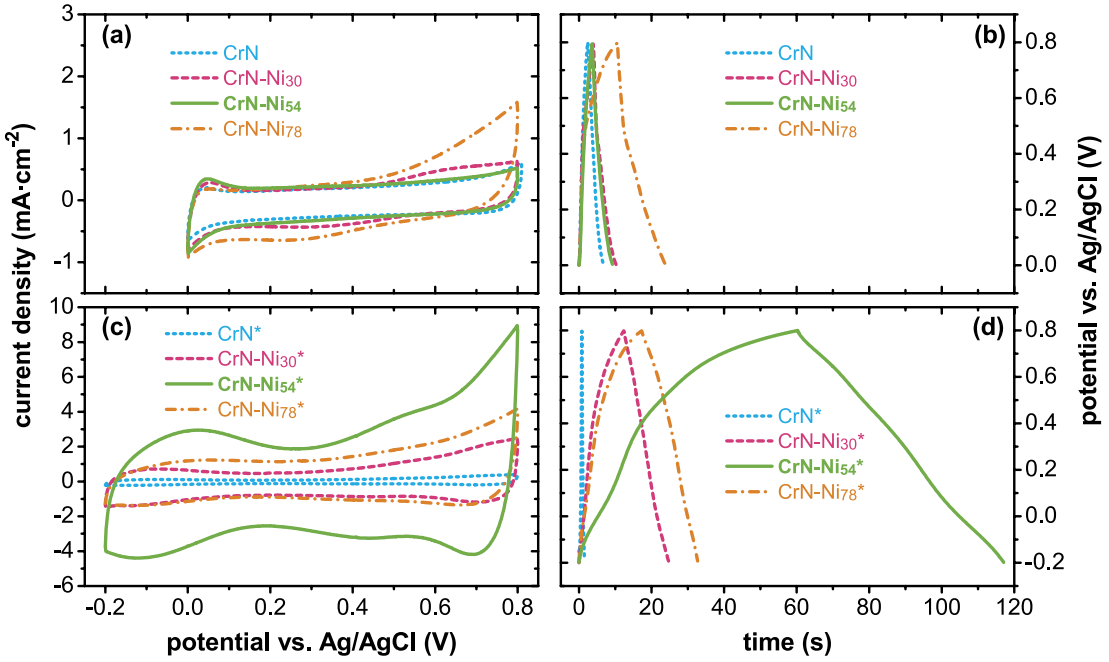

Fig. 8. **(a)** CV curves (scan rate: 100 $mV \cdot s^{-1}$) and **(b)** GCD curves (current density: 1.0 $mA \cdot cm^{-2}$) of CrN, CrN-Ni_{30}, CrN-Ni_{54}, and CrN-Ni_{78} in their as-deposited state. **(c)** CV curves (scan rate: 100 $mV \cdot s^{-1}$) and **(d)** GCD curves (current density: 1.0 $mA \cdot cm^{-2}$) of these coatings after 3.0 M HCl treatment to obtain their highest specific capacitance (CrN*, CrN-Ni_{30}*, CrN-Ni_{54}*, and CrN-Ni_{78}*).

Electrochemical impedance spectroscopy (EIS) was conducted to study the charge transfer and ion diffusion properties of the electrode materials. Fig. 9a and b show the Nyquist plots obtained by these EIS measurements of our samples in their as-deposited state and after the HCl solution treatment leading to their C_a peak-values, respectively. The insets show a detailed view of the high-frequency region, and the equivalent circuit diagram for these EIS measurements is given in Fig. 9c. Just for a brief recall: in such Nyquist plots, Z' and Z'' represent the real and imaginary part of impedance, respectively. At the left side of these diagrams (close to 0 of Z' and Z'', the high-frequency side) a semicircle followed by a straight line indicates capacitive behavior. Their small impe-

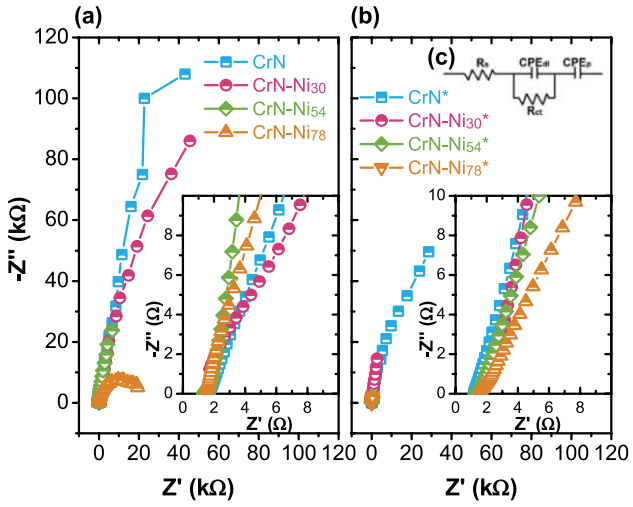

Fig. 9. Nyquist plots of CrN, CrN-Ni_{30}, CrN-Ni_{54}, and CrN-Ni_{78} coatings in their as-deposited state **(a)** and after the 3.0 M HCl treatment to obtain their peak in their specific capacitance **(b)**. **(c)** Equivalent circuit diagram.

dance in the high-frequency region indicates meager charge transfer resistance (R_{ct}), a testament to their intrinsically outstanding electrical conductivity and electrochemical activity [68]. The highest frequency point (the first intersection with the x-axis) refers to the electrolyte resistance (R_s) because, at such high frequencies there is no resistance in capacitance. Therefore, they have similar R_s values, which are 1.2–1.5 Ω due to the resistance of the 0.5 M H_2SO_4 electrolyte [69]. The higher the imaginary part of impedance (hence the steeper the Nyquist curve), the easier the electrolyte can access the surface, and the materials exhibit ideal capacitive behavior [70], which is the case for all of our samples (as-deposited, Fig. 9a, or HCl treated, Fig. 9b) except for the highest Ni-containing coating in its as-deposited state (CrN-Ni_{78}). The HCl-treated samples show a smaller impedance range than the as-deposited ones, suggesting excellent capacitance behavior.

To further investigate the CrN-Ni_{54} thin film electrode's suitability after the 3 h treatment in a 3.0 M HCl solution (CrN-Ni_{54}*) for potential applications, its capacitive behavior is studied by CV curves at different scan rates from 10 to 1000 mV·s^{-1}, see Fig. 10a. Notably, these CV curves show a gradual increase in current density, with quasi-rectangular shapes even up to 1000 mV·s^{-1}, indicating excellent capacitive behavior and high-rate capability. Fig. 10b depicts the CrN-Ni_{54}* electrode's GCD curves at current densities from 0.5 to 10 mA·cm^{-2}. The nearly symmetric potential–time curves for all current densities imply a high charge–discharge Coulombic efficiency (≥97%) and low polarization of this electrode material (supplementary data Fig. S5). With an increase of the current density from 0.5 to 10.0 mA·cm^{-2}, the area-specific capacitance C_a decreases from 62.5 to 42.2 mF·cm^{-2}. This relatively small reduction in C_a by 67.5% during this increase in current density, suggests good reversibility of the electrochemical reaction at the surface of the CrN-Ni_{54}* thin film. Corresponding Coulombic efficiency investigations of CrN-Ni_{30}* and CrN-Ni_{78}* are provided in the supplementary data, Fig. S5. They also depict roughly 100% charge–discharge Coulombic efficiency. The related studies of GCD and CV with different current densities and scan rates for CrN-Ni_{30}* and CrN-Ni_{78}* are provided in the supplementary data, Fig. S6. Compared with another porous CrN thin film, which was obtained by etching away the ~ 19 at% Cu from the CrN–Cu [47], the C_a value of the CrN-Ni_{54}* thin film (with 58.5 mF·cm^{-2} at 1.0 mA·cm^{-2}) is higher than the reported one of 33.1 mF·cm^{-2} (at 1.0 mA·cm^{-2}) for a porous CrN.

The cycling stability of the CrN-Ni_{54}* electrode was proven by 2000 successive CV measurement cycles using a scan rate of 100 mV·s^{-1}. The CV curves of the 1st and 1000th cycle have a similar shape but cover a slightly different area, being unchanged for the subsequent 1000 cycles, Fig. 10c. The capacitance retention, Fig. 10d, clearly shows that the CrN-Ni_{54}* electrode undergoes a more rapid decay down to 91.7% for the first 300 cycles, and after around 600 cycles, a steady-state behavior is obtained. Essentially, there is no change between the 600th and 2000th cycles, during

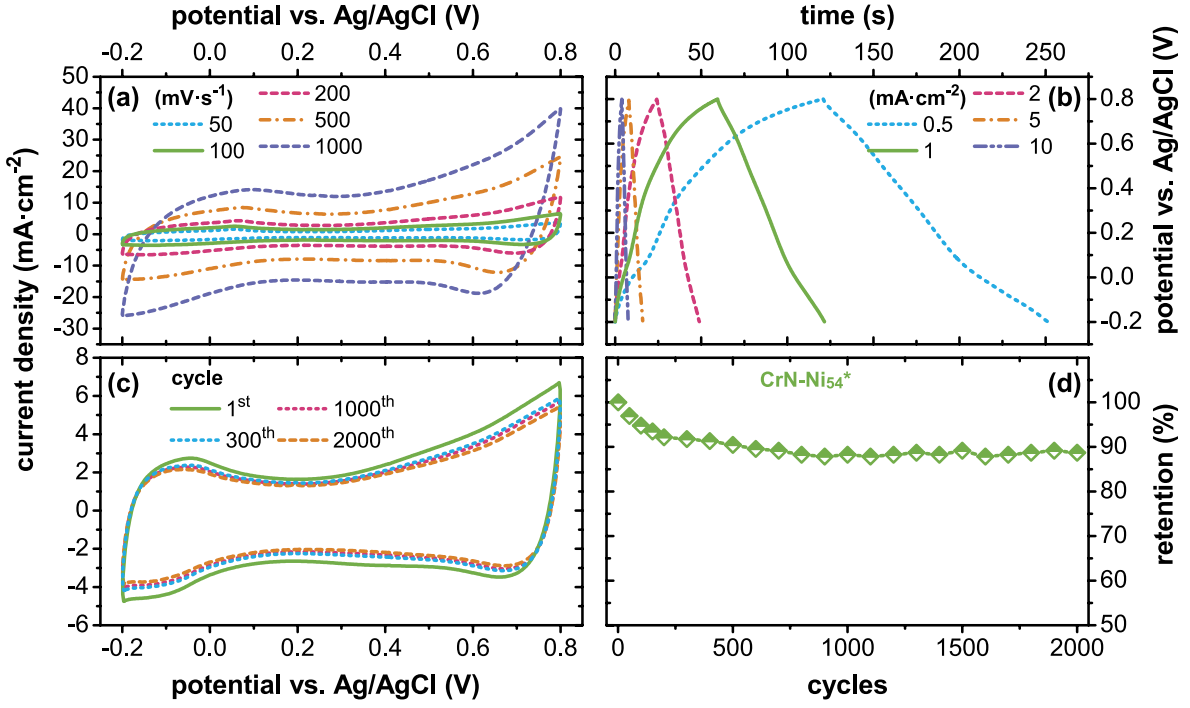

Fig. 10. **(a)** CV curves at different scan rates (in mV·s^{-1}), **(b)** GCD curves at different current densities (at mA·cm^{-2}), **(c)** CV curves of the 1st, 300th, 1000th and 2000th cycle and **(d)** cycling performance at a scan rate of 100 mV·s^{-1}, for the CrN-Ni_{54} coating after the 3 h treatment time in a 3.0 M HCl bath (after which this coating reached its peak area specific capacitance, Fig. 2, due to the formation of a fine porous morphology, Figs. 4 and 5).

which still 88.5 ± 0.5% of the initial capacitance remains. The initial decrease in capacitance comes from the irreversible consumption of the electrode (basically remaining Ni) in the electrolyte. This leaves room to further optimize the pre-treatment procedure. However, the cycling performance is better than that of nitride-based electrodes prepared from nitridation of metal oxides, such as VN@CF (which exhibit 82% capacitance retention after 1000 cycles) [71]. Still, it seems to be slightly less stable than that of other nitride-based electrodes prepared by PVD, such as CrN (92.1% retention after 20,000 cycles) [34], TiVN (99% retention after 10,000 cycles) [72], and CrCuN (94% capacitance retention over 20,000 cycles) [47]. However, our data suggest that after the "running-in" period (for the first 600 cycles), a steady state behavior is obtained during which the area-specific capacitance of the CrN-Ni_{54}* film electrode is unchanged at 88.5 ± 0.5% ($C_a \cong 50.0$ mF·cm^{-2}) of its initial value (58.5 mF·cm^{-2}).

4. Summary and conclusions

We used arc ion plating and a combination of a Cr and $Ni_{80}Cr_{20}$ target to prepare ~ 0.7 μm thin CrN–Ni films with 0, 30.4, 54.2, and 77.6 at.% Ni on top of a ~ 0.3 μm thin CrN adhesion layer. XPS and XRD analyses indicate that the as-deposited CrN–Ni coatings are composed of CrN and metallic Ni phases, without any sign for a Ni–N phase. Post-deposition chemical treatments with HCl solutions of different concentrations and exposure times led to the formation of an interconnected fully percolating pore-network in the Ni-containing parts, as proven by detailed top-view and fracture cross-sectional SEM investigations. Here, specifically, the CrN–Ni film that contained 54.2 at.% Ni in the as-deposited state provided the highest porosity with an average pore size of 30 nm after a 3-h-treatment with 3.0 mol·l^{-1} HCl solution (during which the Ni content decreased to 7.1 at.%).

The electrochemical performance of the HCl-treated CrN–Ni films – benefiting from the porous structure and high specific surface area – was much better than that of the as-deposited CrN and CrN–Ni films. The nanoporous coating that we obtained by the HCl treatment of the 54.2 at.% Ni containing CrN–Ni film, achieved the highest area-specific capacitance of 58.5 mF·cm^{-2} at 1.0 mA·cm^{-2} upon all CrN–Ni films investigated. This value is by a factor of ~ 80 higher than that of the as-deposited CrN and CrN–Ni thin films. Furthermore, this coating also provides an excellent capacitance retention rate. After an initial decay to 88.5 ± 0.5% during the first 600 cycles, a steady-state behavior (with $C_a \cong 50.0$ mF·cm^{-2}) is obtained where the retention rate did not change up to 2000 cycles (highest number of charge–discharge cycles tested here). Based on our results, we can conclude that the combination of transition metal nitrides with Ni and the post-deposition treatment with HCl is very effective in preparing porous transition metal nitrides with a high specific surface area. This allows for the efficient preparation of solid-state thin film supercapacitors.

5. Data Availability

The raw/processed data required to reproduce these findings cannot be shared at this time as the data also are part of an ongoing study.

Declaration of Competing Interest

The authors declare that they have no known competing financial interests or personal relationships that could have appeared to influence the work reported in this paper.

Acknowledgements

This work was supported by the projects of the National Natural Science Foundation of China (Grant No. 51875109), and Natural Science Foundation of Guangdong Province of China (Grant No. 2020A1515010968), and the National Key Research and Development Project of China (Grant No. 2017YFE0125400). ZG thanks the support of the State Scholarship Fund of China (No. 201908440933) during her PhD at TU Wien.

Appendix A. Supplementary material

Supplementary data to this article can be found online at https://doi.org/10.1016/j.matdes.2021.109949.

References

[1] S. Bouhtiyya, R. Lucio Porto, B. Laïk, P. Boulet, F. Capon, J.P. Pereira-Ramos, T. Brousse, J.F. Pierson, Application of sputtered ruthenium nitride thin films as electrode material for energy-storage devices, Scr. Mater. 68 (2013) 659–662, https://doi.org/10.1016/j.scriptamat.2013.01.030.
[2] N.A. Kyeremateng, T. Brousse, D. Pech, Microsupercapacitors as miniaturized energy-storage components for on-chip electronics, Nat. Nanotechnol. 12 (2017) 7–15, https://doi.org/10.1038/nnano.2016.196.
[3] V.S. Bagotsky, A.M. Skundin, Y.M. Volfkovich, Electrochemical Power Sources: Batteries, Fuel Cells, and Supercapacitors (2015).
[4] M. Acerce, D. Voiry, M. Chhowalla, Metallic 1T phase MoS_2 nanosheets as supercapacitor electrode materials, Nat. Nanotechnol. 10 (2015) 313, https://doi.org/10.1038/nnano.2015.40.
[5] Y. Shao, M.F. El-Kady, J. Sun, Y. Li, Q. Zhang, M. Zhu, H. Wang, B. Dunn, R.B. Kaner, Design and mechanisms of asymmetric supercapacitors, Chem. Rev. 118 (2018) 9233–9280, https://doi.org/10.1021/acs.chemrev.8b00252.
[6] B.E. Conway, Electrochemical Supercapacitors: Scientific Fundamentals and Technological Applications, Springer, Boston (1999), https://doi.org/10.1007/978-1-4757-3058-6.
[7] M.S. Balogun, Y. Huang, W. Qiu, H. Yang, H. Ji, Y. Tong, Updates on the development of nanostructured transition metal nitrides for electrochemical energy storage and water splitting, Mater. Today 20 (2017) 425–451, https://doi.org/10.1016/j.mattod.2017.03.019.
[8] T.F. Zhang, Q.X. Xia, Z.X. Wan, J.M. Yun, Q.M. Wang, K.H. Kim, Highly porous carbon nanofoams synthesized from gas-phase plasma for symmetric supercapacitors, Chem. Eng. J. 360 (2019) 1310–1319, https://doi.org/10.1016/j.cej.2018.10.220.
[9] Q. Zhang, X. Wang, Z. Pan, J. Sun, J. Zhao, J. Zhang, C. Zhang, L. Tang, J. Luo, B. Song, Z. Zhang, W. Lu, Q. Li, Y. Zhang, Y. Yao, Wrapping Aligned Carbon Nanotube Composite Sheets around Vanadium Nitride Nanowire Arrays for Asymmetric Coaxial Fiber-Shaped Supercapacitors with Ultrahigh Energy Density, Nano Lett. 17 (2017) 2719–2726, https://doi.org/10.1021/acs.nanolett.7b00854.
[10] W. Raza, F.Z. Ali, N. Raza, Y.W. Luo, K.H. Kim, J.H. Yang, S. Kumar, A. Mehmood, E.E. Kwon, Recent advancements in supercapacitor technology, Nano Energy 52 (2018) 441–473, https://doi.org/10.1016/j.nanoen.2018.08.013.
[11] F. Beguin, V. Presser, A. Balducci, E. Frackowiak, Carbons and electrolytes for advanced supercapacitors, Adv. Mater. 26 (2014) 2219-51, 2283. https://doi.org/10.1002/adma.201304137
[12] K. Karuppasamy, D. Vikraman, J.H. Jeon, S. Ramesh, H.M. Yadav, V.R. Jothi, R. Bose, H.S. Kim, A. Alfantazi, H.S. Kim, Highly porous, hierarchical microglobules of Co3O4 embedded N-doped carbon matrix for high performance asymmetric supercapacitors, Appl. Surf. Sci. 529 (2020), https://doi.org/10.1016/j.apsusc.2020.147147.
[13] T. Xia, Q.H. Wang, W.L. Wu, C.H. Ao, Z. Zheng, C.H. Lu, Z.M. Chen, W. Zhang, Fabrication and characterization of MnO2-Coated carbon fabrics from silk for shape-editable supercapacitors, J. Power Sources 854 (2021), https://doi.org/10.1016/j.jallcom.2020.157289.
[14] A. Ermolieff, M. Girard, C. Raoul, C. Bertrand, T.M. Duc, An XPS comparative study on thermal oxide barrier formation on Nb and NbN thin films, Appl. Surf. Sci. 21 (1985) 65–79, https://doi.org/10.1016/0378-5963(85)90008-X.
[15] N.R. Reddy, M.M. Kumari, M.V. Shankar, K.R. Reddy, S.W. Joo, T.M. Aminabhavi, Photocatalytic hydrogen production from dye contaminated water and electrochemical supercapacitors using carbon nanohorns and TiO2 nanoflower heterogeneous catalysts, J. Environ. Manage. 277 (2021), https://doi.org/10.1016/j.jenvman.2020.111433.
[16] W. Wang, S. Guo, I. Lee, K. Ahmed, J. Zhong, Z. Favors, F. Zaera, M. Ozkan, C.S. Ozkan, Hydrous ruthenium oxide nanoparticles anchored to graphene and carbon nanotube hybrid foam for supercapacitors, Sci. Rep. 4 (2014) 4452–4452. http://doi.org/10.1038/srep04452.
[17] C. Sengottaiyan, R. Jayavel, R.G. Shrestha, T. Subramani, S. Maji, J.H. Kim, J.P. Hill, K. Ariga, L.K. Shrestha, Indium Oxide/Carbon Nanotube/Reduced Graphene Oxide Ternary Nanocomposite with Enhanced Electrochemical Supercapacitance, B. Chem. Soc. Jpn. 92 (2018) 521–528, https://doi.org/10.1246/bcsj.20180338.

[18] J.H. Sung, J.H. Park, D.S. Jeon, D. Kim, M.J. Yu, A.C. Khot, T.D. Dongale, T.G. Kim, Retention enhancement through capacitance-dependent voltage division analysis in 3D stackable TaOx/HfO2-based selectorless memristor, Mater. Des. 207 (2021), https://doi.org/10.1016/j.matdes.2021.109845 109845.
[19] Y. Wei, N. Zhang, C. Jin, J. Shen, J. Xie, Z. Dai, L. Hu, Y. Zeng, Z. Jian, A Bi1/2K1/2TiO3-based ergodic relaxor ceramic for temperature-stable energy storage applications, Mater. Des. 207 (2021), https://doi.org/10.1016/j.matdes.2021.109887 109887.
[20] W.R. Cai, R.K. Kankala, M.T. Xiao, N. Zhang, X.Q. Zhang, Three-dimensional hollow N-doped ZIF-8-derived carbon@MnO2 composites for supercapacitors, Appl. Surf. Sci. 528 (2020), https://doi.org/10.1016/j.apsusc.2020.146921.
[21] Y. Ding, Y.C. Li, Y.J. Dai, X.H. Han, B. Xing, L.J. Zhu, K.Z. Qiu, S.R. Wang, A novel approach for preparing in-situ nitrogen doped carbon via pyrolysis of bean pulp for supercapacitors, Energy 216 (2021), https://doi.org/10.1016/j.energy.2020.119227.
[22] Y. Liang, Y.H. Lu, G.Y. Xiao, J.H. Zhang, H.J. Chi, Y. Dong, Hierarchical porous nitrogen-doped carbon microspheres after thermal rearrangement as high performance electrode materials for supercapacitors, Appl. Surf. Sci. 529 (2020), https://doi.org/10.1016/j.apsusc.2020.147141.
[23] J.H. Zhang, H. Chen, J.B. Bai, M. Xu, C.L. Luo, L.X. Yang, L.J. Bai, D.L. Wei, W.X. Wang, H.W. Yang, N-doped hierarchically porous carbon derived from grape marcs for high-performance supercapacitors, J. Power Sources 854 (2021), https://doi.org/10.1016/j.jallcom.2020.157207.
[24] Z.H. Pan, X.H. Ji, Facile synthesis of nitrogen and oxygen co-doped C@Ti3C2 MXene for high performance symmetric supercapacitors, J. Power Sources 439 (2019), https://doi.org/10.1016/j.jpowsour.2019.227068.
[25] S.Q. Wu, D.H. Wei, Y.B. Yin, Q.Q. Li, H.S. Wang, W.T. Chen, Y.F. Jiang, X.Q. Tao, N, S co-doped activated carbon with porous architecture derived from partial poly (2, 2 '-dithiodianiline) for supercapacitors, J. Energy Storage 33 (2021), https://doi.org/10.1016/j.est.2020.102043.
[26] G.F. Zheng, Z.C. Huang, Z. Liu, Cooperative utilization of beet pulp and industrial waste fly ash to produce N/P/O self-co-doped hierarchically porous carbons for high-performance supercapacitors, J. Power Sources 482 (2021), https://doi.org/10.1016/j.jpowsour.2020.228935.
[27] Y. Feng, S. Chen, J. Wang, B. Lu, Carbon foam with microporous structure for high performance symmetric potassium dual-ion capacitor, J. Energy Chem. 43 (2020) 129–138, https://doi.org/10.1016/j.jechem.2019.08.013.
[28] X.H. Xia, Y.Q. Zhang, D.L. Chao, Q.Q. Xiong, Z.X. Fan, X.L. Tong, J.P. Tu, H. Zhang, H.J. Fan, Tubular TiC fibre nanostructures as supercapacitor electrode materials with stable cycling life and wide-temperature performance, Energy Environ. Sci. 8 (2015) 1559–1568, https://doi.org/10.1039/c5ee00339c.
[29] J. Feng, X. Sun, C.Z. Wu, L.L. Peng, C.W. Lin, S.L. Hu, J.L. Yang, Y. Xie, Metallic Few-Layered VS2 Ultrathin Nanosheets: High Two-Dimensional Conductivity for In-Plane Supercapacitors, J. Am. Chem. Soc. 133 (2011) 17832–17838, https://doi.org/10.1021/ja207176c.
[30] B. Wei, H. Liang, D. Zhang, Z. Qi, H. Shen, Z. Wang, Magnetron sputtered TiN thin films toward enhanced performance supercapacitor electrodes, Mater. Renew. Sustain. Energy 7 (2018) 11, https://doi.org/10.1007/s40243-018-0117-9.
[31] C.N.R. Rao, K. Pramoda, Borocarbonitrides, BxCyNz, 2D Nanocomposites with Novel Properties, B. Chem. Soc. Jpn. 92 (2019) 441–468, https://doi.org/10.1246/bcsj.20180335.
[32] J. Shi, B.L. Jiang, C. Li, F.Y. Yan, D. Wang, C. Yang, J.J. Wan, Review of Transition Metal Nitrides and Transition Metal Nitrides/Carbon nanocomposites for supercapacitor electrodes, Mater. Chem. Phys. 245 (2020), https://doi.org/10.1016/j.matchemphys.2019.122533.
[33] Z. Qi, B. Wei, J. Wang, Y. Yang, Z. Wang, Nanostructured porous CrN thin films by oblique angle magnetron sputtering for symmetric supercapacitors, J. Power Sources 806 (2019) 953–959, https://doi.org/10.1016/j.jallcom.2019.07.325.
[34] B. Wei, H. Liang, D. Zhang, Z. Wu, Z. Qi, Z. Wang, CrN thin films prepared by reactive DC magnetron sputtering for symmetric supercapacitors, J. Mater. Chem. A 5 (2017) 2844–2851, https://doi.org/10.1039/c6ta09985h.
[35] E. Haye, A. Achour, A. Guerra, F. Moulaï, T. Hadjersi, R. Boukherroub, A. Panepinto, T. Brousse, J.-J. Pireaux, S. Lucas, Achieving on chip micro-supercapacitors based on CrN deposited by bipolar magnetron sputtering at glancing angle, Electrochim. Acta 324 (2019), https://doi.org/10.1016/j.electacta.2019.134890 134890.
[36] A. Achour, R.L. Porto, M.-A. Soussou, M. Islam, M. Boujtita, K.A. Aissa, L. Le Brizoual, A. Djouadi, T. Brousse, Titanium nitride films for micro-supercapacitors: Effect of surface chemistry and film morphology on the capacitance, J. Power Sources 300 (2015) 525–532, https://doi.org/10.1016/j.jpowsour.2015.09.012.
[37] X. Lu, G. Wang, T. Zhai, M. Yu, S. Xie, Y. Ling, C. Liang, Y. Tong, Y. Li, Stabilized TiN Nanowire Arrays for High-Performance and Flexible Supercapacitors, Nano Lett. 12 (2012) 5376–5381, https://doi.org/10.1021/nl302761z.
[38] R. Lucio-Porto, S. Bouhtiyya, J.F. Pierson, A. Morel, F. Capon, P. Boulet, T. Brousse, VN thin films as electrode materials for electrochemical capacitors, Electrochim. Acta 141 (2014) 203–211, https://doi.org/10.1016/j.electacta.2014.07.056.
[39] K. Robert, C. Douard, A. Demortière, F. Blanchard, P. Roussel, T. Brousse, C. Lethien, On Chip Interdigitated Micro-Supercapacitors Based on Sputtered Bifunctional Vanadium Nitride Thin Films with Finely Tuned Inter- and Intracolumnar Porosities, Adv. Mater. Technol. 3 (2018) 1800036, https://doi.org/10.1002/admt.201800036.
[40] G. Ma, Z. Wang, B. Gao, T. Ding, Q. Zhong, X. Peng, J. Su, B. Hu, L. Yuan, P.K. Chu, J. Zhou, K. Huo, Multilayered paper-like electrodes composed of alternating stacked mesoporous Mo2N nanobelts and reduced graphene oxide for flexible all-solid-state supercapacitors, J. Mater. Chem. A 3 (2015) 14617–14624, https://doi.org/10.1039/C5TA02851E.
[41] L. Chen, C. Liu, Z. Zhang, Novel (111) oriented γ-Mo_2N thin films deposited by magnetron sputtering as an anode for aqueous micro-supercapacitors, Electrochim. Acta 245 (2017) 237–248, https://doi.org/10.1016/j.electacta.2017.05.102.
[42] F.F. Klimashin, H. Euchner, P.H. Mayrhofer, Computational and experimental studies on structure and mechanical properties of Mo-Al-N, Acta Mater. 107 (2016) 273–278, https://doi.org/10.1016/j.actamat.2016.01.063.
[43] B.B. Wei, F.W. Ming, H.F. Liang, Z.B. Qi, W.S. Hu, Z.C. Wang, All nitride asymmetric supercapacitors of niobium titanium nitride-vanadium nitride, J. Power Sources 481 (2021), https://doi.org/10.1016/j.jpowsour.2020.228842.
[44] B. Peng, H.Q. Li, Q. Zhang, Y.X. Xu, T.F. Wei, Q.M. Wang, F.G. Zhang, K.H. Kim, High-temperature thermal stability and oxidation resistance of Cr and Ta co-alloyed Ti - Al - N coatings deposited by cathodic arc evaporation, Corrosion Science 167 (2020), https://doi.org/10.1016/j.corsci.2020.108490.
[45] O. Ostrovskaya, C. Badini, S.M. Deambrosis, E. Miorin, S. Biamino, E. Padovano, Protection from oxidation of second and third generation TiAl intermetallic alloys by magnetron sputtering deposition of a TiAl/TiAlN coating, Mater. Des. 208 (2021), https://doi.org/10.1016/j.matdes.2021.109905 109905.
[46] Z. Gao, Z. Wu, S. Zhao, T. Zhang, Q. Wang, Enhanced capacitive property of HfN film electrode by plasma etching for supercapacitors, Materials Letters 235 (2019) 148–152, https://doi.org/10.1016/j.matlet.2018.10.032.
[47] B. Wei, G. Mei, H. Liang, Z. Qi, D. Zhang, H. Shen, Z. Wang, Porous CrN thin films by selectively etching CrCuN for symmetric supercapacitors, J. Power Sources 385 (2018) 39–44, https://doi.org/10.1016/j.jpowsour.2018.03.023.
[48] Y.J. Kim, T.J. Byun, H.Y. Lee, J.G. Han, Effect of bilayer period on CrN/Cu nanoscale multilayer thin films, Surf. Coat. Technol. 202 (2008) 5508–5511, https://doi.org/10.1016/j.surfcoat.2008.06.028.
[49] J. Musil, P. Zeman, H. Hruby, P.H. Mayrhofer, ZrN/Cu nanocomposite film - a novel superhard material, Surf. Coat. Technol. 120 (1999) 179–183, https://doi.org/10.1016/S0257-8972(99)00482-X.
[50] P. Zeman, R. Cerstvy, P.H. Mayrhofer, C. Mitterer, J. Musil, Structure and properties of hard and superhard Zr-Cu-N nanocomposite coatings, Mater. Sci. Eng. Struct. Mater. Properties Microstruct. Process. 289 (2000) 189–197, https://doi.org/10.1016/s0921-5093(00)00917-5.
[51] J. Musil, H. Hruby, P. Zeman, H. Zeman, R. Cerstvy, P.H. Mayrhofer, C. Mitterer, Hard and superhard nanocomposite Al-Cu-N films prepared by magnetron sputtering, Surf. Coat. Technol. 142 (2001) 603–609, https://doi.org/10.1016/S0257-8972(01)01200-2.
[52] H. Zeman, J. Musil, J. Vlcek, P.H. Mayrhofer, C. Mitterer, Thermal annealing of sputtered Al-Si-Cu-N films, Vacuum 72 (2003) 21–28, https://doi.org/10.1016/S0042-207x(03)00094-0.
[53] A. Akbari, C. Templier, M.F. Beaufort, D. Eyidi, J.P. Riviere, Ion beam assisted deposition of TiN–Ni nanocomposite coatings, Surf. Coat. Technol. 206 (2011) 972–975, https://doi.org/10.1016/j.surfcoat.2011.03.102.
[54] Z.R. Liu, Y.X. Xu, B. Peng, W. Wei, L. Chen, Q.M. Wang, Structure and property optimization of Ni-containing AlCrSiN coatings by nano-multilayer construction, J. Power Sources 808 (2019), https://doi.org/10.1016/j.jallcom.2019.07.342.
[55] A.V. Chernogor, F.F. Klimashin, A.O. Volkhonskii, I.V. Blinkov, P.H. Mayrhofer, The impact of Ni and Mo on growth-morphology and mechanical properties of arc evaporated Ti-Cr-N hard coatings, Surf. Coat. Technol. 377 (2019), https://doi.org/10.1016/j.surfcoat.2019.124917.
[56] C. Hu, Y.X. Xu, L. Chen, F. Pei, Y. Du, Mechanical properties, thermal stability and oxidation resistance of Ta-doped CrAlN coatings, Surf. Coat. Technol. 368 (2019) 25–32, https://doi.org/10.1016/j.surfcoat.2019.04.026.
[57] S. Calderon Velasco, A. Cavaleiro, S. Carvalho, Functional properties of ceramic-Ag nanocomposite coatings produced by magnetron sputtering, Prog. Mater. Sci. 84 (2016) 158–191, https://doi.org/10.1016/j.pmatsci.2016.09.005.
[58] S.M. Aouadi, D.P. Singh, D.S. Stone, K. Polychronopoulou, F. Nahif, C. Rebholz, C. Muratore, A.A. Voevodin, Adaptive VN/Ag nanocomposite coatings with lubricious behavior from 25 to 1000°C, Acta Mater. 58 (2010) 5326–5331, https://doi.org/10.1016/j.actamat.2010.06.006.
[59] H. Li, C. Zhang, C. Liu, M. Huang, Improvement in corrosion resistance of CrN coatings, Surf. Coat. Technol. (2018), https://doi.org/10.1016/j.surfcoat.2018.07.018.
[60] P.H. Mayrhofer, G. Tischler, C. Mitterer, Microstructure and mechanical/thermal properties of Cr–N coatings deposited by reactive unbalanced magnetron sputtering, Surf. Coat. Technol. 142–144 (2001) 78–84, https://doi.org/10.1016/S0257-8972(01)01090-8.
[61] J.-Z. Kong, C. Li, X.-Y. Sun, Y. Xuan, H.-F. Zhai, A.-D. Li, Q.-Z. Wang, F. Zhou, Improved tribological properties and corrosion protection of CrN coating by ultrathin composite oxide interlayer, Appl. Surf. Sci. 541 (2021), https://doi.org/10.1016/j.apsusc.2020.148606 148606.
[62] P.H. Mayrhofer, H. Willmann, C. Mitterer, Oxidation kinetics of sputtered Cr-N hard coatings, Surf. Coat. Technol. 146 (2001) 222–228, https://doi.org/10.1016/s0257-8972(01)01471-2.
[63] J. Jin, D. Zheng, S. Han, J. Ma, Z. Zhu, Effect of Ni content on the electrical and corrosion properties of CrNiN coating in simulated proton exchange membrane fuel cell, Int. J. Hydrogen. Energ 42 (2017) 1142–1153, https://doi.org/10.1016/j.ijhydene.2016.11.007.

[64] A. Ruden, E. Restrepo-Parra, A.U. Paladines, F. Sequeda, Corrosion resistance of CrN thin films produced by dc magnetron sputtering, Appl. Surf. Sci. 270 (2013) 150–156, https://doi.org/10.1016/j.apsusc.2012.12.148.
[65] J. Huang, B.G. Sumpter, V. Meunier, A Universal Model for Nanoporous Carbon Supercapacitors Applicable to Diverse Pore Regimes, Carbon Materials, and Electrolytes,, Chem. AEuropean J. 14 (2008) 6614–6626, https://doi.org/10.1002/chem.200800639.
[66] P.C. Wo, P.R. Munroe, Z.-T. Jiang, Z. Zhou, K.Y. Li, Z. Xie, Enhancing toughness of CrN coatings by Ni addition for safety-critical applications, Mater. Sci. Eng. A 596 (2014) 264–274, https://doi.org/10.1016/j.msea.2013.12.064.
[67] W.L. Cheng, Z.F. Zhou, P.W. Shum, K.Y. Li, Effect of Ni addition on the structure and properties of Cr–Ni–N coatings deposited by closed-field unbalanced magnetron sputtering ion plating, Surf. Coat. Technol. 229 (2013) 84–89, https://doi.org/10.1016/j.surfcoat.2012.12.032.
[68] H. Cui, G. Zhu, X. Liu, F. Liu, Y. Xie, C. Yang, T. Lin, H. Gu, F. Huang, Niobium nitride Nb_4N_5 as a new high-performance electrode material for supercapacitors, Adv. Sci. 2 (2015) 1500126, https://doi.org/10.1002/advs.201500126.
[69] L. Wang, H. Ji, S. Wang, L. Kong, X. Jiang, G. Yang, Preparation of Fe_3O_4 with high specific surface area and improved capacitance as a supercapacitor, Nanoscale 5 (2013) 3793–3799, https://doi.org/10.1039/C3NR00256J.
[70] Y. Xie, D. Wang, Supercapacitance performance of polypyrrole/titanium nitride/polyaniline coaxial nanotube hybrid, J. Power Sources 665 (2016) 323–332, https://doi.org/10.1016/j.jallcom.2016.01.089.
[71] Y. Wang, M. Jiang, Y. Yang, F. Ran, Hybrid electrode material of vanadium nitride and carbon fiber with cigarette butt/metal ions wastes as the precursor for supercapacitors, Electrochimica Acta 222 (2016) 1914–1921, https://doi.org/10.1016/j.electacta.2016.12.003.
[72] A. Achour, M. Chaker, H. Achour, A. Arman, M. Islam, M. Mardani, M. Boujtita, L. Le Brizoual, M.A. Djouadi, T. Brousse, Role of nitrogen doping at the surface of titanium nitride thin films towards capacitive charge storage enhancement, J. Power Sources 359 (2017) 349–354, https://doi.org/10.1016/j.jpowsour.2017.05.074.

Nanostructured zig-zag γ-Mo_2N thin films produced by glancing angle deposition for flexible symmetrical solid-state supercapacitors

Zecui Gao[a,b,*], Tengfei Zhang[a,*], Qimin Wang[a,c,*], Paul Heinz Mayrhofer[b]

[a] School of Electromechanical Engineering, Guangdong University of Technology, 510006, Guangzhou, China

[b] Institute of Materials Science and Technology, Technische Universität Wien, Getreidemarkt 9, 1060, Vienna, Austria

[c] Key Laboratory of Green Fabrication and Surface Technology of Advanced Metal Materials, Ministry of Education, Anhui University of Technology, 243000, Anhui Maanshan, PR China

*Correspondence: zecui.gao@tuwien.ac.at; tfzhang@gdut.edu.cn; qmwang@gdut.edu.cn

Abstract:

The performance of electrochemical capacitors strongly depends on their accessible surface area, chemical stability, and electrical conductivity. Simple columnar and zig-zag γ-Mo_2N thin-film electrodes were prepared by magnetron sputtering. The latter is obtained by glancing angle deposition (GLAD), which is known for open porous structures due to the ballistic shadowing effect. As intended, the zig-zag structured γ-Mo_2N electrode presents an outstanding area capacitance of 248 mF/cm^2 at a scan speed of 50 mV/s, which is 4 times higher than that of the simple columnar one. Both of them exhibit excellent cycling stability of 95% over 20,000 cycles (at 200 mV/s). The symmetrical solid-state supercapacitor prepared with the zig-zag structured γ-Mo_2N thin film delivers an excellent power density of 107.1 W/cm^3 at 33.8 mWh/cm^3, and its volumetric capacitance is ~3.5 times higher than the simple columnar structured γ-Mo_2N device. Bending tests of such solid-state γ-Mo_2N supercapacitors proved their mechanical flexibility to a bending angel of even 107°. Based on these studies we can conclude that the highly porous zig-zag structured γ-Mo_2N-based electrodes prepared by GLAD combine outstanding electrochemical energy storage capabilities with excellent mechanical flexibility.

Keywords: γ-Mo_2N films; Glancing angle deposition; Flexible symmetric supercapacitor; Solid-state electrolyte

1. Introduction

Used as energy storage devices, supercapacitors (SCs) have the merits of high-power density, fast charge and discharge, long service life and safety [1, 2]. Furthermore, they provide repairability [3], stretchability [4], and wearability [5], enabling them to meet the increasing requirements of commercial applications in flexible electronics. The energy storage properties of SCs are determined mainly by their composition and properties of the electrode materials, like porosity, wettability, conductivity, stability and redox properties. According to the charge storage mechanism, one of the main kind of electrochemical capacitors (ECs) are electrostatic double-layer capacitors (EDLCs), which, close to traditional capacitors, achieve the electrostatic storage of the electrical energy by separation of charge in a Helmholtz double layer at the interface between the surface of a conductive electrode and an electrolyte [4, 6, 7]. The most common examples are carbon-based materials, including carbon nanotubes [8] and graphene [9]. The other kind of ECs are pseudocapacitors, which, more like batteries, electrochemically store electrical energy by Faraday electron charge transfer with redox reactions, intercalation, or electro-sorption. Common examples are transition metal oxides [10], conducting polymers [11, 12], and composite electrodes (such as vanadium nitride @ carbon nanobelts [13]). Since the amount of charge stored per unit voltage in a supercapacitor is predominantly attributed to multiple faradaic and non-faradaic reactions occurring at or near the electrode surface, the electrodes are typically as porous as possible (e.g., nanofiber structures)[14, 15].

Recently, transition metal nitride (TMN) thin films (such as TiN [16], CrN [17-19], VN [20], HfN [21], and Mo_2N [12, 22]) have attracted attention for SCs. The interest in these

compounds is due to their excellent conductivity, high temperature and chemical stability, and high corrosion resistance, enabling a fast charge transfer and long-term service life of SC devices. Especially, the TMNs fabricated by physical vapour deposition (PVD), the most versatile and mature technology for TMNs, are famous for their high crystallinity, purity, and uniformity, as well as excellent substrate adhesion. Typically, the PVD process of TMNs was optimized to allow for dense growth morphologies, as these are needed prerequisites for improved diffusion barrier abilities, corrosion, mechanical and thermal stability, and superior mechanical strength [23]. However, for the application as SC materials, the TMN's should be very porous and rough [24], which can partly be obtained by limiting the adatom diffusion through lower deposition temperatures and higher deposition pressures [22]. Further possibilities to increase the porosity of TMNs are via a high-energetic Kr or Ar ion etching process (as shown for HfN [21]), or by selective leaching of a phase from the coating (as shown for CrN-Ni [25]). Another technique for preparing highly porous structures is glancing angle deposition (GLAD) in which the oblique angle of incidence flux during magnetron sputtering results in atomic shadowing effects [26, 27]. Thereby, porous growth morphologies with single-tilted pillars or zig-zag tilted ones (when alternating the angle of incidence) are conveniently accessible. These unique morphologies lead to special mechanical, magnetic, and optical characteristics [28-30]. Here, we used GLAD to develop highly porous zig-zag tilted nanostructured γ-Mo_2N electrodes (shortly referred to as zig-zag) and compared them with simple columnar structured γ-Mo_2N electrodes (prepared by conventional magnetron sputtering).

Previous reports have highlighted the outstanding catalytic and electrical properties of γ-Mo_2N owing to its large specific surface area, rich intercalation chemistry, excellent chemical and thermal stability, and intrinsically high electrical and ionic conductivity [22, 31-34]. In this work, we further amplify its charge storage capacity by systematically studying the electrochemical properties of the zig-zag γ-Mo_2N single electrode and its behavior in a flexible symmetric solid-state supercapacitor device. As envisioned, the zig-zag γ-Mo_2N electrode presents a 4 times higher specific capacitance than the simple columnar γ-Mo_2N electrode, without sacrificing long-term service life. Moreover, zig-zag symmetrical solid-state γ-Mo_2N supercapacitors also display outstanding volumetric capacitance, energy density and power density, and excellent mechanical flexibility.

2. Materials and methodology

2.1 Thin film deposition

Columnar γ-Mo_2N thin films were fabricated by sputtering a Mo target (99.99% purity) in a mixed Ar/N_2 atmosphere utilizing a custom-built multifunctional physical vapor deposition instrument. The substrate materials were 100-oriented Si platelets (10 × 15 × 0.5 mm^3) and Ni foil (99.99% purity), which were ultrasonically cleaned in acetone and ethanol for 30 min each. After reaching a base pressure below 5 × 10^{-3} Pa, an ion-assisted etching process was carried out in an Ar atmosphere with bias voltage of −600 V for 30 min to remove surface contaminants. The deposition time for the 2,800-nm-thin columnar film was 3h, while rotating the holder at 1.5 rpm (see the schematic, Fig. 1a). The zig-zag tilted microstructure was obtained by alternatingly tilting the sample holder between +36 and −36° (see the schematic, Fig. 1b). Thereby, we prepared a zig-zag coating with six stacks (three at +36° and three at −36°) – each for a deposition time of

30 min, resulting in ~467-nm-thin tilted stacks. Both, the columnar and the zig-zag films were deposited with a discharge power of 2.0 kW, an Ar to N_2 flow rate ratio of 5:1, and a pressure of 0.7 Pa. The chamber temperature was kept constant at 250°C and the bias potential was set at −100 V.

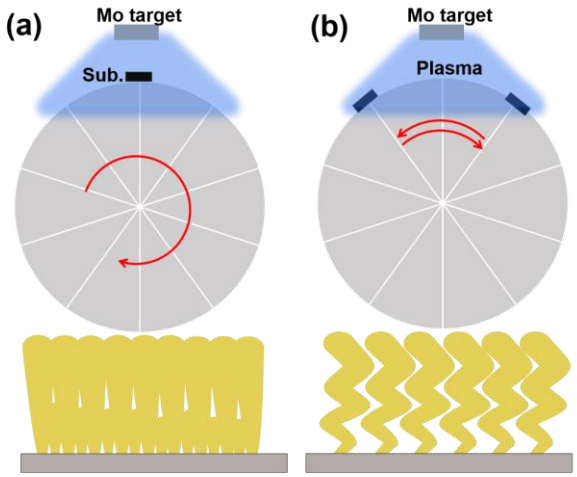

Figure 1. Schematic sketch of the deposition procedure for (a) columnar and (b) zig-zag γ-Mo_2N films, using continuous rotation and alternating movement in front of the target (leading to a glancing angle deposition), respectively.

2.2 Material Characterization

Scanning electron microscopy (SEM, FEI Nova NanoSEM 430) was used to investigate the surface and cross-sectional morphologies of the columnar and zig-zag γ-Mo_2N films, at an accelerating voltage of 10 kV. At the same time, the integrated energy dispersive X-ray spectroscopy (EDX, Oxford instruments X-Max^N) system attached to the SEM, was used to detect their chemical compositions. X-ray diffraction (XRD, Bruker D8 Advance diffractometer) using a Cu Kα X-ray source (40 kV, 40 mA) in Bragg-Brentano configuration, was employed to examine the crystal structure of the films.

2.3. Electrochemical measurements

The electrochemical measurements presented in this work, including cyclic voltammetry (CV), galvanostatic charge-discharge (GCD), and electrochemical impedance spectroscopy (EIS), were systematically conducted on an electrochemical workstation (CHI660E, Shanghai Chenhua Corp.), in a 0.5 M H_2SO_4 aqueous electrolyte. For the straight columnar and the zig-zag γ-Mo_2N film electrodes, the electrochemical performance was evaluated using a conventional 3-electrode setup: the samples with a working area of 0.5 cm^2 as the working electrodes, an Ag/AgCl (sat. KCl) electrode as the reference electrode, and a Pt plate (20 × 20 × 0.5 mm^3) as the counter electrode. CV measurements were performed under 50–1,000 mV/s, and GCD measurements were carried out at current densities of 1–10 mA/cm^2, with an open window potential of −0.2 to +0.2 V. EIS offers Bode and Nyquist plots, which can distinguish between pseudocapacitive, surface-controlled capacitive, and diffusion-limited faradaic mechanisms. EIS measurements were performed at frequencies range from 0.01 Hz to 100 kHz, at a potential perturbation of 5 mV.

For the symmetric flexible solid-state supercapacitor device (SSC), electrochemical properties were characterized in a two-electrode cell. 4 g PVA powder (alcoholysis degree: 99.4%, Aladdin Chemicals) was put into 40 ml of 0.5 M H_2SO_4 solution (98%, Analytical grade), and slowly and continuously stirred at 85°C for 2 hours, until a transparent jelly-like solution was obtained. Two identical pieces of γ-Mo_2N films with a working area of 2.0 cm^2 (on Ni foil substrates) and a separator paper were soaked in the gel electrolyte for 30 min, and then dried under the ambient conditions for 10 min. After that, we sandwiched the separator paper with the two identical electrodes, and packaged them with a vacuum packaging machine to form a flexible symmetrical SSC

device. The flexibility was tested by bonding the SSC devices on the surfaces of laboratory measuring cylinders with sizes of 100, 50 and 10 ml. Therefore, the bending angles are ~57, 66, and 107°, respectively, while the non-bonded device with an effective bonding angle of 0° acted as a reference.

2.4 Calculation

For the single electrodes, the area-specific capacitance (C_a, mF/cm^2) can be calculated based on the CV and GCD curves using the following equations [35], respectively:

$$C_a = {\int I(U)dU}/{[2 \times v \times s \times \Delta U)]}, \quad (1)$$

$$C_a = {I \times \Delta t}/{(s \times \Delta U)}, \quad (2)$$

where $\int IdU$ is the integrated area of a CV curve, at a certain potential sweep rate of v (mV/s), potential window ΔU (V), and electrode surface area s (cm^2). I (mA) and Δt (s) are the discharge current and time in a GCD curve, respectively.

For the symmetric solid-state supercapacitor device, cell-volumetric capacitance (C_{cell}, mF/cm^3) was derived also from both CV and GCD curves using the following equations, respectively:

$$C_{cell} = {\int I(U)dU}/{[2 \times v \times V \times \Delta U)]}, \quad (3)$$

$$C_{cell} = {(I \times \Delta t)}/{(V \times \Delta U)}. \quad (4)$$

The relative energy density (E, mWh/cm^3) and power density (P, W/cm^3) were calculated based on the following equations:

$$\mathrm{E} = {C_{cell} \times \Delta U^2}/{2 \times 3.6}, \quad (5)$$

$$P = {3.6 \times E}/{\Delta t'} \quad (6)$$

where V (cm^3) represents the total volume of the two electrodes in a device.

3. Results and discussion

3.1 Structural characterization

Cross-sectional SEM investigations of the samples prepared with a continuous substrate holder rotation, Fig. 2a, and with alternatingly reverting the sample holder between +36 and −36°, Fig. 2b, prove their intended straight respectively zig-zag tilted columnar structures. Both samples are ~2.8 µm thick and the zig-zag comprises six alternating stacks of ~467 nm each. The more detailed view into the zig-zag morphology, inset of Fig. 2b, clearly shows the separated and rough zig-zag pillars resulting from limited atomic reassembly kinetics and line-of-sight shadowing effects during GLAD [36].

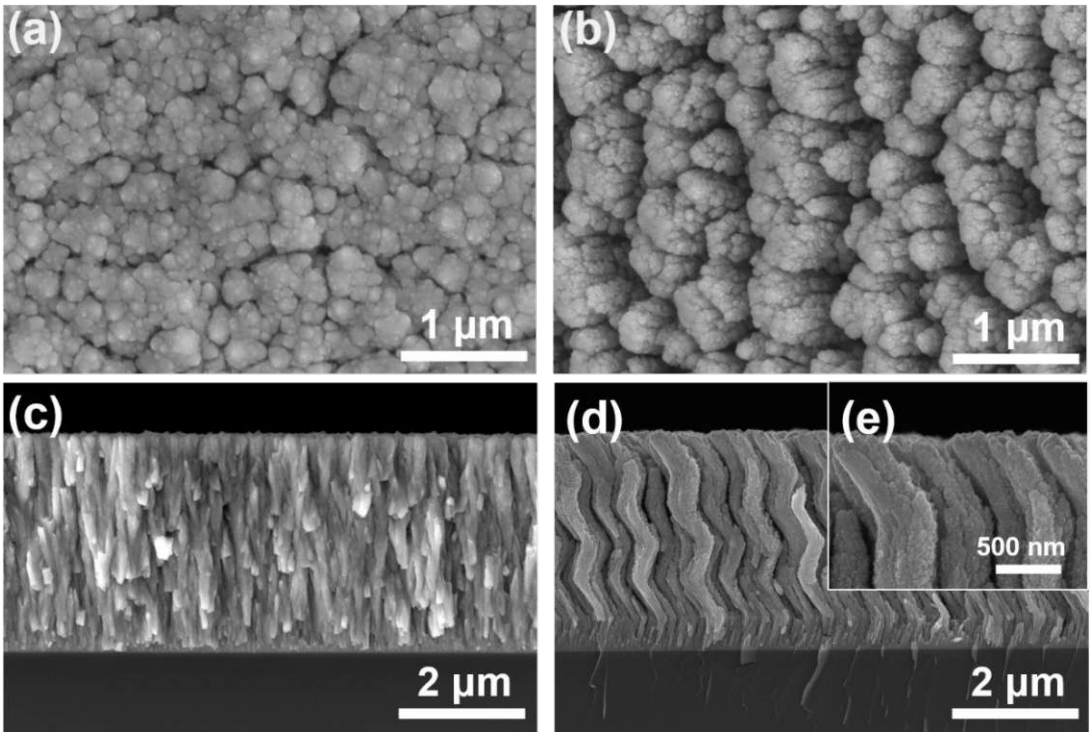

Figure 2. Surface and cross-sectional SEM micrographs of (a, b) columnar and (c, d) zig-zag γ-Mo_2N

The straight and zig-zag columnar samples deliver rough surface structures, see their top view SEM images in Figs. 2c and d, respectively. The surface of the zig-zag sample is even rougher and resembles a cauliflower structure, suggesting an improved specific area (beneficial for the charge absorption) compared to the straight columnar sample. XRD investigations suggest a face-centered cubic γ-Mo_2N structure (with the space group of Pm-3m, ICDD 00-25-1366 [37]) for both samples, Fig. 3. This structure is characterized for γ-Mo_2N with only a half-occupied N-sublattice on which the vacancies are randomly distributed [38]. The most pronounced XRD peaks for both samples are at a diffraction angle of 37.4° suggesting a preferred (111) growth orientation. The zig-zag sample shows a broader full width at half maximum (FWHM), indicating smaller coherently diffracting domain sizes due to the alternating incidence angle of arrival species. According to Bragg's law and the position of these diffraction peaks, the lattice parameters of columnar and zig-zag γ-Mo_2N samples are 4.168 ± 0.015 and 4.186 ± 0.017 Å, respectively. The slightly larger lattice parameters of the zig-zag sample can be explained by its ~2.5 at.% higher nitrogen content than that of the columnar one.

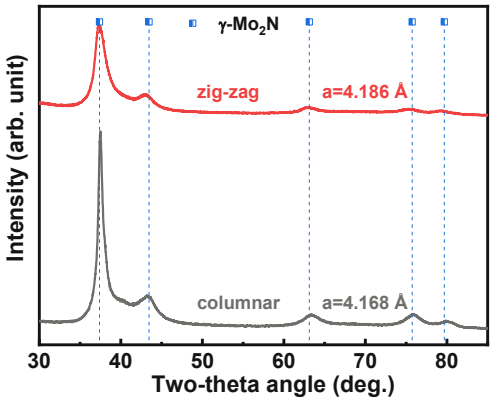

Figure 3. XRD patterns of columnar and zig-zag γ-Mo_2N films.

3.2 Electrochemical characterization of single electrode

The area-specific capacitances of the single columnar and zig-zag γ-Mo_2N electrodes were calculated in two ways: cyclic voltammetry (CV) and galvanostatic charge-discharge (GCD) curves – using Eqs. (1) and (2) – their results are given in Figs. 4a and 4d, respectively. The CV measurements were investigated under scanning rates of 100–1000 mV/s, and the GCD was performed using current densities from 1 to 10 mA/cm^2. As expected, regardless of the method, the area-specific capacitances of the zig-zag γ-Mo_2N electrode are ~4 times the value of the columnar electrode, when measured under the same conditions. With increasing scan rates and current densities, the specific capacitances of the zig-zag electrode decrease from 248.5 to 144.6 mF/cm^2 (from CV), and 195.7 to 77.2 mF/cm^2 (from GCD). The specific capacitance retention ratios of the columnar film also decrease from 87.7 to 55.2 mF/cm^2 (from CV), and 62.4 to 22.8 mF/cm^2 (from GCD). Our zig-zag γ-Mo_2N electrode presents higher specific capacitances than most reported TMN film electrodes, such as porous CrN (58.5 mF/cm^2, at 1.0 mA/cm^2) [25] and nanotube TiN (69.05 mF/cm^2, at 0.3 mA/cm^2) [39]. The sputtered 16-μm-thick VN reached a super high specific capacitance of 1.2 F/cm^2 (at 50 mV/s)[40], suggesting that the zig-zag γ-Mo_2N film electrode could further be improved by increasing the film thickness. Furthermore, even though the areal capacitances decrease as the scan rates increase, the zig-zag γ-Mo_2N still retains 144.6 mF/cm^2 at 1,000 mV/s, which is facilitated by the rapid ion diffusion rate and electron transfer rate.

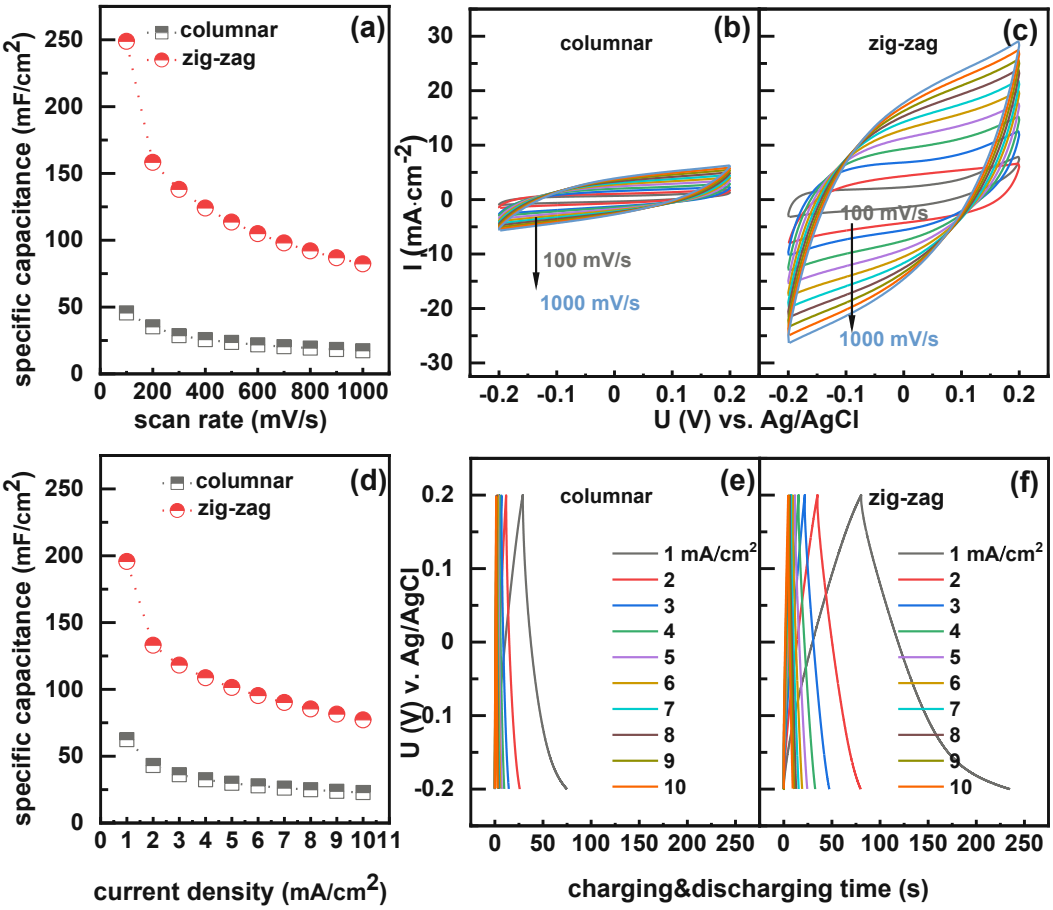

Figure 4. (a) Area-specific capacitance, as a function of scan rate, calculated from the CV curves of (b) columnar and (c) zig-zag γ-Mo_2N film electrodes. (d) Area-specific capacitance, as a function of current densities, calculated from the GCD curves of (e) columnar and (f) zig-zag γ-Mo_2N film electrodes.

Figs. 4b and 4c show the CV curves of columnar and zig-zag γ-Mo_2N electrodes at scanning rates from 100 to 1,000 mV/s, respectively. The improved specific capacitance of the zig-zag sample is clearly visible by comparing the integral areas under the CV curves (at the same scanning rate), since the capacitance is normalized to the geometric area of the CV curve. The quasi-rectangular shape of the cyclic voltammograms suggests an electrochemical storage mechanism similar to that of a Helmholtz double layer. The charge storage mechanism of γ-Mo_2N in H_2SO_4 aqueous solution relies on concurrent

contributions from faradaic electrochemical storage of the active materials (H^+) and double-layer charging [41]. Obviously, the porous zig-zag structure offers more active adsorption sites for H^+ ions in 0.5 M H_2SO_4 solution, as well as a shorter diffusion length of electrons and ions, which gives a higher power density [41]. Therefore, the almost symmetrical rectangular CV curves exhibit remarkable rate performance and good reversibility of the electrodes, even at the high scanning rate of 1,000 mV/s.

Analogically, the GCD curves of columnar and zig-zag γ-Mo_2N electrodes at current densities spanning from 1 to 10 mA/cm^2 are depicted in Figs. 4e and 4f, respectively. According to Eq. (2), the specific capacitance is only related to the discharging time of the GCD curves. For the same current densities, the longer the discharger time the higher is the specific capacitance. Thus, we can easily tell that the zig-zag γ-Mo_2N electrode presents a strongly improved specific capacitance compared to the columnar films. Also, the almost equilateral-triangular GCD curves, as well as decent linear potential-time profiles, provide evidence for an EDLC mechanism (surface-controlled adsorption) storage mechanism and good reversibility of the electrodes. The high current density up to 10 mA/cm^2 displays remarkable rate performance. The utilization of the electrode surface is higher at high current densities [42]. This is because the zig-zag architecture provides a larger specific surface area and more active sites for charge storage, increasing the number of electrolyte ions entering the active material, shortening the diffusion length, and thus offering an extraordinary high supercapacitor performance.

EIS measurements were conducted to further disseminate the interfacial properties of the columnar and zig-zag thin film γ-Mo_2N electrode systems. Figs. 5a and 5b show

Nyquist plots at frequencies of 0.01 to 100 kHz and 0.2 to 100 kHz, respectively. The corresponding simulation result of γ-Mo_2N, Fig. 5c, includes an ohmic resistance (R_s), a charge-transfer resistance (R_{ct}), a constant phase element (CPE), and a Warburg resistance (W). Their values could be determined by curve fitting simulation using Z-view software, or simply read from Fig. 5b. The R_s value is determined by the intersection between Nyquist curves and the horizontal axis in the ultrahigh frequency region, see Fig. 5b. Both electrode systems have roughly similar R_s values of ~1.6 Ω, indicating similar bulk solution resistance, intrinsic resistance of the active material, and interfacial contact resistance. The R_{ct} value can be estimated by deducing the diameter of the semicircle emerging in the high frequency region, see Fig. 5b. The zig-zag γ-Mo_2N electrode displays a semicircle diameter of ~2.26 Ω, while the columnar film only yields 0.48 Ω, leading to a dominance of the Warburg impedance at very low resistances of the columnar electrode. This can be ascribed to a better ohmic contact between the Mo_2N layer and Si current collector. In combination with the XRD results, this could be explained by a lower number of defects in the columnar γ-Mo_2N electrode. At high frequencies, the impedance of the capacitor will be very low and the major part of the current will flow through the capacitor. With decreasing frequencies from 100 kHz to 0.01 Hz, the impedance of the capacitor increases and a bigger fraction of the current flows through the resistor. When the majority of the current flows through the resistor, the total imaginary resistance Z'' will drop as the real part Z' increases. These processes lead to a semicircle in the Nyquist plot. Thus, the absence of semicircles in the high frequency range of the Nyquist plot of the columnar electrode also indicates low resistance values in the electronic charge transfer. The impedance of CPE, the Warburg

diffusion impedance and the total electrochemical impedance of the equivalent circuit could be obtained using the formula in Ref. [39].

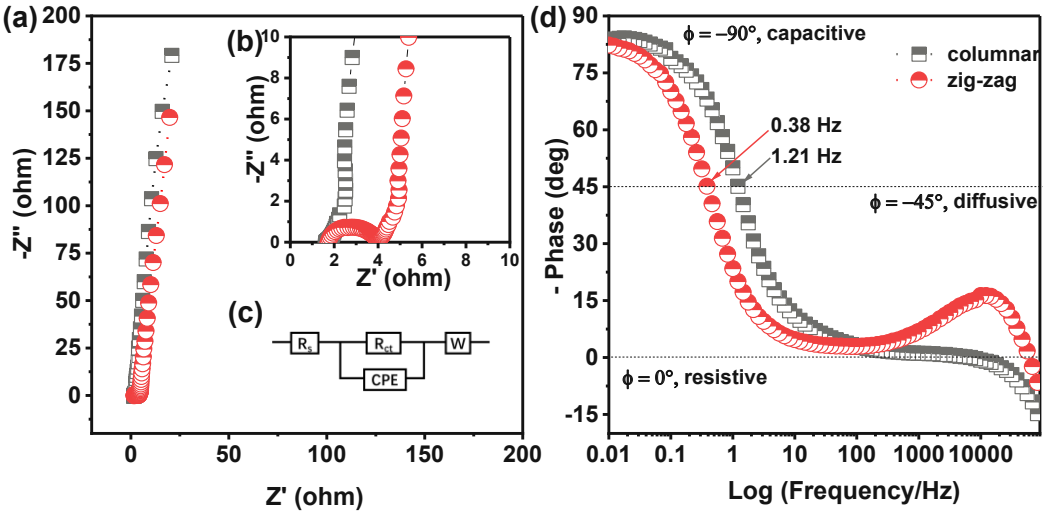

Figure 5. EIS properties of the columnar and zig-zag γ-Mo_2N film electrodes: (a) Nyquist plots in the frequency region from 0.01 to 10 kHz, (b) Nyquist plots in the frequency region from 0.2 to 10 kHz (the high-frequency region), (c) the corresponding Randles circuit, and (d) Bode plots.

The Bode diagram (Fig. 5d) plots the phase shift (y-axis) as a function of the logarithmic scale of the frequency (x-axis). In the low frequency region, the phase angle reaches ~–83° for both electrodes, presenting an excellent capacitive behavior. As marked with dotted horizontal lines in Fig. 5b, an ideal capacitor produces a slope of –90° and an ideal resistor yields 0°. The characteristic frequency (f_0) at the –45° phase angle denotes the crossover frequency of diffusive response, at which capacitive impedance equals the resistive impedance. Therefore, the corresponding characteristic time τ_0 ($\tau_0 = 1/2\pi f_0$) indicates the crossover time between capacitive and resistive behavior. The f_0 is ~1.21 and ~0.38 Hz and the τ_0 is 131.5 and 418.8 ms for the columnar and zig-zag γ-Mo_2N electrodes, respectively. Thus, the zig-zag electrode takes more time

to change from resistive to capacitive processes. But in general, the extremely small τ_0 values strongly suggest an ultrafast-charging process.

The long-term cycling stabilities of the columnar and zig-zag γ-Mo_2N film electrodes were evaluated by CV cycles, at a sweep rate of 200 mV/s. The respective specific capacitance retentions during the CV cycles are plotted in Figs. 6a and 6b. Notably, both electrodes have excellent cycling stability, retaining 94.5 and 96.6% of the original capacitance after 20,000 CV cycles, respectively. Such excellent cycling stability can be attributed to the chemical stability of the Mo_2N films, as well as the excellent adhesion between the film and the substrate facilitated by physical vapor deposition [43]. The stability is comparable to other TMN electrodes, such as TiN/Ni (98.22%/10,000 GCD cycles) [44].

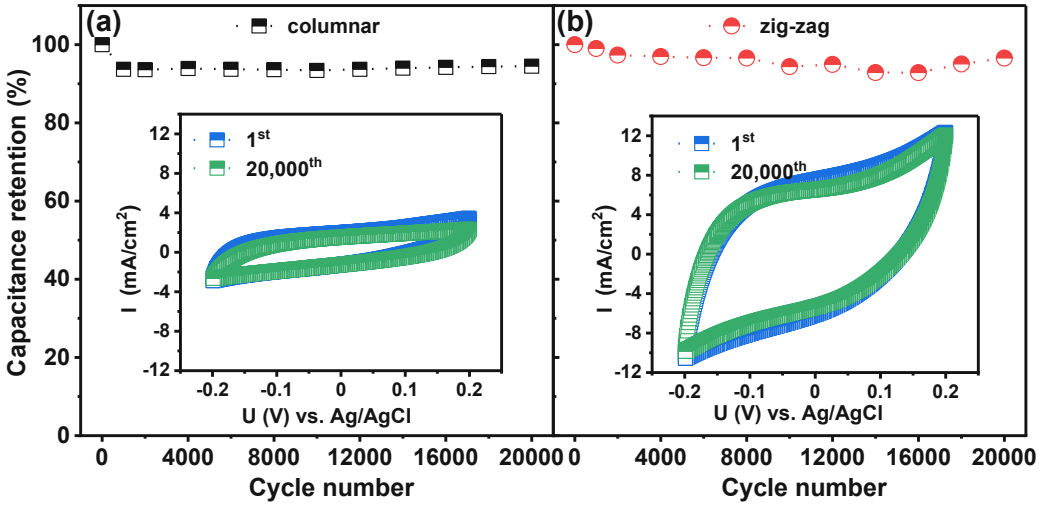

Figure 6. Cycling performance of (a) columnar and (b) zig-zag γ-Mo_2N film electrodes. The insets show CV plots of the 1st and 20,000th CV cycle (at 100 mV/s) of both electrodes, respectively.

While the overall capacitance retention after 20,000 cycles is similarly high for both film architectures, they show slightly different capacitance trends along the way: the specific capacitance of the columnar electrode drops noticeably in the first 1,000 cycles,

but remains stable afterwards. The zig-zag electrode on the other hand, falls slowly, but rises again after 16,000 cycles. The capacitor recovery may be due to an electrochemical etching changing the surface topography [45]. The insets of Figs. 6b and 6d show CV curves of the first and last cycles of the columnar and zig-zag electrodes. After 20,000 CV tests, their CV shapes are changed slightly, but are still rectangular.

3.3 Flexible symmetrical solid-state supercapacitors

In order to encourage the industrial application of γ-Mo_2N film supercapacitors, we assembled two flexible symmetrical solid-state devices from columnar and zig-zag γ-Mo_2N film electrodes, with a (0.5 M) H_2SO_4/PVA gel electrolyte. Their electrochemical performances were also evaluated by CV, GCD, and long-term CV cycling stability. Their volumetric capacitances were calculated form CV (Fig.7a) and GCD (Fig. 7d) curves, using Eqs. (3) and (4), respectively. CV measurements were performed at scanning rates of 50–1,000 mV/s (Figs. 7c and 7d), and GCD measurements under current densities from 1 to 5 mA/cm^3 for the columnar device (Fig. 7e), and 1 to 10 mA/cm^3 for the zig-zag device (Fig. 7f). As shown in Fig. 7a, with increasing scanning rates (from 50 to 1,000 mV/s), the volumetric capacitance retention ratios of the zig-zag device gradually decrease from 17.7 to 5.3 F/cm^3, and that of the columnar device drops from 6.1 to 2.2 F/cm^3. Similarly, as shown in Fig. 7c, with the current densities increasing, the capacitance retention ratios of the zig-zag device gradually decrease from 19.9 to 5.3 F/cm^3 (at 1–10 mA/cm^3), and those of the columnar device drop from 5.7 to 1.9 F/cm^3 (at 1–5 mA/cm^3). The volumetric capacitance of the zig-zag device is also ~3.5 times that of the columnar device, which is also proven in single electrodes. Our zig-zag γ-Mo_2N device exhibits comparable volumetric capacitance to other supercapacitor devices, like

the chrysanthemum-like TiN device (7.78 F/cm^3, at 0.05 mA/cm^3) [46], the CNT/MnO_2 hybrid SC (5.1 F/cm^3, at 16 mA/cm^3) [47], and the MnO_2/CNT/MoO_3/CNT asymmetric supercapacitor (4.9 F/cm^3, at 80 mA/cm^3) [48].

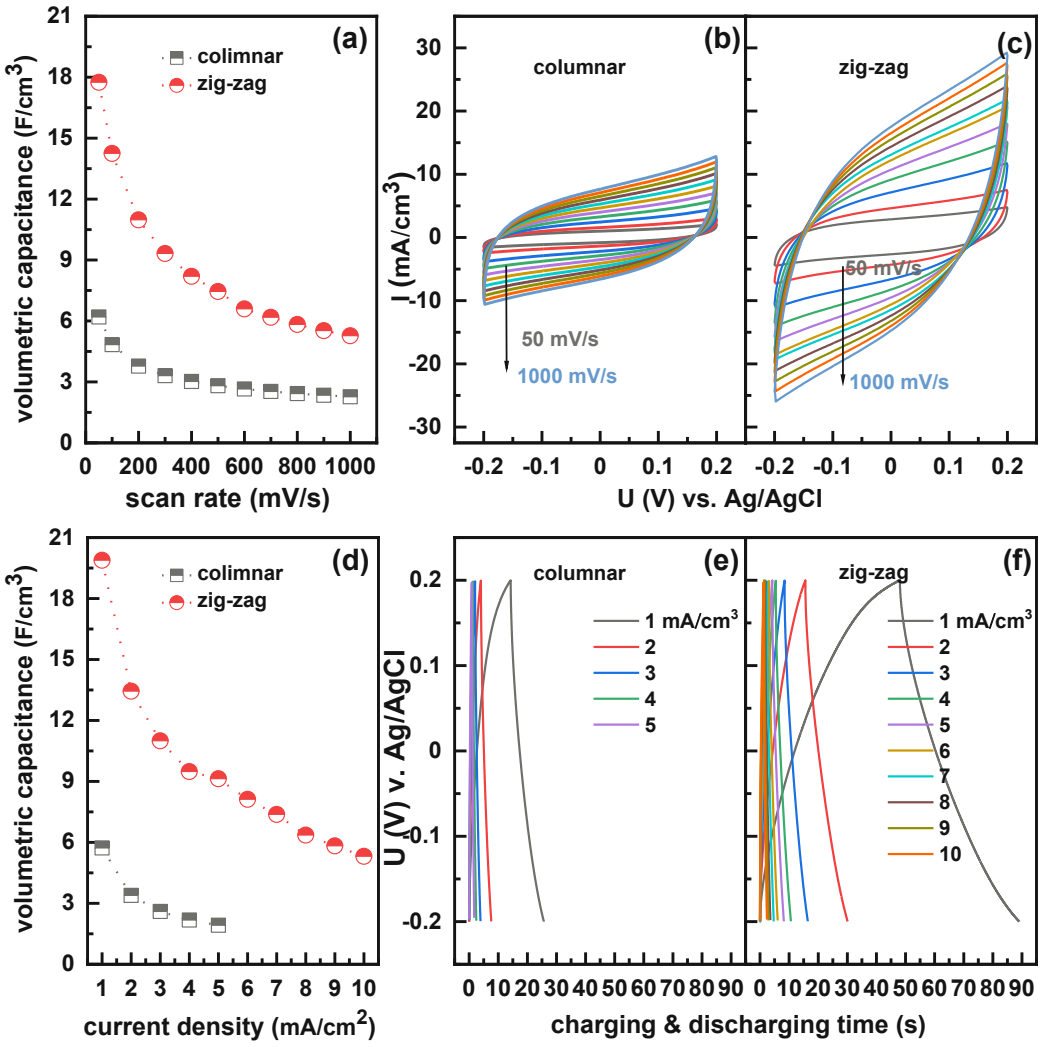

Figure 7. (a) Volumetric capacitances as a function of scan rates calculated from the CV curves of (b) columnar and (c) zig-zag γ-Mo_2N devices. (d) Volumetric capacitances as a function of current densities calculated from the GCD curves of (e) columnar and (f) zig-zag γ-Mo_2N devices.

The rectangular characteristics of the CV curves of the columnar and zig-zag devices remain even up to 1,000 mV/s, indicating typical double-layer capacitance performance and good reversibility. As predicted, the integral area of the CV curves of the zig-zag

device is much larger than that of the columnar device, when compared at the same conditions. All the GCD curves remain nearly symmetrical with their discharging counterpart, while slightly non-linear potential-time profiles contribute to an increased resistance in the devices compared to the single electrodes. The discharge time of the zig-zag device is much longer than that of the columnar device, when compared at the same conditions. The current densities of the columnar device can reach only up to 5 mA/cm^3, which is caused by the insufficient time available for ion diffusion at higher current densities.

To test the cyclic stabilities of the columnar and zig-zag devices, they were subjected to 20,000 CV circles at 100 mV/s. As shown in Figs. 8a and 8b, the capacitances of both devices decayed by approximately 13% (columnar) and 14% (zig-zag) after 20,000 CV cycles. However, the capacitance of the columnar device remained stable first and declined rapidly after 15,000 cycles. That of the zig-zag device decreased within the first 10,000 cycles but then even increased slightly. The insets of Figs. 8a and 8b – showing the respective first and last CV cycles – exhibit no significant changes in the shapes of the first and last CV curves of the columnar and zig-zag devices, but their integrated area declines. Hence, the cycling performance of the devices is not as excellent as that of the single electrodes, but still comparable to the nanopyramids Mo_2N symmetric device (~89.93% retention after 4500 cycles) [22], and some other nitride-based and carbon-based solid-state (symmetric or asymmetric) supercapacitor devices listed in the supplementary information of reference [46].

To further evaluate the electrochemical performance of flexible symmetrical solid-state γ-Mo_2N supercapacitors, power and energy densities are calculated using Eqs. (5)

and (6). As shown in Fig. 9a, the zig-zag device exhibits calculated volumetric energy densities of 49.8, 40.7, 35.1, 33.8 mWh/cm^3 and power densities of 42.9, 64.3, 85.7, 107.1 W/cm^3 at 1, 2, 3, 4, 5 mA/cm^2, respectively. These values are much higher than those of the columnar device (7.1 mWh/cm^3 and 8.2 W/cm^3, at 5 mA/cm^2) and even exceed other nitride-based symmetric supercapacitor devices (e.g., porous and non-porous CrN/CrN [17] [18], as well as chrysanthemum-like TiN [46]). The improved electrochemical performance is a consequence of the zig-zag nanostructure providing abundant active sites and creating efficient uni-directional electron transfer pathways.

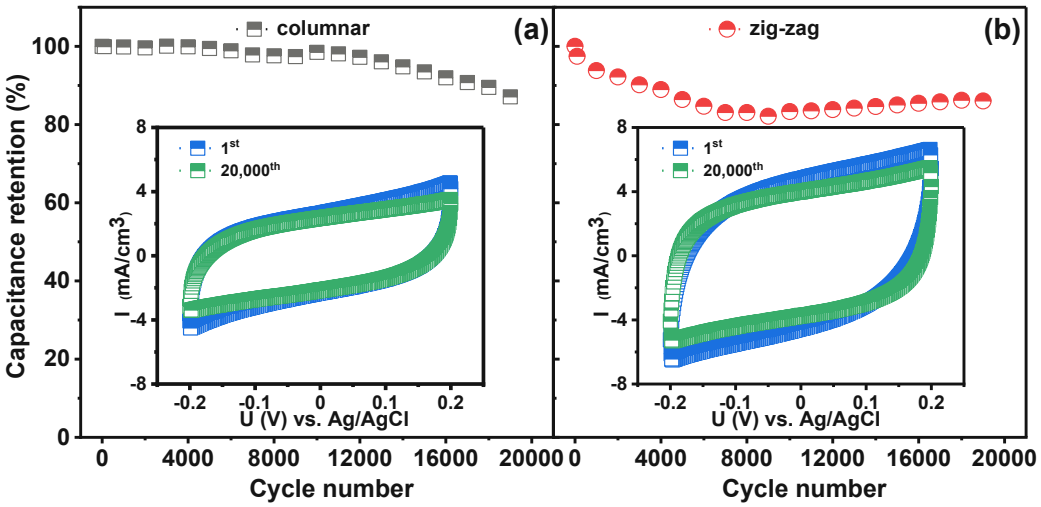

Figure 8. Cycling performance of (a) columnar and (b) zig-zag γ-Mo_2N devices. The insets show the 1st and the 20,000th CV cycle (at 200 mV/s) of columnar and zig-zag devices, respectively.

Recently, wearable electronics have elicited a continuously intensifying surge of interest. Therefore, we also investigated the flexibility of our nanostructured zig-zag symmetrical solid-state γ-Mo_2N film supercapacitor. The flexibility test was carried out by rolling the device onto laboratory measuring cylinders of various sizes (from 100 to 10 ml), to obtain gradually increasing bending angles from ~0 to 107°, see the schematic in Fig. 9b. All CV curves are almost overlapping at different bending angles, even at the

highest bending angle of 107°, which demonstrates excellent flexibility and mechanical stability of the zig-zag device. Also, such good flexibility is a direct result of the chemical stability of the Mo-N bonds and the excellent adhesion between film and substrate. This proves the possibility for further applications in wearable energy storage devices.

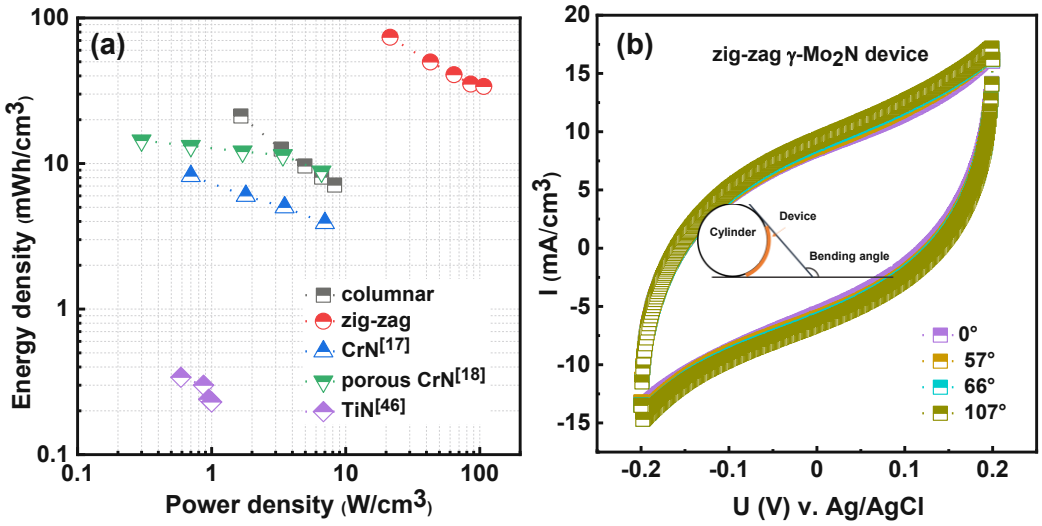

Figure 9. (a) Energy and power densities of the symmetric γ-Mo_2N supercapacitors compared to some available energy storage systems. (b) CV curves of the zig-zag γ-Mo_2N device at different bending angles. The scan rate is 300 mV/s.

4. Conclusions

Zig-zag tilted-structured γ-Mo_2N films have been fabricated by glancing angle magnetron sputtering for supercapacitor electrodes. Compared to the conventional simple columnar-structured γ-Mo_2N electrode, the zig–zag electrode exhibits a 4 times higher area-specific capacitance of 248 mF/cm^2 (at a scan speed of 50 mV/s), without sacrificing cycling stability (96.5% after 20,000 CV cycles, at 200 mV/s). Furthermore, we successfully produced flexible symmetrical solid-state γ-Mo_2N supercapacitors with a 0.5 M H_2SO_4-PVA gel as electrolyte. The zig-zag SCs exhibit ultrafast charging/discharging

capability, which yields an excellent volumetric capacitance of 19.9 F/cm^3 (at 1.0 mA/cm^3) with an extremely high energy density of 73.6 mWh/cm^3 at a power density of 21.4 W/cm^3. Moreover, the zig-zag SC shows a favorable cycling stability, retaining 85% of the initial capacitance after 20,000 CV cycles (at 200 mV/s). In addition, the symmetric zig-zag SCs also shows high mechanical flexibility, to be used for flexible devices. The excellent performance is based on the three-dimensional zig-zag architecture and the high conductivity and structural stability of the γ-Mo_2N films produced by magneton sputtering. Based on our results we can conclude that zig-zag γ-Mo_2N film electrodes prepared by glancing angle deposition provide ultrafast-charging/discharging abilities with excellent stability. They allow to prepare very flexible solid-state supercapacitors to be used for electrochemical energy storage and conversion applications.

Declaration of interests

The authors declare that they have no known competing or financial interests, or personal relationships, that could have influenced the work reported in this paper.

Acknowledgements

The work was financially supported by the project of the National Natural Science Foundation of China (Grant No. 51875109). The National Key Research and Development Program of China (Grant No. 2017YFE0125400) project is also highly acknowledged. Zecui Gao thanks to the finical support of Chinses Scholarship Council during her PhD study time at TU Wien (No. 201908440933). The authors thank Julian Buchinger for the English revision. The authors acknowledge the TU Wien Bibliothek for the financial support through its Open Access Funding Program.

Data availability

The raw data required to reproduce these findings are available to download from [https://data.mendeley.com/drafts/kykwsrxzry].

References

[1] Y. Zhou, W. Guo, T. Li, A review on transition metal nitrides as electrode materials for supercapacitors, Ceram. Int. (2019). https://doi.org/10.1016/j.ceramint.2019.07.151

[2] M.S. Balogun, Y. Huang, W. Qiu, H. Yang, H. Ji, Y. Tong, Updates on the development of nanostructured transition metal nitrides for electrochemical energy storage and water splitting, Materials Today 20 (2017) 425-451. https://doi.org/10.1016/j.mattod.2017.03.019

[3] H. Li, T. Lv, H. Sun, G. Qian, N. Li, Y. Yao, T. Chen, Ultrastretchable and superior healable supercapacitors based on a double cross-linked hydrogel electrolyte, Nature Communications 10 (2019) 536. https://doi.org/10.1038/s41467-019-08320-z

[4] C. Cao, Y. Zhou, S. Ubnoske, J. Zang, Y. Cao, P. Henry, C.B. Parker, J.T. Glass, Highly Stretchable Supercapacitors via Crumpled Vertically Aligned Carbon Nanotube Forests, Adv. Energy Mater. 9 (2019) 1900618. https://doi.org/10.1002/aenm.201900618

[5] G. Wang, H. Wang, X. Lu, Y. Ling, M. Yu, T. Zhai, Y. Tong, Y. Li, Solid-State Supercapacitor Based on Activated Carbon Cloths Exhibits Excellent Rate Capability, Adv. Mater. 26 (2014) 2676-2682. https://doi.org/10.1002/adma.201304756

[6] Z. Fan, Y. Wang, Z. Xie, D. Wang, Y. Yuan, H. Kang, B. Su, Z. Cheng, Y. Liu, Modified MXene/Holey Graphene Films for Advanced Supercapacitor Electrodes with Superior Energy Storage, Adv Sci (Weinh) 5 (2018) 1800750. https://doi.org/10.1002/advs.201800750

[7] Y. Tan, L. Meng, Y. Wang, W. Dong, L. Kong, L. Kang, F. Ran, Negative electrode materials of molybdenum nitride/N-doped carbon nano-fiber via electrospinning method for high-performance supercapacitors, Electrochimica Acta 277 (2018) 41-49. https://doi.org/10.1016/j.electacta.2018.04.214

[8] A. Dang, Y. Sun, C. Fang, T. Li, X. Liu, Y. Xia, F. Ye, A. Zada, M. Khan, Rational design of Ti3C2/carbon nanotubes/MnCo2S4 electrodes for symmetric supercapacitors with high energy storage, Appl. Surf. Sci. 581 (2022) 152432. https://doi.org/10.1016/j.apsusc.2022.152432

[9] A.G. El-Deen, M.K. Abdel-Sattar, N.K. Allam, High-performance solid-state supercapacitor based on Ni-Co layered double hydroxide@Co3O4 nanocubes and spongy graphene electrodes, Appl. Surf. Sci. 587 (2022) 152548. https://doi.org/10.1016/j.apsusc.2022.152548

[10] R.S. Kate, S.A. Khalate, R.J. Deokate, Overview of nanostructured metal oxides and pure nickel oxide (NiO) electrodes for supercapacitors: A review, J. Power Sources 734 (2018) 89-111. https://doi.org/10.1016/j.jallcom.2017.10.262

[11] V.S. Sumana, Y.N. Sudhakar, A. Varghese, G.K. Nagaraja, Pt nanoflower-poly(aniline) electrode material with the synchronized concept of energy storage in supercapacitor, Appl. Surf. Sci. 589 (2022) 152994. https://doi.org/10.1016/j.apsusc.2022.152994

[12] K.C. Seetha Lakshmi, X. Ji, L.-D. Shao, B. Vedhanarayanan, T.-W. Lin, Tailor-made organic polymers towards high voltage aqueous ammonium/potassium-ion asymmetric supercapacitors, Appl. Surf. Sci. 577 (2022) 151918. https://doi.org/10.1016/j.apsusc.2021.151918

[13] M.R. Pallavolu, Y. Anil Kumar, R.R. Nallapureddy, H.R. Goli, A. Narayan Banerjee, S.W. Joo, In-situ design of porous vanadium nitride@carbon nanobelts: A promising material for high-performance asymmetric supercapacitors, Appl. Surf. Sci. 575 (2022) 151734. https://doi.org/10.1016/j.apsusc.2021.151734

[14] S.G. Yuan, S.Y. Pang, J.H. Hao, 2D transition metal dichalcogenides, carbides, nitrides, and their applications in supercapacitors and electrocatalytic hydrogen

evolution reaction, Applied Physics Reviews 7 (2020). https://doi.org/10.1063/5.0005141
[15] M.S. Balogun, W. Qiu, W. Wang, P. Fang, X. Lu, Y. Tong, Recent advances in metal nitrides as high-performance electrode materials for energy storage devices, Journal of Materials Chemistry A 3 (2015) 1364-1387. https://doi.org/10.1039/C4TA05565A
[16] B. Wei, H. Liang, D. Zhang, Z. Qi, H. Shen, Z. Wang, Magnetron sputtered TiN thin films toward enhanced performance supercapacitor electrodes, Materials for Renewable and Sustainable Energy 7 (2018) 11. https://doi.org/10.1007/s40243-018-0117-9
[17] B. Wei, H. Liang, D. Zhang, Z. Wu, Z. Qi, Z. Wang, CrN thin films prepared by reactive DC magnetron sputtering for symmetric supercapacitors, Journal of Materials Chemistry A 5 (2017) 2844-2851. https://doi.org/10.1039/c6ta09985h
[18] B. Wei, G. Mei, H. Liang, Z. Qi, D. Zhang, H. Shen, Z. Wang, Porous CrN thin films by selectively etching CrCuN for symmetric supercapacitors, J. Power Sources 385 (2018) 39-44. https://doi.org/10.1016/j.jpowsour.2018.03.023
[19] M. Arif, A. Sanger, A. Singh, Sputter deposited chromium nitride thin electrodes for supercapacitor applications, Materials Letters 220 (2018) 213-217. https://doi.org/10.1016/j.matlet.2018.02.094
[20] R. Lucio-Porto, S. Bouhtiyya, J.F. Pierson, A. Morel, F. Capon, P. Boulet, T. Brousse, VN thin films as electrode materials for electrochemical capacitors, Electrochimica Acta 141 (2014) 203-211. https://doi.org/10.1016/j.electacta.2014.07.056
[21] Z. Gao, Z. Wu, S. Zhao, T. Zhang, Q. Wang, Enhanced capacitive property of HfN film electrode by plasma etching for supercapacitors, Materials Letters 235 (2019) 148-152. https://doi.org/10.1016/j.matlet.2018.10.032
[22] B. Ranjan, G.K. Sharma, D. Kaur, Rationally synthesized Mo2N nanopyramids for high-performance flexible supercapacitive electrodes with deep insight into the Na-ion storage mechanism, Appl. Surf. Sci. 588 (2022) 152925. https://doi.org/10.1016/j.apsusc.2022.152925
[23] Y. Xu, L. Chen, Z. Liu, F. Pei, Y. Du, Influence of Ti on the mechanical properties, thermal stability and oxidation resistance of Al-Cr-N coatings, Vacuum 120 (2015) 127-131. https://doi.org/10.1016/j.vacuum.2015.07.004
[24] A. Achour, M. Islam, I. Ahmad, L. Le Brizoual, A. Djouadi, T. Brousse, Influence of surface chemistry and point defects in TiN based electrodes on electrochemical capacitive storage activity, Scr. Mater. 153 (2018) 59-62. https://doi.org/10.1016/j.scriptamat.2018.04.051
[25] Z. Gao, Z. Wan, Z. Wu, X. Huang, H. Li, T.F. Zhang, P.H. Mayrhofer, Q. Wang, Synthesis and electrochemical properties of nanoporous CrN thin film electrodes for supercapacitor applications, Mater. Des. 209 (2021) 109949. https://doi.org/10.1016/j.matdes.2021.109949
[26] K. Robbie, M.J. Brett, Sculptured thin films and glancing angle deposition: Growth mechanics and applications, J. Vac. Sci. Technol., A 15 (1997) 1460-1465. https://doi.org/10.1116/1.580562
[27] Z. Qi, B. Wei, J. Wang, Y. Yang, Z. Wang, Nanostructured porous CrN thin films by oblique angle magnetron sputtering for symmetric supercapacitors, J. Power Sources 806 (2019) 953-959. https://doi.org/10.1016/j.jallcom.2019.07.325
[28] S.H. Kim, S.H. Lee, J.S. Yu, Broadband and antireflective characteristics of glancing angle deposited titanium dioxide nanostructures for photovoltaic applications, Thin Solid Films 685 (2019) 53-58. https://doi.org/10.1016/j.tsf.2019.05.067
[29] M.J. Cordill, T. Jörg, O. Glushko, R. Franz, C. Mitterer, Crack deflecting microstructure for improved electro-mechanical lifetimes of flexible systems, Materials Letters 244 (2019) 47-49. https://doi.org/10.1016/j.matlet.2019.02.039

[30] E. Haye, A. Achour, A. Guerra, F. Moulaï, T. Hadjersi, R. Boukherroub, A. Panepinto, T. Brousse, J.-J. Pireaux, S. Lucas, Achieving on chip micro-supercapacitors based on CrN deposited by bipolar magnetron sputtering at glancing angle, Electrochimica Acta 324 (2019) 134890. https://doi.org/10.1016/j.electacta.2019.134890

[31] W. Tillmann, D. Kokalj, D. Stangier, Influence of the deposition parameters on the texture and mechanical properties of magnetron sputtered cubic MoNx thin films, Materialia 5 (2019) 100186. https://doi.org/10.1016/j.mtla.2018.100186

[32] J. Qian, S. Li, J. Pu, Z. Cai, H. Wang, Q. Cai, P. Ju, Effect of heat treatment on structure and properties of molybdenum nitride and molybdenum carbonitride films prepared by magnetron sputtering, Surf. Coat. Technol. 374 (2019) 725-735. https://doi.org/10.1016/j.surfcoat.2019.06.062

[33] T. Wang, J. Zhang, Y. Li, F. Gao, G. Zhang, Self-lubricating TiN/MoN and TiAlN/MoN nano-multilayer coatings for drilling of austenitic stainless steel, Ceram. Int. 45 (2019) 24248-24253. https://doi.org/10.1016/j.ceramint.2019.08.136

[34] G. Ma, Z. Wang, B. Gao, T. Ding, Q. Zhong, X. Peng, J. Su, B. Hu, L. Yuan, P.K. Chu, J. Zhou, K. Huo, Multilayered paper-like electrodes composed of alternating stacked mesoporous Mo2N nanobelts and reduced graphene oxide for flexible all-solid-state supercapacitors, Journal of Materials Chemistry A 3 (2015) 14617-14624. https://doi.org/10.1039/C5TA02851E

[35] L. Liu, B. Shen, D. Jiang, R. Guo, L. Kong, X. Yan, Watchband-Like Supercapacitors with Body Temperature Inducible Shape Memory Ability, Adv. Energy Mater. 6 (2016) 1600763. https://doi.org/10.1002/aenm.201600763

[36] J. Dervaux, P.A. Cormier, P. Moskovkin, O. Douheret, S. Konstantinidis, R. Lazzaroni, S. Lucas, R. Snyders, Synthesis of nanostructured Ti thin films by combining glancing angle deposition and magnetron sputtering: A joint experimental and modeling study, Thin Solid Films 636 (2017) 644-657. https://doi.org/10.1016/j.tsf.2017.06.006

[37] A. Gomathi, A. Sundaresan, C.N.R. Rao, Nanoparticles of superconducting γ-Mo2N and δ-MoN, J. Solid State Chem. 180 (2007) 291-295. https://doi.org/10.1016/j.jssc.2006.10.020

[38] H. Jehn, P. Ettmayer, The molybdenum-nitrogen phase diagram, Journal of the Less Common Metals 58 (1978) 85-98. https://doi.org/10.1016/0022-5088(78)90073-5

[39] Y. Xie, F. Tian, Capacitive performance of molybdenum nitride/titanium nitride nanotube array for supercapacitor, Materials Science and Engineering: B 215 (2017) 64-70. https://doi.org/10.1016/j.mseb.2016.11.005

[40] K. Robert, D. Stiévenard, D. Deresmes, C. Douard, A. Iadecola, D. Troadec, P. Simon, N. Nuns, M. Marinova, M. Huvé, P. Roussel, T. Brousse, C. Lethien, Novel insights into the charge storage mechanism in pseudocapacitive vanadium nitride thick films for high-performance on-chip micro-supercapacitors, Energy & Environmental Science 13 (2020) 949-957. https://doi.org/10.1039/C9EE03787J

[41] P. Pande, P.G. Rasmussen, L.T. Thompson, Charge storage on nanostructured early transition metal nitrides and carbides, J. Power Sources 207 (2012) 212-215. https://doi.org/10.1016/j.jpowsour.2012.01.028

[42] J. Chen, K. Sheng, P. Luo, C. Li, G. Shi, Graphene Hydrogels Deposited in Nickel Foams for High-Rate Electrochemical Capacitors, Adv. Mater. 24 (2012) 4569-4573. https://doi.org/10.1002/adma.201201978

[43] Y.X. Xu, L. Chen, F. Pei, K.K. Chang, Y. Du, Effect of the modulation ratio on the interface structure of TiAlN/TiN and TiAlN/ZrN multilayers: First-principles and experimental investigations, Acta Mater. 130 (2017) 281-288. https://doi.org/10.1016/j.actamat.2017.03.053

[44] Q. Akbar Sial, L. Thai Duy, R. Singh, S. Iqbal, R. Yeasmin, Y.-J. Lee, S.S. Kalanur, H. Seo, A multifunctional TiN/Ni electrode for wearable supercapacitor

and sensor with an insight into charge storage mechanism, Appl. Surf. Sci. 555 (2021) 149718. https://doi.org/10.1016/j.apsusc.2021.149718

[45] L. Chen, C. Liu, Z. Zhang, Novel (111) oriented γ-Mo_2N thin films deposited by magnetron sputtering as an anode for aqueous micro-supercapacitors, Electrochimica Acta 245 (2017) 237-248. https://doi.org/10.1016/j.electacta.2017.05.102

[46] X. Hou, Q. Li, L. Zhang, T. Yang, J. Chen, L. Su, Tunable preparation of chrysanthemum-like titanium nitride as flexible electrode materials for ultrafast-charging/discharging and excellent stable supercapacitors, J. Power Sources 396 (2018) 319-326. https://doi.org/10.1016/j.jpowsour.2018.06.033

[47] L. Du, P. Yang, X. Yu, P. Liu, J. Song, W. Mai, Flexible supercapacitors based on carbon nanotube/MnO2 nanotube hybrid porous films for wearable electronic devices, Journal of Materials Chemistry A 2 (2014) 17561-17567. http://doi.org/10.1039/C4TA04431B

[48] P. Yang, Y. Chen, X. Yu, P. Qiang, K. Wang, X. Cai, S. Tan, P. Liu, J. Song, W. Mai, Reciprocal alternate deposition strategy using metal oxide/carbon nanotube for positive and negative electrodes of high-performance supercapacitors, Nano Energy 10 (2014) 108-116. https://doi.org/10.1016/j.nanoen.2014.08.018

Acta Materialia 234 (2022) 118008

Contents lists available at ScienceDirect

Acta Materialia

journal homepage: www.elsevier.com/locate/actamat

Atomic-scale understanding of the structural evolution of TiN/AlN superlattice during nanoindentation— Part 1: Deformation

Zhuo Chen[a], Yonghui Zheng[a,b], Yong Huang[a], Zecui Gao[c], Huaping Sheng[a], Matthias Bartosik[c,d], Paul H. Mayrhofer[c], Zaoli Zhang[a,*]

[a] Erich Schmid Institute of Materials Science, Austrian Academy of Sciences, A-8700 Leoben, Austria
[b] Key Laboratory of Polar Materials and Devices (MOE), Department of Electronics, East China Normal University, Shanghai 200241, China
[c] Institute of Materials Science and Technology, TU Wien, A-1060 Vienna, Austria
[d] Department of Materials Science, Montanuniversität Leoben, Leoben, A-8700, Austria

ARTICLE INFO

Article history:
Received 2 March 2022
Revised 29 April 2022
Accepted 4 May 2022
Available online 5 May 2022

ABSTRACT

At present, the theoretical predictions of the mechanical properties of transition-metal nitride (TMN) superlattices (SLs) are primarily based on the intrinsic properties of perfect epitaxial nanolayers. However, due to a lack of understanding of the specific strengthening mechanism, the experimentally determined strength, e.g., hardness, of TMN SLs often deviates significantly from the theoretical predictions. Here, by coupling FIB (focused ion beam) sectioning with TEM, we observe the structural evolution of two representatives TiN/AlN SL coatings, i.e., a single-crystalline and a polycrystalline SL, under identical loads. We found that in comparison with the polycrystalline SL, the indented single-crystalline SL forms a larger 'intermixed' region, within which the layer structure transforms into a solid solution under loads. Close TEM characterization demonstrates that the single-crystalline SL deformation is of variety, including the distortion of SL interfaces, polycrystalline deformation (grain rotation) in solid solution, and SL slip deformation. By contrast, columnar grain boundary sliding is the primary deformation mechanism in the polycrystalline SL. And, a relatively large solid-solution zone in single-crystalline SL is attributed to the severe interfacial deformation. The current research unravels TMN SL deformation behavior at the atomic scale.

1. Introduction

Transition-metal nitride (TMN) coatings are of great importance for wear and tribological applications due to their extreme hardness and wear resistance. In the past, it has been realized that monolithic (single layer) TMN coatings can effectively protect cutting tools. However, with increasing demands from industry in terms of material hardness and toughness, multilayer architectures were used to further enhance the performance. It is currently known that when a multilayer with rock-salt/rock-salt superlattice (SL) structure is formed, the toughness and hardness are significantly increased [1–6]. The performance improvement can be attributed to the interface effect in nanoscale multilayer [7–12]. The outstanding toughness and hardness of the SL coatings are related to the interface, which include the effect of misfit dislocations, interface coherency strains, and the modulus difference between the layers materials [7,9,10,13].

Although numerous studies reported on the mechanical properties of TMN multilayer coatings, only a few works explored the deformation behavior of nitride multilayer coatings [14–17]. Since some films using different substrate materials or applying less severe deposition, TMN film tend to exhibit columnar grain structures. Previous work performed nanoindentation and nanoscratch experiments on TMN SL coatings and performed cross-sectional Scanning electron microscope (SEM)/Transmission electron microscope (TEM) characterizations [14–16,18,19]. These structures show that the plastic deformation of the polycrystalline coating is mainly due to the grain rotation and grain boundary sliding of the nanocrystals. The fracture modes were observed to initiate at the columnar boundaries and in the layers parallel to the interfaces [18]. However, the deformation and fracture behaviors of fully epitaxially stable single-crystal coatings with better mechanical properties are rarely reported. Since deformation and fracture behavior are important factors affecting the strength of TMN coatings and

* Corresponding author.
E-mail address: zaoli.zhang@oeaw.ac.at (Z. Zhang).

https://doi.org/10.1016/j.actamat.2022.118008

their industrial applications, it is essential to characterize the microstructural evolution under mechanical loading.

Recent TEM research shows the deformation induced by nanoindentation can result in intermixing of the layer materials in a single-crystalline SL coating (with a small bilayer thickness, Λ=2.5 nm) [20]. However, how the microstructure affects the intermixing and deformation behaviors in TMN SL remains unexplored. In this work, at the atomic scale, we studied the deformation, fracture mechanisms, and the spatial distribution and extent of intermixed regions formed in a single-crystalline SL coating subjected to loads, and then compared the results to those of a polycrystalline SL coating. Using a C_S-corrected TEM, we found that the deformation of the single-crystalline SL coating is more complex, while the deformation of the polycrystalline coating is mainly governed by columnar grain boundary sliding. Hence, due to the difference in the deformation mechanisms, the single-crystalline SL exhibits a larger scale of solid solution zone than the polycrystalline SL.

2. Methods

2.1. Material fabrication

The TiN/AlN superlattice thin film (~ 1.5 μm total thickness, TiN ~1.7 nm, AlN ~0.8 nm) was synthesized using an AJA International Orion 5 lab-scale deposition system equipped with a computer-controlled shutter system. This bilayer period and layer distribution was chosen based on the previous study [21], showing that also the AlN layers fully crystallize to retain their metastable face-centered cubic (fcc) rock-salt (*rs*) structure. The reactive magnetron sputtering process was carried out at 700 °C (substrate temperature) in an Ar/N_2 mixed gas atmosphere with a total pressure of 0.4 Pa and an Ar/N_2 flow ratio of 7 sccm / 3 sccm. To avoid the intermixing of the two layer materials via excessive ion bombardment, we applied a rather low bias potential of –40 V (floating potential was –20 V) to the MgO (100) and Si (100) substrate, just enough to obtain a dense coating morphology. The three-inch Ti and two-inch Al targets were DC-powered setting constant target currents of 1.0 and 0.5 A, respectively. Further details can be found in Ref. [21]. To reduce the substrate effect and achieve better coating quality, the first layer of all coatings is TiN (approximately 5 nm thick). Except for the first TiN layer, other TiN layers maintain a constant thickness of 1.6 nm.

2.2. Material characterization

The nanoindentation was performed with an Ultra Micro Indentation System (UMIS, Fischer-Cripps Laboratories) equipped with a cube corner diamond tip using a maximum load of 100 mN and 150 mN. The maximum load depth is about 1.1 μm. The nanoindentation was carried out at a constant indentation strain rate (loading rate is about 10 mN/s). The FIB cutting positions are chosen near the tip of the indenter and cut along the ⟨100⟩ direction of the SL. During the FIB cutting, a protective layer of platinum with a thickness of about 2.0 μm was deposited on the area of interest. Two 6 μm deep trenches were made on either side of the selected region by coarsely milling at a current of 1.0 nA. After that, the exposed vertical faces of the specimen were coarsely polished by the ion beam using a current of 500 pA. An ion beam is used to cut off the entire bottom end and the vertical part. Finally, it is transferred and welded to a copper TEM grid for finely polishing under conditions of ± 2° and a beam current of 50 pA.

A 300 kV field emission TEM (JEOL ARM300F) equipped with double C_S-correctors were used in this study. Two windowless energy-dispersive X-ray spectroscopy (EDXS) detectors, each of which has an active area of 100 mm^2, are equipped on the microscope, which are very close to the specimen with a high solid angle (1.7 sr). A 200 kV field emission TEM (JEOL 2100F) equipped with an image-side C_S-corrector was used in the high-resolution TEM (HRTEM) study, which demonstrates a resolution of 1.2 Å at 200 kV. The aberration coefficients were set to be sufficient small under which the HRTEM images were taken under slightly overfocus conditions (close to the Scherzer defocus). Scanning TEM (STEM) images shown in this paper were recorded using a high-angle annular dark-field (HAADF) detector, with the detector inner angle/outer angle set to 54 mrad/144 mrad, respectively. Under these conditions, the STEM-HAADF contrasts are nearly proportional to the atomic number (Z-contrast image).

Electron energy-loss spectroscopy (EELS) spectra were recorded in two modes. The point spectra were recorded under the TEM-diffraction mode with a camera length of 25 cm with a dispersion of 0.2 eV per channel. The spectra were processed in Digital Micrograph (DM version 3.42, Gatan, USA). Firstly, the background was subtracted using the power-law model. For comparison, the spectra were then aligned to the N-K edge's onset to examine the variations of N-K and T-L edges, such as the chemical shift and shape change. EELS spectrum-images were acquired in the STEM mode using a dispersion of 0.2 eV per channel, a collection semi-angle of 10 mrad, and a convergence semi-angle of 2.5 mrad. The images were aligned to the N-K first peak and processed in DM. In the end, an energy difference map is obtained using the energy of the N-K first peak subtracting that of the N-K second peak, which can be used to distinguish the solid solution and layered region.

3. Results and discussions

3.1. As-deposited TiN/AlN structures

Superlattice coatings used in the present study are *rs*-TiN/*rs*-AlN deposited on MgO (100) and Si (100) substrates, where the AlN layer thickness is ~ 0.8 nm and the TiN layer thickness is ~ 1.7 nm. An overview of such epitaxial growth structure is displayed in the HAADF image (Fig. 1a). For SL grown on the MgO (100) substrate, since crystal structure and lattice constants between MgO and *rs*-TiN/*rs*-AlN are close, the coating has an entirely epitaxial single-crystalline structure (as seen in Figs. 1a-c). HRTEM (Fig. 1b) clearly reveals the atomic structure of a cubic-TiN/cubic-AlN a perfect epitaxial superlattice, where coating exhibits a single-crystalline structure. Measured interplanar spacings ($d_{(200)}$) in AlN and TiN layers are 2.0 Å and 2.1 Å, respectively, corresponding to the B1- AlN (with a lattice constant of 4.01–4.07 Å, Refs. [22,23]) and B1-TiN (with a lattice constant of 4.24 Å, JCPDF files: 38–1420). The analysis of the selected-area electron diffraction pattern (SAED) in Fig. 1c indicates that the projection direction is along cubic ⟨100⟩. Fig. 1c exhibits the superlattice spots (with some satellite spots), confirming that the periodic SL has a fully epitaxial growth of the cubic structures. In addition, a well-defined epitaxial SL (Figs. 1b-c) corroborates a thin AlN layer can be stabilized in the rock-salt structure.

For the coating grown on the Si substrate, epitaxial growth is not observed due to the presence of a native oxide on the Si (100) surface. The entire coating exhibits a polycrystalline microstructure with columnar growth features (as seen in Fig. 1d, low-magnification STEM-BF (scanning transmission electron microscopy bright-field) image, where the columnar grain boundaries are clearly visible). The width of the columnar crystals grown on the Si (100) substrate is 10–30 nm. The HRTEM observation (Fig. 1e, viewing on ⟨110⟩ direction) shows that the coating growth on the Si (100) substrate also has a rocksalt/rocksalt coherent interface structure within the individual columnar grains. However, the SAED over a larger region (Fig. 1f) presents an intense diffrac-

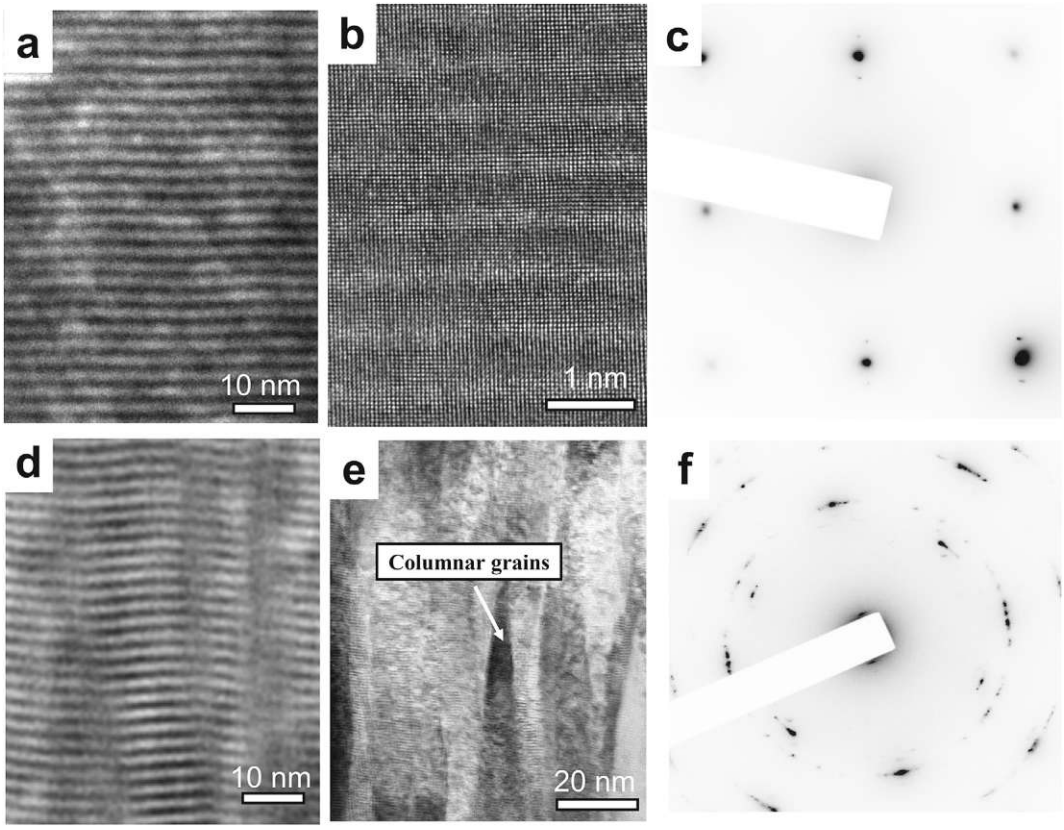

Fig. 1. a-c, as-deposited *rs*-TiN/*rs*-AlN superlattice on MgO (100) substrate. a, A cross-sectional HAADF image. b, A HRTEM image revealing the atomic structure of the as-deposited superlattice. c, A SAED pattern showing a spot pattern with satellite spots. ɒ-f, as-deposited *rs*-TiN/*rs*-AlN superlattice on Si (100) substrate. Due to the natural oxidation of the Si surface, the coating is in fact grown on SiO_x. d, A STEM-BF image. e, A HRTEM image showing the atomic structure. f, A SAED pattern (obtained using an aperture size of about 500 nm) exhibiting a continuous ring pattern.

tion ring in ⟨200⟩ reflection, which proves most of the columnar grains with ⟨100⟩ growth direction, i.e., {200} texture. Notably, both SAED patterns (Figs. 1c and 1f) indicate that the crystal structures are cubic and no wurtzite AlN phase is present in any of the as-deposited coatings (no extra spots/rings appearing). This also signifies that both coatings have a rocksalt/rocksalt SL structure despite being single-crystalline and polycrystalline.

3.2. Intermixing behavior in single-crystalline and polycrystalline SL coatings

3.2.1. Intermixing in the single-crystalline SL coating

Fig. 2a shows a TEM BF (bright-field) cross-sectional view of the indented SL on MgO (100) substrate. When moving close to the surface of the residual impression, the layered morphology cannot be detected anymore, instead a solid solution of uniform composition forms (as seen in the HRTEM image). A HRTEM image (Fig. 2b) shows that the solid solution has a cubic structure projected along the⟨100⟩ direction. Atomic-scale elemental mapping displayed in Fig. 2d reflects that superlattice interface intermixing has occurred at the area close to the indenter tip. Fig. 2d reveals that Al and Ti atoms reside at identical atom column positions, which finally confirms the formation of a cubic $Ti_{1-x}Al_xN$ solid solution from the *rs*-TiN/*rs*-AlN SL. However, at the region away from the impression surface, the coating still has a clear and perfect interface structure (Fig. 2c). Thus, we show that nanoindentation causes mechanical alloying in the TiN/AlN SL, ultimately resulting in the formation of a $Ti_{0.67}Al_{0.33}N$ single-phase solid solution under 100 mN. The solid solution forming process can be schematically illustrated in Fig. 2e, where Ti and Al atoms are randomly distributed in lattice. The chemical composition of this solid solution could be estimated from EDXS results, and it also fits the expected value, i.e., giving $x = 0.8/(1.7 + 0.8) = 0.33$ for $Ti_{1-x}Al_xN$ when mixing a 1.7 nm-thick TiN with a 0.8 nm-thick AlN.

After confirming that nanoindentation triggers interfacial mixing, here, we describe in detail the spatial distribution of the solid solution region at the tip position of the impression. The TEM-BF image in Fig. 3a displays the morphology of the indented coating (under 100 mN) in the impression tip region of the single-crystalline SL. At the position marked in frame (Fig. 3a), an HRTEM image was recorded, shown in Fig. 3b (atomic-resolution image projected in [100] direction). From the image, apparently, the lower part of the area has a layered structure while the upper part is a solid solution (with nearly homogeneous contrast, and no layered features). Therefore, according to Fig. 3b, intermixing of the two layers is observed in film regions up to ~150 nm away from the impression surface. The intermixing phenomenon alters the electronic structure of TiN (or AlN) accordingly [24]. Fig. 3c shows the core-level EELS recorded from the solid solution (near the surface) and the superlattice regions (away from the surface). A close comparison shows that for the solid solution region, the width between the second peak and the first peak of N-K is smaller than that in SL region ($\Delta E_{N\text{-}k} \approx 7$ eV in the solid solution region and $\Delta E_{N\text{-}k} \approx 8.5$ eV in the SL region). Through the fine differences in the electronic structure, we are able to map the distribution of the solid solution. Fig. 3d shows such a map, i.e., the measured energy difference ($\Delta E_{N\text{-}k}$) over a large area. The green-colored area in the upper part of the map corresponds to the solid solution zone, consistent with the HRTEM result, i.e., extending about ~150 nm from the impression surface.

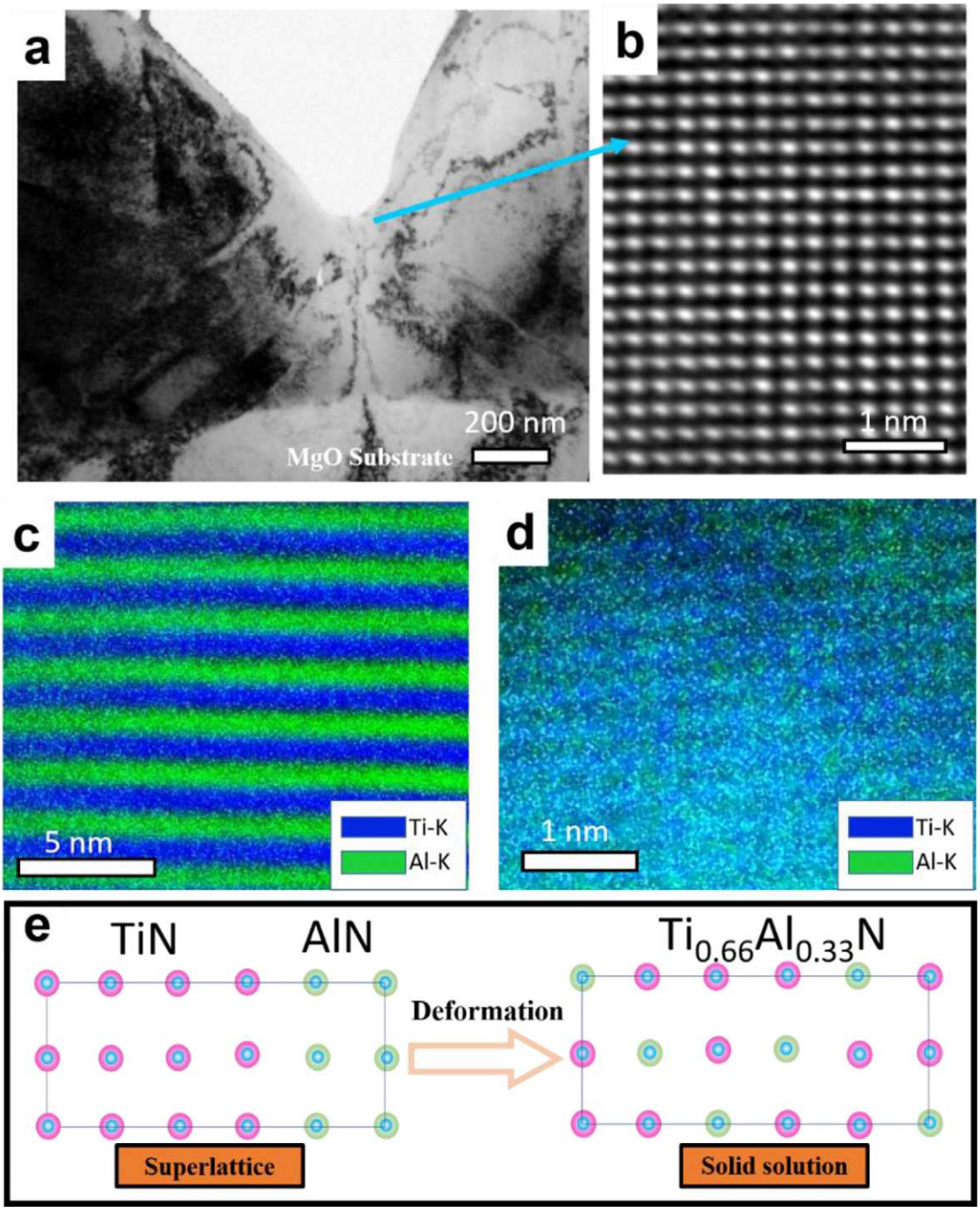

Fig. 2. a, A cross-sectional TEM-BF image of the indented (100 mN) *rs*-TiN/*rs*-AlN SL on MgO (100) substrate. b, A HRTEM image of the indented single-crystalline SL at the surface region. c, The elemental mapping (EDXS) at the position far away from the impression surface. d, Atomic-resolution elemental mapping in the surface region of the impression. e, Schematic atomic model illustration of the intermixing process, where the *rs*-TiN/*rs*-AlN SL evolves into a $Ti_{0.67}Al_{0.33}N$ solid solution.

3.2.2. Intermixing in the polycrystalline sl coating

(i) At the tip position of the impression

A TEM-BF image in Fig. 4a shows the morphology of the indented polycrystalline SL (film grown on the Si (100) substrate) at the tip region. In Fig. 4b, red marker locations indicate many areas with multilayer features. In contrast to the single-crystalline SL coating, we can easily detect multilayer features even at positions close to the impression surface, as shown in Fig. 4b. For the tip region, HRTEM observation (Fig. 4c) shows a solid solution feature, where no layer contrast is observed. More importantly, the observation position of Fig. 4c is only present very close to the tip surface. In comparison with the single-crystalline SL, the nanoindented polycrystalline SL forms a smaller 'intermixed' region. The EELS mapping result also more directly confirm these BF results. The energy difference mapping of the N-K edge (in Fig. 4d) shows that a 7 eV energy gap is detected only with a depth of 60 nm from the tip surface inwards. Thus, our EELS mapping results reveal that the extension of the solid solution in the polycrystalline SL coating at the tip region of the impression is much smaller than that in the single-crystalline SL coating (Fig. 3d).

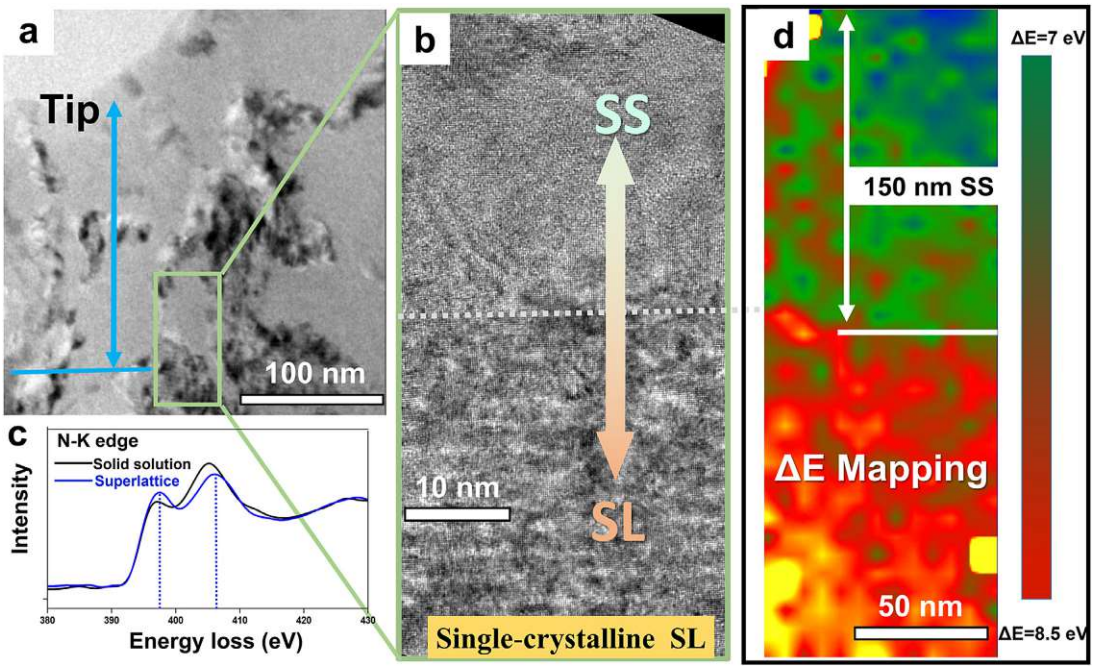

Fig. 3. a, A cross-sectional TEM-BF image of the indented single-crystalline SL at the tip position of the impression. b, A locally enlarged HRTEM image of the transition area (labeled in (a)) from the solid solution region to the SL region. c, EELS spectra (N-K edge) taken from near the surface (solid solution region) and a region away from the surface (SL region). d, EELS mapping using the energy difference ($\Delta E_{N\text{-}k}$) between the second and the first peak of N-K edge. It is approximately 7 eV near the surface (green) and 8.5 eV far away from the surface (red). (For interpretation of the references to colour in this figure legend, the reader is referred to the web version of this article.)

(ii) Comparison of the edge position of the impression

Moreover, there is almost no solid solution formation observable for the area far away from the tip of the polycrystalline SL impression. A HAADF image in Fig. 5a shows the morphology of the indented polycrystalline SL coating at the edge region of the impression. The HAADF image (Fig. 5b, from position 'b') confirms that the surface area of the impression is full of the layer feature. Similarly, the impression surface also exhibits a superlattice structure at position 'c' further away from the tip (Fig. 5c). However, for single-crystalline SL coating, besides the tip region of the impression, intermixing also occurred at the edge region of the impression. The HAADF image presented in Fig. 5d shows an overview of the morphology of the indented coating at the edge region of the impression. In position 'e', the HAADF image (Fig. 5e) shows that the solid solution region (without the presence of layer contrast) is present up to ~50 nm away from the contact surface. As moving further away from the tip, i.e., 'f' position, the HAADF image (Fig. 5f) shows that the 'f' position hardly presents any solid solution feature, but only a severely deformed layer structure. Therefore, compared to the single-crystalline SL coating (Fig. 5e, 5f), almost no layer intermixing has occurred at the edge of the impression of the polycrystalline coating. As already seen, even a very smaller intermixed zone created by nanoindentation, hard to be seen by conventional SAED [16], could still be visualized by utilizing advanced TEM methods.

In summary, for the single-crystalline SL coating, we evidenced the solid solution formation, the spatial extension solid solution zone gradually decreases at the indenter impression edge when moving away from the tip. The largest volume of the solid solution zone was observed rightly underneath the impression tip.

3.3. Deformation and fracture behavior in the single-crystalline SL coating

3.3.1. Deformation in the solid solution region

TEM results (Figs. 1a-c) show that the as-deposited coating grown on the MgO (100) substrate is a [100] grown 'single-crystalline' film with a completely epitaxial superlattice structure. However, after nanoindentation, SAED patterns exhibits obvious grains rotation features in the solid solution region. Here, SAED patterns recorded from 4 different positions (marked in Fig. 6a) are displayed in Fig. 6b. These positions demonstrate diffraction patterns from two solid solution regions (positions **2** and **3**) and two superlattice regions (positions **1** and **4**), as also seen in inserted atomic-resolution HRTEM images (Fig. 6a). In position **2**, the 'ring' feature in SAED pattern is slightly enhanced compared to the as-deposited SL (Fig. 1c). However, more pronounced grains rotation features are observed in the tip region, and the corresponding SAED pattern presents the ring-like pattern (Fig. 6b, positions **3**). This strongly suggests more randomly oriented grains and more severe grain rotation behavior in the solid solution region. In addition, the series of dark-field images (Figs. 6c and 6d, using one portion of {200} reflection) also indicate that the nanocrystalline solid solution has a smaller grain size at the tip region, but a larger grain size further away from the tip region (Figs. 6e and 6f). Here, the created solid solution region (on MgO (100) substrate) in the single-crystalline SL by nanoindentation is mainly composed of equiaxed grains. Differently, the polycrystalline SL on the Si (100) substrate consists of columnar grains with a width of tens of nanometers and a texture characteristic (see Fig. 1d).

Through HRTEM, we further characterized the GB (grain boundary) atomic structures in the solid solution region. Fig. 7a shows a TEM-BF image of the surface region of the impression, where an equiaxed grain with 100 nm in size can be observed. In this grain, HRTEM observations (Figs. 6b-d, the atomic-resolution image projected in [100] direction) hardly show any multilayer features, indicating that such an equiaxed grain is a cubic $Ti_{0.67}Al_{0.33}N$ solid solution instead of the TiN/AlN SL. Further observations performed at different positions (Figs. 7b and c) reveal a 5°–18° tilt angle between the grain boundaries. There is even a sub-grain boundary comprised of an array of edge dislocations within such an equiaxed grain (Fig. 7d). The lattice rotation angle map of the corresponding

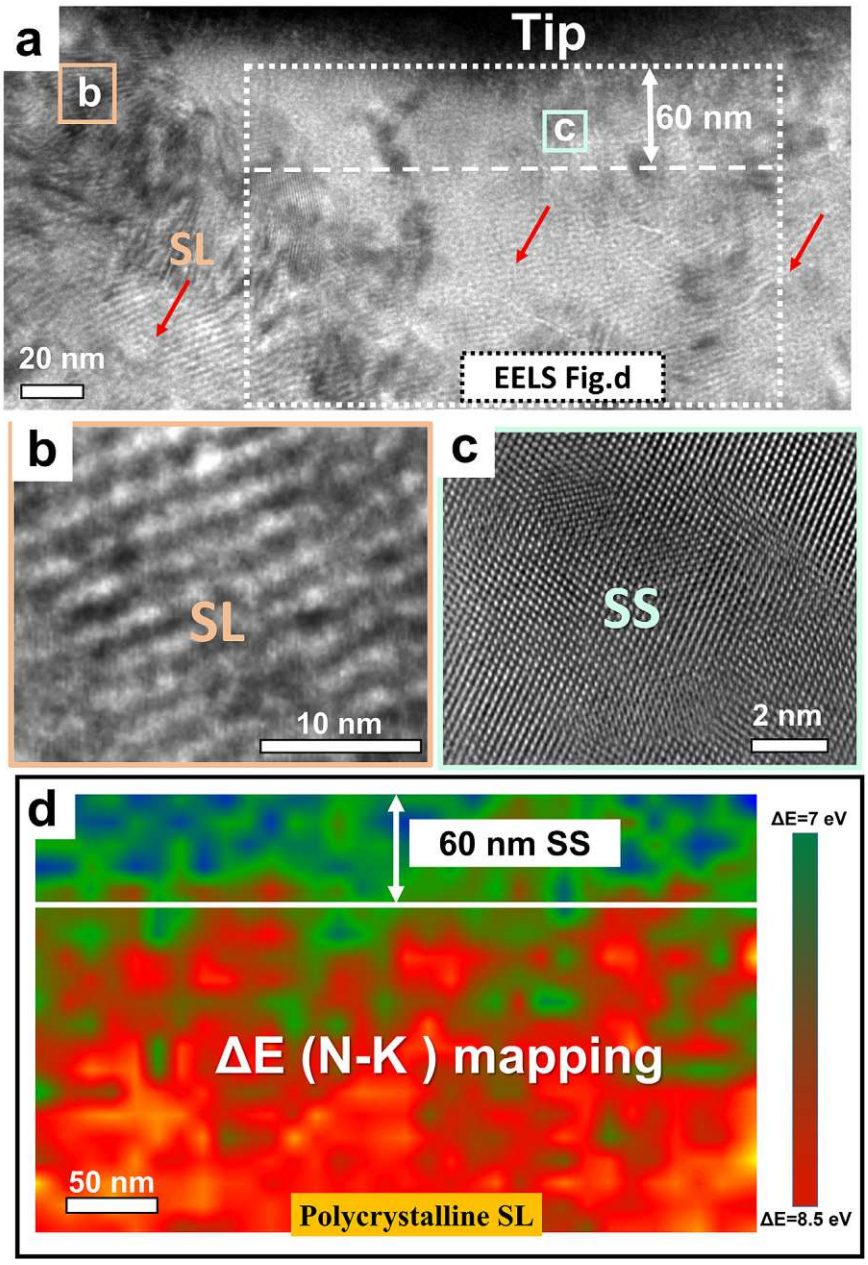

Fig. 4. a, A cross-sectional TEM-BF image of the indented polycrystalline SL at the tip position of the impression, where red labels show the position with multilayer features. b, Enlarged TEM-BF image (position marked in Fig. 4a). c, HRTEM observation at the tip position of the impression. d, EELS mapping of the energy difference between N-K second peak and N-K first peak. The energy difference on the surface (green area) is approximately 7 eV and far away from the surface (red area) is approximately 8.5 eV. (For interpretation of the references to colour in this figure legend, the reader is referred to the web version of this article.)

region reveals that the tilt angle across the boundary is about 2–5° (as shown in Fig. 7e).

For the contact surface of the indenter, we believe that the total volume of the solid solution area increases as the indentation depth increases. This is because the multilayer region accompanied with high dislocation density will continue to transform into a solid solution with proceeding indentation, and finally form a large solid solution region as observed. Previous molecular dynamics (MD) simulation results [20] show that when the load depth is about 3 nm, a solid solution has already been formed. This indicates that the solid solution behavior occurs in the very early stage of the indentation event. After the solid solution is formed, it has the potential to lower the resistance to shear and favors dislocation glide by modifying the electronic effects (high valence electron concentration) and bonding characteristic [25,26]. Since intragranular dislocations are easily redistributed in a solid solution region (from dislocation accumulation before intermixing), the deformation in solid solution region will be mediated by grain rotations, including the structural evolution from the initial larger solid solution grains (come from the SL intermixing)—sub-grainboundaries—small-angle grain boundaries—large-angle grain boundaries. In the tip region of the impression, where the local stress is large, more serious rotation deformation in the nanocrystalline solid solution takes place. This statement is also confirmed by the fact that the tip of the impression possesses much more refined grains and the presence of a larger fraction of high-angle grain boundaries (as seen in the SAED, i.e., Fig. 6b and Supplementary Figs. S1).

3.3.2. SL interface distortion

At the edge area of the impression (Fig. 8a), we observed a special superlattice zone with severely distorted interfaces in the single-crystalline SL. The HAADF image (Fig. 8b) shows the

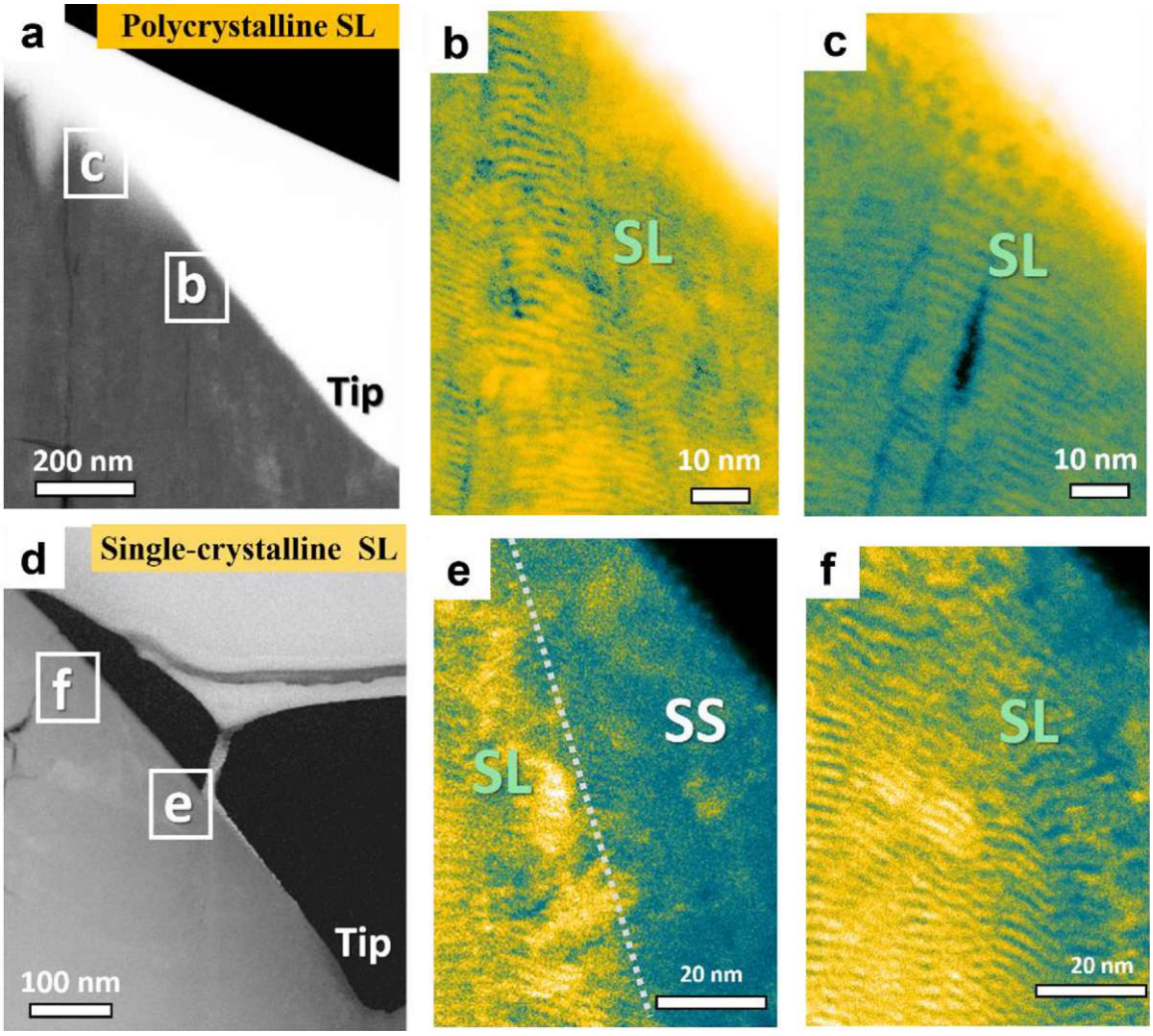

Fig. 5. a, STEM-HAADF image of the indented polycrystalline SL near the edge position of the impression. b and c, Higher magnification HAADF images taken from different locations (as framed in a) showing the distribution of the $Ti_{0.67}Al_{0.33}N$ solid solution zone at the edge position of the impression. d, STEM-HAADF image of the single-crystalline SL near the edge position of the impression. e and f, Higher magnification STEM-HAADF images show the distribution of $Ti_{0.67}Al_{0.33}N$ solid solution on the different edge positions of the impression (as framed in d). 'SS', 'SL', and dotted lines stand for$Ti_{0.67}Al_{0.33}N$ solid solution, TiN/AlN superlattice, and boundaries in-betweens.

morphology of such distorted interfaces, where the interfaces become rather rough and disrupted, and the layer morphology locally exhibits prominent bends and distortions. At the edge of the impression, this interface distortion structure is mainly distributed near the contact surface of the indenter, further deep inside the coating, the 'flat' interface morphology still retains (not shown here). Looking specifically at the structure of the distorted interfaces zone, we observed that the SL here was fragmented into small pieces (Fig. 8c). Compared to the solid solution region, no obvious grain boundary structure between these fragments is found. And, the HRTEM image (Fig. 8d) clearly shows very high densities of edge dislocations present in these distorted interface regions. The dislocations are present not only near the TiN/AlN interfaces but also inside the individual TiN or AlN layer. Thus, these TEM observations unravel that the dislocation densities in the interface distortion region are greatly increased as compared to the as-deposited SL interfaces.

However, we hardly observed the severe interface distortion and bending rightly beneath the tip region of the impression. In Fig. 8e, the contact surface of the impression tip is a solid solution without any layered features (not shown here). Along the compression direction of the indenter, we only observed a 'flat interface' and no distorted interface distribution (as seen in Fig. 8f). Based on the observations, we may simply conclude that SL interface distortions mainly appear at the indenter edge where the shear deformation is dominant, while it is barely distributed at the tip area where the local stress is more concentrated.

3.3.3. SL slip deformation

The deformation of single-crystalline TiN coating has been studied in the past either by TEM or by calculating the crystallographic anisotropy using Schmid's law [27]. The primary slip system for dislocation glide in TiN crystals has been identified. Slip primarily occurs on {110} planes along the ⟨110⟩ directions [27,28]. Our results evidence that slipping, similar to TiN single-crystals, can also be found in single-crystalline TiN/AlN SL coating that occurs at the SL region away from the impression surface and gradually approaching to the MgO substrate.

For a better understanding of the scale of the slip deformation, we also characterized the slip deformation under 100 mN and 150 mN loads (as seen in Fig. 9a and 9b). For the 100 mN-indented sample (Fig. 9a), several slip lines (6 slip lines) along the ⟨110⟩ direction are observed, and the distance between these slip lines is about ~100–150 nm. Under a larger indent load (150 mN,

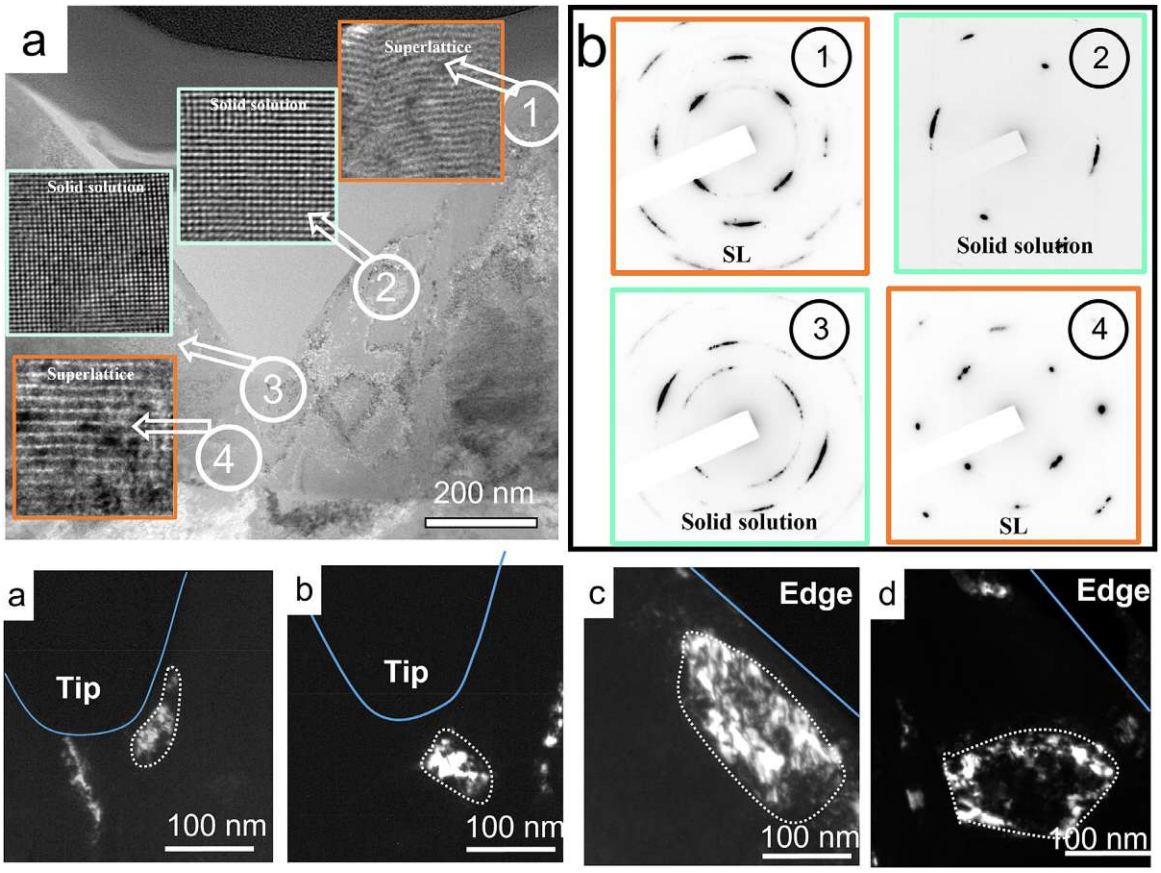

Fig. 6. a, TEM-BF image of the indented single-crystalline SL. Inserted images showing HRTEM images taken from the labeled positions 1–4. b, Corresponding SAED results in positions 1–4. The diameter of the selected area aperture used is about 150 nm. Note the differences in the SAED patterns of the different locations. c-f, TEM dark-field images were taken from the tip of the impression (c and d) and the edge area (e and f) using $\vec{g}$= [200] reflections of the cubic. In Fig. 6b, the enlarged image (position 4, inset) indicates the extra spots, confirming the presence of periodic SL structure. Please note that in Position 1, the faint diffractions due to the surface protective layer (Pt from FIB) are accidentally located at the satellite spot positions.

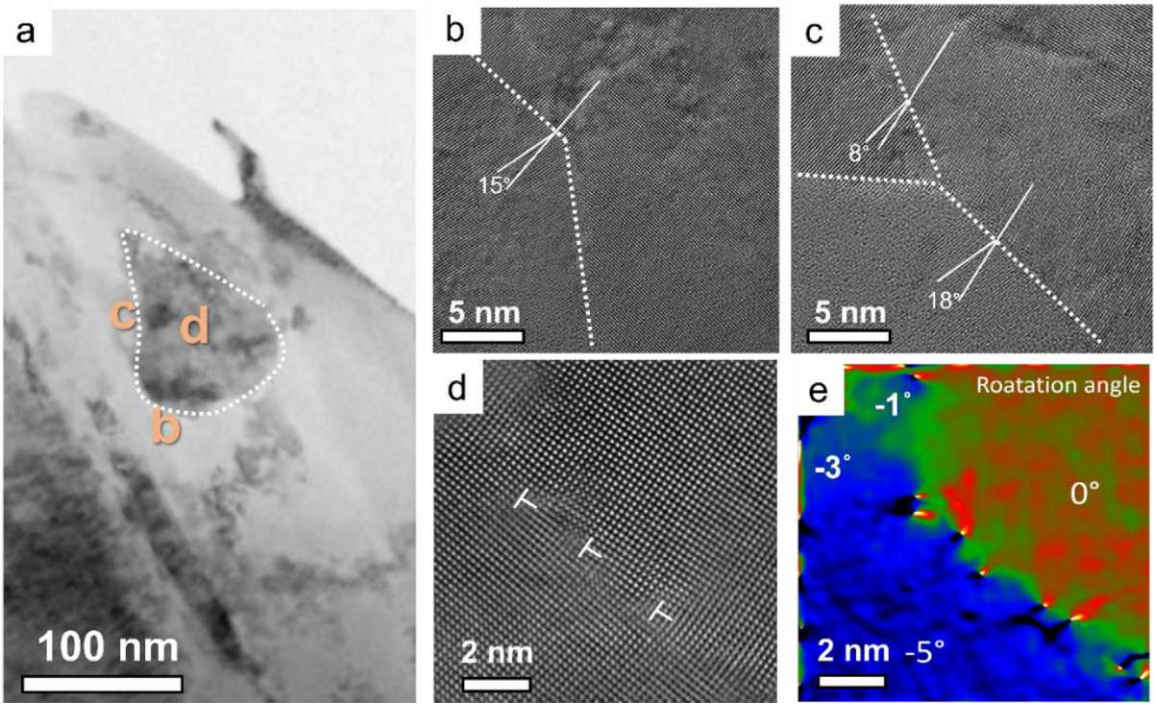

Fig. 7. a, A TEM-BF image of a nanocrystalline solid solution zone (one grain is indicated) in the indented single-crystalline SL. b-d, HRTEM images of grain boundary structures taken from different positions (labeled in a) in the solid solution zone. e, Lattice rotation angle mapping of d. Different boundaries labelled by dotted lines or an array of dislocations are clearly visible.

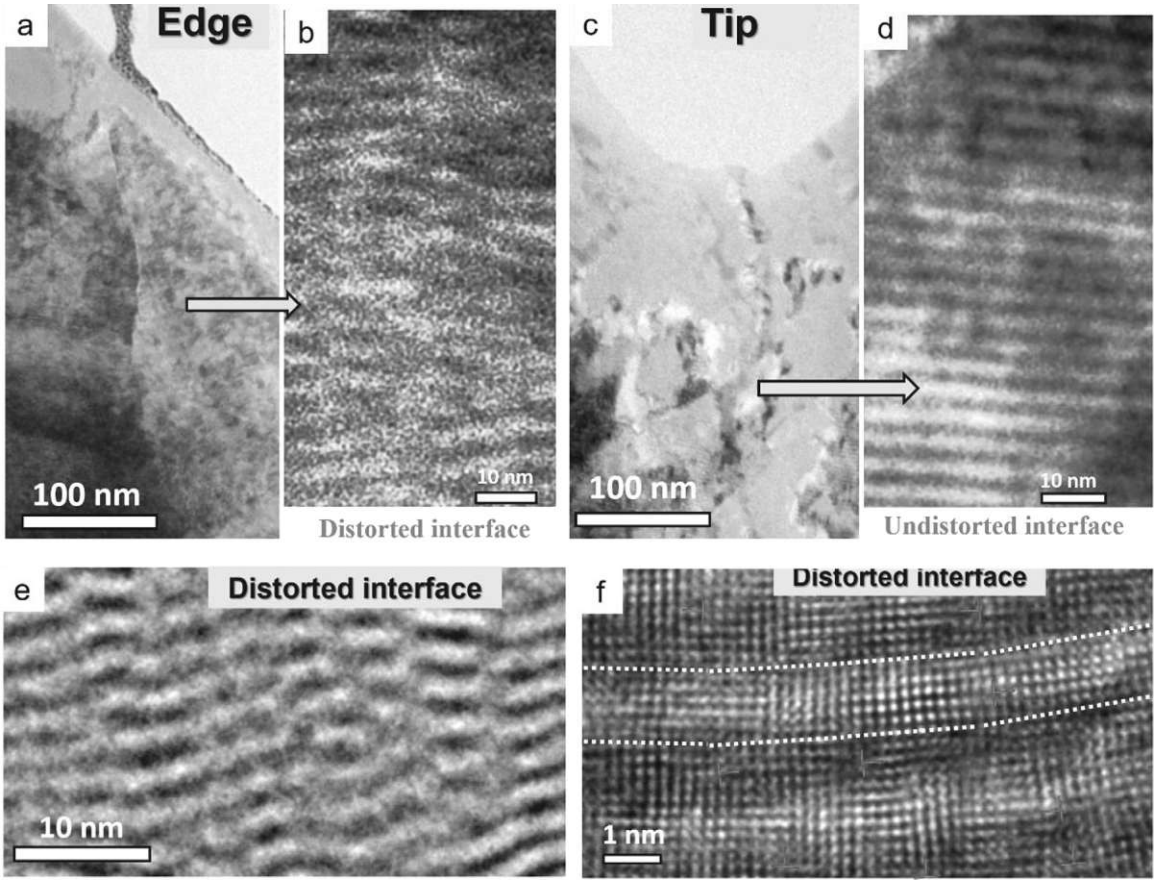

Fig. 8. a, A cross-sectional TEM-BF image of the indented single-crystalline SL at the edge position of the impression. b, A STEM-HAADF image recorded from one position in a showing the morphology SL interfaces. c, A TEM-BF image of the distorted. d, HRTEM observation result of the interface distortion region. e, A cross-sectional TEM-BF image of indented single-crystalline SL at the tip position of the impression. f, the STEM-HAADF observation results from one corresponding position in e.

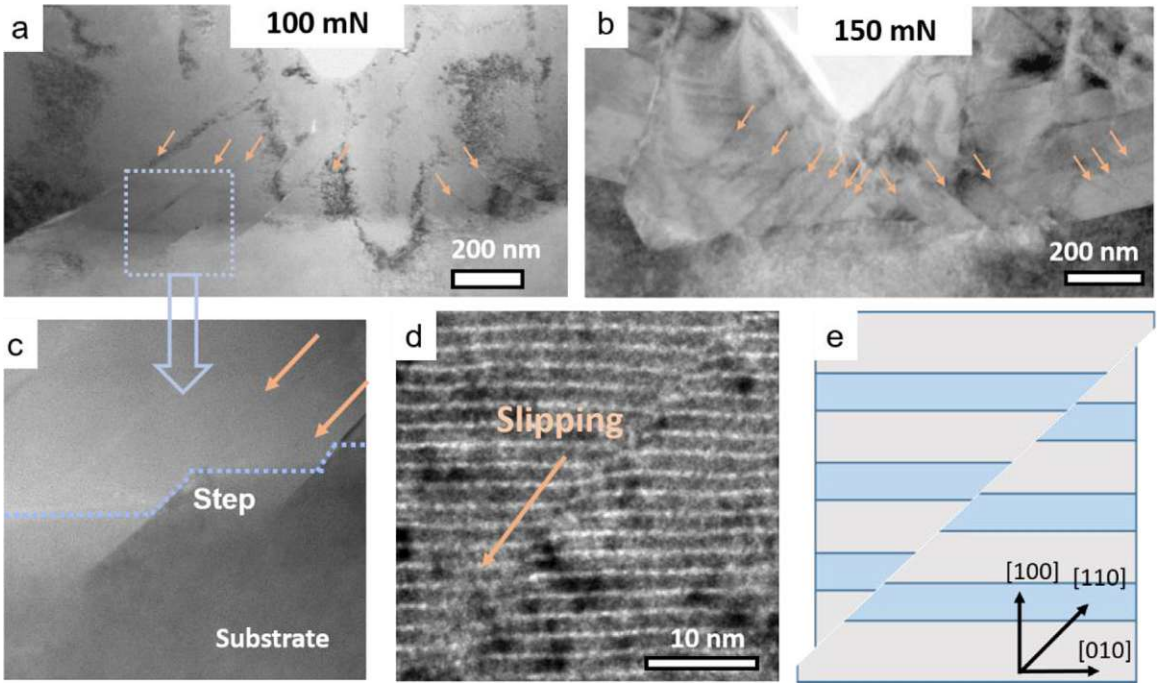

Fig. 9. a, b, Overall morphology of the single-crystalline SL under 100 mN and 150 mN load, respectively. The arrows indicate slip lines. c, The STEM-HAADF results of the corresponding area in a. d, The high magnification TEM BF image shows the slip deformation along the ⟨110⟩ direction. e, A schematic diagram of SL slip direction.

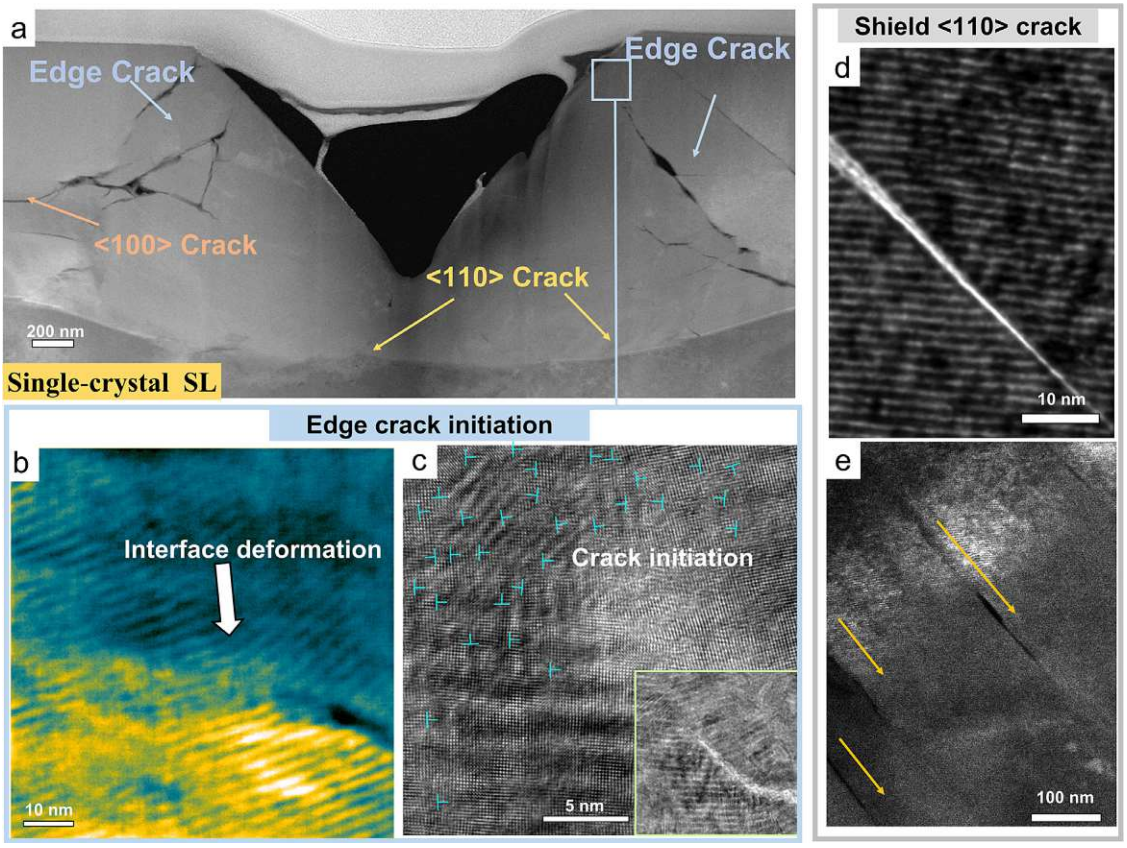

Fig. 10. a, Overview morphology (STEM-HAADF image) of the indented single-crystalline SL (under 100 mN) some cracks along different directions are clearly visible. b, detailed STEM-HAADF observation of the crack initiation region at the edge position of the impression. c, HRTEM observation near the crack initiation. The inserted image shows the low-magnification morphology of the crack tip area. D-e, TEM-BF and STEM-HAADF observations of the fracture behavior in the main slip direction (<110> direction).

Fig. 9b), the scale of slip deformation is greatly increased. Comparatively, the TEM BF result (Fig. 9b) shows that the density of the slip lines at 150 mN (12 slip lines are observed) is significantly higher than that under 100 mN. In addition, the step height on the interface under different loads is also different. Fig. 9c (100 mN) shows the TEM-BF image taken near the substrate area, and an obvious shearing step can be found, where the step height is ~30 nm. For the 150 mN-indented sample, the step height can reach up to ~100 nm. Detailed high-magnification TEM-BF observation (Fig. 9d) confirmed the sliding deformation in the 45° direction of the SL interface, i.e., sliding deformation of the SL along the ⟨110⟩ direction. Meanwhile, the interfaces near the SL slip lines are very flat and smooth, as shown in Fig. 9d A schematic drawing illustrates the sliding process happening along the 45° direction relative to the SL interface (Fig. 9e).

In short, strains generated by nanoindentation in the single-crystalline SL could be released by various deformation mechanisms, depending on the locations relative to the indenter. These cover: a polycrystalline deformation mode (i.e., grain rotation) in the solid solution area just rightly at the tip, distortion of the SL interfaces at the edge of the impression, and SL slip deformation far away from the contact surface.

3.3.4. Fracture in the single-crystalline SL coating

The fracture behavior of the single-crystalline SL coating was closely observed after an indent was made using a sharp cube-corner indenter and a maximum load of 100 mN. Low-magnification HAADF observation (Fig. 10a) shows that cracks are mainly located in the SL area at the edge of the impression, while the solid solution area (at the tip and edge region of the impression surface) barely exhibit any cracks. At the edge of the impression, cracks have an irregular extending direction, e.g., parallel to the interface direction, perpendicular to the interface direction, or along the interface direction at 45°, etc. For the cracks at the impression edge, Fig. 10b through 10c depicts the specific microscopic interface morphology of the initiation area. The interfaces in these areas are severely deformed. HRTEM observation on the corresponding position (Fig. 10c) shows the microscopic morphology of the crack initiation area, where the interface in the front of the crack demonstrates significant distortions and a very high dislocation density (as indicated). Accordingly, we can confirm that the initiation of cracks can be related to the accumulation of dislocations at the SL region of the impression edge. In addition to the edge of the impression, some micro-cracks along the sliding direction are observed. These cracks are titled 45° with respect to ⟨100⟩ growth direction (as seen in Fig. 10d), i.e., cracks along the ⟨110⟩ direction. But these ⟨110⟩ direction cracks can only travel a limited distance, i.e., only about 100 nm into the coating, as shown in Fig. 10e.

In a nutshell, for the single-crystalline SL, cracks mainly initiate and propagate in the SL area that is enriched with the distorted interfaces. Both the solid solution zone and the SL area without interface distortions may effectively prevent crack initiation and propagation.

3.4. Deformation and fracture behavior in polycrystalline SL coating

Polycrystalline SL coating has completely different deformation and fracture mechanisms from the single-crystalline SL coating. Fig. 11a shows the overall morphology of the polycrystalline SL

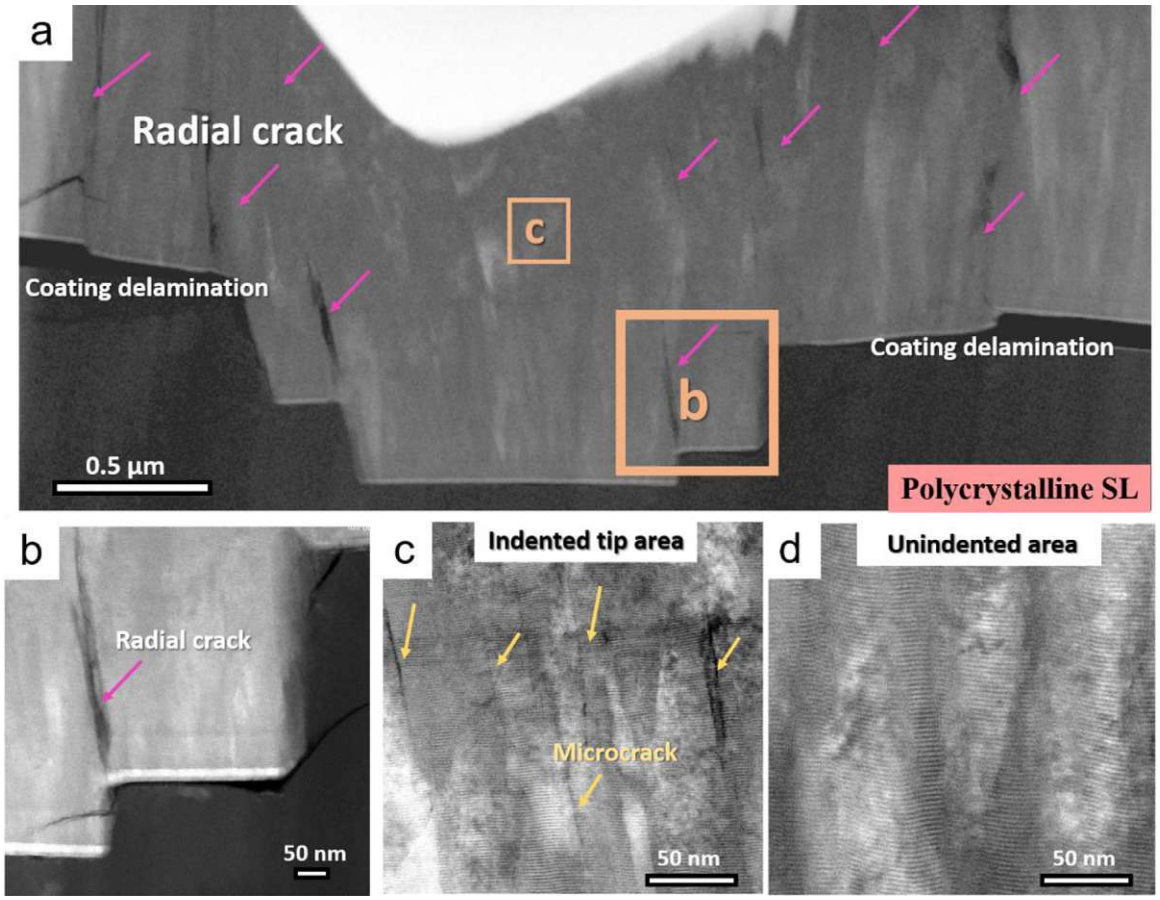

Fig. 11. a, Overall morphology (STEM-HAADF) of the indented polycrystalline SL (under 100 mN) with radial cracks being clearly visible. b and c, Detailed STEM-HAADF observation result of the corresponding areas in a (framed). d, STEM-HAADF observation result of the area not affected by the indentation.

coating after nanoindentation. For the fracture, Fig. 11a depicts that polycrystalline SL coating mainly has radial cracks perpendicular to the interface direction. These macroscopic cracks may propagate a distance of hundreds of nanometers (about 410 ~940 nm) and reach the substrate interface (as seen in Fig. 11b). Meanwhile, the indentation can cause the coating to delaminate from Si substrate (Fig. 11b). In addition to the obvious macroscopic fractures, a high density of micro-cracks is also observed at the tip area of the impression (Fig. 11c). These high-density micro-cracks are found only at the tip area of the impression, barely visible away from the tip (Fig. 11d, crack-free). TEM image shows that the shear steps appear along the column's slide direction, and continue to the coating-Si substrate interface. The formation of radial cracks can be considered as the gap between two adjacent steps be fractured by imposing more restraint and restraint on the columnar slip at the coating-substrate interface [16]. Furthermore, due to the lack of an epitaxial relationship and more unstable Si-N bonding [29], the film on the Si substrate easily delaminates and causes catastrophic failure.

As seen in Fig. 11a, the deformation in the polycrystalline SL coating is mainly governed by the sliding of columnar grain boundaries [30]. The strains generated by nanoindentation are released through shearing of the columnar grains. In Fig. 11a, the obvious sliding steps at the height of 80–350 nm in the substrate are observed, and the SL films are pushed into the substrate. Compared with the sliding step near the coating substrate of the single crystal SL (100 mN in Fig. 9a, and 150 mN in Fig. 9b, where comparably small steps), the polycrystalline coating demonstrates larger sliding steps. Since significant energies could be dissipated by sliding deformation, this actually prevents large-scale interface distortion and alloying in the polycrystalline SL coating.

For columnar grain boundaries, it is easy to cause stress concentration during deformation. As a result, the interface distortion, dislocation accumulation and SL alloying can occur only near the GBs or crack regions. Fig. 12a depicts the multilayer morphology near the impression tip. Near the columnar GB (Fig. 12b), SL interfaces are obviously bent and distorted. Furthermore, the interface of the local area adjacent to the GB is not very clear (near yellow label), which implies a mixing phenomenon. However, a few nanometers away from the columnar GB (Fig. 12c), the interfaces are sharp, un-deformed and present a 'flat' feature. In addition to the GB region, a small-scale interface distortion and SL intermixing can also be observed near the cracks. Fig. 12d shows the morphology of one crack nearby in the columnar crystals. HRTEM observations (Fig. 12e) reveal that no layer features near the crack (as marked by the dotted-line area). This proves that there exists a localized intermixing zone adjacent to the crack. Meanwhile, HRTEM observations (Fig. 12f) also reveal the interface distortion near the crack and a high amount of dislocations (as indicated). However, it should be mentioned that the high dislocation density and the interface distortions appear only in the very vicinity of the crack. About 5 nm away from the crack (Fig. 12g, position 'g' labeled in Fig. 12d), the interfaces exhibit a perfectly coherent state and maintain a low dislocation density. Therefore, these atomic-resolution observations indicate that the interfacial intermixing and interfacial deformation in polycrystalline SL still occur locally (near the crack or GB) but with a low scale.

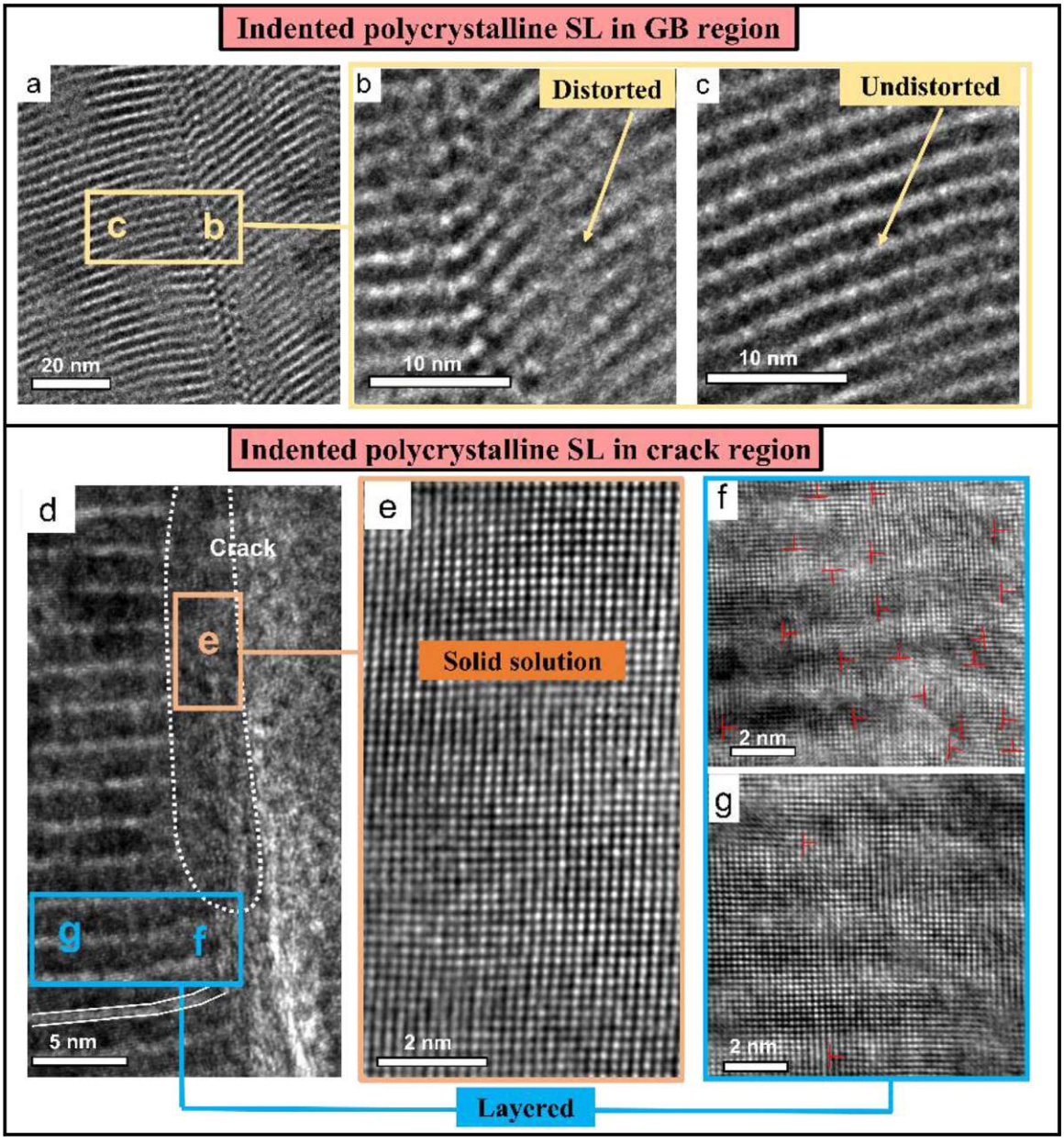

Fig. 12. a-c, A TEM-BF image of the indented polycrystalline SL from the columnar GB region. d, A TEM-BF image of near radial crack front in the polycrystalline SL. The white marked area demonstrates no multilayer feature is present next to the front of the crack. e-g, HRTEM observation results of the corresponding areas marked in d without layered features (e) and with layered features (f, g).

4. Conclusions

The microstructures of nanoindented single-crystalline and polycrystalline TiN/AlN SLs (Λ=2.5 nm) were intensively investigated using Cs-corrected TEM and FIB sectioning. Through atomic-scale TEM observations, we observe a variety of deformation mechanisms to be active in the single-crystalline SL coating, including SL interface distortion, SL slip deformation, solid solution formation and polycrystalline grain rotation in the solid solution. However, columnar grain boundary sliding along the loading direction is the predominant deformation mechanism in the polycrystalline SL coating, and interface distortion and SL alloying occur only locally in regions near the columnar grain boundaries. Hence, due to the difference in the deformation mechanisms, the single-crystalline SL exhibits a larger scale of solid solution than the polycrystalline S. For single-crystalline SL, the largest volume of the solid solution zone was observed rightly underneath the impression tip, and the spatial extension of this zone gradually decreases at the indenter's impression edge when moving away from the tip.

Declaration of Competing Interest

The authors declare that they have no known competing financial interests or personal relationships that could have appeared to influence the work reported in this paper.

Acknowledgements

This work is financially supported by FWF P 33696 (Z.C, Y.H., Z. Z). The authors thank M. Fallmann, for the film deposition and SEM characterization, and the USTEM at TU Wien for the TEM sample preparation. Z.G. thanks the China Scholarship Council (CSC, 201908440933) for the support. This work is also supported by FWF I 4720 (M.B.).

Supplementary materials

Supplementary material associated with this article can be found, in the online version, at doi:10.1016/j.actamat.2022.118008.

References

[1] H.A. Jehn, Multicomponent and multiphase hard coatings for tribological applications, Surf. Coat. Technol. 131 (1) (2000) 433–440.
[2] B.O. Postolnyi, V.M. Beresnev, G. Abadias, O.V. Bondar, L. Rebouta, J.P. Araujo, A.D. Pogrebnjak, Multilayer design of CrN/MoN protective coatings for enhanced hardness and toughness, J. Alloys Compd. 725 (2017) 1188–1198.
[3] H. Holleck, V. Schier, Multilayer PVD coatings for wear protection, Surf. Coat. Technol. (1995) 328–336 76-77.
[4] S.J. Bull, A.M. Jones, Multilayer coatings for improved performance, Surf. Coat. Technol. 78 (1) (1996) 173–184.
[5] G.S. Kim, S.Y. Lee, J.H. Hahn, S.Y. Lee, Synthesis of CrN/AlN superlattice coatings using closed-field unbalanced magnetron sputtering process, Surf. Coat. Technol. 171 (1) (2003) 91–95.
[6] J. Lin, J.J. Moore, B. Mishra, M. Pinkas, W.D. Sproul, Nano-structured CrN/AlN multilayer coatings synthesized by pulsed closed field unbalanced magnetron sputtering, Surf. Coat. Technol. 204 (6) (2009) 936–940.
[7] R. Hahn, M. Bartosik, R. Soler, C. Kirchlechner, G. Dehm, P.H. Mayrhofer, Superlattice effect for enhanced fracture toughness of hard coatings, Scr. Mater. 124 (2016) 67–70.
[8] J. Buchinger, N. Koutná, Z. Chen, Z. Zhang, P.H. Mayrhofer, D. Holec, M. Bartosik, Toughness enhancement in TiN/WN superlattice thin films, Acta Mater. 172 (2019) 18–29.
[9] J.S. Koehler, Attempt to design a strong solid, Phys. Rev. B 2 (2) (1970) 547–551.
[10] N. Koutná, P. Řehák, Z. Chen, M. Bartosik, M. Fallmann, M. Černý, Z. Zhang, M. Friák, M. Šob, P.H. Mayrhofer, D. Holec, Correlating structural and mechanical properties of AlN/TiN superlattice films, Scr. Mater. 165 (2019) 159–163.
[11] P.C. Yashar, W.D. Sproul, Nanometer scale multilayered hard coatings, Vacuum-Vacuum 55 (3) (1999) 179–190.
[12] R.G. Hoagland, R.J. Kurtz, C.H. Henager, Slip resistance of interfaces and the strength of metallic multilayer composites, Scr. Mater. 50 (6) (2004) 775–779.
[13] Z. Zhang, X. Gu, D. Holec, M. Bartosik, P.H. Mayrhofer, H.P. Duan, Superlattice-induced oscillations of interplanar distances and strain effects in the CrN/AlN system, Phys. Rev. B 95 (15) (2017) 155305.
[14] J.J. Roa, E. Jiménez-Piqué, R. Martínez, G. Ramírez, J.M. Tarragó, R. Rodríguez, L. Llanes, Contact damage and fracture micromechanisms of multilayered TiN/CrN coatings at micro- and nano-length scales, Thin Solid Films 571 (2014) 308–315.
[15] K. Bobzin, T. Brögelmann, N.C. Kruppe, M. Arghavani, J. Mayer, T.E. Weirich, Plastic deformation behavior of nanostructured CrN/AlN multilayer coatings deposited by hybrid dcMS/HPPMS, Surf. Coat. Technol. 332 (2017) 253–261.
[16] A. Azizpour, R. Hahn, F.F. Klimashin, T. Wojcik, E. Poursaeidi, P.H. Mayrhofer, Deformation and cracking mechanism in CrN/TiN multilayer coatings, Coatings 9 (6) (2019) 363.
[17] J. Buchinger, L. Löfler, J. Ast, A. Wagner, Z. Chen, J. Michler, Z.L. Zhang, P.H. Mayrhofer, D. Holec, M. Bartosik, Fracture properties of thin film TiN at elevated temperatures, Mater. Des. 194 (2020) 108885.
[18] N.J.M. Carvalho, J.T.M. De Hosson, Deformation mechanisms in TiN/(Ti,Al)N multilayers under depth-sensing indentation, Acta Mater. 54 (7) (2006) 1857–1862.
[19] S.J. Lloyd, A. Castellero, F. Giuliani, Y. Long, K.K. McLaughlin, J.M. Molina-Aldareguia, N.A. Stelmashenko, L.J. Vandeperre, W.J. Clegg, Observations of nanoindents via cross-sectional transmission electron microscopy: a survey of deformation mechanisms, Proceedings of the Royal Society A: Mathematical, Phys. Eng. Sci. 461 (2060) (2005) 2521–2543.
[20] Z. Chen, Y. Zheng, L. Löfler, M. Bartosik, G.K. Nayak, O. Renk, D. Holec, P.H. Mayrhofer, Z. Zhang, Atomic insights on intermixing of nanoscale nitride multilayer triggered by nanoindentation, Acta Mater. 214 (2021) 117004.
[21] M. Fallmann, Z. Chen, Z.L. Zhang, P.H. Mayrhofer, M. Bartosik, Mechanical properties and epitaxial growth of TiN/AlN superlattices, Surf. Coat. Technol. 375 (2019) 1–7.
[22] S. Uehara, T. Masamoto, A. Onodera, M. Ueno, O. Shimomura, K. Takemura, Equation of state of the rocksalt phase of III–V nitrides to 72 gpa or higher, J. Phys. Chem. Solids 58 (12) (1997) 2093–2099.
[23] L.H. Shen, X.F. Li, Y.M. Ma, K.F. Yang, W.W. Lei, Q.L. Cui, G.T. Zou, Pressure-induced structural transition in AlN nanowires, Appl. Phys. Lett. 89 (14) (2006) 141903.
[24] D. Holec, R. Rachbauer, D. Kiener, P.D. Cherns, P.M.F.J. Costa, C. McAleese, P.H. Mayrhofer, C.J. Humphreys, Towards predictive modeling of near-edge structures in electron energy-loss spectra of AlN-based ternary alloys, Phys. Rev. B 83 (16) (2011) 165122.
[25] D.G. Sangiovanni, L. Hultman, V. Chirita, I. Petrov, J.E. Greene, Effects of phase stability, lattice ordering, and electron density on plastic deformation in cubic TiWN pseudobinary transition-metal nitride alloys, Acta Mater. 103 (2016) 823–835.
[26] D.G. Sangiovanni, L. Hultman, V. Chirita, Supertoughening in B1 transition metal nitride alloys by increased valence electron concentration, Acta Mater. 59 (5) (2011) 2121–2134.
[27] M. Odén, H. Ljungcrantz, L. Hultman, Characterization of the induced plastic zone in a single crystal TiN(001) film by nanoindentation and transmission electron microscopy, J. Mater. Res. 12 (8) (2011) 2134–2142.
[28] L. Hultman, M. Shinn, P.B. Mirkarimi, S.A. Barnett, Characterization of misfit dislocations in epitaxial (001)-oriented TiN, NbN, VN, and (Ti,Nb) N film heterostructures by transmission electron microscopy, J. Cryst. Growth 135 (1) (1994) 309–317.
[29] Y. Wang, W. Wang, S. Fang, B. Dai, J. Zhu, The interface characteristics of TiN(100)/MgO(100) multilayer on oxidized Si(100) substrate via first-principle calculations and experimental investigation, Mol. Simul. 47 (7) (2021) 552–559.
[30] H.R. Azizpour A, F.F. Klimashin, T. Wojcik, E. Poursaeidi, P.H. Mayrhofer, Deformation and cracking mechanism in CrN/TiN multilayer coatings, Coatings 9 (2019) 363.

Acta Materialia 234 (2022) 118009

Contents lists available at ScienceDirect

Acta Materialia

journal homepage: www.elsevier.com/locate/actamat

Atomic-scale understanding of the structural evolution in TiN/AlN superlattice during nanoindentation—Part 2: Strengthening

Zhuo Chen[a], Yonghui Zheng[a,b], Yong Huang[a], Zecui Gao[c], Huaping Sheng[a], Matthias Bartosik[c,d], Paul H. Mayrhofer[c], Zaoli Zhang[a,*]

[a] Austrian Academy of Sciences, Erich Schmid Institute of Materials Science, Leoben A-8700, Austria
[b] Key Laboratory of Polar Materials and Devices (MOE), Department of Electronics, East China Normal University, Shanghai 200241, China
[c] Institute of Materials Science and Technology, TU Wien, Vienna A-1060, Austria
[d] Department of Materials Science, Montanuniversität Leoben, Leoben A-8700, Austria

ARTICLE INFO

Article history:
Received 2 March 2022
Revised 29 April 2022
Accepted 4 May 2022
Available online 5 May 2022

Keywords:
Transition metal nitride coating
Superlattice
HRTEM
Nanoindentation
Deformation
Strengthening

ABSTRACT

The mechanical properties of superlattice (SL) TMN (transition-metal nitrides) coatings with different as-deposited structures are often quite different. These differences in mechanical properties can be attributed to distinct deformation and strengthening mechanisms. Here, we discuss the strengthening mechanisms of single- and poly-crystalline SLs under nanoindentation loads. We observe that the dislocation behaviors during nanoindentation, such as dislocation accumulation and crossing interfaces, are responsible for the strengthening of single-crystalline SL coating, whereas no such pronounced strengthening is observed in the polycrystalline SL. We further reveal the monoclinic phase transformation occurring at the SL, solid solution zone, and crack tip region in the single-crystalline coating. Phase transformation alters the SL interface's structure, facilitating dislocation accumulation. Consequently, it raises the theoretical yield stress of single-crystalline coating. For polycrystalline coating, we observed a localized monoclinic phase present only near the crack tip. The current research unravels TMN SL strengthening mechanism at the atomic scale.

1. Introduction

Since the mid-1980s, the deposition method and the growth mechanism of super-hard TMN (transition-metal nitride) multilayer coatings have been reported [1–6]. For the early coatings, it was just a simple arrangement of two TMNs with different compositions alternately with the thickness of hundreds of nanometers. However, further studies show that a significant reduction of the thickness of the TMN layers (reduce to a several nanometers) and applied rock-salt/rock-salt superlattice structure could greatly enhance thin film hardness and toughness [2,3,6–11].

Previous experimental results show that multilayer coatings of various scales have significant hardness values [8,12]. This has been ascribed to different dislocation mechanisms at different scales. For the bilayer thickness with sub-micro to micro-meters, dislocations will pile up at the interface [13,14]. For the thinner period thickness, the slip of a single dislocation loop is restricted in the isolation layer, i.e., the confined layer slip (CLS) mechanism [15–17]. For the period thickness with a few nanometers, a single dislocation can cut across the interface, i.e., Koehler strengthening [18–20]. At present, among these strengthening mechanisms, the difference in shear modulus-related Koehler strengthening mechanism [18] is regarded as the main strengthening mechanism for the nanoscale periodical SL (superlattice) TMN (transition-metal nitride) coatings. However, this known strengthening mechanism is mainly affected by the intrinsic mechanical properties (i.e., shear modulus difference) of the as-deposited states and hardly involves the specific microstructure evolution during the deformation process. Therefore, to understand the underlying strengthening or softening mechanisms at deformation process, micro-scale, nanoscale and atomic-scale observations are required and essential.

By coupling FIB (focused ion beam) sectioning with C_S-corrected HRTEM (high-resolution TEM) observations, we found that nanoindentation induced single-crystalline SL large-scale interfacial mixing, dislocation accumulation, grain rotation, SL <110> slip, and poly-crystalline columnar grain boundary sliding (Part

* Corresponding author.
E-mail address: zaoli.zhang@oeaw.ac.at (Z. Zhang).

https://doi.org/10.1016/j.actamat.2022.118009

1, [21]). These deformation behaviors will essentially affect the strengthening of SLs. Moreover, detailed TEM characterization also confirmed the local phase transition behavior occurred, as predicted by theoretical simulations [22–27], which could also influence the strengthening of SL coatings. The phase transition triggers the accumulation of dislocations at the interfaces, which leads to higher theoretical yield stress than would be expected from traditional Koehler strengthening in the single-crystalline SL. In addition to the increase in hardness, based on the previous AIMD (ab initio molecular dynamics) calculations [26] and our experimental observations, the phase transition process that occurred can theoretically lead to a higher toughness, which could be a new toughening mechanism. To the end, we endeavor to clarify the SL strengthening mechanisms at the atomic scale.

2. Methods

Details of the thin film fabrication and TEM characterization methods are described in Part 1 [21].

For the dislocation density, HRTEM recorded at 600–800 Kx was used. For detailed statistical methods, please refer to our previous work in Ref. [28]. The dislocation density was obtained according to the following formula, $\rho = N/A$, where ρ is the dislocation density, N is the number of dislocations, A is the area. The strain field was calculated on the C_S-corrected HRTEM images by the geometric phase analysis (GPA) method. According to the GPA algorithm, the displacement field can be obtained by selecting two non-collinear Bragg vectors in the power spectrum generated from a HRTEM image. Shear strain map (ε_{xy}) was calculated with respect to this reference lattice defined by $\vec{g}_1 = [100]$ and $\vec{g}_2 = [010]$.

3. Results

3.1. Comparison of experimentally observed deformation

Detailed atomic-resolution studies of the deformation in SLs were shown in Part 1 [21]. To show the correlation of deformation and strengthening of SLs, here, several key points about deformation are highlighted. For the single-crystalline SL, after nanoindentation, HRTEM image exhibits the GB (grain boundary) feature in the solid solution region (as seen in Fig.1a), where the angle between two {100} planes is about 17°. This indicates that grain rotational deformation has occurred here. And, at the SL region (or undistorted region) away from the impression surface and gradually approaching the MgO substrate, the large-scale SL [110]-slip deformation occurs. The HRTEM observation (Fig. 1b) clearly demonstrates the interface structure near the slip deformation region, showing the interface is perfect and coherent. The slip deformation here is mainly formed by 1/2 a <110> full dislocation slip and crossing the SL coherent interface, and accompanied by step formation at the interface. At the edge area of the impression, we also observed a special superlattice zone with severe distorted (Fig. 1c). Therefore, there are multiple deformation mechanisms in the single-crystalline SL, as schematically shown in Fig. 1d.

In contrast, for polycrystalline SL, SAED result (selected-area electron diffraction pattern, Supplementary Fig. S1) shows there is a slight grain rotation at the indenter tip. This means, the grain rotation in polycrystalline SL is not as pronounced as in single-crystalline SL. Furthermore, the intragranular <110> slip deformation is also not the dominant deformation mechanism in polycrystalline SL (as seen in Supplementary Fig. S2). Due to the large crystallographic orientation difference in out-of-plane directions between columnar crystals (as seen in Supplementary Fig. S3), this makes it difficult that <110> slip deformation in columnar crystals extends into its adjacent columnar grains. The intragranular slipping will be limited by the width of columnar grains. Taken together, we believe that columnar grain GB sliding is the dominant deformation mode in the polycrystalline SL (Fig. 1e). The scale of other deformation behaviors, i.e., interface intermixing, interface distortion, grain rotation, and SL slipping, is considerably lower than that in the single-crystalline SL. Fig. 1f illustrates the distribution of the solid solution region, the SL interface distorted area, and the SL interface undistorted zone in the polycrystalline SL.

In short, three distinct zones (solid solution, SL distorted interfaces, and SL undistorted interfaces) are generally recognized after nanoindentation of SLs, which corresponds to distinct deformation behaviors, as summarized in schematic Fig. 1d,f.

3.2. Dislocation density variations

For the single-crystalline SL coating, EELS and HAADF observations (in Part 1 [21]) demonstrate that the tip region of the impression has a larger-scale solid solution distribution, but no severely deformed interfaces are observed (as shown in Fig. 1d). At the impression edge region, the SL interface has severe deformation and consists by dislocation pile-up. Therefore, understanding the dislocation distribution in these regions are necessary for the understanding of the hardening mechanism of SL coatings.

(i) Dislocation density variations at the impression edge.

Fig. 2a shows the transition region from the SL structure to the intermixed solid solution at the edge of the impression. The measured local dislocation distribution (plotted in Fig. 2b) reveals that the SL area possesses an extremely higher dislocation density as compared to the solid solution area, implying a dislocation accumulation in the SL area at the edge of the impression. The partially enlarged HRTEM images (Fig. 2b) also directly visualize the significant difference in the dislocation density.

(ii) Dislocation density variations beneath the impression tip.

At the tip region of the impression in the single-crystalline SL, comprehensive TEM observations showed no dislocation accumulation at the SL and solid solution (SS) interface. In Fig. 3a, a SL feature (with layered contrast) is shown on the left-hand side, where the dislocation density is significantly lower compared to the SL at the edge region (Fig. 2a). Moving to the middle of the image that the dislocation densities were statistically determined, a local increase of dislocation density at the transition area could be observed (as seen in Fig. 3b). When reaching the solid solution and inwards, the dislocation density drops rapidly, which approach to the similar value in the edge region (Fig. 2b).

At the tip area, we attribute the lower dislocation density in the SL to the higher local stress and more pronounced intermixing behavior. Close to the tip, the higher local stress will drive a larger-scale intermixing, transforming the SL into a solid solution, and consequently reducing the scale of the deformed interfaces with a high dislocation density. In other words, the larger driving force causes more adequate intermixing of the interfaces. Simultaneously, the presence of larger solid solution volume leads to more pronounced polycrystalline deformation behavior and a higher grain boundary density (as seen in the SAED result, Fig. 6 in Part 1 [21]). On the one hand, possessing a significantly high fraction of high-angle grain boundaries in the solid solution region can effectively absorb dislocations. On the other hand, the deformation (via GB sliding or grain rotation) of nanocrystalline solid solution greatly dissipates the external energy, thereby effectively protecting the SL (below the solid solution area) from further intermixing, deformation, and dislocation accumulation. Contrarily, when the solid solution area is smaller or lacks at the edge of the impression, the SL interfaces cannot be effectively protected. Thus, significant interface distortion and dislocation accumulation occur.

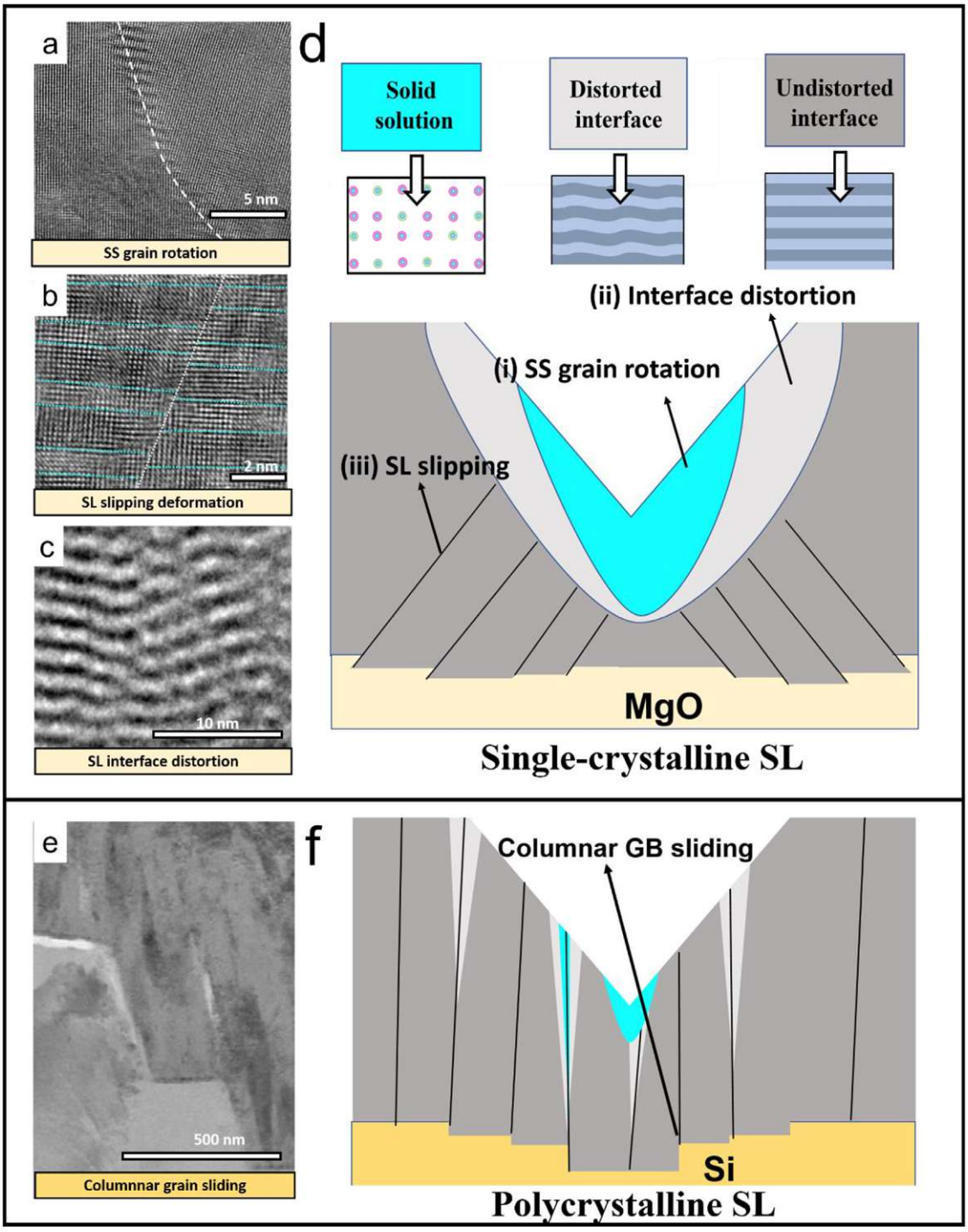

Fig. 1. a–c, HRTEM and TEM-BF images showing different deformation behaviors in an indented single-crystalline SL. **d**, A schematic distribution of three distinct zones and corresponding deformation modes in the single-crystalline SL. **e**, A STEM-BF image of the indented area clearly showing the columnar grain sliding in polycrystalline SL. **f**, A schematic distribution of three distinct zones and corresponding deformation modes in an indented polycrystalline SL. Due to the presence of native oxide, the coating is actually grown on SiO_x. Note that different color shadows designate different deformations.

For polycrystalline SL, dislocation accumulation only appears in the very vicinity of the crack or GBs, while the interior of the columnar display a lower dislocation density (shown in Part 1 [21] and Section 4.2). Thus, polycrystalline SL does not exhibit significantly larger dislocation accumulation regions than single-crystalline SL. To sum up, our results indicate that there is a competitive relationship between the different deformation mechanisms, which may affect the possible strengthening behaviors (as will be seen in the discussion).

3.3. Local phase transformation

The previous classical interface theory considers that the dislocation accumulation or dislocation pile-up in the multilayer structure generally occurs in the bilayer thickness of a few hundred nanometers [8,17,20]. For multilayer interface, when the dislocation core dimension approaches the layer thickness, the interface barrier to slip transmission decreases [12,17]. Therefore, multilayer

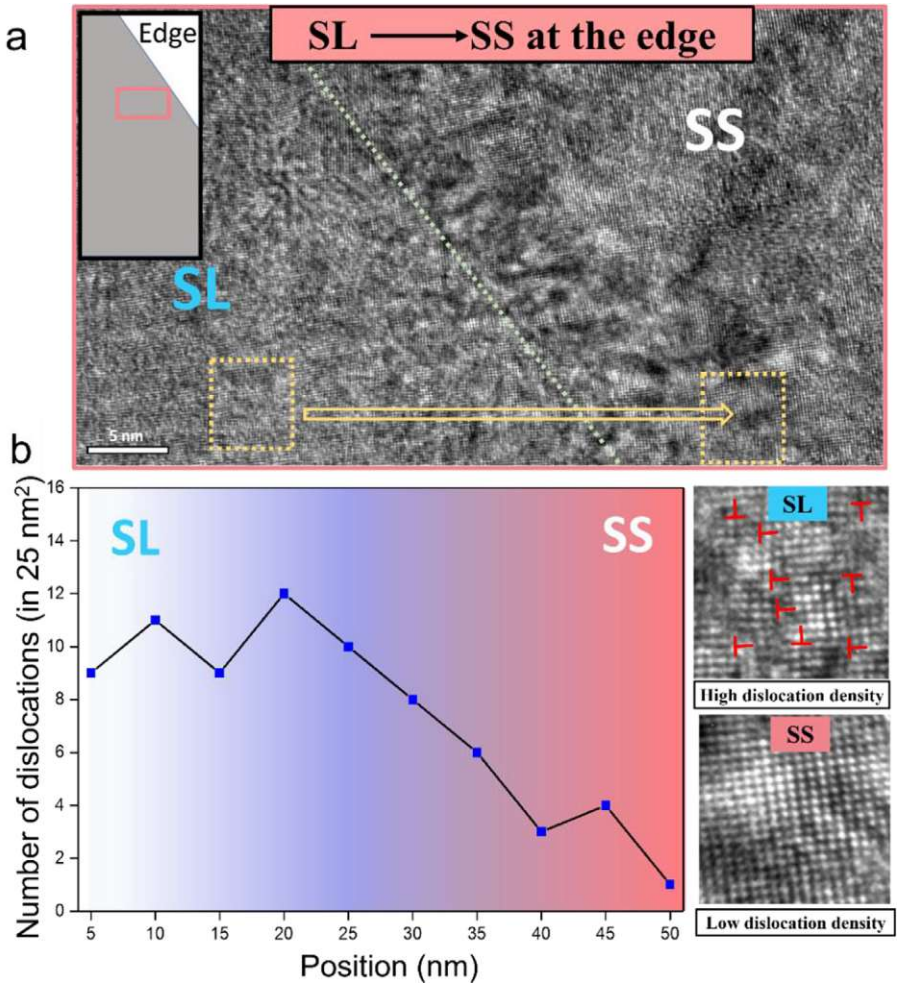

Fig. 2. a, a schematic drawing and HRTEM observation on the transition region from the solid solution to SL (separated by dotted line) at the edge of the impression of the indented single-crystalline SL. **b,** The dislocation density distribution along the indicated yellow frames in **a**, and two clippings of representative HRTEM images on the panel **b** showing the different density of dislocations. Here, only edge dislocations are counted within 5 nm × 5 nm region (yellow frames in **a**). (For interpretation of the references to colour in this figure legend, the reader is referred to the web version of this article.).

coatings with extremely small periodic thickness are not conducive to dislocation accumulation.

However, our TEM observations show results that contradict previous theories, i.e., detailed atomic-resolution observations corroborate a significant dislocation accumulation at the $\Lambda = 2.5$ nm SL coating. To explore potential explanations for the pronounced dislocation accumulation at the TiN/AlN SL interfaces, we propose that it is related to the formation of an AlN phase transition as predicted by previous simulations [23,29]. It is well known that AlN has several modifications, i.e., a stable wurtzite structure B4 with hexagonal symmetry and two metastable phases with cubic symmetry: B1 (rock-salt structure, NaCl prototype) and B3 (sphalerite structure, ZnS prototype) [30–33]. Due to the lower interfacial energy, AlN is stabilized in its metastable rocksalt structure in the as-deposited TiN/AlN SL. However, previous experiment observations (TEM results of indented TiN/AlN SL [27] and ZrN/$Zr_{0.63}Al_{0.37}N$ SL [34]), AIMD, DFT, and classical MD simulations all have shown that deformation can trigger phase transformation in AlN or Al alloyed TMN [22–27]. These phase transformations in AlN include B4–B1, B3–B1, B1–B3, and B1–B4 processes under indentation, tension, or shear deformation process. In contrast, for *rs*-TiN, DFT predicts that no phase transition occurs under deformation, and its failure mechanism is brittle cleavage [35].

(i) Phase transformation at the SL region.

As observed, the area with the severely distorted interfaces and dislocation accumulation is mostly distributed at the edge of the impression with high shear stresses. In these shear deformation regions, the monoclinic phase was exactly detected by detailed HRTEM investigations, as predicted by AlN shear deformation simulation [23]. Fig. 4a is an HRTEM image taken from the interface distortion region of the single-crystalline SL coating, where the AlN layer (with brighter contrast) exhibits obvious lattice distortions, i.e., a square lattice transforms to a quadrilateral one. The corresponding area in Fig. 4b clearly indicates that the AlN (100)/(010) lattice angle has reached 11°, corresponding to a shear strain of ~12%. In contrast, the adjacent TiN layer still maintains a square lattice and relatively lower shear strain. Using DFT simulations, Zhang and Veprek [23] demonstrated that the AlN phase transformation along the shear deformation path occurs through creating a series of monoclinic structures. Therefore, according to these simulation results, we may attribute such a high shear deformation taking place in the local AlN layer to the monoclinic phase formation (Fig. 4b, see the HRTEM image simulation results of the monoclinic phase using a space group of C2/m, monoclinic structure reference to Ref. [23], both simulated and experimental images match well).

In fact, the local phase transformation behavior that happened in the SL can reasonably explain the pronounced dislocation accumulation in the SL region. Since the crystal structure of the *rs*-TiN layer is stable during deformation, the volume expansion caused

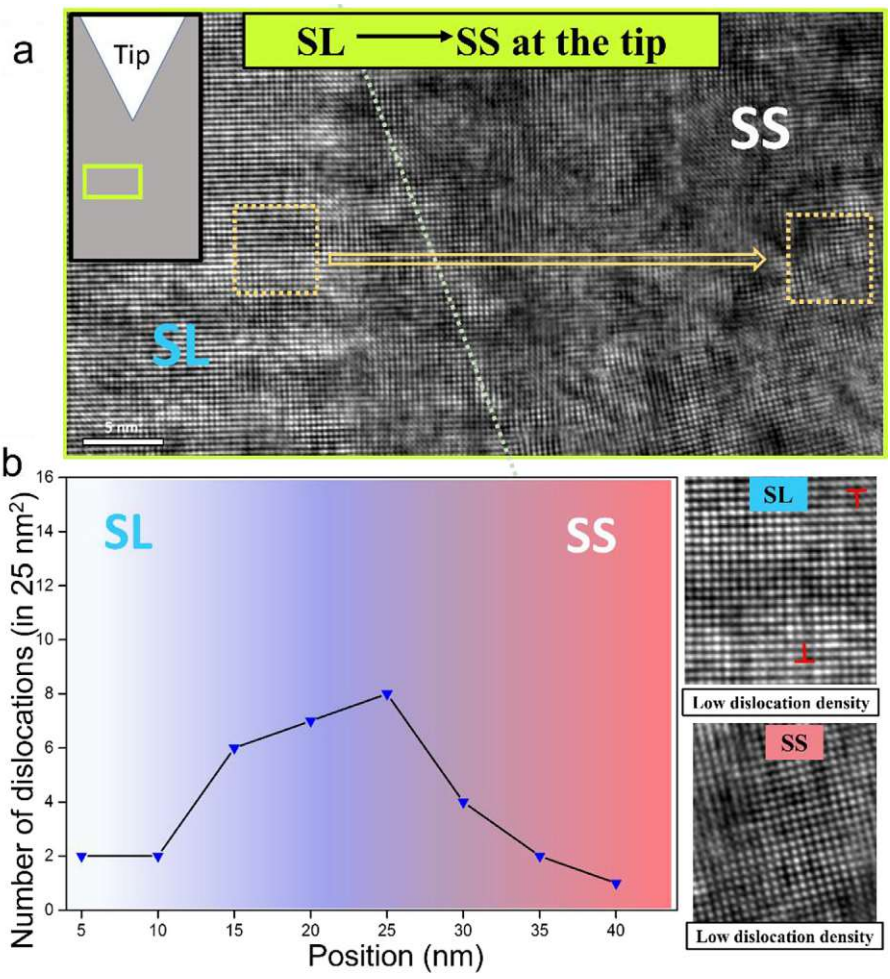

Fig. 3. **a,** a schematic drawing and HRTEM observation on the transition area from the solid solution (SS) to SL at the tip of the impression (indented single-crystalline SL). **b,** The dislocation distribution in the corresponding area (**a**, yellow frame), and two clippings of representative HRTEM images on the panel **b** showing the different density of dislocations. Here, only edge dislocations are counted within 5 nm × 5 nm region (yellow frames in **a**). Note that the difference in dislocation density beneath the tip and at the edge (referring to Fig. 2). (For interpretation of the references to colour in this figure legend, the reader is referred to the web version of this article.).

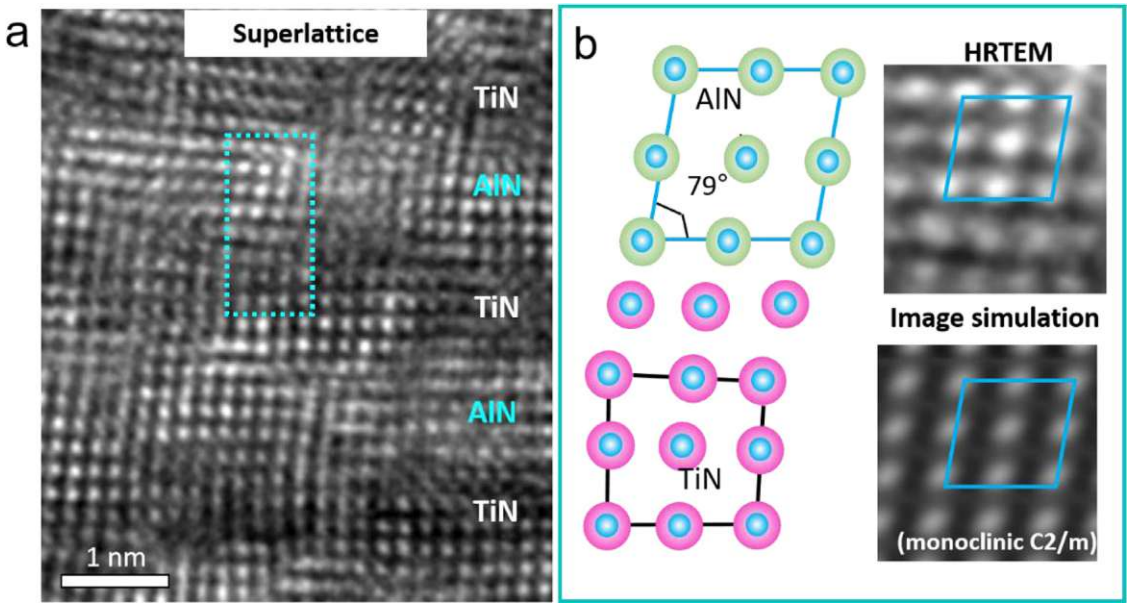

Fig. 4. **a,** A detailed HRTEM observation on a deformed interface region of indented single-crystalline SL. **b,** The monoclinic AlN and cubic TiN atomic models of the corresponding area in **a**, and a clipping of HRTEM experimental image, simulated image of the AlN layer using a monoclinic phase structure (C2/m) are shown on the panel **b**.

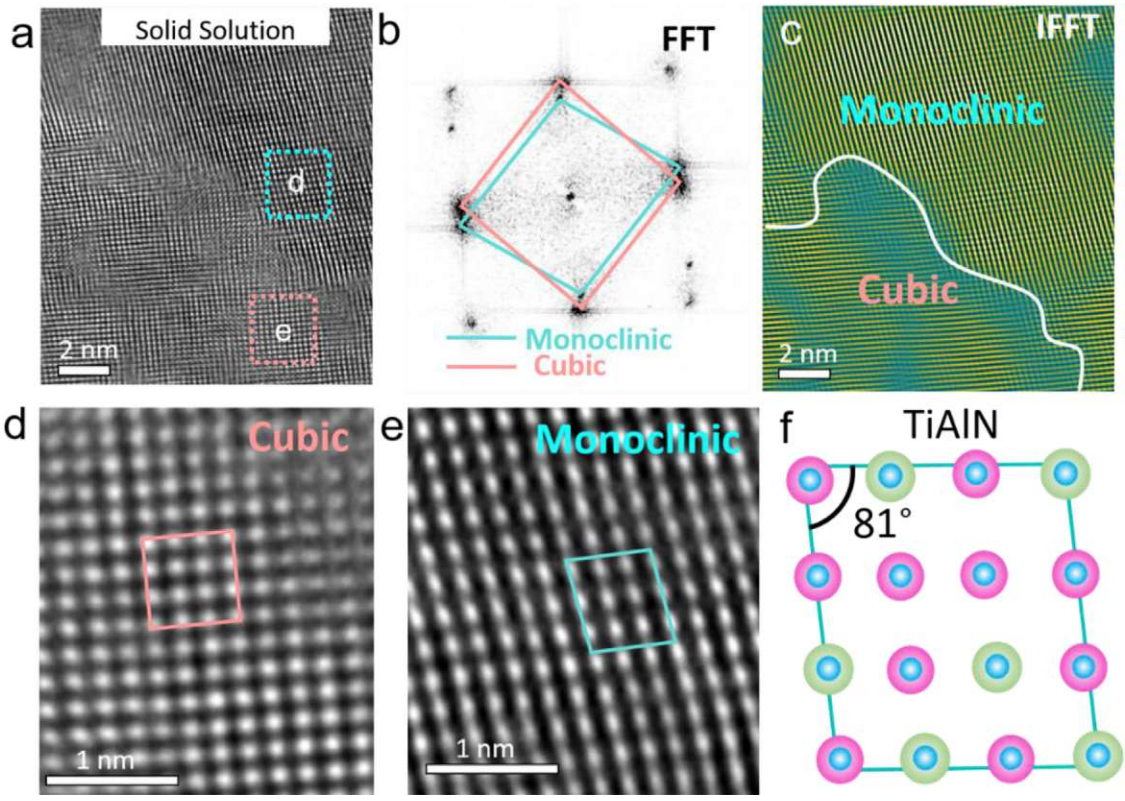

Fig. 5. **a,** Detailed HRTEM observation of the monoclinic phase in the solid solution region of the single-crystalline SL. **b,** Fast Fourier transform result of **a. c,** Inverse Fast Fourier transform of **a**, clearly showing the distribution of the cubic phase and the monoclinic phase. **d and e,** A partially enlarged image of **a f,** A model of the monoclinic solid solution is attached.

by the phase transformation in the AlN layer of the SL area will be constrained by the *rs*-TiN layer. This results in the formation of additional misfit dislocations on the interface to accommodate the lattice strain of the two layers. In addition, because the *rs*-TiN/*rs*-AlN coherent interface state is destroyed, the gliding of dislocation on the preferred slip system will be severely hindered by the rock-salt/monoclinic interface. Thus, we believe that the local phase transformation mediates the interface structure (by forming a "new" interface structure), which subsequently acts as a stronger barrier to dislocation glide, and eventually facilitates dislocations accumulation.

(ii) Phase transformation in the intermixed zone ($Ti_{1-x}Al_xN$).

Here, we also detected phase transformation in the intermixed region, i.e., $Ti_{0.67}Al_{0.33}N$ solid solution region. For $Ti_{1-x}Al_xN$, the cubic structures appeared with a critical maximum Al solubility of 0.4 to 0.9, while for the higher Al concentrations the metastable wurtzite phase could form [36–41]. Thus, the cubic structure is a stable phase for $Ti_{1-x}Al_xN$ (x = 0.33). Recent AIMD simulations by Sangiovanni et al. [26] predicted the phase transformation for $Ti_{1-x}Al_xN$ solid solution (B1-B4). In this work, although no B4 phase was observed in the solid solution region of the indented sample, HRTEM results revealed that there exists a greater extent of the monoclinic phase. Fig. 5a shows an HRTEM image of the $Ti_{0.67}Al_{0.33}N$ solid solution region, where two different crystal structures are clearly distributed. The FFT result in Fig. 5b shows the quadrilateral-shaped and cubic-shaped reflections, confirming the existence of the cubic and monoclinic structures in Fig. 5a. The result of the regional IFFT (Inverse Fast Fourier transform, Fig. 5c) shows that the upper part of the image is a monoclinic phase with a dislocation-free quadrilateral structure while the lower-left part is a cubic phase with a square lattice. The enlarged atomic resolution images (Fig. 5d,e) clearly show different lattices and angles, where the lattice angle of the monoclinic phase region is 81°. An atomic model of the monoclinic solid solution is presented in Fig. 5f accordingly. We further verify such a phase transformation by analyzing the interplanar spacing variations (Supplementary Fig. S4). The measured spacings are significantly larger in the monoclinic region than in the cubic area.

Actually, the phase transition observed in the AlN layer or solid solution region mainly exists in the single-crystal SL coating. However, it is hardly seen in the intragranular AlN layer or $Ti_{0.67}Al_{0.33}N$ solid solution region of the indented polycrystalline TiN/AlN coating. This may be relevant to the less solid solution scale and lower local stress state in polycrystalline SL, where most of the loading energy is dissipated through columnar grain boundary sliding.

(iii) Phase transformation at the crack tip.

Apart from the above observations, our HRTEM analysis revealed a monoclinic phase structure present at the crack tip (both in single-crystalline SL and poly crystalline SL). Fig. 6a is one HRTEM image taken near the edge crack (a low-mag image is inserted) in the single-crystalline SL. Two magnified atomic images (Fig. 6b,c) reveal the phase transition behavior of a cubic structure toward a monoclinic structure near the crack tip. The enlarged image (Fig. 6c) indicates that the lattice angle of the monoclinic phase region is 81°, close to the result in Fig. 5e.

Although no phase transition in the intragranular AlN layer or $Ti_{0.67}Al_{0.33}N$ solid solution region in polycrystalline SL is observed, a larger stress concentration in GBs or crack tip may trigger a localized phase transition. Fig. 6d presents the HRTEM image recorded near the crack tip in the polycrystalline SL. A cubic lattice structure retains inside the columnar crystal (Fig. 6e), whereas in the front of the crack, the monoclinic structure (with a lattice plane angle of ~82°) is also observed, as the enlarged HRTEM image (Fig. 6f) shown. In Supplementary Materials (Fig. S5), we performed fur-

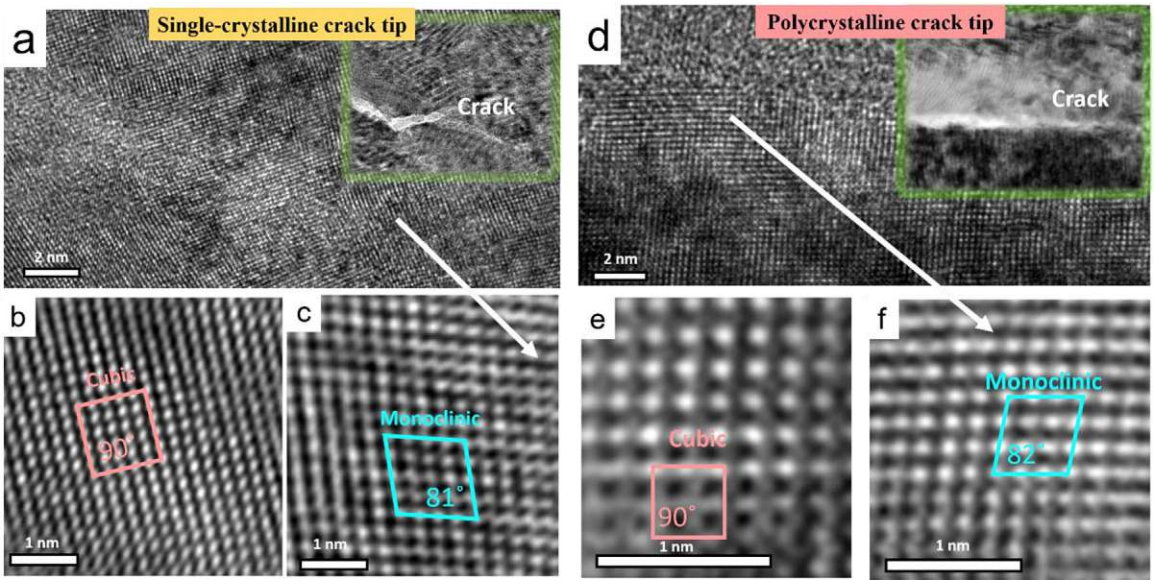

Fig. 6. **a,** The HRTEM observation of the crack tip in the single-crystalline SL. **b** and **c,** the phase structures at bulk and rightly in the front of the tip (labeled in **a**). **d,** The HRTEM observation of the crack tip in the polycrystalline SL. **e** and **f,** the phase structures at bulk and rightly in the front of the tip (labeled in **d**). The monoclinic phase is found near the crack (in **c, f**). Two low-magnified images (insets in **a** and **d**) indicating the crack locations.

ther HRTEM observations on monoclinic phase transition behavior near the crack in the <110> direction, and its structure and lattice-planes angle (α=γ=90°, β~81°) are consistent with those in the <100> direction (Fig. 6e).

In sum, **(1)** monoclinic phase transformation is observed in the distorted interfacial AlN layer and near-surface $Ti_{0.67}Al_{0.33}N$ solid solution region in the single-crystalline SL. **(2)** the phase transformation occurring in the distorted interfacial AlN layer facilitates dislocations accumulation. **(3)** A greater extent of phase transformation emerges in the $Ti_{0.67}Al_{0.33}N$ solid solution region of the single-crystalline SL. **(4)** the monoclinic phase structure is observed also at the crack tip region in the single-crystalline and polycrystalline SLs.

4. Discussions

4.1. On yield stress in different deformation areas

Now, it is well-established that extremely hard TMN/TMN SL coatings are obtained when grown on MgO substrates. A superhard coating with hardness values greater than 50 GPa was firstly reported in 1987 by Helmersson et al. [2] who demonstrated an enormous increase in the hardness of single-crystalline TMN SL epitaxially grown on MgO substrates by reactive magnetron sputtering. However, using different substrate materials (Si, Al_2O_3 or steel) or applying less severe deposition and growth conditions results in the growth of polycrystalline SL films. Generally, the hardness of these polycrystalline SL coatings is not as high as that of single-crystalline SL coatings [42]. Here, the 2.5 nm bilayer-period coating exhibits a higher hardness when grown on the MgO (100) substrate than on the Si (100) substrate [43]. Nevertheless, the hardness of the polycrystalline SL is obviously larger than that of the monolithic TiN (about 22 GPa) [43], implying that the polycrystalline SL still has a strengthening behavior, but is less significant than in the single-crystalline SL.

We propose that the origin of the different hardness of single-crystalline SL and polycrystalline SL is related to their different deformation behaviors. Currently, the interface hardening effect for nanoscale bilayer-thickness TMN coatings is mainly attributed to the Koehler strengthening, i.e., single dislocation crossing the interface. In this work, the presented TEM results suggest that multiple deformation mechanisms are active in the single-crystalline SL (as seen in the schematic image of Fig. 1d. These microstructures and deformation mechanisms may include SL region interface distortion, SL region slip deformation, grain rotation, and GB sliding in the solid solution region. Thus, our nanoindentation experiments confirmed that Koehler strengthening is not the sole hardening mechanism.

For the single-crystalline SL, regions with different deformation mechanisms might have completely different local stress states and dislocation behaviors, which result in different hardening or softening. Fig. 7a shows the dislocation distribution (HRTEM result) and the stress state (GPA result) of the area with interface distortion in the single-crystalline SL coatings. According to the GPA result, the local shear strain of the corresponding region may vary from -10% to +10%. We believe that the extremely high dislocation density and local stress here are mainly due to the local phase transformation in the AlN layer, which results in the interface structure evolution from the initial coherent to heterophase incoherent interface with a high misfit of lattices. On the one hand, this increases the density of misfit dislocations on the rock-salt/monoclinic interface. On the other hand, compared to a perfectly cubic/cubic coherent interface, a semi-coherent or incoherent interface with a higher stress state will make a single dislocation glide across the interface more difficult, facilitate dislocations accumulation on the 2.5 nm-bilayer-period SL interfaces (as seen in Fig. 7b).

According to the dislocation density in the deformed region, we may estimate the yield stress by Taylor's strengthening law [44], where increased yield stress (in an *rs*-TiN or AlN layer) can be expressed as:

$$\Delta\sigma = M\alpha\mu b\sqrt{\rho} \quad (1)$$

Where M is Taylor factor, α is a numerical factor (typically, in *fcc* crystal $a \approx 0.35$ [45]), μ is the shear modulus, b is the magnitude of the dislocation Burgers vector and ρ is the dislocation density. Here, the Taylor factor is 3.33 for nitrides [20], the shear modulus μ for TiN is 183 GPa [46], the Burgers vector is 0.21 nm (1/2a [100] type). Therefore, according to the dislocation density in Fig. 7a (here it is considered that the TiN layer has a similar dis-

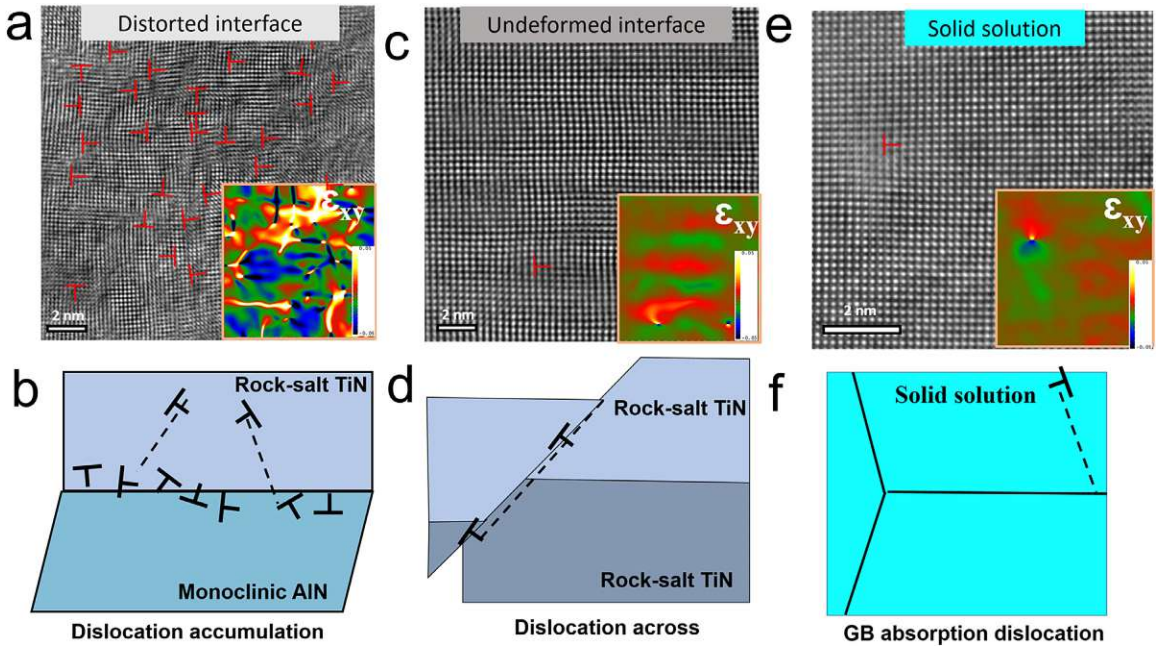

Fig. 7. **a,** A HRTEM image showing the dislocation distribution and strain field (GPA results) in the distorted interface region. **b,** a schematic diagram of dislocation behavior in the deformed interface. **c,** A HRTEM image showing the dislocation distribution and stress field (GPA results) in the un-deformed interface region. **d,** a schematic diagram of dislocation behavior in the un-deformed interface. **e**, A HRTEM image showing the dislocation distribution and stress field ε_{xy} (GPA results) in the solid solution region. **f,** a schematic diagram of the large-angle GB absorption dislocation behavior in the solid solution region.

location density to the AlN layer), the yield stress of the TiN layer will be at least increased by 16.3 GPa. For the *rs*-AlN layer (μ is 211 GPa [46]), the yield stress will further increase by 18.7 GPa.

Fig. 7c shows the dislocation distribution (HRTEM result) and the shear stress state (GPA result) for the un-deformed interface region, i.e. slip deformation region. Compared to Fig. 7a, the un-deformed interface region has a very low dislocation density (misfit dislocations of the coherent interface region) and a fully coherent stress state. Given the perfect coherent interface, a dislocation will more easily pass through the interface along the <110> direction leading to complete large-scale slip deformation (as seen in schematic image Fig. 7d and the TEM result in companion paper [21]. Therefore, the yield stress here can be described by the Koehler strengthening model. According to Koehler's theory, the maximum increased yield stress (σ) can be obtained by [18]:

$$\Delta\sigma = M\frac{\pi(\mu_1-\mu_2)}{8(\mu_1+\mu_2)}\mu\sin\theta \tag{2}$$

With consideration to the primary {110}<110> slip system, θ takes the value of 45° for the <100> SL. μ_1 *and* μ_2 are the shear modulus in different layers (in this work, μ_1 is the shear modulus of rs-AlN and μ_2 is the shear modulus of rs-TiN) Therefore, the yield stress of a single dislocation crossing the interface will increase by 12.0 GPa.

For nanoscale SLs, the influence of dislocation core should be considered. For the revised Koehler's theory, the increased yield stress can be simplified as [47]:

$$\Delta\sigma = M\frac{2\alpha(\mu_1-\mu_2)}{\pi}\sin\theta\left(\frac{b^2}{4x^2+b^2}+\frac{b}{2x}tan^{-1}\frac{2x}{b}\right) \tag{3}$$

where α is $1/4\pi$ and $(1\text{-}\nu)/4\pi$ for screw and edge dislocations ($\nu_{TiN} = 0.225; \nu_{TiN} = 0.174$ [46]), x is the distance between the interface and the dislocation. Thus, the revised yield stress of a single dislocation crossing the interface will increase by [8]:

$$M\frac{(1-\nu)(\mu_1-\mu_2)\sin\theta}{\pi^2} \le \Delta\sigma \le M\frac{(\mu_1-\mu_2)\sin\theta}{\pi^2} \tag{4}$$

Therefore, for the revised Koehler's theory, the maximum increased yield stress of a single dislocation crossing the interface will rise by ~6.4 GPa.

Based on the above analysis, in a word, dislocation accumulations lead to the increase of the yield strength in the single – crystalline SL.

4.2. On the hardness of single-crystalline and polycrystalline SL coatings

In this work, we argue that the TiN/AlN SL hardness enhancement may be also related to the interlayer phase transformation mediated Taylor's strengthening mechanism, except the other factor, i.e. Koehler strengthening. As analyzed in the previous section, in general, for the single-crystalline TiN/AlN SL, the interface distortion region with dislocation accumulation can provide a greater strengthening behavior (compared to the Koehler strengthening). This implies that the dislocation accumulations associated with the phase transformation in AlN provides a higher theoretical hardness.

In the solid solution region, due to the disappearance of the layer interfaces and the interfacial stress field (as seen in Fig. 7e and inside the GPA result), the solid solution zone will reduce the yield stress of the dislocation gliding. At the same time, since the GBs in the solid solution can effectively absorb dislocations (as seen in Fig. 7f), this causes hardly dislocation accumulation in the alloyed area (confirmed by Fig. 2). As a result, the alloying process of the interfaces thus severely suppresses Koehler's strengthening and Taylor's strengthening. And, the deformation of a larger-scale solid solution is through more grain rotations that will consume the load energy. Therefore, the intermixing of the SL interfaces is not conducive to the coating maintaining mechanical strength.

In general, the polycrystalline TiN/AlN SL's strength is not as good as the single-crystalline TiN/AlN SL coating (coatings with different bilayer periods are included) [43]. As shown in Fig. 8, the nanoindentation load/depth curves (using Berkovich and cube corner tips) indicate a higher strength for single-crystalline TiN/AlN

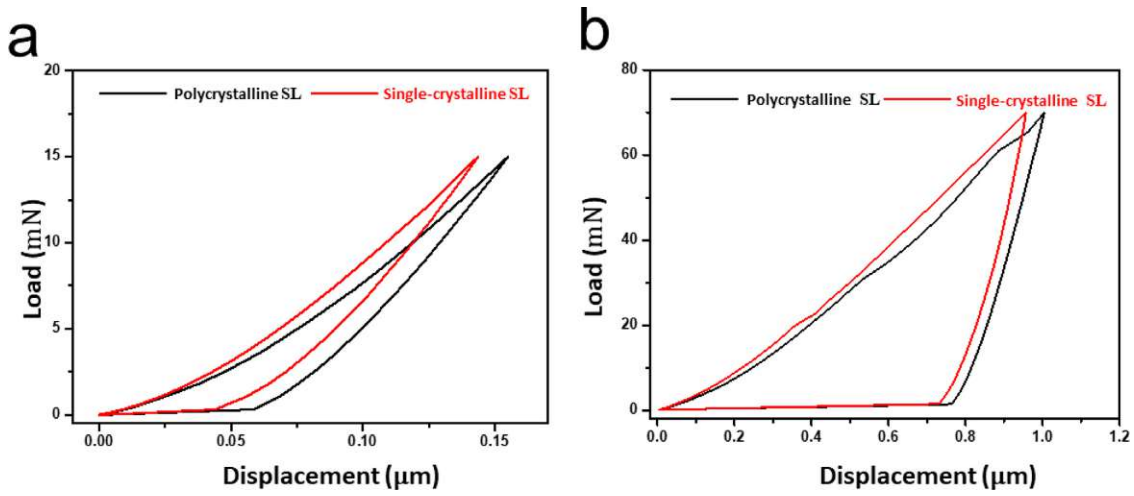

Fig. 8. a, Nanoindentation curves for the TiN/AlN films (polycrystalline and single-crystalline SL) with the Berkovich tip. **b,** Nanoindentation curves for the TiN/AlN films (polycrystalline and single-crystalline SL) with the cube corner tip.

SL, i.e., a smaller loading depth at the same loading. Furthermore, the nanoindentation load-unload curve (Fig. 8a) displays that both single-crystalline and polycrystalline SLs show the elastoplastic deformation behavior and with the similar elastic strain. The difference lies in that the single-crystalline SL has a higher elastic modulus, while the polycrystalline SL has a higher plastic strain. It could be speculated that the better plasticity in the polycrystalline SL could be attributed to its large-scale GB sliding deformation behavior.

Although polycrystalline TiN/AlN SL coating (for this work) hardness (H of 31.8 ± 0.8 GPa [43]) enhancement is lower than that of the single-crystalline TiN/AlN SL (H of 37.0 ± 0.5 GPa [43]), its hardness is still higher than that of the monolithic polycrystalline or single-crystalline coatings [2,48,49]. We consider that the deformation mechanism for the polycrystalline SL coating is dominated by columnar grain sliding along the load direction (as seen in Fig. 1f). Such a predominant sliding deformation hinders the occurrence of many other potential deformations and strengthening behavior of TiN/AlN SL, e.g., interface distortion, dislocation pile-up or dislocation crossing interfaces. Through TEM observations, we found interface distortion (Fig. 9a) and an increase in dislocation density near the GBs of the columnar grains, while the interior of the columnar grains still maintains un-deformed layered structures with a lower dislocation density (as seen in Fig. 9b,c). Due to the local increase of the dislocation density at the GBs (as seen in the schematic diagram of Fig. 9d), the coating may form immobile regions with high yield stress, thereby increasing the yield stress for GB slip. Thus, we speculate that the deformation of the interfaces near the columnar GBs can still strengthen the polycrystalline SL coating to a certain extent. However, further studies are necessary to pinpoint and quantify the relevant hardening effect in polycrystalline SL.

In a word, dislocation accumulation and crossing dominate the strengthening of single –crystalline SL while no such pronounced strengthening is observed in polycrystalline SL. Consequently, single-crystalline SL generally exhibits a higher strength.

4.3. Toughening mechanisms in TiN/AlN SLs

Previous work [43] showed that the hardness/modulus ratio in single-crystalline SL TiN/AlN SL (Λ = 2.5 nm) was ~0.093, while it was ~0.088 in polycrystalline SL. No matter single-crystalline SL and polycrystalline SL, the hardness (H)/modulus (E) ratio is generally much higher than monolithic TiN films. Empirical indicators of a high H/E value unveil that the thin film enhances toughness and wear resistance [50].

The superlattice toughening effect can be explained as the stress field at the coherent interface. The lattice parameter difference of Δa = 0.2 Å (between *rs*-TiN and *rs*-AlN, JCPDF files: 38–1420 TiN, 25–1495 *rs*-AlN) results in a coherent strain ε_c of ~5% on the *rs*-TiN/*rs*-AlN coherent interface. Therefore, the TiN layer is affected by the compressive stress, which will close the cracks and impede crack growth across the interface. For the severely distorted interface region in the single-crystalline SL, the high density of dislocations in this region leads to the stress concentration, microcrack propagation and fracture. Meanwhile, due to the destruction of the coherent interface structure (caused by local phase transformation), the lack of coherency stresses will also weaken the toughening effect of the interface. However, the volume expansion triggered by the phase transformation process may compress the surrounding area and promote the closure of other cracks, which still contributes to the toughening of the SL structure. The AIMD simulation by Koutná *et al.* showed that the local B1-B4 phase transformation of the AlN layer in the TiN/AlN SL could increase the ultimate fracture strain by about 8% under a certain bilayer thickness [27], which exemplified the phase transformation enhanced toughness in the TiN/AlN multilayer.

The formation of the solid solution zone in the single-crystalline SL is also conducive to improving the toughness. The tensile deformation simulation showed that the perfect single-crystalline $Ti_{1-x}Al_xN$ solid solution with phase transformation behavior (B1–B4) can increase its ultimate fracture strain to 50%, resulting in super toughness [26]. Although no B4 phase was observed in our indented sample, HRTEM images revealed the presence of a monoclinic $Ti_{0.67}Al_{0.33}N$ phase. The phase transformation in the solid solution can effectively relax the deformation energy, and suppress the crack initiation through effective volume expansion. Theoretically, the phase transformation from cubic to wurtzite AlN is associated with a molar volume expansion of about 20% [51]. According to our estimated results (Supplementary Fig. S6 and FFT result in Fig. 5b), the monoclinic solid solution is approximately 12–13% larger (according to two-dimensional regions) than the cubic solid solution in the projection direction. Therefore, it suggests that the formation of a monoclinic phase is still conducive to its volume expansion.

The toughening effect via the solid solution formation can be briefly summarized as follows: (i) The energy dissipation and volume expansion caused by the phase transformation of $Ti_{0.67}Al_{0.33}N$

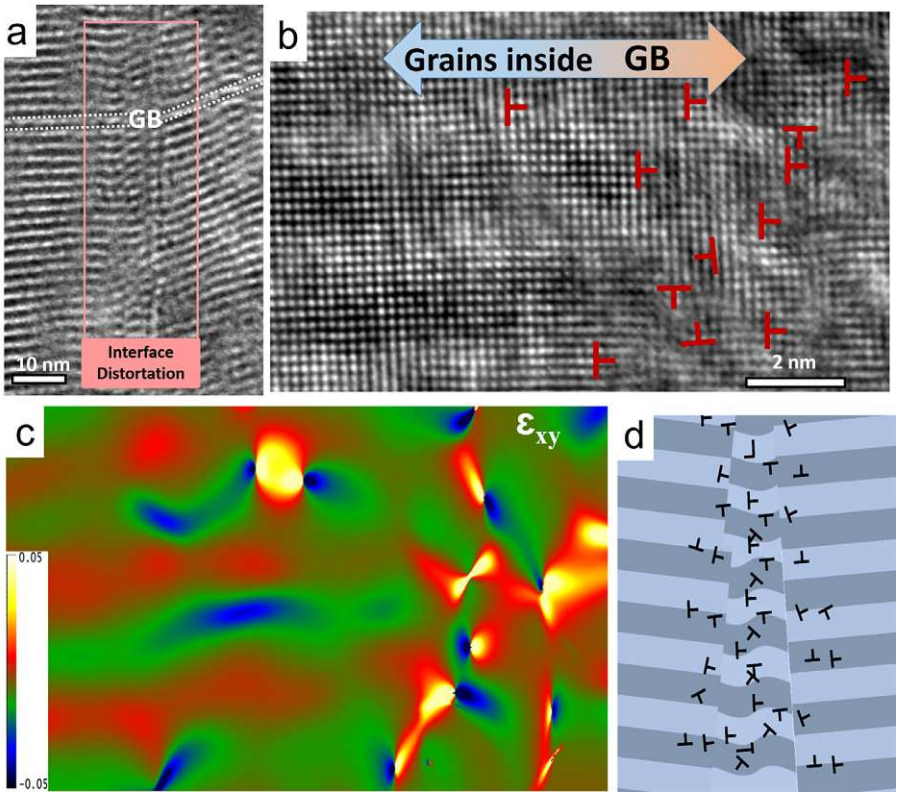

Fig. 9. a, TEM-BF image of the indented polycrystalline SL from the columnar GB region, where the labelled region shows significant interface distortions. **b,** Dislocation distribution near the GB in the indented polycrystalline SL. **c,** Strain field (GPA results of ε_{xy}) of **b.d,** An schematic drawing illustrates its deformation behavior in one columnar grain boundary.

from the cubic to the monoclinic. (ii) The formation of a ternary solid solution will also enhance the valence electron density to increase its inherent toughness [52–55]. (iii) The polycrystalline deformation behavior (Grain rotation or GB sliding) in the solid solution zone not only dissipates its deformation energy, but also avoids stress concentration and thus inhibits crack initiation.

In short, combining the above analysis with TEM observations, we may conclude that the solid solution formation is highly beneficial for improving the toughness of SLs.

5. Conclusion

This work verified the strengthening behavior of the single-crystalline SL coating under different deformation mechanisms. And it confirmed that the accumulation of dislocations related to phase transformation could provide more dominant strengthening than Koehler strengthening. Simultaneously, the intermixing of the interfaces greatly weakens the Koehler strengthening behavior and limits the extension of the Taylor strengthening area (the area with dislocation accumulation). Thus, we propose that the hardening of the single-crystalline SL depends on the combined effects of different strengthening mechanisms and the properties of the solid solution of the layer materials. However, the hardening behavior of single-crystalline SL, i.e., dislocation accumulation or dislocation crossing interface, are not observed in the polycrystalline SL. Consequently, polycrystalline SL generally exhibits a relatively lower hardness. Meanwhile, the solid solution formed by interfacial intermixing in the single-crystalline SL also shows phase transformations to take place, which renders the excellent toughening effect.

Declaration of Competing Interest

The authors declare that they have no known competing financial interests or personal relationships that could have appeared to influence the work reported in this paper.

Acknowledgments

This work is financially supported by FWF P 33696 (Z.C, Y.H., Z. Z). The authors thank M. Fallmann, for the thin film synthesis and SEM characterization, and the USTEM at TU Wien for the TEM sample preparation.Z.G. thanks the China Scholarship Council (CSC, 201908440933) for the support. This work is also supported by FWF I 4720 (M.B.).

Supplementary materials

Supplementary material associated with this article can be found, in the online version, at doi:10.1016/j.actamat.2022.118009.

References

[1] W. Schintlmeister, W. Wallgram, J. Kanz, Properties, applications and manufacture of wear-resistant hard material coatings for tools, Thin Solid Films 107 (2) (1983) 117–127.
[2] U. Helmersson, S. Todorova, S.A. Barnett, J.E. Sundgren, L.C. Markert, J.E. Greene, Growth of single-crystal TiN/VN strained-layer superlattices with extremely high mechanical hardness, J. Appl. Phys. 62 (2) (1987) 481–484.
[3] H. Holleck, H. Schulz, Preparation and behaviour of wear-resistant TiC/TiB_2, TiN/TiB_2 and TiC/TiN coatings with high amounts of phase boundaries, Surf. Coat. Technol. 36 (3) (1988) 707–714.
[4] H. Holleck, M. Lahres, P. Woll, Multilayer coatings—influence of fabrication parameters on constitution and properties, Surf. Coat. Technol. 41 (2) (1990) 179–190.

[5] P.B. Mirkarimi, L. Hultman, S.A. Barnett, Enhanced hardness in lattice-matched single-crystal TiN/$V_{0.6}Nb_{0.4}N$ superlattices, Appl. Phys. Lett. 57 (25) (1990) 2654–2656.
[6] J.E. Sundgren, J. Birch, G. Håkansson, L. Hultman, U. Helmersson, Growth, structural characterization and properties of hard and wear-protective layered materials, Thin Solid Films 193-194 (1990) 818–831.
[7] L. Hultman, M. Shinn, P.B. Mirkarimi, S.A. Barnett, Characterization of misfit dislocations in epitaxial (001)-oriented TiN, NbN, VN, and (Ti,Nb) N film heterostructures by transmission electron microscopy, J. Cryst. Growth 135 (1) (1994) 309–317.
[8] P.C. Yashar, W.D. Sproul, Nanometer scale multilayered hard coatings, Vacuum 55 (3) (1999) 179–190.
[9] M. Kobayashi, Y. Doi, TiN and TiC coating on cemented carbides by ion plating, Thin Solid Films 54 (1) (1978) 67–74.
[10] W.D. Nix, Mechanical properties of thin films, Metall. Trans. A 20 (11) (1989) 2217.
[11] J.E. Sundgren, Structure and properties of TiN coatings, Thin Solid Films 128 (1) (1985) 21–44.
[12] R.G. Hoagland, R.J. Kurtz, C.H. Henager, Slip resistance of interfaces and the strength of metallic multilayer composites, Scr. Mater. 50 (6) (2004) 775–779.
[13] G.S. Was, T. Foecke, Deformation and fracture in microlaminates, Thin Solid Films 286 (1) (1996) 1–31.
[14] P.M. Anderson, C. Li, Hall-Petch relations for multilayered materials, Nanostruct. Mater. 5 (3) (1995) 349–362.
[15] J.D. Embury, J.P. Hirth, On dislocation storage and the mechanical response of fine scale microstructures, Acta Metall. Mater. 42 (6) (1994) 2051–2056.
[16] M.A. Phillips, B.M. Clemens, W.D. Nix, A model for dislocation behavior during deformation of Al/Al_3Sc (fcc/L12) metallic multilayers, Acta Mater. 51 (11) (2003) 3157–3170.
[17] A. Misra, J.P. Hirth, R.G. Hoagland, Length-scale-dependent deformation mechanisms in incoherent metallic multilayered composites, Acta Mater. 53 (18) (2005) 4817–4824.
[18] J.S. Koehler, Attempt to design a strong solid, Phys. Rev. B 2 (2) (1970) 547–551.
[19] S.I. Rao, P.M. Hazzledine, Atomistic simulations of dislocation–interface interactions in the Cu-Ni multilayer system, Philos. Mag. A 80 (9) (2000) 2011–2040.
[20] X. Chu, S.A. Barnett, Model of superlattice yield stress and hardness enhancements, J. Appl. Phys. 77 (9) (1995) 4403–4411.
[21] Z. Chen, Y. Zheng, Y. Huang, Z. Gao, H. Sheng, M. Bartosik, P.H. Mayrhofer, Z. Zhang, Atomic-scale understanding of the structural evolution of TiN/AlN superlattice during nanoindentation— Part 1: deformation, Acta Materialia (2022) 118008.
[22] H. Xiang, H. Li, T. Fu, Y. Zhao, C. Huang, G. Zhang, X. Peng, Molecular dynamics simulation of AlN thin films under nanoindentation, Ceram. Int. 43 (5) (2017) 4068–4075.
[23] R.F. Zhang, S. Veprek, Deformation paths and atomistic mechanism of B4→B1 phase transformation in aluminium nitride, Acta Mater. 57 (7) (2009) 2259–2265.
[24] V.I. Ivashchenko, P.E.A. Turchi, R.V. Shevchenko, L. Gorb, J. Leszczynski, First-principles investigations of the pressure-induced phase transformations and properties of crystalline and amorphous AlN, Phys. Rev. Mater. 4 (11) (2020) 113605.
[25] R.F. Zhang, S.H. Sheng, S. Veprek, Mechanism of the B3 to B1 transformation in cubic AlN under uniaxial stress, Phys. Rev. B 76 (7) (2007) 075208.
[26] D.G. Sangiovanni, F. Tasnádi, L.J.S. Johnson, M. Odén, I.A. Abrikosov, Strength, transformation toughening, and fracture dynamics of rocksalt-structure $Ti_{1-x}Al_xN(0\leq x\leq 0.75)$ alloys, Phys. Rev. Mater, 4 (3) (2020) 033605.
[27] N. Koutná, L. Löfler, D. Holec, Z. Chen, Z. Zhang, L. Hultman, P.H. Mayrhofer, D.G. Sangiovanni, Atomistic mechanisms underlying plasticity and crack growth in ceramics: a case study of AlN/TiN superlattices, Acta Mater. 229 (2022) 117809.
[28] X. Gu, Z. Zhang, M. Bartosik, P.H. Mayrhofer, H. Duan, Dislocation densities and alternating strain fields in CrN/AlN nanolayers, Thin Solid Films 638 (2017) 189–200 (Supplement C).
[29] R.F. Zhang, S.H. Sheng, S. Veprek, Mechanism of the $B3$ to $B1$ transformation in cubic AlN under uniaxial stress, Phys. Rev. B 76 (7) (2007) 075208.
[30] D. Chen, X.L. Ma, Y.M. Wang, Thickness-dependent structural transformation in the AlN film, Acta Mater. 53 (19) (2005) 5223–5227.
[31] A. Madan, I.W. Kim, S.C. Cheng, P. Yashar, V.P. Dravid, S.A. Barnett, Stabilization of Cubic AlN in Epitaxial AlN/TiN Superlattices, Phys. Rev. Lett. 78 (9) (1997) 1743–1746 .
[32] Z. Zhang, Z. Chen, D. Holec, C.H. Liebscher, N. Koutná, M. Bartosik, Y. Zheng, G. Dehm, P.H. Mayrhofer, Mapping the mechanical properties in nitride coatings at the nanometer scale, Acta Mater. 194 (2020) 343–353.
[33] Z. Chen, D. Holec, M. Bartosik, P.H. Mayrhofer, Z. Zhang, Crystallographic orientation dependent maximum layer thickness of cubic AlN in CrN/AlN multilayers, Acta Mater. 168 (2019) 190–202.
[34] K. Yalamanchili, F. Wang, H. Aboulfadl, J. Barrirero, L. Rogström, E. Jiménez-Pique, F. Mücklich, F. Tasnadi, M. Odén, N. Ghafoor, Growth and thermal stability of TiN/ZrAlN: effect of internal interfaces, Acta Mater. 121 (2016) 396–406 Supplement C.
[35] S.H. Jhi, S.G. Louie, M.L. Cohen, J.W. Morris, Mechanical instability and ideal shear strength of transition metal carbides and nitrides, Phys. Rev. Lett. 87 (7) (2001) 075503.
[36] U. Wahlström, L. Hultman, J.E. Sundgren, F. Adibi, I. Petrov, J.E. Greene, Crystal growth and microstructure of polycrystalline $Ti_{1-x}Al_xN$ alloy films deposited by ultra-high-vacuum dual-target magnetron sputtering, Thin Solid Films 235 (1) (1993) 62–70.
[37] M. Zhou, Y. Makino, M. Nose, K. Nogi, Phase transition and properties of Ti–Al–N thin films prepared by r.f.-plasma assisted magnetron sputtering, Thin Solid Films 339 (1) (1999) 203–208.
[38] B. Grossmann, N. Schalk, C. Czettl, M. Pohler, C. Mitterer, Phase composition and thermal stability of arc evaporated $Ti_{1-x}Al_xN$ hard coatings with $0.4\leq x\leq 0.67$, Surf. Coat. Technol. 309 (2017) 687–693.
[39] K. Kutschej, P.H. Mayrhofer, M. Kathrein, P. Polcik, R. Tessadri, C. Mitterer, Structure, mechanical and tribological properties of sputtered $Ti_{1-x}Al_xN$ coatings with $0.5\leq x\leq 0.75$, Surf. Coat. Technol. 200 (7) (2005) 2358–2365.
[40] A. Hörling, L. Hultman, M. Odén, J. Sjölén, L. Karlsson, Mechanical properties and machining performance of $Ti_{1-x}Al_xN$-coated cutting tools, Surf. Coat. Technol. 191 (2) (2005) 384–392.
[41] P.H. Mayrhofer, D. Music, J.M. Schneider, Influence of the Al distribution on the structure, elastic properties, and phase stability of supersaturated $Ti_{1-x}Al_xN$, J. Appl. Phys. 100 (9) (2006) 094906.
[42] M. Stueber, H. Holleck, H. Leiste, K. Seemann, S. Ulrich, C. Ziebert, Concepts for the design of advanced nanoscale PVD multilayer protective thin films, J. Alloy. Compd. 483 (1) (2009) 321–333.
[43] M. Fallmann, Z. Chen, Z.L. Zhang, P.H. Mayrhofer, M. Bartosik, Mechanical properties and epitaxial growth of TiN/AlN superlattices, Surf. Coat. Technol. 375 (2019) 1–7.
[44] G.I. Taylor, The mechanism of plastic deformation of crystals. Part I.—Theoretical, Proc. R. Soc. Lond. Ser. A 145 (855) (1934) 362–387 Containing Papers of a Mathematical and Physical Character.
[45] B. Devincre, L. Kubin, T. Hoc, Physical analyses of crystal plasticity by DD simulations, Scr. Mater. 54 (5) (2006) 741–746.
[46] M.B. Kanoun, S. Goumri-Said, Effect of alloying on elastic properties of ZrN based transition metal nitride alloys, Surf. Coat. Technol. 255 (2014) 140–145.
[47] E.S. Pacheco, T. Mura, Interaction between a screw dislocation and a bimetallic interface, J. Mech. Phys. Solids 17 (3) (1969) 163–170.
[48] C.-S. Shin, D. Gall, N. Hellgren, J. Patscheider, I. Petrov, J.E. Greene, Vacancy hardening in single-crystal TiN_x(001) layers, J. Appl. Phys. 93 (10) (2003) 6025–6028.
[49] T. Lee, K. Ohmori, C.S. Shin, D.G. Cahill, I. Petrov, J.E. Greene, Elastic constants of single-crystal TiN_x(001) ($0.67\leq x\leq 1.0$) determined as a function of x by picosecond ultrasonic measurements, Phys. Rev. B 71 (14) (2005) 144106.
[50] A. Leyland, A. Matthews, On the significance of the H/E ratio in wear control: a nanocomposite coating approach to optimised tribological behaviour, Wear 246 (1) (2000) 1–11.
[51] Q. Xia, H. Xia, A.L. Ruoff, Pressure-induced rocksalt phase of aluminum nitride: a metastable structure at ambient condition, J. Appl. Phys. 73 (12) (1993) 8198–8200.
[52] M. Mikula, D. Plašienka, D.G. Sangiovanni, M. Sahul, T. Roch, M. Truchlý, M. Gregor, L.u. Čaplovič, A. Plecenik, P. Kúš, Toughness enhancement in highly NbN-alloyed Ti-Al-N hard coatings, Acta Mater. 121 (2016) 59–67.
[53] L. Zhou, D. Holec, P.H. Mayrhofer, Ab initio study of the alloying effect of transition metals on structure, stability and ductility of CrN, J. Phys. D Appl. Phys. 46 (36) (2013) 365301.
[54] D. Holec, L. Zhou, R. Rachbauer, P.H. Mayrhofer, Alloying-related trends from first principles: An application to the Ti–Al–X–N system, J. Appl. Phys. 113 (11) (2013) 113510.
[55] D.G. Sangiovanni, L. Hultman, V. Chirita, Supertoughening in B1 transition metal nitride alloys by increased valence electron concentration, Acta Mater. 59 (5) (2011) 2121–2134.

Resume

A self-motivated, active & highly ambition graduate with a specialty in materials engineering and interpersonal skills

Profile:

Name: Zecui Gao **Gender:** Female

Born: [redacted]

Languages: English (C1); German (B1); Chinese (C2)

E-mail: zecui.gao@tuwien.ac.at

Tel.: [redacted]

[redacted]

Education:

- **2019/10-2022/10:** Doctoral program in materials science, TU Wien, Austria
  - Achieved: 4 publications in high-impact journals;
  - Research field: Ceramic coatings for applications in demanding environments.
  - Skills: Built a PVD system (assistant); Operated TEM and FIB equipment;
- **2016/09-2019/06:** Master program in mechanical engineering, Guangdong University of Technology, China
  - Achieved: 1 publication;
  - Research field: Ceramic coatings for energy storage applications.
  - Skills: Built a PVD (assistant); Operated PVD, SEM, XRD equipment.
- **2012/09-2016/07:** Bachelor program in materials science and engineering, Anhui University of Technology
  - Research field: Inorganic non-metallic materials, ceramics and cement
  - Skills: Writing of computer code, office and CAD software, welding, turning

- Experience:
  - Internship experience: Internship in Huasheng Vacuum Coating Company for 2 months, assisting in PVD machine manufacturing, cutting-tool coatings deposition, and product quality inspection.

- Conference experience: The 20th Plansee Seminar, poster presentation, May 30-June 3, 2022, Reutte, Austria; The 48th International Conference on Metallurgical Coatings and Thin Films (ICMCTF), oral presentation, May 22-27 2022, San Diego, California, USA.

- Award experience: Chinese Scholarship Council, 2019/10-2022/10

Publications:

- **Z. Gao**, J. Buchinger, N. Koutná, T. Wojcik, R. Hahn, P. H. Mayrhofer, *Acta Materialia,* 231 (2022) 117871.
- Z. Chen, Y. H. Zheng, Y. Huang, **Z. Gao**, H. P. Sheng, M. Bartosik, P. H. Mayrhofer, Z. L. Zhang, *Acta Materialia* (2022) 118008
- Z. Chen, Y. H. Zheng, Y. Huang, **Z. Gao**, H. P. Sheng, M. Bartosik, P. H. Mayrhofer, Z. L. Zhang, *Acta Materialia* (2022) 118009
- **Z. Gao**, Z. X. Wan, Z. Wu, X. L. Huang, H. Q. Li, T. F. Zhang, P. H. Mayrhofer, Q. M. Wang, Materials & Design 209 (2021) 109949
- **Z. Gao**, Z. T. Wu, S. S. Zhao, T. F. Zhang, Q. M. Wang, *Materials Letters,* 235 (2019) 148-152.

Abilities:

- Independent engineering researcher:
  - Advanced knowledge of many coating technologies and equipment;
  - Microstructure analysis using X-ray diffraction and electron microscopy techniques (SEM, FIB-SEM, EDS, TEM);
  - Mechanical testing techniques: bi-directional wear test, nanoindentation, in-situ micromechanical testing (such as, bending, tensile, and compressive tests, under some environmental conditions);
  - electrical workstations for electrochemical corrosion and kinetics tests;
  - Strong and independent writing and presenting skills
- IT skills:
  - Familiar with office software, as well as Origin, Photoshop, CAD, Python, and more;
- Language skills: Skilled English, basic German, and native Chinese in speech and writing;
- Good communication skills and learning ability;

- Team work spirit
- Leadership skills

Hobbies:

- Trail running
- Skiing, swimming, cycling, and bouldering

References:

- Prof. Paul H. Mayrhofer: paul.mayrhofer@tuwien.ac.at
- Prof. Qimin Wang: qmwang@gdut.edu.cn
- Dr. Julian Buchinger: julian.buchinger@infineon.com